MATHEMATICAL MODELLING FOR TOPOGRAPHICALLY INFLUENCED CELL MIGRATION AND THE MODULATING EFFECT OF CONNEXIN MIMETIC PEPTIDE GAP27 ON CONNEXIN 43 CYCLING AND 2-D SCRAPE WOUND CLOSURE: APPLICATIONS TO CUTANEOUS WOUND HEALING

Adam J. Mitchinson

A thesis submitted in partial fulfilment

of the requirements of Liverpool John Moores University

for the degree of Doctor of Philosophy

February 2022

I declare that the work presented in this thesis was carried out by myself at Liverpool John Moores University, Liverpool, UK, except where due acknowledgement is made, and has not been submitted for any other degree.

Adam J. Mitchinson (Candidate)

Date: 28th February 2022

To my family.

Contents

Acknowledgements **xi**

Abstract **xiii**

1 Introduction **1**

1.1 Cutaneous wounds and their cost 1

1.2 Biology of cutaneous wounds 3

1.2.1 The structure and composition of human skin 3

1.2.2 Cutaneous wound repair 4

1.2.3 Impaired healing and the role of connexins 7

1.2.4 Directed cell migration 9

1.2.5 Topographically influenced cell migration 10

1.3 Mathematical modelling studies 13

1.4 Thesis motivations and contributions 18

1.5 Methodology 21

1.5.1 Individual cell migration model 21

1.6 Thesis overview 27

2 A stochastic model for topographically influenced cell migration **30**

2.1 Introduction 30

2.1.1 Topographically influenced cell migration 30
2.1.2 Modelling studies 36
2.1.3 Motivations and contributions 39
2.2 Methods 42
2.2.1 Model 42
2.2.2 Method of parameter estimation 46
2.2.3 Experimental data 48
2.2.4 Migration metrics 50
2.2.5 Numerical implementation 52
2.3 Results 58
2.3.1 Parameter estimation 58
2.3.2 Initial conditions 62
2.3.3 Parametrised migration model with uniform linear topographies 64
2.3.4 Model predictions with randomly perturbed linear topographies 67
2.4 Discussion 74

3 A mathematical model for connexin 43 cycling and its dynamical modulation by connexin mimetic peptide Gap27 86

3.1 Introduction 86
3.1.1 Connexin 43 structure and life cycle 86
3.1.2 Connexin mimetic peptides 89
3.1.3 Modelling studies 90
3.1.4 Motivations and contributions 93
3.2 Methods 95
3.2.1 Model formulation 95

3.2.2 Reaction scheme 96
3.2.3 ODE system 99
3.2.4 Nondimensionalisation 100
3.2.5 Plaque state distribution $p_i(t)$: derivation of moment ODEs . . 104
3.2.6 Updated model system 111
3.2.7 Numerical implementation 113
3.3 Results 114
3.3.1 Initial conditions 114
3.3.2 Cx43 cycling without Gap27 115
3.3.3 Cx43 cycling with Gap27 125
3.4 Discussion 129

4 A mathematical model for connexin 43 based cell-cell interaction influenced cell migration and its dynamical modulation by connexin mimetic peptide Gap27 during 2-d scrape wound closure 134

4.1 Introduction 134
4.1.1 Connexins and cutaneous wound repair 134
4.1.2 Modelling studies 139
4.1.3 Motivations and contributions 144
4.2 Methods 146
4.2.1 Model 146
4.2.2 Numerical implementation 153
4.3 Results 159
4.3.1 Initial conditions 159
4.3.2 Scrape wound model with Gap27 163

4.3.3 Scrape wound model without Gap27 170

4.4 Discussion 174

5 Discussion **179**

List of Figures

1.1 Diagram to illustrate the structure and major components of human skin. 5

2.1 Schematic diagram to illustrate the components of the model topographic bias term. 45

2.2 Flow chart to illustrate the algorithmic approach chosen to conduct the parameter grid search for the model. 48

2.3 Schematic diagram to illustrate the measurement of 'orientation angle', θ, for a sample time increment. 53

2.4 Surface topographies generated using MATLAB, featuring 9μm, 6μm and 2μm groove widths with constant ridge width 1μm, from linear and uniform to directionally random and disordered. 57

2.5 Contour plots for model kinesis parameters, β and α, at fixed values for bias parameter, κ, resulting from a grid search optimisation for the four different topographies we consider: flat, 9μm groove width, 6μm groove width and 2μm groove width. 61

2.6 Metric data derived from Kim et al. [105] and the parametrised model for average groove widths 2.6μm, 6.3μm and 8.6μm and uniform groove widths 2μm, 6μm and 9μm, respectively. 62

2.7 Parametrised model migration trajectories over gradient fields of four different topographies: flat, 9μm groove width, 6μm groove width and 2μm groove width. 68

2.8 Orientation angle θ° and migration speed s (μm/h) distributions for four different topographies: flat, 9μm groove width, 6μm groove width and 2μm groove width. 69

2.9 Mean-squared displacement (MSD) (μm) over time t for flat, 9μm, 6μm and 2μm groove width topographies. 70

2.10 Model migration trajectories over gradient fields of four topographies with linear 2μm groove and 1μm ridge width topographic features perturbed stochastically in the direction orthogonal to the ridge/groove plane with four different 'noise' levels: $\rho = 0$, $\rho = 0.2$, $\rho = 0.35$ and $\rho = 0.5$. 75

2.11 Orientation angle, θ°, and migration speed, s (μm/h), distributions for the four topographies in Figure 2.10. 76

2.12 Model migration trajectories over gradient fields of four topographies with linear 6μm groove and 1μm ridge width topographic features, perturbed using the method described in *Methods* 2.2.5 using four different 'noise' levels determined by feature perturbation parameter ρ: $\rho = 0$, $\rho = 0.2$, $\rho = 0.35$ and $\rho = 0.5$. 77

2.13 Orientation angle, θ°, and migration speed, s (μm/h), distributions for the four topographies in Figure 2.12. 78

2.14 Model migration trajectories over gradient fields of four topographies with linear 9μm groove and 1μm ridge width topographic features, perturbed using the method described using four different 'noise' levels determined by feature perturbation parameter ρ: $\rho = 0$, $\rho = 0.2$, $\rho = 0.35$ and $\rho = 0.5$. 79

2.15 Orientation angle θ° and migration speed s ($\mu m/h$) distributions (left and right column, respectively) for the four topographies in Figure 2.14. 80

2.16 Orientation angle standard deviation, θ°_σ, and mean migration speed, s_μ (μm/h), against feature perturbation parameter, ρ, for 2μm, 6μm and 9μm groove width topographies. 81

3.1 Three diagrams to illustrate: **A.** the Cx43 cycling process, **B.** the structure of Cx43 and **C.** gap junction channels. 91

3.2 Nondimensionalised system without Gap27 solved for time t with all model parameters set equal. 103

3.3 Plaque states at equilibrium represented as a discrete distribution of plaque states i. 103

3.4 Concentration-adjusted plaque state distributions at equilibrium, p^*_i/p (blue), plotted alongside shifted geometric distributions, $G_s(\rho)$ (red). . 110

3.5 Derived moment equilibria, p^*_{avg}, p^*_{var} and p^*_{skew} (dotted-crossed), with $\hat{p}^*_{avg}$, $\hat{p}^*_{var}$ and $\hat{p}^*_{skew}$ (solid-circle), under variation to parameters $\widehat{k}_1/\widehat{k}_{-1}$, $\widehat{k}_2$ and $\widehat{k}_u$. 113

3.6 Averaged system without Gap27 variables over t for three different initial (nondimensional) concentrations of hemichannels h, $h(0) = 0$, $h(0) = 1$, $h(0) = 10$. 117

3.7 Averaged system without Gap27 equilibria as a function of gap junction formation/dissociation parameter ratio $\widehat{k}_1/\widehat{k}_{-1}$. 120

3.8 Averaged system without Gap27 equilibria as a function of gap junction/plaque binding parameter $\widehat{k}_2$. 121

3.9 Averaged system without Gap27 equilibria as a function of (within plaque) gap junction internalisation parameter $\widehat{k}_u$. 123

3.10 An example scenario in which a small concentration of large plaques form over t for averaged system without Gap27. 125

3.11 Averaged system with Gap27 for three different initial concentrations of g_{27}. 127

3.12 Averaged system with Gap27 over t for variations to hemichannel-Gap27 association/dissociation parameter ratio $\widehat{k}_{G27}/\widehat{k}_{-G27}$. 129

4.1 Schematic diagram to illustrate the three different cell-cell interaction scenarios considered in the model between neighbouring cells. 151

4.2 Diagram to illustrate the time-dependency of $p(\tau)$ in the cell-cell influenced migration model. 152

4.3 Flow chart to illustrate the algorithmic approach to numerical implementation of the model outlined in Section 4.2.2. 154

4.4 Flow chart to illustrate the cell packing algorithm outlined in Section 4.2.2. 156

4.5 Unpacked and packed initial cell configurations for the computational scrape wound. 157

4.6 Initial cell configuration for the 2-d computational scrape wound model 160

4.7 $p(\tau)$, where $p^* = 2.0835$, with varied initial concentrations for Gap27, $g_{27}(0)$. 166

4.8 Migration trajectories across the domain at time points $T = 300$, $T = 1350$ and $T = 2400$ (rows) with no Gap27, $g_{27}(0) = 0$ (left), and Gap27, $g_{27}(0) = 1500$ (right) when p^* is large. 167

4.9 Cell configurations across the domain at time points $T = 300$, $T = 1350$ and $T = 2400$ (rows) with no Gap27, $g_{27}(0) = 0$ (left), and Gap27, $g_{27}(0) = 1500$ (right) when p^* is large. 168

4.10 Coarse grained space of the spatial domain over T with no Gap27, $g_{27}(0) = 0$ (top), and with Gap27, $g_{27}(0) = 1500$ (bottom) when p^* is large. 169

4.11 Wound width (computed from coarse grained space) over T with (a) no Gap27, $g_{27}(0) = 0$, and (b) with Gap27, $g_{27}(0) = 1500$, and p^* large. . 170

4.12 Mean squared displacement (MSD, μm) over T with no Gap27, $g_{27}(0) = 0$, and Gap27, $g_{27}(0) = 1500$, and p^* large. 170

4.13 Migration trajectories across the domain at time points $T = 300$, $T = 1350$ and $T = 2400$ (rows) for small and large p^* (columns). 172

4.14 Cell configurations across the domain at time points $T = 300$, $T = 1350$ and $T = 2400$ (rows) for small and large p^* (columns). 173

List of Tables

2.1 Estimated migration metric data, θ^*_σ and s^*_μ, for flat and linearly ridged/grooved (with average groove widths: 8.6μm, 6.3μm and 2.6μm) topographies from Kim et al. [105]. 50

2.2 Migration model parameter combinations for flat, 9μm, 6μm and 2μm groove width topographies, determined by grid search optimisation with Kim et al. migration data [105]. 64

3.1 Substitutions used for the nondimensionalisation of system Eq. (3.14)-(3.24) 101

3.2 Rescalings used for the nondimensionalisation of system Eq. (3.14)-(3.24) 101

3.3 Equilibrium point ϵ_p for the 'base' model (without Gap27), approximated using MATCONT. 119

Acknowledgements

I would, first and foremost, like to thank all three of my primary supervisors for the project, Dr Mark Pogson, Dr Steve Webb and Dr Ivo Siekmann, without whom this project wouldn't have materialised. Mark, thank you for all the help with the topography model and of course assembling the project in the first place! Steve, I'd like to thank you for all the generous help and guidance you gave to me throughout the two years we worked on the project together, particularly for the topography and connexin models and your technical expertise. Ivo, I'd like to thank you for your help with all parts of the project, in particular the final chapter, but also for the constant encouragement and patience which helped me to get to the submission stage, which I thought from time to time might not happen.

I'd also like to thank my other project supervisors, Dr Mark Murphy and Dr Rob Wilkinson. Mark, thank you for all your help with the biology and biotech side of the project, the experimental data-sets and generally all the interest you maintained in the project from the start. Rob, thank you for taking over from Ivo in one of the supervisory roles on the project supervisory team, I really appreciate you stepping in. I'd like to give a special thanks Dr Patricia Martin, whose expertise with connexins has been invaluable both to me personally in understanding these tiny proteins, and the modelling process in general.

I'd also like to thank Dr Gabriela Czanner, Dr Darren Conway and Dr Taybia Mo-

hammed for their generous assistance in data analysis, biological understanding and providing experimental data for *Chapter* 2 which, unfortunately, don't appear in the final thesis but was crucial in the progression of the project. Dr Ina Deutschmann, I'd like to thank you for being a constant source of (remote) motivation for getting this thesis done, if you're reading this it means (somehow) I managed it!

To my "academic siblings", Chantelle, Terry and Andy, I'd like to thank you for all the indispensable help and guidance you have given to me throughout my time as a postgraduate but, most importantly, for your wonderful and enduring friendship. I quite simply wouldn't have enjoyed the PhD without you guys.

I'd like to give a special thanks to Dave and Michelle at Symphony Music, for being such generous employers and giving me my old job back. And to my good friend Tom, for making Fridays such a welcome break from writing.

And finally, to my family, to whom this thesis is dedicated. I'd like to thank my parents, Debbie and John, for taking care of me whilst I finish this, my sister Rachael, husband Chris, my nephews Freddy and Harry and all my extended family. And finally our feline companions Blossom and Bluebell for their spirit-lifting antics!

Abstract

Cutaneous wounds represent a serious economic and health burden for many developed nations. In the U.K., around 2.2 million people a year receive wound care, absorbing roughly 4% of total NHS annual expenditure. Chronic cutaneous wounds in particular may possess poor prognoses. Diabetic foot ulcers, for example, carry a five-year mortality rate comparable to cancer. The prevalence of chronic wounds amongst developed nations is anticipated to rise further, with increasing incidence of conditions strongly associated with chronic wound aetiology, such as obesity and diabetes.

A common feature among chronic wounds is the dysfunctional regulation of connexin proteins in cutaneous tissue, which ordinarily modulates in a carefully orchestrated manner post-injury to enable effective healing. Experimental studies targeted to the restoration of the typical spatio-temporal expression pattern of connexins post-injury have shown accelerated and improved healing outcomes across a range of *in vitro*, *in vivo* animal and *ex vivo* human models, and now clinical trials - with various connexin-targeted agents established as promising therapeutic candidates.

Physical properties of the extracellular environment have long been known to regulate cellular behaviours. Cutaneous tissue presents a huge range of topographic configurations that cells must navigate in order to carry out reparative function during wound repair. Surface 'topography' has since been established in the experimental literature as a major regulator of cell migration behaviour. The capacity for topography to influence migration has been shown to have significant applications in biomaterial and bioimplant design and development, including advanced wound healing treatments like 'skin substitutes'.

In this thesis, we propose three new mathematical models pertaining to these applications. We derive a stochastic model for topographically influenced cell migration, based on a biased Ornstein-Uhlenbeck cell model. We use this model to probe the influence of linearly and randomly organised topographies on migration trajectory behaviour and how the gradual introduction of random perturbations to linear features changes this behaviour, with the intention to further understand how surface imperfections introduced by surface fabrication impact migration.

We then derive a mathematical model for connexin 43 (Cx43) cycling dynamics and its dynamical modulation by connexin mimetic peptide Gap27, using mass action kinetics. We use this model to further understand how the introduction of Gap27 may function to affect Cx43-based species dynamics.

Finally, we derive a mathematical model for Cx43-based cell-cell interaction influenced cell migration and its dynamical modulation by Gap27 within a 2-d computational model of a scrape wound. We use this model to investigate how Cx43 dynamics might affect cell migration behaviour and population invasion of a scrape wound and how Gap27 might modulate these cellular behaviours.

Chapter 1

Introduction

1.1 Cutaneous wounds and their cost

A cutaneous wound may broadly be described as damage sustained to the skin which results in impairment to its regular anatomical structure and function [1, 2]. Cutaneous wounds typically emerge from an injurious event which may result from trauma (surgical incision, for example) or prolonged stress (such as with pressure ulceration) [1, 2]. The regular healing process can become disrupted by the presence of local (e.g. bacterial infection) or systemic (e.g. diabetes mellitus) conditions, making the wound hard-to-heal and cause the wound to have different clinical presentations [1, 2]. Examples of such 'chronic' wounds include venous, leg, pressure and diabetic foot ulcers [1, 2].

Wounds represent an enormous economic burden, particularly for developed countries. In the UK, it is estimated that around 2.2 million adults receive wound care by the NHS annually, costing about £5 billion a year or around 4% of total NHS annual expenditure - comparable to the annual NHS expenditure on obesity [3, 4, 5, 6]. An estimated £1.9 billion of this cost is attributable to the treatment of leg ulcers. Pressure and diabetic foot ulcers each incurring an annual cost of around £500 million [5]. The majority of

this huge annual healthcare cost is allocated to hospitalisation and nursing care, some of the most valuable resources in the healthcare system [3].

In the U.S., around 6.5 million people annually undergo treatment for a chronic wound, costing the healthcare system an estimated $25 billion [7]. In Scandinavia, wound care incurs an average cost of around 2-4% of annual healthcare expenditures [7]. As a whole, developed countries are conservatively estimated to spend around 1–3% of total healthcare expenditure on the management and treatment of chronic wounds [8]. Such figures look set to rise, with the increasing prevalence of conditions strongly associated with chronic wound aetiology, including obesity, diabetes and age [7].

The human cost can be devastating. Diabetic foot ulcers, for example, have been shown to have a five-year mortality rate comparable to cancer, around 30%, and carry a high risk of severe complications including infection and limb amputation [9, 10]. Chronic wounds can be particularly deadly for older patients. A study by Khor et al. found pressure ulcers in hospitalised adults aged 65 and over to have a 12-week mortality rate of 66% [11]. Living with chronic wounds can also be particularly distressing. A recent review article by Olssen et al. reported that patients with chronic wounds typically report low health-related quality of life (HRQoL) scores, pain and disability being particularly troubling for patients [8].

Standard wound care treatments, e.g. tissue debridement and administration of antimicrobial agents, are often rendered ineffective once a chronic persistent pathology has been established within a wound [1]. Thus there is a pressing need for more effective wound treatments, in particular to resolve complex chronic cutaneous wounds [9].

1.2 Biology of cutaneous wounds

1.2.1 The structure and composition of human skin

Human skin comprises two distinct layers: a densely cellular outer epidermis and, lying beneath, a vascular collagen-rich dermis with a sparse cell population [12]. The epidermis is a specialised epithelium consisting mostly of tightly packed keratinocytes, interspersed with an array of other cell types e.g. melanocytes, Langerhans and Merkel cells, arranged into four well defined sub-strata: the stratum basale, a layer of cells which attach to the dermal-epidermal junction defined by the basement membrane; the intermediary strata spinosum and granulosum; and the stratum corneum, the surface layer of cornified keratinocytes termed 'corneocytes' [13]. Corneocytes at the stratum corneum continually exuviate, making way for keratinocytes that advance progressively away from their moorings at the basement membrane through the intermediary strata towards the surface, taking on strata-specific functional adaptations on their journey [13]. Keratinocytes in the basal layer are typically replaced by resident stem cell differentiation, thus establishing a cycle of epidermal regeneration [13]. The epidermis also contains hair follicles, sebaceous and sweat glands, typically bedded deep within the dermis [14]. Throughout the strata cells are compacted together, component cells adhering to each other via adhesive desmosomes and adherens junctions, conferring principally via gap junction channels which directly link the cytoplasms of neighbouring cells [13].

Beneath the dermal-epidermal junction lies the dermis, much of which is composed of a well vascularised collagenous connective tissue termed extracellular matrix (ECM). ECM is made up of a dense network of interconnected fibrils (mostly collagen, but includes a range of other proteins such as laminin and fibronectin) providing mechanical

support to the epidermis. ECM typically accommodates a comparatively sparse cell population, mostly fibroblast cells (though macrophage and mast cells also make up a significant proportion) that maintain, repair and remodel matrix structures; though ordinarily quiescent unless activated by endogenous agents [15, 16, 17]. The dermis is also home to a comprehensive network of microvasculature providing nourishment and aid to the epidermis and epidermal appendages [14]. Below the dermis lies subcutaneous adipose tissue which functions primarily as an energy cache, holds substantial vasculature and influences regulation of growth factors [14].

A diagram to illustrate the structure and major components of human skin, particularly the epidermis, is presented in Figure 1.1.

1.2.2 Cutaneous wound repair

A primary function of cutaneous tissue is to protect against the harsh conditions of the external environment and so any compromise to the integrity of these tissues must see a quick response to avoid further tissue degradation. Cutaneous wounds are typically 'patched up' with a haemostatic clot which begins to form immediately post-injury and the damaged or missing tissues subsequently reconstituted and remodelled over the days and weeks that follow [12].

Cutaneous wound repair is complex, it involves a careful orchestration of a vast network of interactions between cells, tissues, biochemical and biomechanical factors. Healthy repair follows a typical pattern and is generally classified into four major temporally dependent phases: haemostasis, inflammation, proliferation and remodelling [1].

In the haemostatic phase, platelet-ECM contact, caused by spillage from cut vasculature, triggers platelet aggregation into a small cellular plug. The plug provides a surface for coalescence of coagulation complexes, this in turn initiating a coagulation

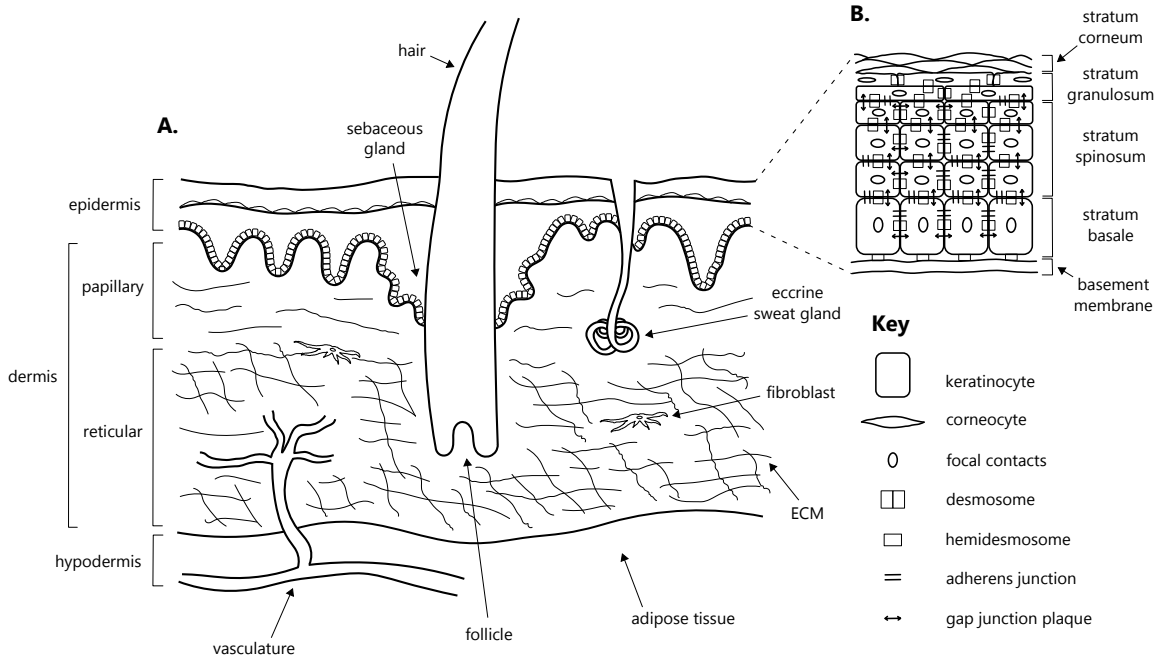

Figure 1.1: Diagram to illustrate the structure and major components of human skin. **A.** Cross-sectional illustration of human cutaneous tissue. The tissue can be grouped into two major components: epidermis and dermis; with the hypodermis lying (subcutaneously) beneath the dermis. Extracellular matrix (ECM) composes much of dermal tissue. The top layer of dermal tissue typically accommodates epidermal protrusions, called the papillary dermis. Beneath is a denser layer of tissue called the reticular dermis. **B.** Magnified cross-sectional illustration of the epidermis and its major cellular and structural components. The epidermis can be split into its component layers: the basement membrane, immediately anchored above is the stratum basale, followed by the stratum spinosum, the stratum granulosum and topped by a surface layer of corneocytes, the stratum corneum. Cells in the epidermis adhere by focal contacts (oval), desmosomes (rectangle) and adherens junctions (parallel lines), conferring via gap junction channels (double-headed arrow).

cascade resulting in a much larger and more robust fibrin clot. The clot stabilises the wounded region and provides a constant source of vasoactive and chemotactic growth factors, cytokines and chemokines, functioning later on in the healing cascade as a mechanically stable matrix for subsequent infiltration by various cell types [1, 14].

Passive vasodilation then enables neutrophils to extravasate around, then migrate into, the wounded region guided by attractants within the clot, followed soon thereafter by monocytes which differentiate into macrophages, this marking the start of the inflammatory phase. Both neutrophils and inflammatory macrophages extract debris and

foreign material from the wound, phagocytosing bacteria and other micro-organisms. These cells also release various growth factors, cytokines and chemokines that activate endothelial and fibroblast cells, stimulating angiogenesis and granulation tissue formation respectively [2].

Concurrent with (though initiating slightly after) the inflammatory phase is the growth or proliferative phase, in which new tissue and vasculature are generated both to replace damaged and lost structures and to aid healing. Soon after clot formation, wound-edge keratinocytes initiate phenotypic changes which enable their migration into the clot. With time, and contraction of the tissue beneath, the migrating keratinocytes re-establish a new epithelium which matures into a new fully stratified epidermis [2, 12, 14].

In response to various biochemical signals released by platelets, neutrophils, macrophages and wound-edge keratinocytes, activated endothelial cells are stimulated to migrate into surrounding tissue and develop new vasculature to support healing and replace that lost to injury. Fibroblasts are also stimulated to migrate into the clot, gradually dissolving and reshaping it leaving a stronger more collagenous matrix in its place. The resulting densely vascularised new matrix tissue is known as granulation tissue [2, 12, 14].

The wound is matured by persistent remodelling of the granulation tissue. Fibroblasts differentiate into myofibroblasts whose local contractile pressure on matrix fibrils globally contracts the tissue, helping to re-establish epithelial continuity, accelerating reepithelialisation. Over time ECM takes on a more organised and collagenous form. Eventually, once the healed tissue is sufficiently matured, any excess cells apoptose, surplus microvasculature dissolve to protect the wider vascular system and metabolic activity tapers back to pre-injury levels, leaving a sparsely populated scar tissue [18].

The scar tissue resulting from a healed wound is typically only around 70% the tensile strength of unwounded tissue, unlike in fetal tissue the repair process in adult humans is not perfectly regenerative [1].

1.2.3 Impaired healing and the role of connexins

Cutaneous wounds sometimes fail to heal, the result typically being described as a 'chronic wound'. Fundamental causes for impaired healing may be either or both local (e.g. hypoxia, bacterial infection) and systemic (e.g. metabolic or vascular disease, age), creating the kind of physiological conditions from which dysfunction in the healing cascade can arise [1]. Systemic conditions in particular can prompt a complex and diverse set of healing dysfunctions. Diabetes mellitus, for example, is associated with impaired and delayed cellular activity which sets up persistent inflammation, and the wound bed prone to colonisation by particularly pathogenic hard-to-treat bacteria, along with a host of other associations disruptive to the healing process [2, 14].

A common feature of chronic wounds with different aetiologies is the dysfunctional regulation of connexin proteins. Connexins are a family of small conformationally similar proteins which come together intracellularly to form functional hemichannels (or 'connexons') and, with subsequent adherence to other cells, gap junction channels at the cell membrane. The spatio-temporal regulation of different connexins throughout the repair process is thought to be critical to enable effective healing [19, 20].

The most common connexin in cutaneous tissue is connexin 43 (Cx43), expressed in particularly high concentrations in suprabasal keratinocytes, forming many of the gap junction channels residing in this region, but is also expressed in dermal fibroblasts [21, 22]. In the hours post-injury, Cx43 in regions proximal to the wound is ordinarily temporarily down-regulated, with other connexins up-regulated in its place. Cx43

expression slowly swells back to pre-injury levels in the region in the coming days [22, 23, 24].

Different connexins are thought to confer variable gating characteristics on the hemichannels and gap junction channels which they jointly compose, and it is proposed that the observable post-injury changes to connexin expression initiate a progressive spatial partitionment of tissues around the wound which helps cells to coordinate collective behaviours like migration and proliferation so crucial to the inflammatory and growth phases of healing [19, 20].

Disruption to the typical expression patterns of connexins post-injury has been associated with impaired healing. For example, a study by Sutcliffe et al. found that the marked up-regulation of dermal and epidermal Cx43 was a distinct characteristic among punch biopsy samples taken from the visibly discernible edges of human diabetic, venous and pressure ulcers [25]. The abnormal up-regulation of wound-edge Cx43 post-injury is found to be a distinct feature among chronic wounds across a range of human and animal studies [22, 26, 27].

Moreover, studies that have targeted Cx43 for knockdown, transient down-regulation or disruption to channel function have typically shown accelerated and improved healing in animal models [28, 29, 30]. This has led to great interest in targeting Cx43 for therapeutic use and the development of Cx43-based wound treatment protocols. Antisense oligonucleotides, for example, which target connexin expression, have shown considerable efficacy in accelerating healing in animal models, and is the main active ingredient in the drug candidate *'Nexagon'*, targeted at the treatment of corneal wounds [21, 31]. Connexin mimetic peptides (CMPs), which interfere with channel function by conformationally mimicking molecular connexin sequences and binding to connexins,

have also shown promise in enhancing wound closure across a range of *in vitro* 2-d and 3-d skin models, *in vivo* animal models and *ex vivo* human skin [21]. CMPs have also been useful in elucidating the potential roles of connexins in wound healing. Wright et al., for instance, showed CMP-induced reduction in connexin-based channel activity increased migration rates in keratinocytes and fibroblasts and significantly accelerated 2-d scrape wound closure; thus demonstrating that the transient cessation of intercellular communication may play an important role in cells adopting migratory phenotypes during the healing process [32].

1.2.4 Directed cell migration

Cell migration, at a general level, is characterised as the translocation of individual or multiple cells [33]. It is of critical importance to multicellular organisms, being influential in many physiological and pathophysiological processes including wound healing, morphogenesis [34], immune response and cancer metastasis [35]. The means by which most eukaryotic animal cells migrate is known as 'crawling' [33]. Crawling is the result of complex interplay between constituent biopolymers of the cell cytoskeleton. During motion, the biopolymer 'actin' undergoes polymerisation, extending the cytoskeleton outward as 'filopodia'. The filopodia then senses candidate areas for adhesion to the underlying substrate. Adhesion triggers de-adhesion in the direction opposing the newly adhered filopodia. Mechanical potential generated through interaction between actin filaments and myosin motor proteins are thought to produce enough force to ratchet the cell forward in the direction of the leading filopodia [33, 36]. Cell types which maintain crucial function in cutaneous healing, e.g. epithelial, macrophage, fibroblast and endothelial, migrate by means of the 'crawling' motility cycle.

However, the extracellular environment is complex and migrating cells must traverse a

diverse range of microenvironments containing various stimuli and bio-cues in order to conduct reparative functions. It remains unclear as to how cells incorporate the huge array of guidance and directional cues from the surrounding extracellular environment into the intrinsic motility system to produce directed migrations [37].

Cells have long been known to sense and respond to their environment, the many environmental factors affecting migration being well-documented. Chemical and physical components of the local microenvironment can cause migration to become oriented – known as 'taxis' – or disoriented – known as 'kinesis' [38]. Directionally random migration typically occurs in the absence of stimulative environmental cues (e.g. a featureless 2-d surface) or in the uniform presence of a motogenic signal (a stimulant of the intrinsic motility system of a cell e.g. a growth factor driving chemokinesis) [37]. A cell's migration can be modulated by the presence of some asymmetric cue, described as a gradient [37]. The most well studied type of directed cell migration is chemotaxis, in which cells respond to a local soluble chemical gradient. Types of physically directed migration include that prompted by substrate stiffness or 'rigidity', cells appearing to favour stiffer substrates when in motion - known as durotaxis [39]; substrate adhesiveness - haptotaxis [40], surface topography and matrix topology - referred to traditionally as 'contact guidance' [41, 42].

1.2.5 Topographically influenced cell migration

Among the many physical cues to which cells respond *in vivo* is the varied topology and topography presented by the complex 3-d fibrillar structure of the ECM. A huge body of *in vitro* experimental studies show that substrate topography can directionally alter the migration behaviour of individual cells. For example, studies focusing on topographies with micron scale grooves have shown fibroblasts [43, 44], neurons

[45], endothelial [43], epithelial [46] and smooth muscle cells [43] to migrate along the surface grooves in clear alignment with groove orientation. Topographies with lattice arrangement have been shown to prompt preferential cell migration along the long side of rectangular grids [47]. On topographies with micron scale pillar features fibroblasts have been shown to exhibit more tortuous migration paths and higher speeds [48].

The topographic regulation of cell migration has significant biomedical applications, a substantial experimental research literature is dedicated to its exploitation for biomaterials and bioimplant design. A major application is in tissue engineering, where topographies can be used to influence cell positioning and population of tissue 'scaffolds' and the subsequent *in vitro* development and application of various tissues [49]. An example is a 'skin substitute', an advanced topical treatment for cutaneous wounds designed to mimic the structure and composition of native epidermis, dermis or fully integrated cutaneous tissue, with dual primary intentions of both providing wound coverage and stimulating cellular infiltration, neovascularisation and new tissue deposition, in effect 'reviving' the healing process [2]. The scaffold structure used to develop and carry the substitute may be constructed of natural (e.g. collagen, sterilised ECM) or synthetic biomaterial; contain cells (autologous or nonautologous), growth factors and cytokines or be acellular or decellularised; and be produced by a variety of manufacturing techniques which may influence topology, topography and material characteristics of the scaffold [2, 14, 50]. Skin substitutes approved for clinical application, such as *'Integra'* and *'Apligraf'* (decellularised and populated bovine collagen structures, respectively), have shown success in the treatment of selected burn wounds [14].

Another significant application for topographies is to improve integration of implanted medical devices (e.g. structural, dental, and cosmetic). A major reason for the failure

of some medical implants is due to tissue encapsulation caused by migration, adhesion and proliferation of cells around the device, so that the implant becomes completely enveloped by cells and unintegrated with the tissue. This is a particular issue for dental implants, leading to bacterial infection in spaces between tissue and implant, inflammation and subsequent removal of the implant [51]. Other problems include immune-mediated cell migration. Immune cells such as macrophages have been shown to accumulate on surfaces with certain topographic features [52]. The presence of macrophages upon medical implants is thought to contribute to the inflammatory responses observed in the failure of some medical implants [53]. Medical devices with topographies specially designed and engineered to regulate or inhibit such migration could improve clinical outcomes for implantation.

1.3 Mathematical modelling studies

The mathematical modelling literature pertaining to cutaneous wound healing stretches back over thirty years. Early prolific and influential authors include J.D. Murray, J.A. Sherratt and P.K. Maini, amongst others, whose work collectively has studied most of the main phases of cutaneous wound healing. Modelling literature in this area today is abundant, benefiting from increased inter-disciplinary practice and improved technology, leading to large complex and realistic models.

Though mathematical models have been used to study all phases of cutaneous wound healing, most modelling attention has been focused to specific components of re-epithelialisation, tissue remodelling and contraction, and angiogenesis (for in-depth reviews of re-epithelialisation, remodelling and contraction models see Murray's Mathematical Biology II [54] and Maini, Olsen and Sherratt's review of wound contraction models [55], for a recent comprehensive review of angiogenesis models see Guerra, Belinha and Jorge [56]) encompassed by the inflammatory and proliferative phases of healing [57, 58, 59]. Many early studies focused modelling to foundational elements of re-epithelialisation and, more generally, the directed migration and proliferation of cells around the wound space; typically favouring either an individual or continuum-based modelling approach, single-scale and often confined to one or two spatial dimensions.

A classic early study by Sherratt and Murray characterised both the migratory and proliferative elements of re-epithelialisation using a two-field PDE model, the total change in cell population over time described by a diffusion (for migration) and a chemically regulated logistic growth term (for proliferation), the diffusing chemical described in a separate coupled field [60].

Another early study by Tranquillo and Murray proposes a model of fibroblast-driven

wound contraction built upon earlier models of cell-matrix interaction in morphogenesis developed by Murray and co-workers. The authors define a 'base' three-field PDE model (in 1-d), describing: fibroblast concentration, determined by migration, cell mitosis, death and ECM deformation; ECM concentration, determined by ECM-fibroblast deformation; and ECM/fibroblast composite concentration, determined by fibroblast and ECM concentrations and a force balance between traction force of cells and viscoelastic properties assigned to ECM. This 'base' model is extended by incorporating a soluble mediator of fibroblast behaviour and dynamical properties of the ECM, considering spatially-dependent modulation to traction forces, proliferation, chemotaxis and ECM synthesis. The authors are able to parametrise all extensions to the model which are able to reproduce the characteristic exponential decay in the wound area over time observed experimentally [61].

In more recent modelling literature, we see a trend for larger and more complex models, often multi-scale, three-dimensional and frequently use hybrid modelling approaches to span composite scales [58]. These more complex characterisations enables the study of systems more comparable in complexity to actual biological systems and can provide valuable dynamic and mechanistic insights but can become difficult to analyse.

Due to its wide-ranging influence on various physiological and disease processes, directed cell migration has received much attention by modellers. Cell-based chemotaxis in particular, has been studied widely using a number of different approaches including individual-based biased random walks [62], pseudopod-based models [63], and automata, as well as classic Keller-Segel-based models [38]. As it began to emerge experimentally just how responsive cell can be to their physical environment, modellers also began to probe physical cell-substrate interactions. Modellers have studied

cell-fibril interactions [64], durotaxis [65], cell-topography interactions [66], cell-matrix interactions and most recently multi-cue environments [67].

Topographically influenced cell migration has been extensively studied in experimental-based literature over recent years. The recent proliferation in experimental study has been broadly motivated by the therapeutic potential presented by bioengineering and biomaterial research. Much of the literature aims principally to elucidate the cell mechanisms responsible for the cell-substrata interaction in native tissues and subsidarily for technological progress e.g. improved integrability of biocompatible scaffolds and implants. The modelling literature pertaining to this interaction is, by comparison, relatively sparse. Early migration models to incorporate topographic components often modelled cell-fibril contact guidance or contained within larger models of ECM dynamics in which cell-topography interaction was dynamically interdependent.

Tranquillo and co-workers, notably Barocas, were such early authors, proposing a model for contact guidance within larger frameworks modelling the dynamics of tissue equivalents (T.E.s, e.g. collagen gels). The authors describe contact guidance as an anisotropic diffusion, directed by alignment of fibrils in a fibrillar network within the T.E. [68].

Dallon and co-workers describe cell-ECM interaction using a hybrid approach with discrete cells on a continuous vector field representing fibril directions within an ECM. One particular theoretical study simulates fibroblast remodelling of ECM and fibrin clot to examine the effects of cell speed, density and flux on fibril orientation and alignment, with the aim of identifying factors that influence scar tissue formation [64].

More recent modelling work has begun to explore how migration is affected by classes of topography often studied in experimental biomaterial literature e.g. grooved, spher-

ical, curved and pitted. Such work typically features descriptive biophysical models motivated by quantifying morphological and stress changes that occur when cells move in relation to some of the topographical features described, for example see Heydari et al. [66] and Winkler et al. [69]. A more in-depth review of this literature is presented in *Chapter* 2 - *Introduction*.

The physiological ubiquity of connexin proteins, and their influence on composition and function of inter-cellular channels, hemichannels and gap junction channels, has drawn considerable attention from mathematical modellers. Gap junction channel properties and functions in particular have been well-studied, many modelling works particularly focusing on channel conductance and permeability.

An early study by Vogel and Weingart modelled gap junction channels as an electrical circuit, describing channel gating in response to transjunctional voltage and variable conductance states [70]. Other studies have used network-based cell population models explore the influence of gap junction conductance on cardiac arrhythmias [71], probe synchrony of electrical activity via gap junctions in β-cell clusters in the pancreas [72] and describe Ca^{2+} wave propagation through gap junction channels in a cell neighbourhood [73].

A study by Mondal et al. looked into how morphology of the channel 'pore', conferred by different connexin types in channel composition, influenced channel flux [74]. Bressloff proposed a model of diffusing particles within a 1-d domain of gap junction connected cells, and used it to derive effective permeability of the gap junction joining the two cells [75].

The influence of connexins in wound repair appears to a relatively unexplored area in the mathematical modelling literature. A significant early attempt to address this

explicitly is presented in a study group report published online by Roberts et al. [76]. The authors propose four different models: a 2-d cellular Potts approach [77] modelling a connexin-based switch between migratory and proliferative behaviours proximal to a 'wound'; a cellular automata approach describing fibroblast migration around wound edges, cells assigned with an associated connexin-based proclivity to aggregate, the introduction of a connexin-mimetic peptide (CMP) reducing the binding effects of connexin and wound width; a discrete-point wound model, based on models published by Dallon, Sherrat and Maini [64, 78], introducing an additional connexin-based adhesive pull from neighbouring cells and set the computational domain within a 2-d scrape wound model; and a continuum (PDE) approach with four main components: cell density, Cx43 concentration, signalling molecule concentration and connexin mimetic peptide (CMP) concentration, to model the transient down-regulation of Cx43 at wound edges and its effect on migratory and proliferative phenotypes, and effect of CMP an *in vitro* scrape wound assay.

More recently, a study by Montgomery et al. investigated how connexin mimetic peptide αCT1 affects scar tissue formation using a computational scrape wound model, looking in particular at how αCT1 influenced fibroblast migration during healing. Results suggested the peptide could diminish cell sensitivity to physical guidance cues [79].

We present a more detailed consideration of the modelling literature pertaining to connexins and connexins in wound repair in *Chapter* 3 - *Introduction* and *Chapter* 4 - *Introduction*.

1.4 Thesis motivations and contributions

Topographies have been shown to modulate many different cell behaviours, and can present powerful guidance cues for cell migration. Cutaneous tissue presents a huge range of different topographic configurations for cells to traverse. The alignment of certain regions of dermal ECM (corresponding to tension lines) could provide an important guidance cue for fibroblast invasion into a wound site in the ensuing days post-injury [80]. Topographies have also shown utility in wound healing treatments such as in the effective development of skin substitutes, influencing population and positioning of cells on tissue scaffolds, amongst other applications. Whilst cell-matrix interactions, particularly fibrillar-based contact guidance, have been frequently modelled in the literature, stretching back thirty years, topographically influenced migration models tailored to biotechnology applications has only relatively recently emerged and is still in its infancy. Expansion of this modelling literature has the potential to streamline the experimental process by characterising migration responses to specific classes of topographies, enabling experimentalists to focus on topographies featuring surface geometries and dimensions most useful for inducing certain migration distributions, patterns and behaviours.

Healthy cutaneous tissue contains an expansive, differential and dynamically adaptable expression of connexin proteins. This connexin network modulates spatio-temporally in response to cutaneous injury, the dysregulation of which is strongly associated with the aetiology of chronic non-healing wounds. Agents targeted to correct such dysregulation, in particular to restoring the transient down-regulation of Cx43 at the wound edge in the hours immediately post-injury, have shown success in improving healing outcomes. Although there exists a sizeable modelling literature exploring properties and function

of gap junction channels, the fundamental connexin cycling dynamics which underpin channel functions appears to have been overlooked. A small number of modelling studies look at the influence of connexins on wounds, probing specifically their influence on migration and proliferation behaviour and how the addition of mimetic peptides could alter this to produce the kinds of therapeutic outcomes reported. We use this small body of literature as a basis on which to develop a new model describing connexin 43 influence on cell-cell interactions within a migrating population, and use it to test the influence of a CMP on scrape wound closure.

In the presented thesis, we propose to make the following contributions:

(i) **Derive a stochastic model for topographically influenced cell migration.** Based on a biased Ornstein-Uhlenbeck (OU) cell model, we model individual cells as discrete-points whose velocity is determined by an OU process directionally biased by a surface gradient field, the cell guided towards contour directions. We parametrise the model using published metric data for *in vitro* fibroblast migration on a linear surface topography with variable groove dimensions. We test the parametrised migration model for topographies with both linear features and linear features with random perturbations with dimensions approximating those in the data-set. Findings suggest the introduction of random perturbations to linear features significantly disrupts highly directional migration, particularly for linear features with smaller dimensions. Findings could have implications for experimentalists looking to use coarse surface fabrication methods to induce highly directional migration in fibroblast cells. See *Chapter* 2.

(ii) **Derive a mathematical model for Cx43 cycling dynamics and its dynamical modulation by connexin mimetic peptide Gap27.** We formu-

late a reaction scheme for Cx43 cycling dynamics with Gap27 binding kinetics, from which we derive a full ODE model using mass action kinetics. We reduce the large system by considering only distribution moments of the sub-system of plaque states, deriving moment ODEs and introducing them into the ODE system. We explore the dynamical behaviour of the model under variation to initial concentrations and model parameters both without and with Gap27. Findings suggest Gap27 has an effect on only transient behaviour of the model over time, leaving equilibria unaffected. See *Chapter* 3.

(iii) **Derive a mathematical model for Cx43-based cell-cell interaction influenced cell migration.** Using both developed models for individual cell migration and Cx43 cycling with Gap27, we derive a coupled model for Cx43-based cell-cell influenced cell migration. We assign discrete-point cells spatial components which interact dependent on proximity with other cells within a population and total gap junction plaque concentration variable from the Cx43 cycling model. We test the model within a computational model of a scrape wound assay in 2-d and explore how plaque concentration and Gap27 variables, p and g_{27}, affect migration behaviour and its subsequent closure. Findings suggest Gap27 could induce scrape wound closure by reducing cell clustering prompted by high gap junction plaque concentrations. Findings also suggest Gap27 works in a concentration-dependent manner and may not improve wound closure if gap junction plaque concentration is already low. See *Chapter* 4.

1.5 Methodology

1.5.1 Individual cell migration model

We use an approach first introduced by Dunn and Brown for modelling random cell motility [81], further developed by Stokes, Lauffenburger and Williams [62] amongst other authors for taxis behaviours. The approach is to model a single cell's velocity with a stochastic differential equation, typically based around an Ornstein-Uhlenbeck process, giving a complete model for the migration trajectory of an individual cell. Since its introduction as a model for cell migration, the approach is typically adopted when individual cell directionality (often under some environmental condition) is of principal interest and the micro-components of migration (e.g. motility machinery) are of less interest.

Origins in Brownian motion

The Ornstein-Uhlenbeck process has its origins in the first mathematical constructions of Brownian motion, a physical phenomenon (named after botanist Robert Brown) in which the movements of small particles suspended in a surrounding medium appear erratic, seemingly random [82]. Work by Einstein, Smoluchowski and Langevin (amongst others) in the early 20th century helped to establish a mathematical study of the phenomenon; the results of which helped to establish the existence of the atom [83]. In Langevin's interpretation, the velocity of the Brownian particle is described by Newton's second law of motion, the total force acting on the particle a combination of two distinct forces: one is Stokes' drag, to account for resistance acting on the particle by the surrounding medium, and the other a randomly fluctuating force, thought to be the effect of random collisions with atoms and/or molecules within the medium

[83, 84, 85]. The scalar Langevin equation (after scaling by mass) is given by Eq. (1.1)

$$\frac{du(t)}{dt} = -\beta u(t) + F_r(t), \tag{1.1}$$

where $u(t)$ is particle velocity, $\beta > 0$ is some constant and $F_r(t)$ is a loosely characterised stochastic process with zero mean and is temporally uncorrelated [86].

The first mathematically rigorous construction of Brownian motion is credited to Norbert Wiener [82, 86]. Wiener's characterisation of Brownian motion did not include a 'drift' like in Langevin's 'physical' interpretation, and so the characterisation may be viewed as more of a robust construction of the random term in Langevin's interpretation.

A standard scalar Wiener process over the interval $[0, T]$ is a random variable $W(t)$ that depends continuously on $t \in [0, T]$ and satisfies the following conditions [83, 87, 88, 89]:

(i) $W(0) = 0$.

(ii) For $0 \leq a < b \leq T$, the increment $W(b) - W(a)$ has normal probability distribution with mean $\mu = 0$ and variance $\sigma^2 = b - a$ (equivalently, $W(b) - W(a) \sim \sqrt{b-a}N(0,1)$).

(iii) For $0 \leq a < b < c < d \leq T$, increments $W(b) - W(a)$ and $W(d) - W(c)$ are independent.

We may write a standard scalar Wiener process as the solution $z(t)$ to the stochastic differential equation (SDE)

$$dz(t) = dW(t). \tag{1.2}$$

The standard diffusion equation (with fixed diffusion coefficient) describes the time evolution of its probability density function (p.d.f.) $p(z,t)$

$$\frac{\partial p(z,t)}{\partial t} = \frac{1}{2}\frac{\partial^2 p(z,t)}{\partial z^2}. \tag{1.3}$$

Ornstein-Uhlenbeck (OU) process

If in the Langevin equation the random term is characterised by a Wiener process, the solution to the resultant stochastic process is known as an Ornstein-Uhlenbeck (OU) process, after formalising work by L. Ornstein and G.E. Uhlenbeck [90]. An OU process in differential form,

$$du(t) = -\beta u(t)dt + \sqrt{\alpha}dW(t), \tag{1.4}$$

where $\beta > 0$ and $\alpha > 0$ are constants. In integral form,

$$u(t) = u(0)e^{-\beta t} + \sqrt{\alpha}e^{-\beta t}\int_0^t e^{\beta\tau}dW(\tau), \tag{1.5}$$

where the integral is an *Itô* stochastic integral [83, 86, 89]. In differential form, we refer to the solution $u(t)$ since $dW(t)$ is not differentiable.

The OU process $u(t)$ is both a Gaussian and Markov process, with mean

$$E(u(t)) = u(0)e^{-\beta t}, \tag{1.6}$$

clearly, the first term of the solution, and variance

$$Var(u(t)) = \frac{\alpha}{2\beta}[1 - e^{-2\beta t}]. \tag{1.7}$$

The forward Fokker-Planck equation for the OU process $u(t)$ is the p.d.f. $p(u,t)$ [89, 90, 91]

$$\frac{\partial p(u,t)}{\partial t} = \beta\frac{\partial}{\partial u}(up(u,t)) + \frac{\alpha}{2}\frac{\partial^2 p(u,t)}{\partial u^2}, \tag{1.8}$$

where, if $\beta = 0$ and $\alpha = 1$ we recover the p.d.f. for the Wiener process. The OU process may be loosely interpreted as a mean-reverting Wiener process, the strength of reversion determined by β.

The Wiener process is not of bounded variation. A consequence of this is that the integral in Eq. (1.5) is stochastic, rather than the more typical Riemann-Stieltjes integral. We use the *Itô* interpretation for stochastic integration since it is non-anticipative, though in situations where the random term is additive (like, for example, in Eq. (1.4)) both *Itô* and *Stratonovich* interpretations lead to the same equation form (this is evident from the conversion formula) [83].

An OU model for individual cell migration

The OU process was first proposed as a model for individual cell migration by Dunn and Brown in their 1987 paper "A unified approach to analysing cell motility" [81], and has since been used frequently in the literature. In the model, an individual cell is considered a point particle whose velocity changes over time according to the OU process. The time evolution of a cell's velocity is interpreted as the combination of both resistance to cell motion and random cell accelerations, approximating the character of motion observed of 2-d *in vitro* 'crawling' based cell migrations. The model enables the description of movement to remain 'high-level', implicitly describing the influence of such physical factors as cell adhesion, viscous drag, energy loss and directionally random pseudopod growth within the model terms. The major limitation being that without explicit model mechanisms for such processes, we cannot expect to extract mechanistic insights from the model. Instead the model is well suited to investigating migration directionality at a 'high-level', in situations where mechanistic insights are not a primary motivation. The model is particularly useful to describe taxis-type

migration behaviour, where typically the OU process is seen as a 'fundamental' migration behaviour expressed by cells in an unstimulated environment and this becomes augmented in the presence of some external cue, typically achieved in models through biasing the OU process.

The Langevin-OU based equation used as a model of random individual cell migration in the presented research is given in the following form:

$$d\boldsymbol{v}(t) = -\beta \boldsymbol{v}(t)dt + \sqrt{\alpha} d\boldsymbol{W}(t), \tag{1.9}$$

where $\boldsymbol{v}(t)$ and $\boldsymbol{W}(t)$ (denoting velocity and the Wiener process respectively) are both now vector processes (either 2 or 3 spatial dimensions) and α is a parameter which determines the magnitude of random cell accelerations.

Cell velocity and position can be found using the relationship existent between acceleration, velocity and position by subsequent integrations of Eq. (1.9). The calculations are computationally practical using appropriate numerical methods.

Numerical approximation of the OU process

We can obtain approximations $\boldsymbol{v}^*(t)$ to the solution $\boldsymbol{v}(t)$ through stochastic Taylor expansions, the Euler-Maruyama method providing a 1st order approximation [83, 87]. Discretising the interval $[t_0, t]$ in to n steps, each Δt, at every step k we approximate

$$\boldsymbol{v}^*(t_{k+1}) = \boldsymbol{v}^*(t_k) - \beta \boldsymbol{v}^*(t_k)\Delta t + \sqrt{\alpha}\Delta \boldsymbol{W}_k, \tag{1.10}$$

where

$$\Delta \boldsymbol{W}_k = [\boldsymbol{W}_{k+1} - \boldsymbol{W}_k] \sim \sqrt{\Delta t} N(0, 1), \tag{1.11}$$

and $k = t_0, ..., t$, where $\Delta t = t_{k+1} - t_k$ is step size.

In the case where the random noise is additive, the Euler-Maruyama has both strong and weak order of convergence 1. If, in the stochastic Taylor expansion, we attempt to add the next higher order terms we would obtain the Milstein method (see [83, 87, 92]) however the additional terms evaluate to zero and the Milstein scheme reduces to an Euler-Maruyama scheme [83].

The stochastic Runge-Kutta method offers better approximations for the deterministic term in the OU equation with strong order of convergence 1.5, but not for the stochastic term and comes with the disadvantage of being more cumbersome to apply [83].

An exact numerical method for solving the Langevin-OU equations was derived by D.T. Gillespie using the probabilistic and statistical properties of the equations [91]. This method utilizes the expected value, μ; variance in velocity V, σ_V^2; variance in position X, σ_X^2 and covariance between V and X, k_{VX}. See Eq. (1.12)-(1.15).

$$\mu \equiv e^{-\beta \Delta t}, \tag{1.12}$$

$$\sigma_V^2 = \frac{\alpha}{2\beta}(1 - \mu^2), \tag{1.13}$$

$$\sigma_X^2 = \frac{\alpha}{\beta^3}[\beta \Delta t - 2(1 - \mu) + 1/2(1 - \mu^2)], \tag{1.14}$$

$$k_{VX} = \frac{\alpha}{2\beta^2}(1 - \mu)^2, \tag{1.15}$$

where α and β are parameters and Δt is a time increment.

Updating formulas for velocity V and position X are given by Eq. (1.16)-(1.17) (wherein n_1 and n_2 are statistically independent random numbers from a normal distribution):

$$V(t + \Delta t) = V(t)\mu + \sigma_V n_1, \tag{1.16}$$

$$X(t+\Delta t) = X(t) + V(t)\tau(1-\mu) + \left(\sigma_X^2 - \frac{k_{VX}^2}{\sigma_X^2}\right)^{1/2} n_2 + \frac{k_{VX}}{\sigma_V} n_1. \tag{1.17}$$

We use the exact method derived by Gillespie for computational model simulations of the standard OU process (Eq. (1.9)). We then employ the exact Gillespie method to set the step size suitably small for the Euler-Maruyama method, which we use for simulations of subsequent models which feature extra drift components.

1.6 Thesis overview

The thesis which follows is divided into two distinct parts. The first part focuses on the topography application, with the aim to determine to which extent different topographies affect fibroblast migration. The second part focuses on the connexin application, with the aim to determine how treatment with Gap27 affects Cx43-based gap junction and plaque species dynamics and its subsequent effect on interaction and migration behaviour, and ultimately invasion into a scrape wound.

In the first part of the thesis, *Chapter* 2, we expand on the physiological and biomedical significance of topographically influenced migration and walk through the experimental literature charting migration responses to different topographic features e.g. linear, lattice, pillar and pit, also reviewing surface fabrication techniques employed to generate such features. We survey the modelling literature in greater detail, focusing on cell-matrix, mechano-sensing and cell-topography models. See *Chapter* 2 - *Introduction.*

We then present the derivation for our migration model, in which a cell moves according to an OU process but accounts for the surface gradient field of an underlying topography. We present an overview of our chosen method of parameter estimation, the experimental set-up used to obtain the migration data we use in the parametrisa-

tion of the model and define migration metrics used for the fitting procedure. We also detail numerical implementation of the model and our approach to generating numerical approximations of linearly organised topographies used in the experiments. See *Chapter* 2 - *Methods*.

In *Chapter* 2 - *Results*, we present the outcome of the parameter estimation, followed by parametrised model output. We present migration trajectory and metric data for the parametrised migration model across four distinct topographies and two types of surface gradient arrangements: a flat topography and three linear topographies each featuring a different groove width. We then introduce the migration model to the same linear topographies but with increasing random perturbation to probe how migration might respond to surface imperfections introduced experimentally by fabrication method. See *Chapter* 2 - *Results*.

In the first sub-division of the second part of the thesis, *Chapter* 3, we introduce the structure, life cycle and physiological importance of Cx43 and its dynamical modulation by connexin mimetic peptides such as αCT1, Gap20, Gap26 and Gap27. We further explore the relevant modelling literature on gap junction channel properties and function. See *Chapter* 3 - *Introduction*.

We then detail explicitly the formulation of our reaction scheme for Cx43 cycling dynamics with Gap27 binding kinetics and derive by the law of mass action our full model ODE system. We then present a derivation of moment ODEs for the system plaque state distribution which we introduce, replacing the original system. We then set out the numerical implementation of the model and its numerical steady-state stability analysis. See *Chapter* 3 - *Methods*.

We present system behaviour without Gap27 and discuss the effects of initial concen-

trations and model parameters on the system at equilibrium, culminating in the presentation of a biologically realistic scenario of two neighbouring interacting cells featuring a small concentration of large gap junction plaques at equilibrium. We then consider the model with Gap27, exploring how initial Gap27 concentration and hemichannel-peptide binding/dissociation rate affect system behaviour. See *Chapter* 3 - *Results*.

In the second and final sub-division of the thesis, *Chapter* 4, we further expand on the role of connexins in wound repair, with a focus on Cx43. We discuss connexin function in healthy repair, its dysregulation and implication in abnormal repair, the positive outcomes of connexin-targeted treatments, connexin influence on migration behaviour and the mechanical properties of Cx43. We further review the modelling literature pertaining to connexin-influenced migration and its influence in wound healing. See *Chapter* 4 - *Introduction*.

We then specify the derivation of our Cx43 influenced cell-cell migration model, introducing spatial components to the discrete-point cell model and assigning proximity based interaction terms, influenced by gap junction plaques. We then present a computational framework describing the spatial elements of a conventional scrape wound assay, for which we use a circle packing algorithm, within which the migration model is tested. See *Chapter* 4 - *Methods*.

We present model output for the model without and with Gap27 and examine how the scrape wound responds over time for different plaque concentrations. We first present how Gap27 induces closure of the scrape wound over time when the plaque concentration (at system equilibrium) is high. We then present how the scrape wound can be induced to close without Gap27 if plaque concentration (at equilibrium) is low. See *Chapter* 4 - *Results*.

Chapter 2

A stochastic model for topographically influenced cell migration

2.1 Introduction

2.1.1 Topographically influenced cell migration

Cells have long been known to be guided by physical structure. In 1914, zoologist Ross G. Harrison published a series of experiments cataloguing the response of embryonic frog cells to solid physical structures, such as fibrillar spider web. Harrison found an overwhelming preference for the cells not only to attach to the spider web rather than the surface film, but also to elongate and migrate along the structure guided by its direction [93]. The phenomenon observed by Harrison was later termed 'contact guidance' by Weiss in his 1941 paper on nerve growth [94], describing the alignment, elongation and directed migration of cells following the long axis of a fibrillar structure [95]. Contact guidance is thought to serve as a major regulator of cell migration behaviour within the body, particularly within the extracellular matrix (ECM), which is composed almost entirely of fibrillar networks to cell scale [17]. The prevalence of ECM

within the body confers a prominent role for contact guidance in crucial physiological processes such as dermal wound healing and immune response [80, 96], in addition to pathophysiologies such as cancer metastasis [37, 97].

Topographically influenced cell migration describes a broader class of physical cell guidance, in which, modulation to migration behaviour can be induced by the spatial arrangement of physical surface gradients. These cell-substrate interactions can prompt a whole range of migration behaviours across many different cell types, and is thus also, like contact guidance, physiologically significant. To migrate *in vivo*, cells must traverse a huge range of topographic configurations presented by various physiological structures [42, 98, 99, 100, 101]. An example is dermal tissue, which is composed of fibrillar ridge-like structures of varying dimension scale and density (ECM) and contained by a planar pillar-like topography (dermal-epidermal junction) and a smooth flat or curved topography (hypodermis); see *Chapter* 1 - *Introduction*. The arrangement of dermal ECM has also been shown to be associated with the distribution of tension or 'Langer' lines, with a corresponding anisotropic structure. These tissue orientations have been favoured for surgical incision due to improved healing and reduced scarring [80, 100].

The influential role these interactions maintain within the body, and their physiological ubiquity, has motivated considerable exploration of exploitative potential for biomedical applications, in particular biomaterials design for tissue engineering [100]. One such application is in skin substitute development, an advanced treatment for cutaneous wound healing [102], through topographic control of cell positioning and population of tissue scaffolds prior to implantation [49]. Another such application is in the surface modification of implantable medical devices, with the goal of improving integration. Integration with the *in vivo* environment is a significant biomedical challenge [103],

and the failure of medical implants can often be attributable to complications such as inflammation [51, 53, 96] and tissue encapsulation [51], within which migration plays a central role. Medical devices featuring surface topographies engineered to regulate such migration could improve clinical outcomes for implantation.

The biomedical applicability of topographically influenced migration has driven extensive experimental study in recent years [101]. There is an abundance of *in vitro* experimental studies charting migration responses of many cell types (including fibroblast [43], endothelial [43], epithelial [46], smooth muscle cells [43] and neurons [104]) to different topographic features (e.g. groove/ridge [105, 43, 80, 106, 107], pillars [108, 109, 110], pits [111]) of varied geometry (e.g. groove with triangular or trapeze-shaped wells with various dimensions [41]), dimension (e.g. variable groove to ridge width ratios [105]) and scale (micron and sub-micron [43]). To illustrate some of the general trends in the experimental literature we will select results from some pertinent studies to present. For further exploration of this area of research, see any of the comprehensive review articles: [48, 112, 113, 114, 115].

Topographies with linear ridge/groove features have been widely reported to affect alignment and migration in many different cell types; predominantly fibroblast, epithelial, endothelial and smooth muscle cells. Kaiser and Bruinink observed fibroblast (NIH3T3) migration on grooved substrates (width 9.8μm and depth 1μm) was "mainly bidirectional", further analysis showed 61% of cells were polarised with orientations within 10 degrees of the groove orientation [106]. Dalton et al. reported significantly higher migration distances when cells followed rather than traversed microgrooves at depths of both 1μm and 5μm in epithelial (bovine corneal) cells [46]. Biela et al. found fibroblasts (HFF-1) to be much more sensitive to linear ridge/groove dimensions

than endothelial (HCAEC) and smooth muscle cells (HCASMC), groove depths of as little as 50nm prompting changes to morphology and orientation. The authors also found smaller ridge/groove widths prompted greater alignment for all cell types, and deeper grooves increased groove-oriented migration, fibroblasts exhibiting the most pronounced behaviour of all cell types across all dimensional variations (ridge/groove widths: 2μm-10μm, depths: 50nm-200nm)[43].

In addition to migration directionality, many studies have reported ridge/groove dimensions to influence migration speed. Kaiser, Reinmann and Bruinink showed fibroblasts (NIH3T3) to have highest migration velocity on substrates with shallower wider grooves and narrower ridges (depth 5μm, groove width 32μm and ridge width 5μm) [41]. Similarly, Doyle et al. reported fibroblasts (NIH3T3) cultured on 1.5μm wide fibril-inspired ridge patterns exhibited two to three times higher migration speeds than on flat surfaces, highest migration speeds were observed at ridge widths of 2.5μm [107]. A study by Kim et al. reported preferential fibroblast (NIH3T3) migration towards regions with intermediate ridge densities (5.6-6.9μm) on an anisotropic linear topography with constant ridge width 1μm and depth 400nm but variable groove width 1-9.1μm. Fastest migrations were also observed on intermediate ridge densities, the most clearly aligned and directional cells however were found to be at higher ridge densities (smaller groove widths) [105]. In another study, Kim et al. (different authors to the aforementioned study) found ridges parallel to the long axis of a scrape wound severely limited migration into the wound region, whereas perpendicular ridges encouraged migration into the wound, resulting in superior covering rates for all ridge dimensions tested. Highest migration speeds were seen with intermediate ridge dimensions, and showed to be the only visibly closed scrape wound over the experimental time interval of 48

hours [80].

Topographies with lattice arrangements have also been reported to induce physical alignment and directed migration. A study by Mai et al. showed that smooth muscle cells (BASM) aligned and migrated along the long axis of rectangular grids when cultured on a substrate with lattice arranged rectangular columns [47]. Jeon et al. observed a similar effect in fibroblasts (NIH3T3), where migration predominantly followed the long axis of rectangular grids, migration speeds increasing as this axis was lengthened, grid ratios of 1:2 and 1:4 having significant effects, if the grid size remained below cell size [116]. Kim et al. found that fibroblasts (NIH3T3) cultured on an anisotropic lattice substrate with variable grid density migrated preferentially toward regions with smaller grid sizes [117].

Pillar topographies have been shown to have different effects on migration. Fibroblasts (NIH3T3) cultured on substrates with 1.78μm high 10.3μm diameter pillars spaced 15.76μm apart transmigrated erratically with branched cell morphology between pillars, but with higher linear speeds than on flat surfaces [108]. Sochol et al. investigated how cells would respond to an array of micropillars with variable diameters [109]. The authors found endothelial (BAE) cells migrated toward substrate regions with larger diameter pillars, with higher speeds. The larger diameter pillars were shown to have higher stiffness properties and so cells were seen to respond simultaneously to both topographic and rigidity gradients. A study conducted by Saez et al. demonstrated epithelial (MDCK) migration to be preferential along the long axis of oval-shaped micropillars. Similarly, the long axis of the oval-shaped pillars had higher stiffness properties compared to the short axis and so migration was again a combined response to different gradient cues [110].

Holes, wells and pit topographies have been reported to have intriguing effects on migration. Fibroblasts (hTERT-BJ1) cultured on arrays of micro-scale pits (depth 4.8μm) with variable diameters (7μm, 15μm and 20μm) and spacing (20μm and 40μm) showed significantly higher migration speeds on surfaces featuring smaller holes (7μm) and spacing (20μm). Cells were also observed to adapt size and morphology to pit shapes at all diameters, whilst showing significantly higher proliferation on smaller diameter pits [111].

Surface topography has also been shown to influence other cellular behaviours for a range of different cell types, including adhesion (e.g. Dalby et al. observed reduced surface adhesion and spreading in fibroblasts (hTERT-BJ1) on nanocolumns [118]), proliferation (e.g. Choi et al. reported nanotip substrates with smaller prominences induced higher proliferation in fibroblasts (HFF-1) compared with taller nanotips [119]) and even differentiation (e.g. Steinberg et al. showed the magnitude of interspacing between micropillars can influence differentiation of early keratinocytes (IHGK) [120]).

Surface fabrication methods

To produce surface topographies with variable geometries, experimentalists must select from a diverse set of surface processing methods, including lithography-based techniques, electro-spinning, etching techniques (e.g. laser or acid), polishing and blasting techniques [48]. Lithography-based methods are often favoured to fabricate precise geometries but can be prohibitive due to factors such as cost and availability of equipment and fabrication time [44, 48]. This has led experimentalists to explore the use of other methods that may be able to produce comparable topographies without such disadvantages. Irving et al. explored the use of laser etching and abrasive polishing to generate uniform linear ridge/groove type topographies (μm and nm scale, respec-

tively) comparable to those producible with lithography-based methods. Whilst both methods could produce broadly uniform linear patterns, closer examination of the surfaces revealed imperfections due to coarse fabrication, exhibiting sub-patterns such as an oscillating groove depth and randomly distributed pits [44]. The focused use of coarser surface processing methods could be a way to accelerate the experimental process and, if suitably refined, could ultimately lead to reductions in manufacturing time and cost for associated biomedical applications.

2.1.2 Modelling studies

Early modelling studies to incorporate topographic cues into mathematical models of cell migration typically focused on cell-matrix interactions, where migration and fibril behaviour were dynamically inter-dependent. Often these interactions were treated as a general class, targeted more specifically to the *in vivo* cell microenvironment, or *in vitro* application to tissue equivalents (T.E.s) e.g. collagen gels. Significant early work in this area was published by Tranquillo and co-authors, in which the authors model cell-matrix contact guidance as an anisotropic diffusion. Notably, this modelling approach formed part of Barocas and Tranquillo's anisotropic biphasic theory for T.E. mechanics, describing the feedback effect of migration dynamics on the biomechanical properties and orientation of a fibrillar network within a T.E. and the network's subsequent impact on migration orientation. Within the biphasic T.E., the cell migration was determined only to affect the fibrillar network and have no effect on an interstitial media, each 'phase' determined by a set of mechanical force balances. The study showed promising comparisons to experimental studies in different simulated experimental setups [68].

Dallon, Sherratt and co-workers published a series of spatial models to probe cell-matrix

dynamics in scar tissue formation. The authors propose a hybrid discrete-continuous modelling framework describing discrete cells which migrate according to guidance cues given by a 2-d vector field describing fibril orientations in a fibrillar network of collagen, and later an embedded field representing fibrin. Authors review how cell parameters including migration speed, flux and polarisation affect the spatial arrangement of the tissue vector field (using streamlines), before introducing additional vector fields for additional proteins e.g. fibrin [64], diffusing growth factors and chemoattractants [121].

Painter investigated the contrasting strategies of both amoeboidal and mesenchymal modes of cell migration within variably oriented matrix patterns defined by static 2-d vector fields [122]. The author adapts transport equation models for cell and matrix densities specifically to model the amoeboidal case, where migrating cells don't degrade and only transiently deform matrix, and mesenchymal, where cells actively degrade matrix with proteolytic activity and thus reshape it. Results show cell density for the amoeboidal model could be confined on a matrix field with an embedded 2-d oriented/disoriented pattern whereas the mesenchymal model could under some parameter conditions overcome confinement to spread over the whole field.

For other models focused on cell-matrix interactions *in vivo* such as those described see also: [123, 124].

More recent modelling studies however have begun to utilise the recent experimental biotechnology literature outlined in the previous section, focusing on the effect of various non-dynamic surface topography arrangements on cell behaviours, including migration. Heydari et al. address the relative lack of computational tools capable of predicting cell response to topography by proposing a computational framework for a general 3-d 'virtual cell model', tailored in application to mesenchymal stem cells.

The authors use a discrete force-based approach, creating the model with composite interacting parts: membrane and nucleus structures, both modelled with a triangulated network of vertices with assigned viscoelastic properties; cytoplasmic and cytoskeletal components, modelled with an interacting network; intracellular chromatin proteins, modelled with bead-spring models; and substrate topography, another triangulated elastic network. The model could predict cell and nucleal elongation on a numerically modelled ridged/grooved topography, the degree of elongation shown to increase with groove depth, and also with increasing substrate rigidity [66].

Winkler, Aranson and Ziebert proposed an abstract lamellipodia-based individual cell model, which migrated in continuous fields describing various substrata scenarios: confinement (planar and tunnel), curvature and linear ridged/grooved topographies. The model is a 4-field 3-d PDE model, consisting of a scalar phase field for the cell domain and vector field for actin orientation which interact with two static phase fields defining substratum configuration. Results displayed a range of realistic migration and morphological behaviours, such as bullet-like morphology when the cell was confined in tunnels and morphological/migratory alignment with parallel ridged/grooved features, dependent on feature dimension [69].

Another predominant modelling trend is to focus on mechanosensing or mechanotransductive mechanisms of the cell responsible for generating the cell behaviours observed over topographies. Examples of such models include: [125, 126, 127].

2.1.3 Motivations and contributions

Cells have long been known to respond to surface topography. The structure of the native extracellular micro and nano environment presents a wide spectrum of different topographies for cells to traverse. The capacity of the physical extracellular environment to regulate cellular behaviours, including migration, has found significant application in biomaterials and bioimplant design. Topographically influenced cell migration has been extensively studied experimentally in an effort to characterise responses of different cell types to specific classes of topographic features e.g. linear ridge/groove, lattice, pillar, pit, curvature. Despite a profusion of experimental study, and clear prevalent trends, for example the orientation of numerous cell types to migrate in alignment with linear ridge/groove features, key questions still appear to remain about how these interactions occur and exactly how the diverse set of experimental outcomes are produced across varied topographic arrangements and cell types. Jeon, Simon and Kim summarised in their 2014 review that "shapes and sizes of surface patterns needed to affect specific cellular activities and interaction mechanisms between cells and patterned surfaces have not yet been determined" [115]. However, a recently published theoretical model suggests a potential mechanism of action. The model proposes cell alignment and topographically directed migration could result from physical focal adhesion confinement inducing development of oriented contractile cytoskeletal components (actin stress fibres), elongating cell shape and thus predisposing the cell to pursue an oriented direction [101, 128].

Modelling literature has traditionally focused on cell-matrix interactions and only recently have studies begun to focus on classes of topographies reflecting the interest in the biomaterials literature. It appears there is a general lack of mathematical and

computational models to help experimentalists in the design and development of surface topographies to influence migration behaviours. This observation was expressed by Heydari et al. in their 2017 modelling study, stating "there are very few methods available for robust and accurate modeling that can predict cell behavior prior to experimental evaluations" [66]. An expanded modelling literature could help to streamline the experimental process, enabling experimentalists to focus surface development to the most effective topographic geometries, spatial arrangements and dimensions.

In this work we develop a cell migration model and apply it to determine to which extent different topographies can induce directional movement of migrating fibroblast cells. We will focus on movement on highly structured surfaces generated by capillary force lithography which have parallel linear ridge/groove features [105]. Preliminary results for another data set comprising polished metal surfaces [44] were previously presented by Conway [129]. Like Dallon and co-authors, we use a discrete-point approach that incorporates directional cues from an underlying gradient field representing some topography. Our modelling approach differs in that there is no dynamical reciprocation between the cell and gradient field directions and we assume the point cell migrates according to an Ornstein-Uhlenbeck process without environmental cues. The aim is to explore how migration trajectories over time respond to linearly and randomly organised topographies and predict how this behaviour might evolve if linear topographic features became gradually disordered, the intention being to model how surface imperfections introduced by coarse fabrication might affect migration.

The presented work contributes the following:

(i) **Derive a stochastic model for topographically influenced migration.** The model is based on a biased Ornstein-Uhlenbeck process, in which individual

cell velocity is influenced by some external condition by way of a directional bias. Spatially, a discrete point represents cell position on a 2-d vector field representing the physical surface gradients of a topography. See *Methods* 2.2.1.

(ii) **Parametrise model with published metric data.** Using a grid search optimisation method we parametrise the model using metric data derived from experimental *in vitro* migration on a linear anisotropic topography (variable ridge density / groove width), see *Methods* 2.2.2-2.3.1. We review parametrised model trajectory and metric output for four different topographies: flat, 9μm, 6μm and 2μm groove width. See *Results* 2.3.3.

(iii) **Predict how migration characteristics change when uniform linear topographic features become gradually more disordered.** We gradually introduce random perturbations to uniform linear topographic features for 9μm, 6μm and 2μm groove widths, and use the parametrised model to predict how migration might respond to increasing 'disorderedness' in surface gradients. Downstream, more precise predictions could help experimentalists in selecting surface processing methods to produce desired migration characteristics. See *Results* 2.3.4.

2.2 Methods

2.2.1 Model

The model is based on an Ornstein-Uhlenbeck (OU) cell model, as first introduced by Dunn and Brown [81]. The model comprises a single stochastic differential equation (SDE) defining the velocity-time evolution of an individual point cell by a combination of force terms, see Eq. (2.1). Cell velocity, $\boldsymbol{v}(t)$, may be found through solving the original model equation, from which an individual migration trajectory may be constructed.

$$d\boldsymbol{v}(t) = -\beta\boldsymbol{v}(t)dt + \sqrt{\alpha}d\boldsymbol{W}(t), \tag{2.1}$$

where β is resistance to motion, α controls random acceleration and $\boldsymbol{W}(t)$ is the 2-d vector Wiener process.

A prevalent characteristic in many cell types is for migration trajectories to follow linear ridge/groove directions (see *Introduction* 2.1.1). To capture this important behavioural characteristic within the model, some modification to the basic velocity behaviour is required since migration is no longer directionally random. Our approach is to introduce a directional bias, as an additional term, into the original model equation. A similar approach is used by Stokes, Lauffenburger and Williams in modelling the chemotaxis of endothelial cells, in which the bias was dependent upon cell position in relation to a chemical gradient [62].

To construct a topography-based directional bias, we assume cells avoid steep physical gradients in their migrations, confining migration to approximate contour directions (as reported in ridge/groove guided migration *in vitro*, e.g. [107]). Inherent in this assumption is the notion that a cell is able to identify physical gradients and

by some mechanism reorient its direction. This may not be unreasonable, given the mechanosensing capabilities of cell membrane and cytoskeletal components [108, 130]. We also see cell reorientations documented in various other physically-based taxis phenomena e.g. durotaxis [39].

First, we define some surface topography as the continuous scalar field $T(x, y)$. The vector field defining local steepest gradients on $T(x, y)$ is defined by the gradient field $\boldsymbol{\nabla} T(x, y)$, where $\boldsymbol{\nabla} \equiv \left(\frac{\partial}{\partial x}, \frac{\partial}{\partial y} \right)$. If the point $X = (x_1, y_1)$ defines a position on the vector field $\boldsymbol{\nabla} T(x, y)$, the steepest gradient locally at X is defined as $\boldsymbol{G}_X$, Eq. (2.2).

$$\boldsymbol{G}_X = \boldsymbol{\nabla} T(x_1, y_1). \tag{2.2}$$

To define opposing contour directions at the point X, orthogonal to $\boldsymbol{G}_X$, orthogonal rotations are calculated through rotation matrices. Contours are represented by $\boldsymbol{c}$ and $-\boldsymbol{c}$, Eq. (2.3)-(2.4).

$$\boldsymbol{c} = \begin{bmatrix} \cos(\frac{\pi}{2})x_1 & - & \sin(\frac{\pi}{2})y_1 \\ \\ \sin(\frac{\pi}{2})x_1 & + & \cos(\frac{\pi}{2})y_1 \end{bmatrix} = \begin{bmatrix} -(\boldsymbol{\nabla} T)_y \\ (\boldsymbol{\nabla} T)_x \end{bmatrix}, \tag{2.3}$$

$$-\boldsymbol{c} = \begin{bmatrix} \cos(-\frac{\pi}{2})x_1 & - & \sin(-\frac{\pi}{2})y_1 \\ \\ \sin(-\frac{\pi}{2})x_1 & + & \cos(-\frac{\pi}{2})y_1 \end{bmatrix} = \begin{bmatrix} (\boldsymbol{\nabla} T)_y \\ -(\boldsymbol{\nabla} T)_x \end{bmatrix}. \tag{2.4}$$

To construct the topographic bias term, we specify three components: a primary directional cue $\boldsymbol{\gamma}$, orthogonal to the direction of steepest gradient local to cell position on the topography; a weighting $\sin(\phi)$, which determines magnitude of reorientation; and a coefficient κ, the controlling parameter within the biased OU model equation.

We assume the contour direction most likely to be selected as the primary directional

cue $\boldsymbol{\gamma}$ is that most similarly aligned with the cell velocity direction. To discern between contours, we evaluate the directional similarity between cell velocity $\boldsymbol{v}$ and contour directions $\boldsymbol{c}$ and $-\boldsymbol{c}$ using angle ϕ, defined as the argument between $\boldsymbol{v}$ and $\boldsymbol{c}$. The directional cue $\boldsymbol{\gamma}$ is assigned based upon simple threshold conditions for ϕ.

If angle $\phi < \frac{\pi}{2}$, contour direction $\boldsymbol{c}$ is favoured since $\boldsymbol{v}$ aligns with greater similarity to $\boldsymbol{c}$ than to $-\boldsymbol{c}$. If however, $\phi > \frac{\pi}{2}$, contour $-\boldsymbol{c}$ is now favoured since $\boldsymbol{v}$ aligns more towards $-\boldsymbol{c}$ than $\boldsymbol{c}$. If in the case that $\phi = \frac{\pi}{2}$, where $\boldsymbol{v}$ aligns exactly with $\boldsymbol{G}_X$, the favoured contour direction is selected with random probability. $\boldsymbol{\gamma}$ is defined in Eq. (2.5).

$$\boldsymbol{\gamma} = \begin{cases} \boldsymbol{c}, & \text{if} \quad \phi < \frac{\pi}{2}. \\ -\boldsymbol{c}, & \text{if} \quad \phi > \frac{\pi}{2}. \\ \boldsymbol{c} \quad \text{or} \quad -\boldsymbol{c}, & \text{if} \quad \phi = \frac{\pi}{2}. \end{cases} \tag{2.5}$$

Angle ϕ may be defined using the dot product, with the calculation symmetric about the line defined by $\boldsymbol{c}$, Eq. (2.6).

$$\phi = \arccos\left(\frac{\boldsymbol{v} \cdot \boldsymbol{c}}{|\boldsymbol{v}||\boldsymbol{c}|}\right). \tag{2.6}$$

To calibrate the magnitude of cell reorientation, a weighting $\sin(\phi)$ is incorporated into the bias term. The weighting is applied primarily to reorient maximally toward directional cue $\boldsymbol{\gamma}$ when $\boldsymbol{v} = \boldsymbol{G}_X$, and negate the bias influence altogether if $\boldsymbol{v} = \boldsymbol{c}$ or $\boldsymbol{v} = -\boldsymbol{c}$ and so the cell migrates according only to the OU process.

The bias term, whose elements are illustrated schematically in Figure 2.1, is defined by Eq. (2.7).

$$\boldsymbol{\varphi}(t) = \kappa \boldsymbol{\gamma} \sin(\phi). \tag{2.7}$$

Incorporating Eq. (2.7) into the standard OU cell model completes the definition for our topographically influenced migration model, Eq. (2.8).

$$d\boldsymbol{v}(t) = \Big(\boldsymbol{\varphi}(t) - \beta \boldsymbol{v}(t)\Big)dt + \sqrt{\alpha} d\boldsymbol{W}(t), \tag{2.8}$$

where $\boldsymbol{\varphi}(t)$ is a vector directional bias.

Subsequent integrations of Eq. (2.8) results in displacements over time for an individual point cell given by variable $\boldsymbol{x}(t)$, by Eq. (2.9).

$$d\boldsymbol{x}(t) = \int_0^t \boldsymbol{v}(t')dt'. \tag{2.9}$$

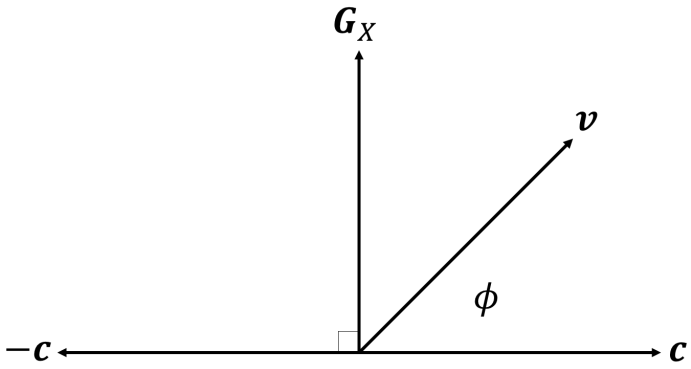

Figure 2.1: Schematic diagram to illustrate the components of the model topographic bias term. Left to right: orthogonal direction anticlockwise from $\boldsymbol{G}_X$ is the contour direction $-\boldsymbol{c}$, $\boldsymbol{G}_X = \boldsymbol{\nabla} T(x_1, y_1)$ is the steepest local gradient at the point $X = (x_1, y_1)$, $\boldsymbol{v}$ is cell velocity, $\boldsymbol{c}$ is the clockwise contour direction from $\boldsymbol{G}_X$ and ϕ is angle $\boldsymbol{c}$ makes with $\boldsymbol{v}$.

2.2.2 Method of parameter estimation

To estimate model parameters we use a grid search optimisation method. We favour this method for a few reasons: the size of the model parameter set is relatively small, this limiting the overall search space (to three dimensions); we can also leverage available experimental migration data to reduce the search space still further; and, application of the method is straightforward algorithmically (function evaluation nested within iterative search).

Let parameter space $P = (\alpha, \beta, \kappa) \in \mathbb{R}^3_+$. We reduce the search space using a combination of coarse grain grid searches and average migration path length (derived from fibroblast speed measured experimentally by Kim et al. [105]) to define parameter boundaries above or below which simulated average migrations are unrealistic. For each component of P, we define a lower bound $P_1 = (\alpha_1, \beta_1, \kappa_1)$ and an upper bound $P_n = (\alpha_n, \beta_n, \kappa_n)$, giving an interval within which to search e.g. $[\alpha_1, \alpha_n]$. We then discretise the interval into a finite set of m uniformly spaced points producing a 'grid' of m^3 points over which to calculate an objective function [131].

We choose to define our objective function as a simple error function ϵ which evaluates the difference between a set of simulated and experimentally derived average migration metrics. The goal is to minimise ϵ within our bounded discretised parameter space. For a given parameter set $P_{a,b,c} = (\alpha_a, \beta_b, \kappa_c)$, ϵ is calculated by Eq. (2.10).

$$\epsilon = \sum_{i=1}^{N} \frac{(\theta_{i;sim} - \theta_{i;exp})^2}{\theta_{i;exp}^2}, \tag{2.10}$$

where $\theta_{i;exp}$ is the ith experimentally derived metric and $\theta_{i;sim}$ the ith simulated metric. N is total number of metrics.

To illustrate algorithmically, for a given parameter set e.g. $P_{a,b,c} = (\alpha_a, \beta_b, \kappa_c)$, we

initiate a large number of replicate model simulations and calculate a selection of average migration metrics capturing some key characteristic about average migration behaviour (e.g. directionality, displacement), either equivalent to or can be reasonably compared to metric data derived from experimental analysis of *in vitro* migration. We then use the simulated and experimentally derived metrics to obtain a value for ϵ, which is stored. We then move onto a simulation with a new parameter set e.g. $P_{a,c,c} = (\alpha_a, \beta_c, \kappa_c)$, iterating systematically in this manner through each predefined parameter range for α, β and κ. A flow chart which illustrates this algorithmic approach is presented in Figure 2.2.

For each of the different surface topographies, we proceed through the grid search initially with a coarse grid to define search boundaries and establish a preliminary range over which P is minimal. We then refine the search grid to avoid skipping over optimal solutions in our iterations, keeping m as large as we can whilst maintaining reasonable computation time.

Due to the stochastic nature of the model, minima positions change between model simulations with equivalent search and migration parameters. To account for this, we do not seek to identify individual minima, instead we look for general regions of the search space with consistent minima for duplicate simulations. Conducting duplicate simulations also reduces the chance that we wrongly select parameter regions which contain non-optimal solutions due to numerical error.

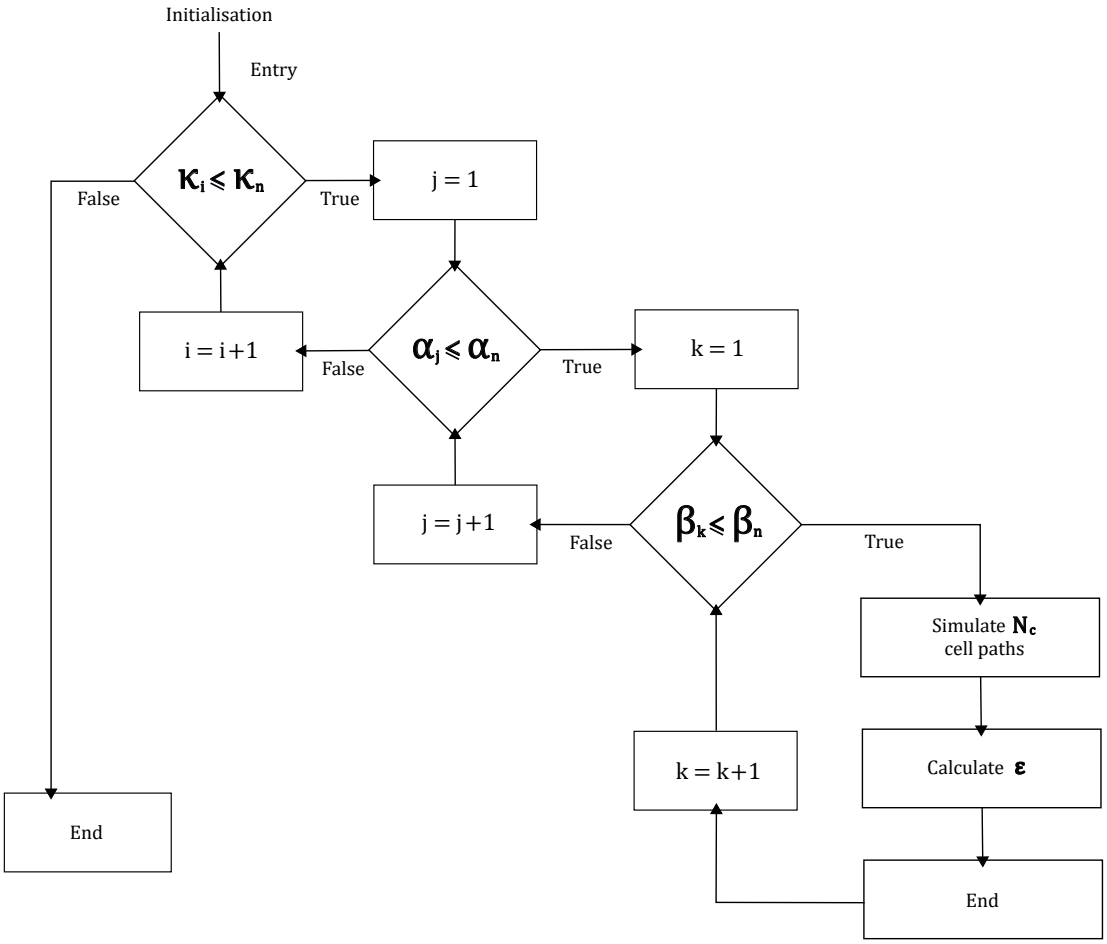

Figure 2.2: Flow chart to illustrate the algorithmic approach chosen to conduct the parameter grid search for the model. The general approach taken is to hold two parameters constant whilst iterating through one parameter range, simulating N_c cell paths and calculating ϵ for each individual parameter set, before incrementally adjusting the originally held parameters and repeating. To illustrate, in the initial state of the algorithm κ_1 and α_1 are held constant whilst migration paths and subsequently ϵ are simulated for $\beta_1, ..., \beta_n$. After the model simulation for β_n, the value for α changes, from α_1 to α_2, with κ_1 held constant whilst we again repeat simulations for $\beta_1, ..., \beta_n$, and so on until κ_n is reached and the algorithm ends. The result is a value for ϵ for each individual parameter combination resulting from discretisation of the interval $[P_1, P_n]$.

2.2.3 Experimental data

Fibroblast migration with a linear variable groove width (μm-scale) topography

To parametrise the model we use metric data extracted from a study by Kim et al. published in the journal *Biomaterials* (for details see [105]). The study probed fibroblast (NIH3T3) migration on an anisotropic substratum with precisely fabricated

topographic features created using capillary force lithography (CFL). The CFL method was used specifically to generate a reproducible surface pattern of parallel alternating ridges and grooves with uniform groove depth of $400n$m and ridge width of 1μm but variable groove widths from 1μm to 9.1μm, spaced in increasing $100n$m increments from densely to sparsely spaced ridges. Cells were seeded at relatively low density to enable individual tracking and fluorescent microscopic images taken every 15 minutes over 12 hours producing a time-lapse sequence.

To quantify orientation of cells compared to groove direction, at 14 hours post-culture the authors measured the acute angle between the longest axis of the cell, the 'polarised' cell direction, and groove direction, generating a distribution of 'polarisation angles' for cells across the variable groove widths on the substratum.

To ascertain whether groove width had a discernible affect on migration speed, the authors tracked individual cells through the time-lapse sequence and calculated speed between increments for each cell. Speeds for each cell were averaged, these average cell speeds were then averaged by substratum position to give a single average speed for the local population.

Kim et al. found that groove-oriented migration was more pronounced in substratum regions with narrower grooves, shown by increased linearity in migration trajectories and smaller standard deviations for polarisation angle distributions. Migration was also selective, showing a discernible preference towards intermediate groove widths, where average migration speed was highest.

The authors captured clear relationships between groove width and migration directionality and displacement with polarisation angle and migration speed metric statistics. Results showed a clear monotonic decrease in standard deviation of polarisation angle

distributions with decreasing groove width (cells becoming more oriented to the groove direction). There was also an optimal groove width for average speed, which were shown to be the intermediate widths.

We use these metric statistics, polarisation angle standard deviation θ^*_σ (°) and average migration speed s^*_μ (μm/h), in the grid optimisation calculation to parametrise our model. In lieu of explicit data values, we estimate values directly from the study figures which display θ^*_σ (°) and s^*_μ (μm/h) for flat and grooved areas of the topography using a pixel measurement tool. We present estimated values in Table 2.1.

Table 2.1: Estimated migration metric data, θ^*_σ and s^*_μ, for flat and linearly ridged/grooved (with average groove widths: 8.6μm, 6.3μm and 2.6μm) topographies from Kim et al. [105].

Average groove width	θ^*_σ (°)	s^*_μ (μm/h)
Flat (no gradient)	47	28
8.6μm	38	29
6.3μm	20	40
2.6μm	12	34

2.2.4 Migration metrics

The aim with the chosen optimisation method is to closely approximate key properties of *in vitro* fibroblast migration with those which emerge from the proposed migration model. To make appropriate comparison for the calculation of ϵ we base our selection of model metrics on those used in the aforementioned study by Kim et al. [105].

(i) **Orientation angle**. In the study by Kim et al., the authors approximate cell direction by measuring the acute angle between the long axis of a cell and groove direction, taken as a single measurement for each cell at the end of a time course, this termed the 'polarisation angle', θ^*. The values θ^* for every cell in a given locale were accumulated to give a distribution of polarisation angles for different

regions of the substrate, from which a distribution mean, θ^*_μ, and standard deviation, θ^*_σ, were calculated.

We replicate this for the migration model by introducing an analogous angle metric defined as the argument between cell velocity direction and groove direction, termed 'orientation angle', θ. In-keeping with the computation of θ^*, we set the calculation symmetric about directions orthogonal to groove direction $\boldsymbol{L}$ and determine the position of 0° to be at both opposing groove directions $\boldsymbol{L}$ and $-\boldsymbol{L}$. We measure θ with positive angles clockwise from the groove direction, keeping the angle range acute, $-90° \leq \theta \leq 90°$ (see Figure 2.3).

We compute θ between numerical time increments, j and $j+1$, for every increment and each cell i in a given simulation, to give a distribution of 'orientation angles' for the whole simulation, $\theta_{ij,j+1}$, where $i = 1, ..., N_c$ and $j = 1, ..., N_t - 1$, from which we then calculate the mean, θ_μ, and standard deviation, θ_σ, given by Eq. (2.11) and Eq. (2.12) respectively.

$$\theta_\mu = \frac{1}{N_c(N_t-1)} \sum_{i=1}^{N_c} \sum_{j=1}^{N_t-1} \theta_{ij,j+1}, \tag{2.11}$$

where i is the ith cell and j is the jth increment. N_c is total number of cells and N_t is total number of increments.

$$\theta_\sigma = \sqrt{\frac{1}{N_c(N_t-1)} \sum_{i=1}^{N_c} \sum_{j=1}^{N_t-1} (\theta_{ij,j+1} - \theta_\mu)^2}. \tag{2.12}$$

(ii) **Migration speed**. The authors of the Kim et al. study calculated migration speed from point-to-point cell trajectories tracked through a time-lapse sequence, giving a sequence of point-to-point speeds for each cell over time (9 hours at 15 minute intervals). The sequence of speeds for each cell was then averaged, and

cells grouped by substratum position (average groove width) to give distributions by 'average groove width' from which an average migration speed, s^*_μ, was calculated for each.

To replicate the calculation of s^*_μ, we compute migration speed s from individual cell displacements as with orientation angles, between increments j and $j+1$ for every increment for each cell i in a given simulation, to give a distribution of migration speeds, $s_{ij,j+1}$, from which we calculate the mean migration speed, s_μ, Eq. (2.13).

$$s_\mu = \frac{1}{N_c(N_t-1)} \sum_{i=1}^{N_c} \sum_{j=1}^{N_t-1} s_{ij,j+1}. \tag{2.13}$$

(iii) **Mean-squared displacement (MSD)**. MSD is a measure of average displacement from an original starting position over a specified time increment [62]. In terms of cell migration, we define the MSD $< D^2 >$ as the squared distance travelled by each cell during time interval t, summed and averaged over the total number of cells N_c to migrate during that time interval, given by Eq. (2.14).

$$< D^2 >= \frac{1}{N_c} \sum_{i=1}^{N_c} [\boldsymbol{x}_i(t) - \boldsymbol{x}_i(0)]^2, \tag{2.14}$$

where $\boldsymbol{x}_i(t)$ is the position of the cell i at time t and $\boldsymbol{x}_i(0)$ is the position at the start of displacement.

2.2.5 Numerical implementation

We use MathWorks MATLAB 2020a as the chosen software environment to implement the model algorithmically and solve the model by numerical methods, enabling us to run computational simulations of the model and from this generate figures.

We solve the model using an Euler-Maruyama scheme [87] to obtain an approximation

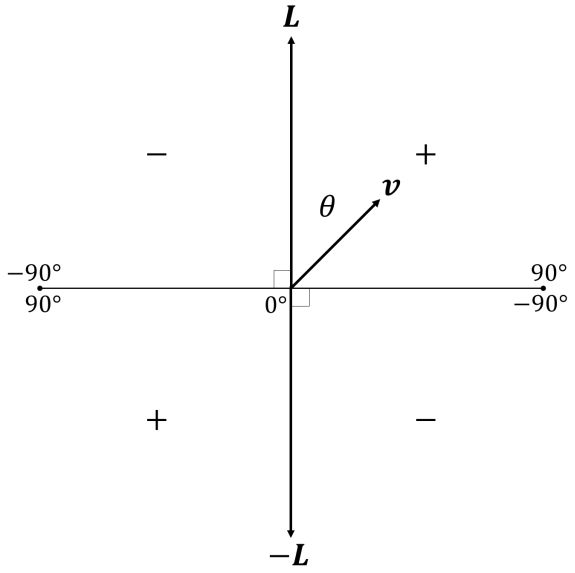

Figure 2.3: Schematic diagram to illustrate the measurement of 'orientation angle', θ, for a sample time increment. θ is measured as the argument between cell velocity $\boldsymbol{v}$ and groove direction $\boldsymbol{L}$ or $-\boldsymbol{L}$, dependent on the sign of the 'vertical' component $\boldsymbol{v}$. The calculation is symmetric about the directions orthogonal to groove direction $\boldsymbol{L}$, 0° at both opposing groove directions $\boldsymbol{L}$ and $-\boldsymbol{L}$. θ is measured with positive angles clockwise from the groove direction, in the range $-90° \leq \theta \leq 90°$.

for cell migration velocities, obtaining subsequent cell positions by numerical integration. To maintain reasonable approximations we use sub-increments (increments smaller than set experimental increments over which the simulation will run) so that numerical increments are always small. To ascertain how small these numerical increments should be we compare mean-squared displacement (MSD) over time from simulations of the (unbiased) OU process obtained using an exact numerical method (Gillespie, [91]) and the Euler-Maruyama method. We fix numerical increment size small enough to minimise this error without compromising on computation time for a large number of model simulations and a fine grid search, the selection being heuristic. We proceed with consistent sub-increments for all simulations.

To compare the model with experiments by Kim et al. [105], described in *Methods* 2.2.3, we approximated surface topographies using MATLAB to generate matrices with data values corresponding to 'depth' values, spatially distributed to approximate

the arrangements of topographic features in the study (uniform linear constant ridge / variable groove widths), details follow in *Methods* 2.2.5.

Once the surface topography is represented numerically, we compute an approximate gradient field of the surface using MATLAB's numerical gradient function '*gradient*'. This gradient field is then accessed during the model simulation to influence cell orientation and re-orientation.

Due to the stochastic nature of the model, we run many repeat model simulations to replicate many sample cell migration paths on the surface. We then compute the selection of average migration metrics detailed in *Methods* 2.2.4.

Topography generation

To create linear topographies comparable to those featured in the study by Kim et al. [105], we generate simulated approximations of topographies with selected groove widths numerically using MATLAB and test how closely each topography can approximate corresponding migration metrics during the fitting procedure.

The general numerical approach we take to generate the topographies is a grid-based method. We define a 'substrate' matrix, tracing the topography boundaries, and assign a 'depth' value to relevant indices in the matrix corresponding to groove depth. To approximate a 'flat' topography (i.e. to cell-scale, no significant gradients present) we idealise and assume there is no gradient at all present on the surface, using simply a matrix with homogeneous depth values. To approximate linear topographies we use the approximation for the flat topography (e.g. a matrix of zeroes), and assign depth values for all indices in a column of the matrix at uniform intervals across all columns in the matrix, generating linear topographic features up to the boundary; non-zero values representing ridges and zero values representing grooves.

We assign spatial units based on fitting the model migration trajectory metrics on trial surfaces to metrics from Kim et al., adjusting dimensions as necessary and ensuring boundaries are large enough to accommodate the trajectory range. Spatial units were assigned $1 \times 1\mu m^2$ to one matrix index. To approximate topography dimensions in the experimental study, we set groove width on three separate topographies to two, six and nine matrix indices (2μm, 6μm and 9μm), ridges to one matrix index width (1μm), assigning a uniform depth of 0.4μm and matrix dimensions to 1000×1000 indices ($1000 \times 1000\mu m^2$). The result, presented in Figure 2.4 (a)-(c), is a set of linear topographies with varied groove widths and uniform ridge width and depth.

To probe the effect surface processing imperfections might have on migration trajectories and associated directional and displacement properties, we devise a method to progressively introduce 'noise' to already generated linear topographic features. Our approach is to incrementally perturb the linear feature in the plane orthogonal to ridge / groove direction with additive noise. The method we use is to draw index locations to place new depth values from a Gaussian distribution, the mean centred on the axis of the linear feature. We vary the level of 'randomness' around the linear feature with the distribution variance, ρ. When $\rho = 0$ the arrangement of surface gradients are perfectly linear without noise, increasing ρ introduces higher levels of randomness to the feature, making it more 'noisy' and less linear.

We do this numerically using MATLAB's pseudo-random number generator '*randn*' and round to the nearest integer for index values to assign a depth value. We use the same method across topographies with linear 9μm, 6μm and 2μm groove widths, keeping the range for ρ consistent between groove widths, rather than groove width dependent. The result, presented in Figure 2.4, is a set of topographies with 9μm, 6μm

and 2μm groove widths (columns, left to right) ranging from linear and uniform (a)-(c) ($\rho = 0$) to directionally random and disordered (m)-(o) ($\rho = 10$).

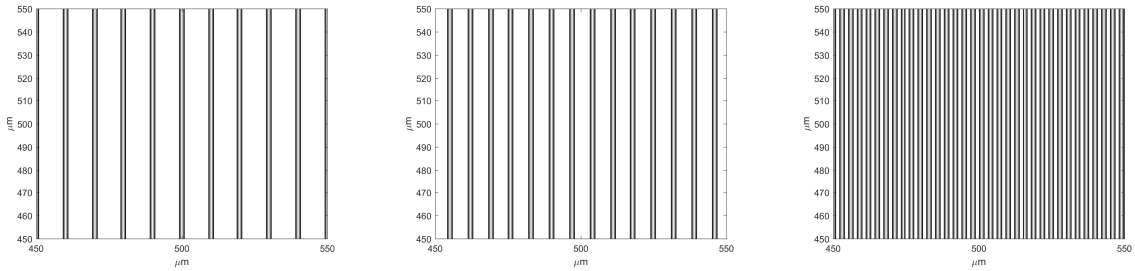

(a) 9μm groove width. $\rho = 0$.

(b) 6μm groove width. $\rho = 0$.

(c) 2μm groove width. $\rho = 0$.

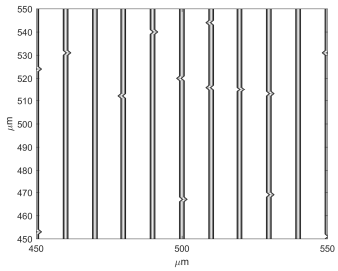

(d) 9μm groove width. $\rho = 0.2$.

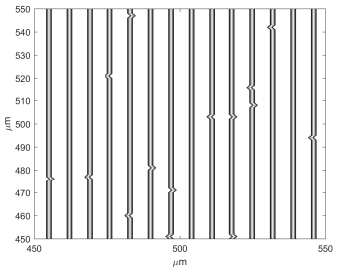

(e) 6μm groove width. $\rho = 0.2$.

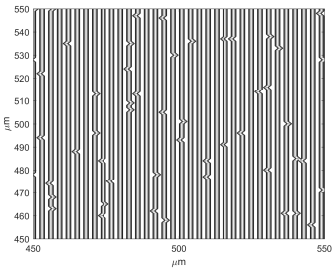

(f) 2μm groove width. $\rho = 0.2$.

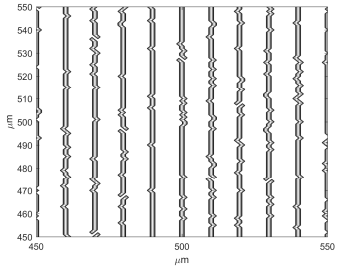

(g) 9μm groove width. $\rho = 0.35$.

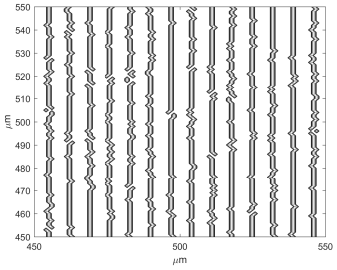

(h) 6μm groove width. $\rho = 0.35$.

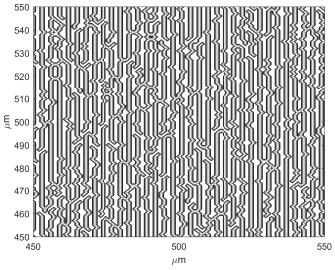

(i) 2μm groove width. $\rho = 0.35$.

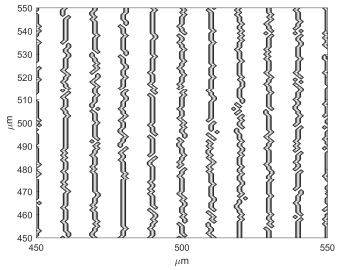

(j) 9μm groove width. $\rho = 0.5$.

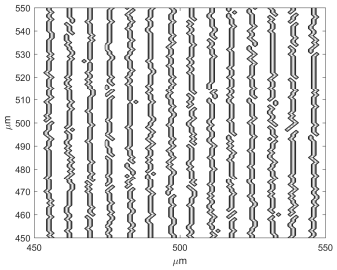

(k) 6μm groove width. $\rho = 0.5$.

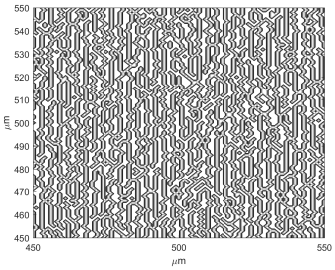

(l) 2μm groove width. $\rho = 0.5$.

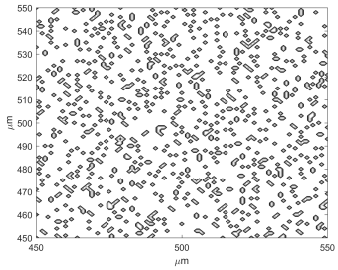

(m) 9μm groove width. $\rho = 10$.

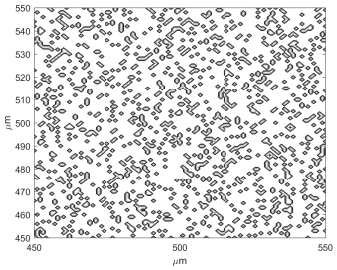

(n) 6μm groove width. $\rho = 10$.

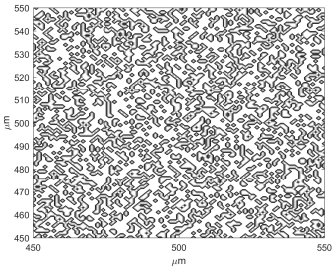

(o) 2μm groove width. $\rho = 10$.

Figure 2.4: Surface topographies generated using MATLAB, featuring 9μm, 6μm and 2μm groove widths with constant ridge width 1μm (columns, left to right), from linear and uniform (a)-(c) through increasing levels of additive feature noise, determined by feature perturbation parameter ρ (rows), to directionally random and disordered (m)-(o), no longer resembling ridges and grooves. Depth: 0.4μm. Grid dimensions: $1000 \times 1000\mu\text{m}^2$.

2.3 Results

2.3.1 Parameter estimation

The general approach we take to establish search boundaries P_1 and P_n for a given topography is to identify non-viable regions of the parameter space using both coarse grid searches and *in vitro* migration data from the previously described experimental study by Kim et al. [105]. We start with a grid search for the flat topography which can be conducted in terms of just model kinesis parameters, β and α (since bias parameter κ has no effect), giving a 2-dimensional grid search. We then use search boundaries located for the flat topography as preliminary boundaries for subsequent grid searches on the grooved topographies, which we further refine in course.

For the flat topography, we first establish search boundaries by coarse searching over substantial ranges for both parameters and simultaneously, identify parameter regions where average simulated migration path length L_{sim} was significantly above average experimental path length L_{exp} over an equal time course (i.e. where $L_{sim} \gg L_{exp}$). With search boundaries P_1 and P_n established, we then conduct a more refined grid search.

For each of the linear topographies (9μm, 6μm and 2μm groove widths, respectively) we use boundaries P_1 and P_n for the flat topography and coarse search to update P_1 and P_n, this time iterating through increasing values for κ to establish approximate search boundaries for κ. We then update the boundaries P_1 and P_n for the search on each topography and proceed to refine the discretisation for the search. We repeat this for all the grooved topographies.

We present in Figure 2.5 contour plots which illustrate where the minima are reproducibly located for (a) flat topography at $\kappa = 0$ (the choice of κ is arbitrary, since there

are no surface gradients), (b) 9μm groove width topography at $\kappa = 1$, (c) 6μm groove width topography at $\kappa = 0.75$ and (d) 2μm groove width topography at $\kappa = 0.5$. The colour bar represents values for the error function ϵ, the range fixed arbitrarily small at $0 \leq \epsilon \leq 0.03$, plotted over an axes for kinesis parameters β and α at fixed values for κ. Minima (i.e. ϵ values closest to zero) are coloured blue. The blue asterisks represent numerically approximated minima points (details follow). The blue line is a polynomial function fit to β-α grid points marked by the blue asterisks.

We see clearly in Figure 2.5 (a) that multiple parametrisations are feasible for the flat topography. We see, with the help of a polynomial fit, an approximately quartic relationship between β and α at minima over the approximate parameter ranges $0.06 < \beta < 1.24$ and $0.03 < \alpha < 3$, respectively (limited by grid resolution).

To estimate individual parameter combinations for the flat topography we fit a polynomial function to an identified region of minima and use the fitted function to approximate values for β and α. The numerical approach is as follows: define a region of minima as that which satisfies $\epsilon \leq 0.03$, then identify mid-point locations of the region across β (approximate minima, blue regions in Figure 2.5 (a)) and, excluding clear outliers, fit an appropriate polynomial function to the set of approximated minima using a numerical fitting tool, (MATLAB's *fit* function). We see in Figure 2.5 (a) (blue line), the method captures the major β-α relationship present at the region of minima and yields reasonable approximate parametrisations for model output. We present the polynomial function through minima in Figure 2.5 (a), $\hat{f}$, in Eq.(2.15).

$$\hat{f}(\beta) = -6.102\beta^4 + 11.79\beta^3 - 5.577\beta^2 + 2.189\beta - 0.1469, \tag{2.15}$$

whose range $\hat{f}(\beta)$ gives an approximation for α at minima, over the approximate domain $0.06 < \beta < 1.24$.

By contrast, in Figure 2.5 (b)-(d), we see clear identifiable parameter combinations for β and α at given κ values for each of the grooved topographies. This persists through ranges for κ for each of the linear topographies (results not shown). Generally, the ranges for β and α over which these minima occur through κ for the grooved topographies are significantly smaller than those for the flat topography.

To estimate individual parameter combinations for these topographies, we constrain $\epsilon \leq 0.025$ and take the median β value, β_η, over the resulting region of minima, choosing α at an arbitrary minimum for β_η.

In Figure 2.5 (b), we see minima (for which $\epsilon \leq 0.03$, arbitrarily) occur over the approximate ranges $0.07 < \beta < 0.23$ and $0.003 < \alpha < 0.1$ for the 9μm groove width topography at $\kappa = 1$. Minima persist through an approximate range $0.02 < \kappa < 10$ (results not shown). In Figure 2.5 (c) we see minima occur over the approximate ranges $0.03 < \beta < 0.079$ and $7.58 \times 10^{-4} < \alpha < 0.01$ for the 6μm groove width topography at $\kappa = 0.75$. Minima persist through an approximate range $0.15 < \kappa < 5$ (results not shown). In Figure 2.5 (d), we see minima occur over the approximate ranges $0.07 < \beta < 0.13$ and $2 \times 10^{-3} < \alpha < 0.01$ for the 2μm groove width topography at $\kappa = 0.5$. Minima persist through an approximate range $0.15 < \kappa < 5$ (results not shown).

To demonstrate closeness of metrics derived from the parametrised model, θ_σ and s_μ, to those derived from Kim et al. [105], θ^*_σ and s^*_μ, using the methods described for choosing individual parameter combinations, we plot the metrics on the same axes in Figure 2.6.

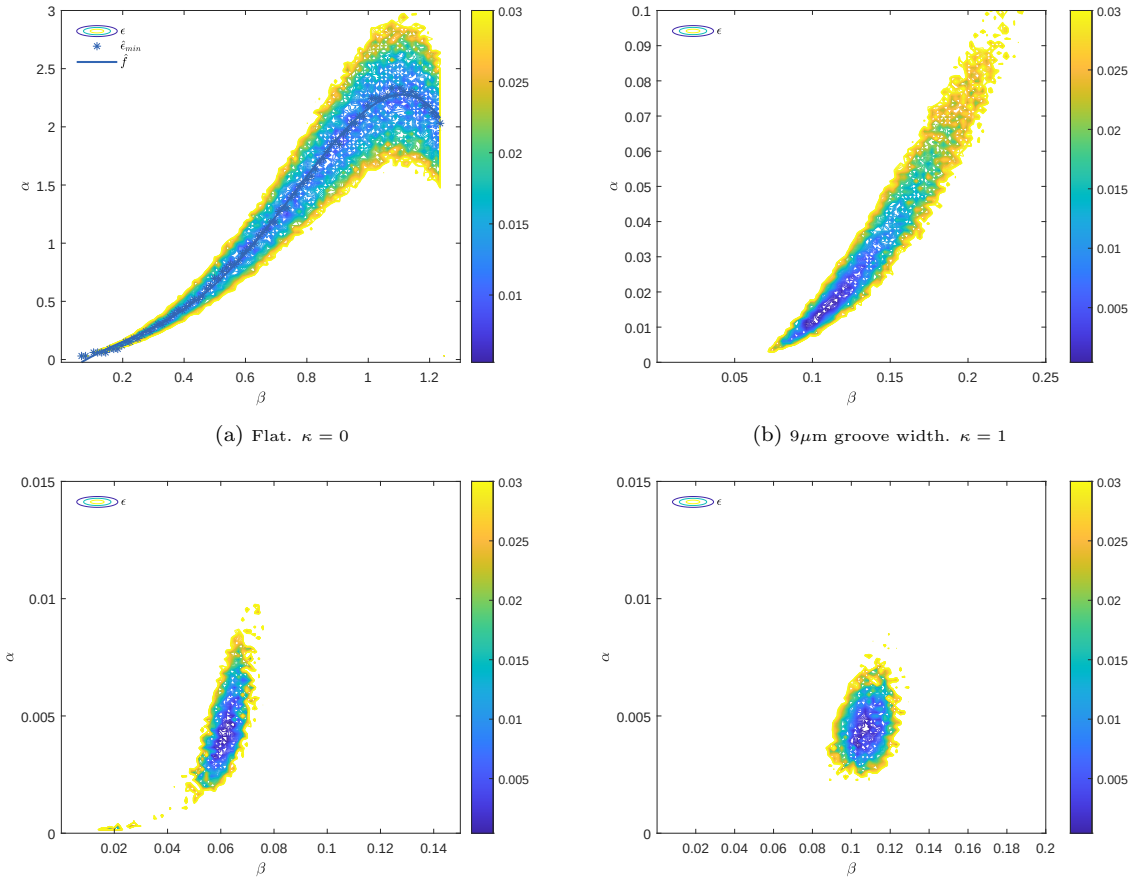

(a) Flat. $\kappa = 0$

(b) 9μm groove width. $\kappa = 1$

(c) 6μm groove width. $\kappa = 0.75$

(d) 2μm groove width. $\kappa = 0.5$

Figure 2.5: Contour plots resulting from a grid search optimisation for four different structured topographies: (a) flat, (b) 9μm groove width (c), 6μm groove width and (d) 2μm groove width, across specific ranges for model kinesis parameters β and α at fixed values for model bias parameter κ. Colour bar represents evaluated values of error function ϵ. Blue asterisk denotes approximate minimum values for ϵ, $\hat{\epsilon}_{min}$ (see text for details of approximation). Blue line is a polynomial function $f(\hat{\beta})$ fitted to the set of points $\hat{\epsilon}_{min}$ (see text for definition). Note that in (a) flat: α and β are non-identifiable, the relationship approximately quartic, and in (b)-(d) 9μm, 6μm and 2μm: α and β are identifiable with uncertainty for a given κ. Changes to κ do not influence ϵ for (a), however there is a range for κ for which different and equally valid (under the condition $\epsilon \leq 0.03$) parameter spaces exist for (b)-(d), such that the choice of κ is arbitrary within each range. (a) flat: $\kappa = 0$. (b) 9μm: $\kappa = 1$. (c) 6μm: $\kappa = 0.75$. (d) 2μm: $\kappa = 0.5$. Simulation parameters: $m = 100$, number of cells $N_c = 100$, time (mins) $T = 540$, ranges for β and α evident in (a)-(d).

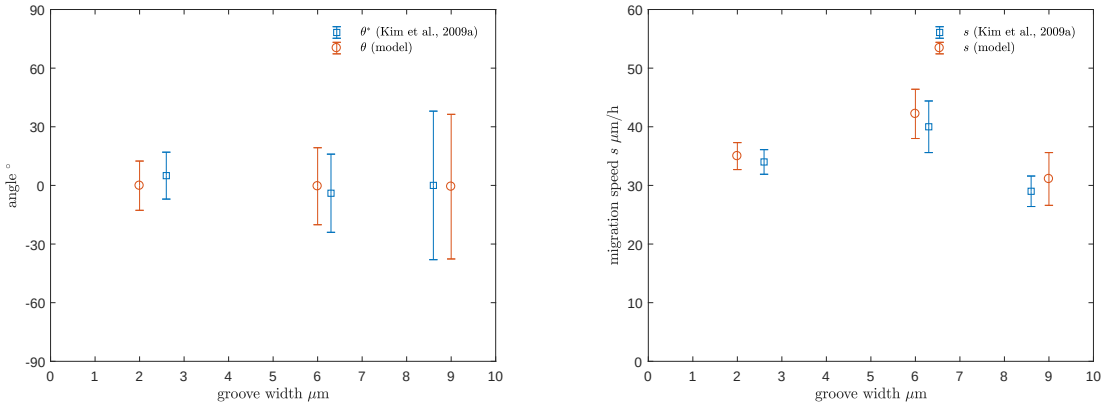

(a) Polarisation and orientation angles θ^* and θ.

(b) Migration speed s^* and s.

Figure 2.6: Metric data derived from Kim et al. [105] (blue) and the parametrised model (orange) for average groove widths 2.6μm, 6.3μm and 8.6μm and uniform groove widths 2μm, 6μm and 9μm, respectively. (a) polarisation angle θ^* from Kim et al. (square: mean θ^*_μ; error bar: $\theta^*_\mu \pm$ SD θ^*_σ) and orientation angle θ from the parametrised model (circle: mean θ_μ; error bar: $\theta_\mu \pm$ SD θ_σ). (b) migration speed s^* from Kim et al. (square: mean s^*_μ; error bar: $s^*_\mu \pm$ SEM $s^*_{\sigma M}$) and s from the parametrised model (circle: mean s_μ; error bar: $s_\mu \pm$ SD s_σ). Grid dimensions: $1000 \times 1000\mu\text{m}^2$. Migration parameters: $\beta = 0.1$, $\alpha = 0.013$, $\kappa = 1$ (9μm groove width); $\beta = 0.06$, $\alpha = 0.004$, $\kappa = 0.75$ (6μm groove width); $\beta = 0.11$, $\alpha = 0.005$, $\kappa = 0.5$ (2μm groove width). Simulation parameters: $N_c = 100$ cell paths, $T = 540$ minutes, $N = 36$ increments, $X_{init} = (500\mu\text{m},500\mu\text{m})$ is the fixed initial position.

2.3.2 Initial conditions

First, we review migration trajectory and metric output for topographies with linear 9μm, 6μm and 2μm groove widths, using parameter combinations derived from the parameter estimation method. Then, we use estimated parameters to predict by simulation how trajectory behaviour might evolve when presented with linear topographies of equal dimensions but with graded random perturbations to linear topographic features.

For the first stage, we use only flat and linear topographies generated as outlined in *Methods* 2.2.5 and used for the parameter estimation. All four topographies have been generated on a square matrix representing $1000 \times 1000\mu\text{m}^2$ and feature either no gradient (the flat surface) or 1μm wide 0.4μm high linear 'ridge' features (parallel to the vertical axis) spaced either 9μm, 6μm and 2μm apart. A $100 \times 100\mu\text{m}^2$ plot window of each linear topography are presented in Figure 2.4 (top row) (a)-(c).

For predictions, we introduce random perturbations to linear topographic features for

each groove width / ridge frequency, to give a set of graded directionally linear to random topographies to test, as outlined in *Methods* 2.2.5. Initially we test, for each groove width, four topographies with gradually increasing levels of random perturbation to linear features using feature perturbation parameter ρ; $\rho = 0$ (linear), $\rho = 0.2$, $\rho = 0.35$ and $\rho = 0.5$. The result is a set of topographies with constant feature height but 'ridge' and 'groove' width varying from uniform to spatially variable dependent on randomised location and magnitude of perturbations. We then extend the range for ρ to test how migration metrics evolve with uniform linear features to completely random and disordered, where ridges and grooves become irregularly spaced / scaled pillar features; see Figure 2.4 (bottom row) (m)-(o). To accommodate higher displacement on more disordered topographies, we increase topography boundaries to $2000 \times 2000 \mu\text{m}^2$. To set migration model parameters we use the methods outlined in *Results* 2.3.1. For the flat topography, we use the function $\hat{f}$ and select the median β value within the approximated domain given to generate an individual parameter combination. For the other topographies, we use the methods already outlined in *Results* 2.3.1. For continuity we use κ values presented in Figure 2.5 for result output. Individual parameter combinations with which we proceed for the topographies described are presented in Table 2.2. We also keep these parameters constant when testing the model with the randomly perturbed topographies.

For simulations, we fix the initial position of migration trajectories constant for each individual simulation and between different simulations. To accommodate trajectories, we set the initial position in the centre of each set of topographies, for simulations in *Results* 2.3.3, where topography domain is $1000 \times 1000 \mu\text{m}^2$, the initial position is (500μm, 500μm) and for *Results* 2.3.4, where topography domain is $2000 \times 2000 \mu\text{m}^2$, ($1000 \mu$m,

1000μm). We also fix the number of cell trajectories in simulations to $N_c = 100$ for clarity in trajectory plots and accompanying metrics, unless otherwise stated.

To match the time-lapse speed measurement in the study by Kim et al., we set simulation time for every cell to $T = 540$ minutes split into $N = 36$ increments each of 15 minute duration, and set Euler-Maruyama sub-increments a tenth smaller. Time parameters are kept constant between all simulations.

Table 2.2: Migration model parameter combinations (to 3 d.p.) for flat, 9μm, 6μm and 2μm groove width topographies, determined by grid search optimisation with Kim et al. migration data [105], and methods outlined in *Results* 2.3.1.

Topography	β	α	κ
Flat (no gradient)	0.650	1.068	0.000
9μm groove width	0.100	0.013	1.000
6μm groove width	0.060	0.004	0.750
2μm groove width	0.110	0.005	0.500

2.3.3 Parametrised migration model with uniform linear topographies

In Figure 2.7, we present individual cell migration trajectories for the parametrised model on (a) flat, (b) 9μm, (c) 6μm and (d) 2μm groove width topographies. We see in Figure 2.7 (a)-(d) a clear trend for trajectories to acquire gradually more linearity and more closely follow the groove direction from flat, (a), through topographies with decreasing groove widths to the narrowest groove width, (d).

In Figure 2.7 (a), we see trajectories for the flat topography show no clear directional preference at all, appearing directionally random and particularly tortuous, exploring only a small central radius of the surface surrounding the simulation starting position, (500μm,500μm).

In Figure 2.7 (b), we see trajectories for the 9μm grooved topography show some clear alignment with the groove direction, demonstrating some preference to migrate in a general direction approximating the groove direction, though still maintaining discernible stochasticity.

In Figure 2.7 (c), trajectories for the 6μm grooved topography display considerable directional linearity and a clear preference to follow groove direction, trajectories tending to diverge around the starting position, (500μm,500μm), and follow groove direction in opposing directions. Trajectory displacements are also noticeably larger for this topography, some approaching the domain boundaries over the simulation.

Finally, in Figure 2.7 (d), we see trajectories for the 2μm grooved topography exhibit the most prominent directional linearity of all the topographies, aligning strictly with groove direction. Trajectories show a similar trajectory divergence around the starting position and displace perceptibly far over the simulation, but less than for the 6μm groove width.

The trend we see in trajectory behaviour is also reflected in orientation angle, θ°, and migration speed, s μm/h, distributions for each of the topographies shown in Figure 2.8 (left and right columns, respectively).

We see clearly in Figure 2.8 (left column), the spread in θ distributions with decreasing groove widths, (a)-(g), reduces markedly; captured by θ standard deviation, θ_{σ}. This general pattern resembles that observed by Kim et al. [105] in cell polarisation angle, θ^{*}, distributions for topographies with comparable dimensions.

We see for the flat topography in Figure 2.8 (a), the distribution for θ is approximately uniform in the range $-90^{\circ} \leq \theta \leq 90^{\circ}$, with mean $\theta_{\mu} = -0.785^{\circ}$ (heavy red dash) and standard deviation $\theta_{\sigma} = 52.4^{\circ}$ (light red dash). This supports the earlier observation

that trajectories on the flat topography show no apparent directional preference.

In Figure 2.8 (c), the distribution for θ for the 9μm topography takes on a Gaussian character, showing a greater proportion of angles measured around zero, consistent with the observation that trajectories show some preference to migrate in the general groove direction. For this topography, mean $\theta_\mu = -0.631^\circ$ and standard deviation reduces to $\theta_\sigma = 37.0^\circ$.

For the 6μm topography in Figure 2.8 (e), we see the distribution for θ maintain a Gaussian character with an even greater proportion of angles around zero, with mean $\theta_\mu = -0.416^\circ$ and standard deviation reducing quite significantly to $\theta_\sigma = 19.7^\circ$.

For the 2μm topography in Figure 2.8 (g), the distribution for θ is also Gaussian with clearly the smallest spread of all distributions, with mean $\theta_\mu = -0.140^\circ$ and standard deviation reducing further to $\theta_\sigma = 12.6^\circ$.

In Figure 2.8 (right column) we see a different trend in the distributions for s, which clearly change character across decreasing groove widths (b)-(h). We also see an optimal intermediate groove width for s; the highest average speed, s_μ, on the 6μm grooved topography (f). We see a similar trend in migration speed, s^*, distributions in Kim et al. [105], where intermediate groove widths were observed to prompt optimal speeds.

We see for the flat topography in Figure 2.8 (b), the distribution for s is right-skewed with mean and median speed $s_\mu = 30.4\mu$m/h and $s_\eta = 28.8\mu$m/h respectively, with first and third quartiles $s_{Q_1} = 18.4\mu$m/h and $s_{Q_3} = 41.1\mu$m/h.

In Figure 2.8 (d), for the 9μm topography, we see the distribution maintains a right-skew with similar mean and median speeds $s_\mu = 31.1\mu$m/h and $s_\eta = 29.4\mu$m/h and wider inter-quartile range, $s_{Q_1} = 15.4\mu$m/h and $s_{Q_3} = 44.4\mu$m/h.

In Figure 2.8 (f), for the 6μm topography, we see the distribution becomes less dis-

cernibly skewed and shows much higher mean and median speeds, $s_\mu = 42.2\mu$m/h and $s_\eta = 42.5\mu$m/h, and a markedly increased first quartile, $s_{Q_1} = 32.6\mu$m/h, and third quartile, $s_{Q_3} = 52.5\mu$m/h. This supporting the observation that the 6μm grooved topography prompts much higher speeds on average than for the other groove widths.

In Figure 2.8 (h), for the 2μm topography, the distribution assumes a clear Gaussian character and reduced mean and median speeds, $s_\mu = 35.0\mu$m/h and $s_\eta = 34.7\mu$m/h, with first and third quartiles, $s_{Q_1} = 28.6\mu$m/h and $s_{Q_3} = 41.0\mu$m/h, respectively.

The trend we observe between groove width and migration speed s is also reflected in the mean-squared displacement (MSD) of migration trajectories in Figure 2.9, for flat (blue), 9μm (red), 6μm (yellow) and 2μm (purple) topographies. MSD is perceptibly greater for the 6μm grooved topography (yellow) over simulation time than for any of the other topographies; approximately an order of magnitude larger than for the flat topography.

2.3.4 Model predictions with randomly perturbed linear topographies

To investigate how migration characteristics change when topographic features become less uniform (such as surface imperfections introduced by coarse fabrication), the model will be tested upon different topographies with features ranging from uniform and directionally linear to non-uniform and directionally random.

The approach is to numerically generate topographies with linearly arranged 'ridges' and 'grooves', each with a groove width comparable to those in the experimental study by Kim et al. [105] (9μm, 6μm and 2μm), and gradually perturb these linear features with incrementally increasing magnitude; for details see *Methods* 2.2.5. We run model simulations for each of these topographies and test how the migration behaviour evolves

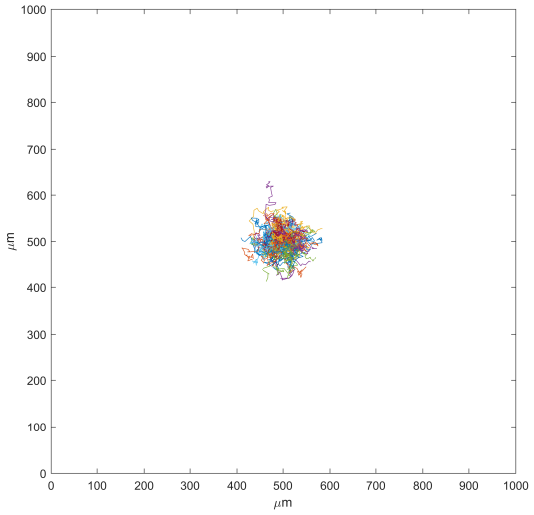

(a) Flat.

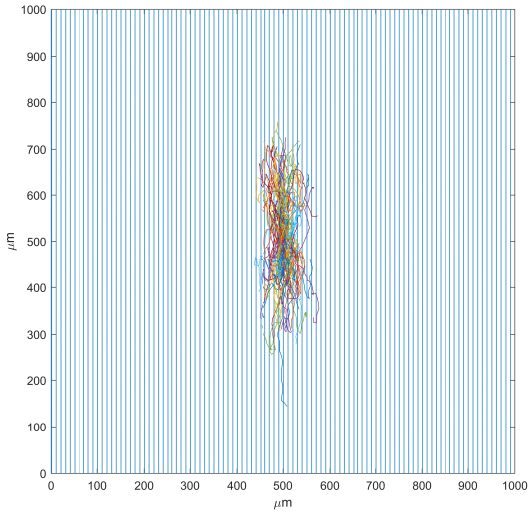

(b) 9μm groove width.

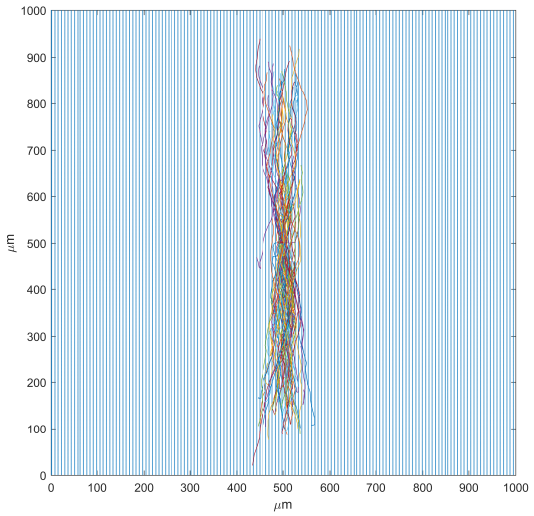

(c) 6μm groove width.

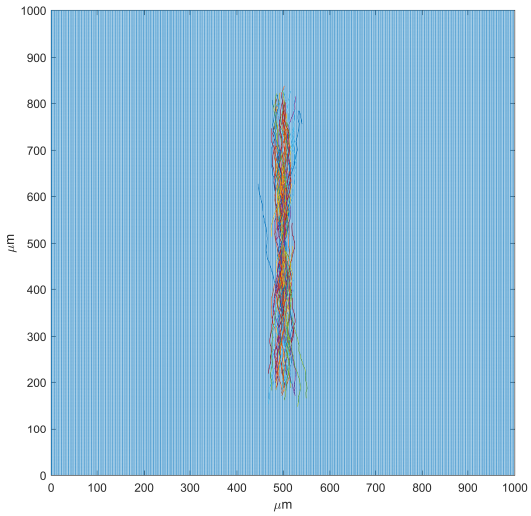

(d) 2μm groove width.

Figure 2.7: Parametrised model migration trajectories (multi-colour) over gradient fields (blue) of four different topographies: (a) flat (no gradient), (b) 9μm groove width, (c) 6μm groove width and (d) 2μm groove width, (b)-(d) with constant ridge width 1μm and depth 0.4μm. Trajectories develop a clear linearity when introduced to the linearly grooved topographies, the extent of linearity present dependent on the groove width. We see a clear trend for trajectories to show more pronounced linearity with decreasing groove width (b)-(d). Grid dimensions: $1000 \times 1000\mu\text{m}^2$. Migration parameters: (a) $\beta = 0.65$, $\alpha = 1.07$, $\kappa = 0$, (b) $\beta = 0.1$, $\alpha = 0.013$, $\kappa = 1$, (c) $\beta = 0.06$, $\alpha = 0.004$, $\kappa = 0.75$, (d) $\beta = 0.11$, $\alpha = 0.005$, $\kappa = 0.5$. Simulation parameters: $n = 100$ cell paths, $T = 540$ minutes, $N = 36$ increments, $X_{init} = (500\mu\text{m},500\mu\text{m})$ is the fixed initial position.

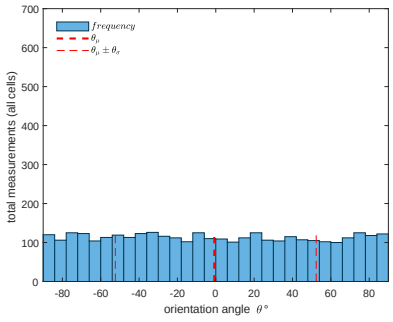

(a) Flat. $\theta°$.

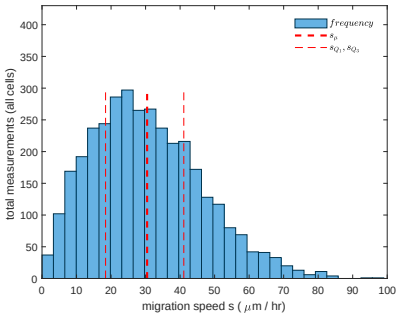

(b) Flat. s μm/h.

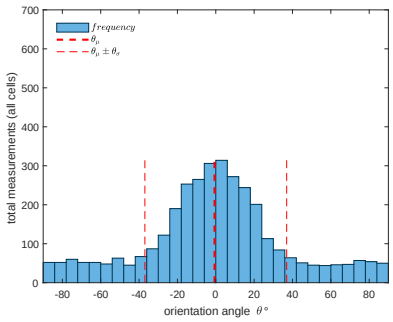

(c) 9μm groove width. $\theta°$.

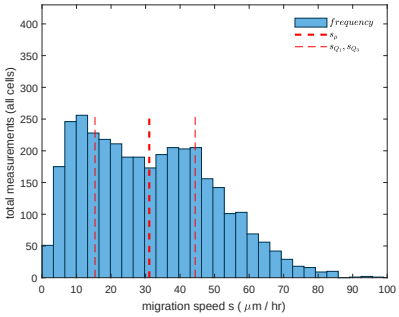

(d) 9μm groove width. s μm/h.

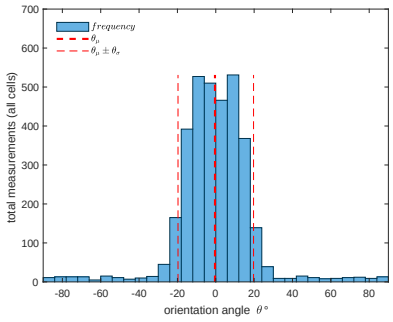

(e) 6μm groove width. $\theta°$.

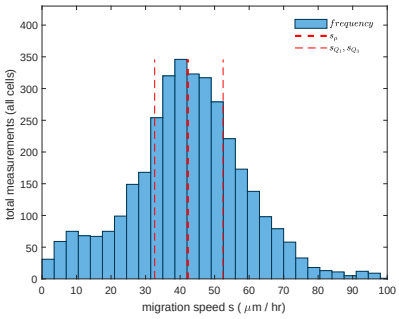

(f) 6μm groove width. s μm/h.

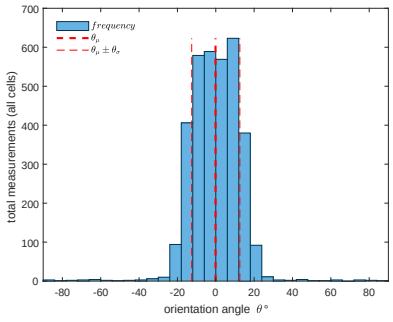

(g) 2μm groove width. $\theta°$.

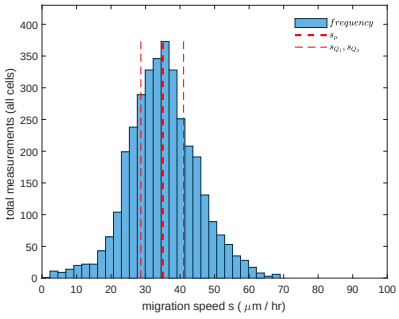

(h) 2μm groove width. s μm/h.

Figure 2.8: Orientation angle, $\theta°$, (left column) and migration speed, s (μm/h), (right column) distributions for the four different topographies (rows): (a)-(b) flat, (c)-(d) 9μm groove width, (e)-(f) 6μm groove width and (g)-(h) 2μm groove width. Distributions for both θ and s display total measurements taken for all cells at $N = 36$ increments over $T = 540$ minutes simulation time (for details see *Methods* 2.2.4). We see θ distributions (left column) acquire a Gaussian character for the linearly grooved topographies (b)-(d) and a groove width dependence for standard deviation, θ_σ, (red, light). We see s distributions (right column) change character with groove width and exhibit an optimal average speed, s_μ, (red, heavy) for the 6μm groove width topography. Grid dimensions, migration and simulation parameters: (see Figure 2.7).

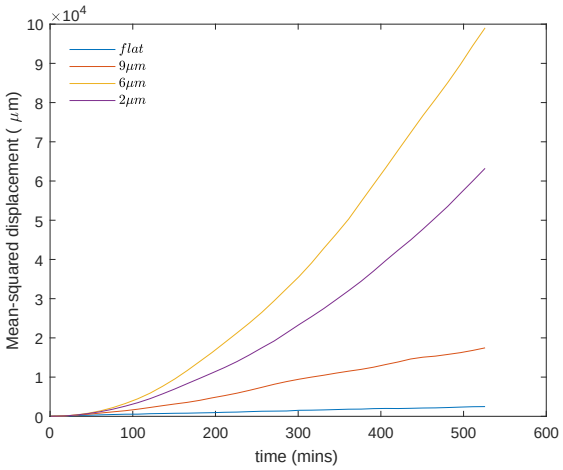

Figure 2.9: Mean-squared displacement (MSD) (μm) over time t for flat (blue), 9μm (red), 6μm (yellow) and 2μm (purple) groove width topographies. We see MSD over time t is greatest for the 6μm groove width topography (yellow) compared to the other topographies, markedly greater than for the flat topography (blue). Grid dimensions, migration and simulation parameters: (see Figure 2.7).

in response to incrementally more randomly arranged topographic features.

We first consider the set of topographies with a 2μm groove width, first presented in Figure 2.4 (right column). In Figure 2.4 (c) we see the uniform linear 2μm groove width topography has the narrowest groove width of all the topographies presented and, descending the column, sustains the clearest loss in uniform linearity over ρ compared to other groove widths.

We present in Figure 2.10, migration trajectory behaviour for the set of topographies with a 2μm groove width and (a) linear features and (b)-(d) randomly perturbed features. We see in Figure 2.10 a clear trend for trajectories to lose directional linearity across the set of topographies (a)-(d), dependent on ρ. The degree of unpredictability in trajectory direction appears to increase with ρ, mirroring the increasing level of 'disorderedness' in the topographies, prompting visibly more tortuous trajectories. Though trajectories appear to maintain some perceptible degree of general directionality in alignment with groove direction, displacements on average clearly spanning a much greater proportion of the vertical (groove direction) compared to the horizontal

axis (trajectories mostly confined to the middle third of the domain boundaries, see Figure 2.10 (a)-(d)). Notably, ρ also appears to prompt an increase in trajectory displacements, clearly extending greater distances and exploring a greater proportion of the surface over simulation time with increase to ρ.

We see in Figure 2.11, clear trends for both accompanying orientation angle, $\theta°$, and migration speed, s μm/h, distributions (left and right columns, respectively) through values for ρ (rows).

We see in Figure 2.11 (left column) distributions for θ for the more linearly organised topographies, (a) and (c), appear approximately Gaussian but, with increase to ρ, evolve into bimodal distributions for the more disordered topographies, (e) and (g), all distributions approximately symmetric about $\theta = 0°$. Standard deviations, θ_σ, (red, light) broaden significantly with increase to ρ. For the linear topography ($\rho = 0$), (a), $\theta_\sigma = 12.5°$, and for the most disorganised topography we present ($\rho = 0.5$), (g), $\theta_\sigma = 36.8°$, supporting the earlier observation that trajectories lose directional linearity with increase to ρ.

We see in Figure 2.11 (right column), distributions for s shift markedly in the horizontal axis (s μm/h) with increase to ρ and display a clear monotonic increase in mean migration speed, s_μ, rising from $s_\mu = 35.0\mu$m/h for (b), where $\rho = 0$, to $s_\mu = 69.2\mu$m/h for (h), where $\rho = 0.5$. The character of the distributions also change through ρ, which we see are uni-modal and right-skewed at lower values for ρ, (b) and (d), and acquire more symmetry with increase to ρ, (f) and (h).

For the intermediate groove width topography, 6μm, we see in Figure 2.4 (central column) ridge features are less densely packed than for the 2μm topography and maintain some discernible linearity through all levels of perturbations we test (column, (b)-(k)).

We present in Figure 2.12, migration trajectory behaviour for the set of topographies with a 6μm groove width and (a) linear features and (b)-(d) randomly perturbed features. We see in Figure 2.12 trajectories clearly lose directional linearity with increase to ρ, in a manner similar to that observed for the 2μm topographies. Most notable is the degree of trajectory displacement introduced with ρ, extending out to domain boundaries when $\rho = 0.5$, (d). Though, as with Figure 2.10, trajectories appear to maintain some general directionality, spanning much greater absolute distance in the vertical versus horizontal axis.

In Figure 2.13 we see trends in distributions for θ (left column) and s (right column) generally resemble those observed in Figure 2.11 for the 2μm topographies.

Distributions for θ (left column) clearly shift in character from Gaussian for the more linearly organised topographies, (a) and (c), to bimodal with increase to ρ, θ_σ increasing from $\theta_\sigma = 18.6°$ (a) to $\theta_\sigma = 34.3°$ (g).

In distributions for s (right column), we see a significant positive shift in the s axis with increase to ρ, surging from $s_\mu = 42.3\mu$m/h at $\rho = 0$, (b), to $s_\mu = 97.2\mu$m/h at $\rho = 0.5$, (h). We observed a similar shift in s distribution character with ρ with the 2μm topographies, uni-modal where at lower ρ the distribution is right-skewed and becomes more symmetrical with increase to ρ.

For the widest groove width topography, 9μm, we see in Figure 2.4 (left column) ridge features are least densely distributed of all the topographies tested. We see feature perturbations appear relatively insignificant compared to groove width and features clearly maintain an approximate linearity through the levels of perturbation we test (column, (a)-(j)).

We present in Figure 2.14, migration trajectory behaviour for the set of topographies

with a 9μm groove width and (a) linear features and (b)-(d) randomly perturbed features. We see in Figure 2.14, as with the other topographies in Figure 2.10 and 2.12, trajectories lose clear directional linearity with increase to ρ, becoming markedly more tortuous. Trajectories, however, still remain confined to a central $500 \times 800\mu\text{m}^2$ strip of the domain through ρ. Overall displacement appears to increase with ρ and is observably less significant than for the other groove width topographies.

In Figure 2.15 we see trends in both θ (left column) and s (right column) distributions that are subtler than that observed for the 2μm and 6μm sets of topographies in Figure 2.11 and 2.13, respectively. We see both distributions for θ and s maintain largely stable characteristics with increase to ρ, over the range for ρ presented.

Distributions for θ (left column) maintain a consistently Gaussian character through ρ, θ_σ rising only moderately from $\theta_\sigma = 37.0°$ at $\rho = 0$, (a), to $\theta_\sigma = 42.2°$ at $\rho = 0.5$, (g).

Distributions for s (right column), we see remain uni-modal but maintain a positive-skew with increase to ρ, with steadily broadening quartiles and a small monotonic increase to s_μ, from $s_\mu = 31.1\mu$m/h, (b), to $s_\mu = 49.5\mu$m/h, (h).

If we increase ρ such that linear topographic features for all groove widths become almost completely randomly organised, varying only in feature density, the resulting topographies take on a form like those presented in Figure 2.4 bottom row (m)-(o), where topographies comprise randomly arranged pillar like features. To see how migration behaviour evolves with ρ, we run model simulations for each groove width topography with ρ changing at a hundred increments in the range $0 \leq \rho \leq 10$. We plot the resulting curves for θ_σ and s_μ against ρ in Figure 2.16 for 2μm (blue), 6μm (red) and 9μm (yellow) groove width topographies.

In Figure 2.16 (a), we see curves for θ_σ across all topographies increase rapidly in the interval $0 < \rho \leq 1$, all eventually stabilising in the interval $45° < \theta_\sigma < 50°$; close to θ_σ for migration simulated for the flat topography. The steepness of gradient for the initial transients is dependent on the groove width of the topography, the curve for 2μm most rapid, followed by that of the 6μm then 9μm groove widths. Interestingly, we see the curve for θ_σ for the 2μm rise and remain above that for the 6μm groove width at around $\rho = 0.35$.

In Figure 2.16 (right), we see s_μ is clearly ρ dependent for all topographies, the curves also increasing rapidly over the approximate interval $0 < \rho \leq 2$, but appear to taper down as ρ is increased, each curve exhibiting a maximum s_μ. Interestingly, despite s_μ for the 9μm groove width topographies (yellow curve) prompting the slowest migration of all topographies over small ρ, s_μ steadily increases higher than the curve for the 2μm groove width topographies (blue) with increasing ρ. We see the 6μm groove width topographies always maintain the highest s_μ over ρ but the 2μm and 9μm groove width topographies dependent on ρ; 2μm higher below around $\rho = 1.56$ and 9μm higher above.

2.4 Discussion

In this study, we proposed a mathematical model for topographically influenced cell migration. We parametrised the model using experimental data derived from *in vitro* fibroblast migration on linearly ridged/grooved topographies published in a study by Kim et al. [105], in the journal *Biomaterials*. We used the parametrised model to predict how migration might alter if random perturbations were introduced to linearly organised topographic features. The aim was to capture principal behavioural charac-

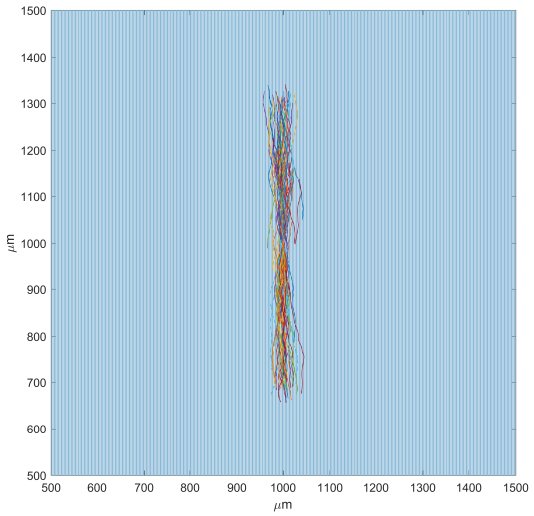

(a) 2μm groove width. $\rho = 0$.

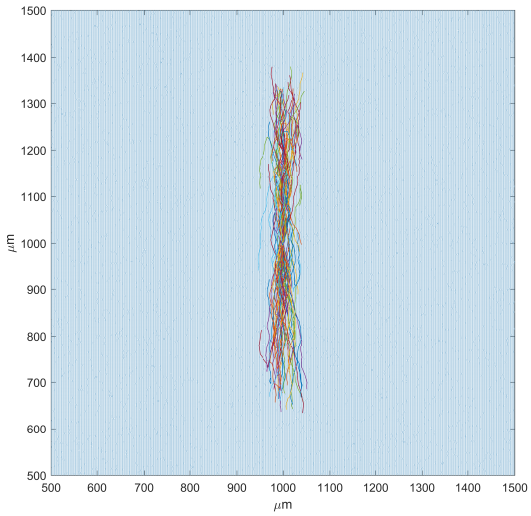

(b) 2μm groove width. $\rho = 0.2$.

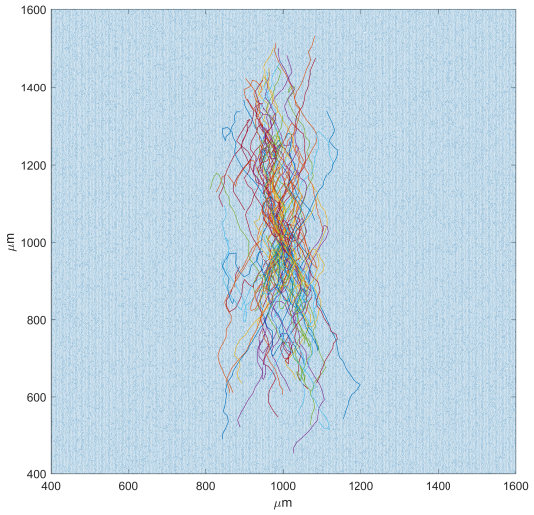

(c) 2μm groove width. $\rho = 0.35$.

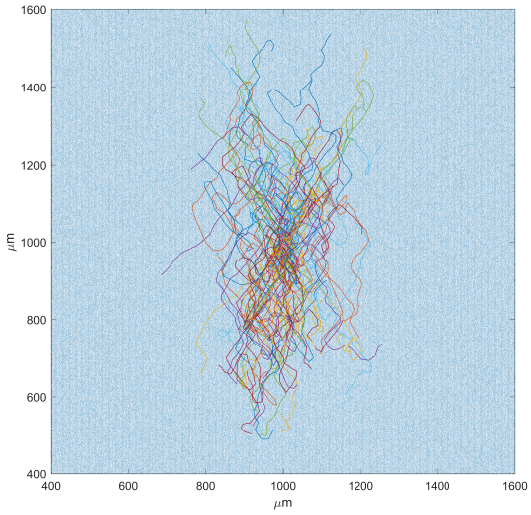

(d) 2μm groove width. $\rho = 0.5$.

Figure 2.10: Model migration trajectories (multi-colour) over gradient fields (blue) of four topographies with linear 2μm groove and 1μm ridge width topographic features perturbed stochastically in the direction orthogonal to the ridge/groove plane with four different 'noise' levels, determined by feature perturbation parameter ρ (see *Methods* 2.2.5): (a) $\rho = 0$ (linear), (b) $\rho = 0.2$, (c) $\rho = 0.35$ and (d) $\rho = 0.5$. Trajectories begin to lose directional linearity with the introduction of feature perturbation, the degree of directional unpredictability dependent on ρ (increasing with ρ). Grid dimensions: $2000 \times 2000\mu\text{m}^2$. Depth: 0.4$\mu$m. Migration parameters: (a)-(d) $\beta = 0.11$, $\alpha = 0.005$, $\kappa = 0.5$. Simulation parameters: (a)-(d) $n = 100$ cell paths, $T = 540$ minutes, $N = 36$ increments, $X_{init} = (1000\mu\text{m},1000\mu\text{m})$ is the fixed initial position.

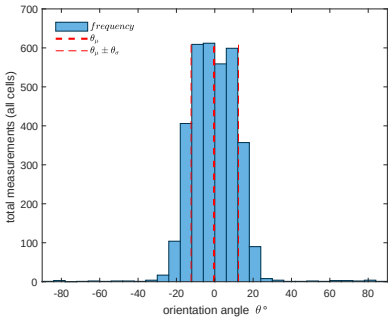

(a) 2μm groove width. $\rho = 0.$ θ°.

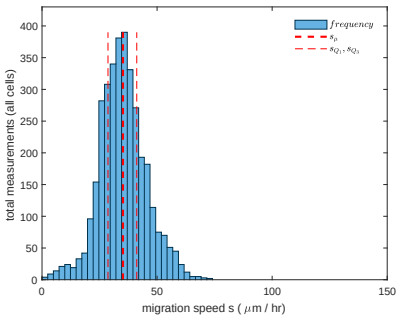

(b) 2μm groove width. $\rho = 0.$ s μm/h.

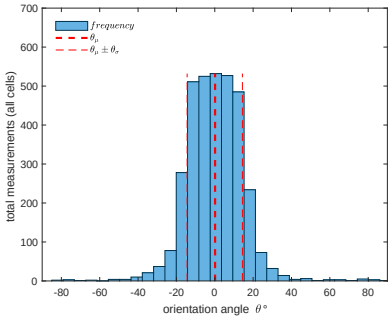

(c) 2μm groove width. $\rho = 0.2$. θ°.

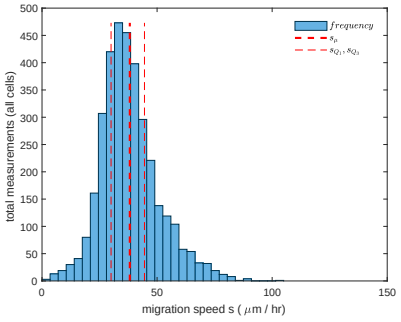

(d) 2μm groove width. $\rho = 0.2$. s μm/h.

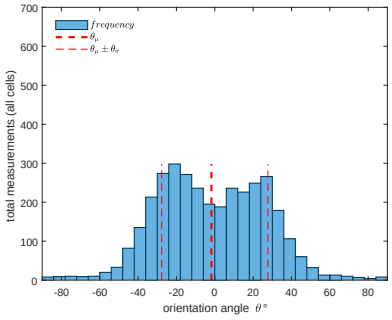

(e) 2μm groove width. $\rho = 0.35$. θ°.

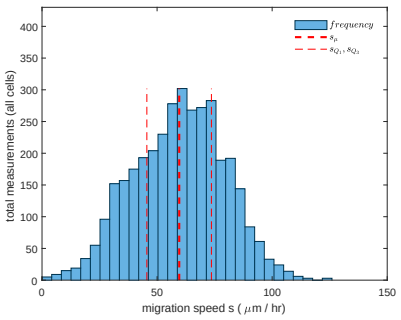

(f) 2μm groove width. $\rho = 0.35$. s μm/h.

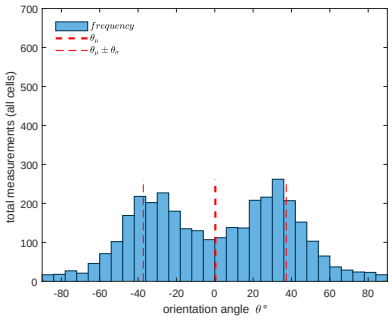

(g) 2μm groove width. $\rho = 0.5$. θ°.

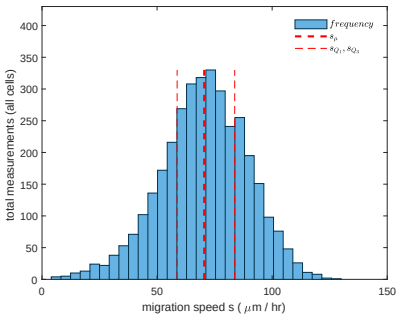

(h) 2μm groove width. $\rho = 0.5$. s μm/h.

Figure 2.11: Orientation angle, θ°, and migration speed, s (μm/h), distributions (left and right column, respectively) for the four topographies in Figure 2.10 (rows): (a)-(h) 2μm groove width; (a)-(b) $\rho = 0$, (c)-(d) $\rho = 0.2$, (e)-(f) $\rho = 0.35$ and (g)-(h) $\rho = 0.5$. We see θ distributions (left column) shift from Gaussian to bimodal with increase to ρ (a)-(g), accompanied by increase to θ_σ (red, light). We see s distributions (right column) become markedly right-shifting with increase to ρ (b)-(h) and a clear monotonic increase in s_μ (red, heavy) with ρ. Grid dimensions, migration and simulation parameters: (see Figure 2.10).

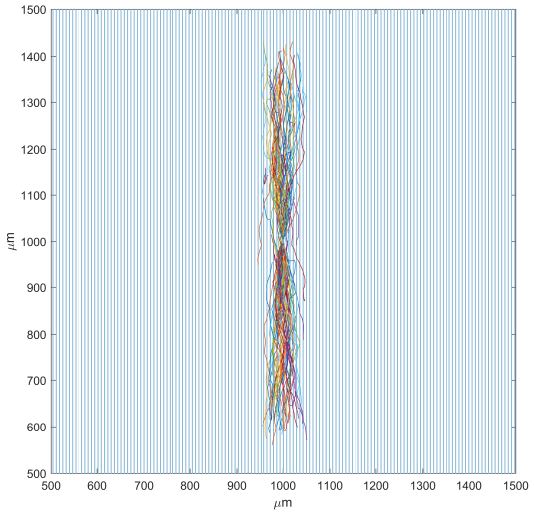

(a) 6μm groove width. $\rho = 0$.

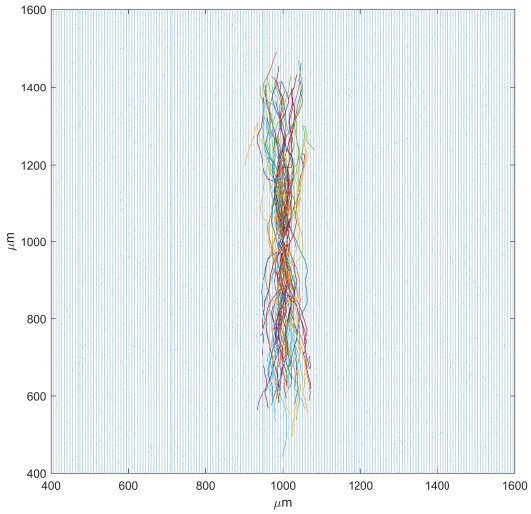

(b) 6μm groove width. $\rho = 0.2$.

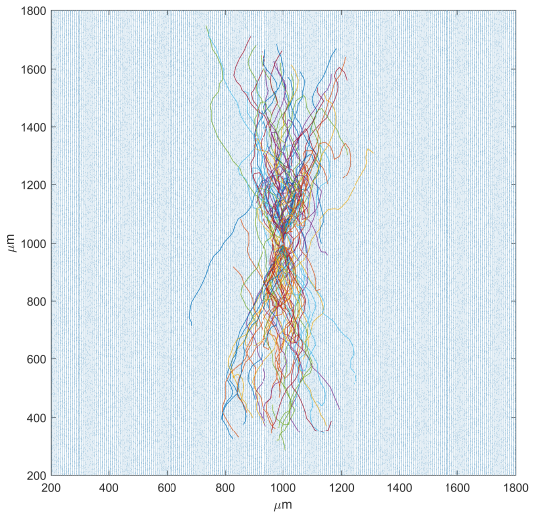

(c) 6μm groove width. $\rho = 0.35$.

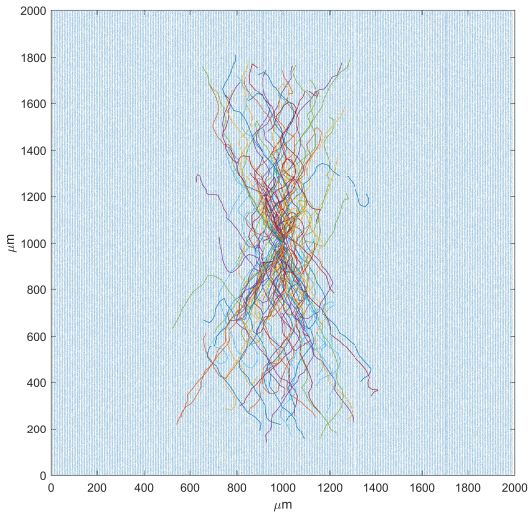

(d) 6μm groove width. $\rho = 0.5$.

Figure 2.12: Model migration trajectories (multi-colour) over gradient fields (blue) of four topographies with linear 6μm groove and 1μm ridge width topographic features, perturbed in the manner described in *Methods* 2.2.5 using four different 'noise' levels determined by feature perturbation parameter ρ: (a) $\rho = 0$, (b) $\rho = 0.2$, (c) $\rho = 0.35$ and (d) $\rho = 0.5$. Similar to Figure 2.10, trajectories clearly lose directional linearity with the introduction of feature perturbation, the degree of directional unpredictability also dependent on ρ (similarly, increasing with ρ). Notably, trajectories show much more significant dispersal as ρ is increased; see (d). Grid dimensions: $2000 \times 2000\mu\text{m}^2$. Depth: 0.4$\mu$m. Migration parameters: (a)-(d) $\beta = 0.06$, $\alpha = 0.004$, $\kappa = 0.75$. Simulation parameters: (a)-(d) $n = 100$ cell paths, $T = 540$ minutes, $N = 36$ increments, $X_{init} = (1000\mu\text{m},1000\mu\text{m})$ is the fixed initial position.

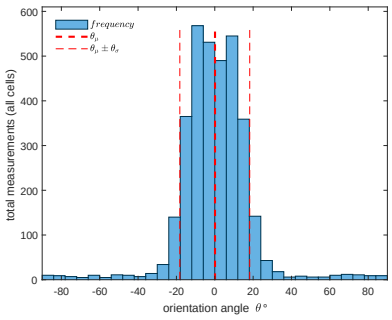

(a) 6μm groove width. $\rho = 0$. θ°.

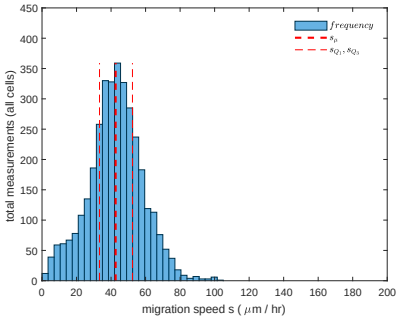

(b) 6μm groove width. $\rho = 0$. s μm/h.

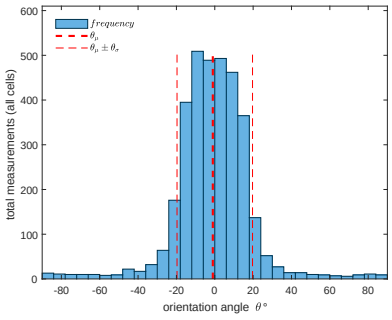

(c) 6μm groove width. $\rho = 0.2$. θ°.

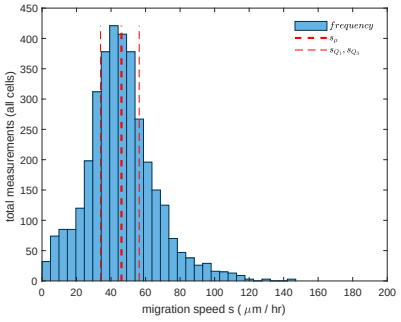

(d) 6μm groove width. $\rho = 0.2$. s μm/h.

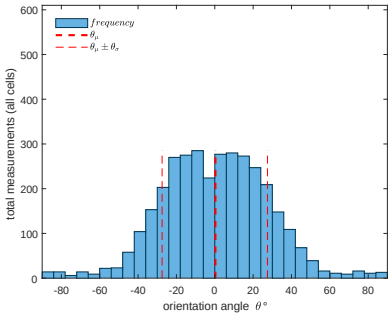

(e) 6μm groove width. $\rho = 0.35$. θ°.

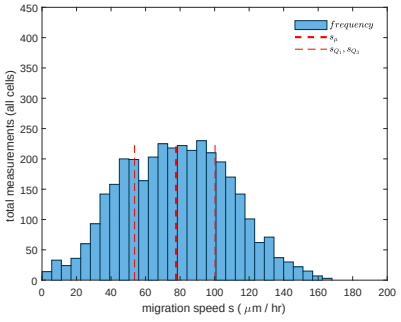

(f) 6μm groove width. $\rho = 0.35$. s μm/h.

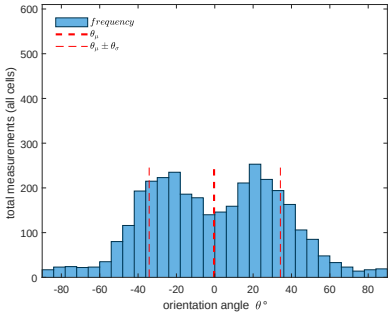

(g) 6μm groove width. $\rho = 0.5$. θ°.

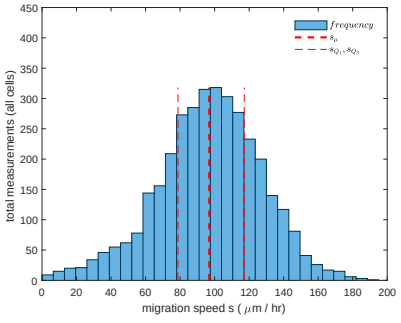

(h) 6μm groove width. $\rho = 0.5$. s μm/h.

Figure 2.13: Orientation angle, θ°, and migration speed, s (μm/h), distributions (left and right column, respectively) for the four topographies in Figure 2.12 (rows): (a)-(h) 6μm groove width; (a)-(b) $\rho = 0$, (c)-(d) $\rho = 0.2$, (e)-(f) $\rho = 0.35$ and (g)-(h) $\rho = 0.5$. For θ distributions (left column) we see a clear shift in character from Gaussian to bimodal with increase to ρ, and only a moderate rise in θ_σ (red, light). In s distributions (right column) we see a clear trend for increased distribution symmetry and a surge in s_μ (red, heavy) with increase to ρ. Grid dimensions, migration and simulation parameters: (see Figure 2.12).

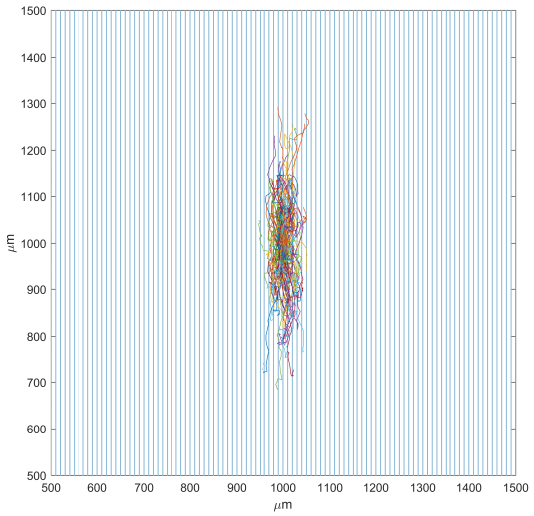

(a) 9μm groove width. $\rho = 0$.

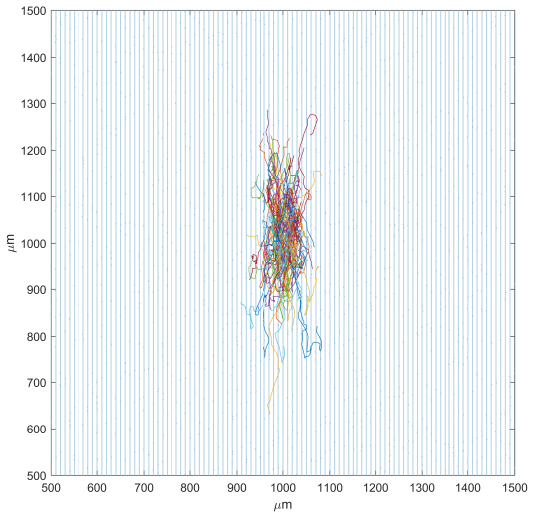

(b) 9μm groove width. $\rho = 0.2$.

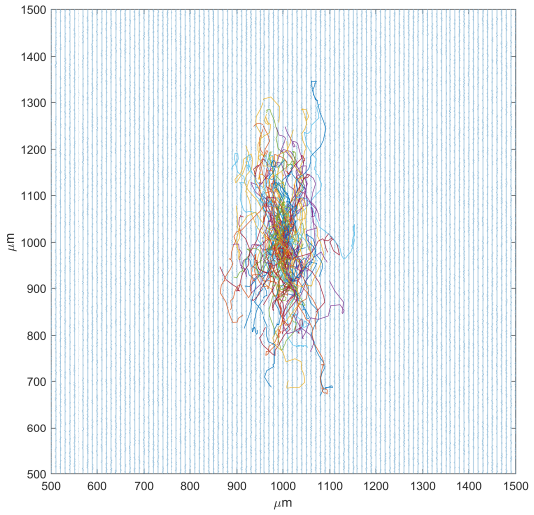

(c) 9μm groove width. $\rho = 0.35$.

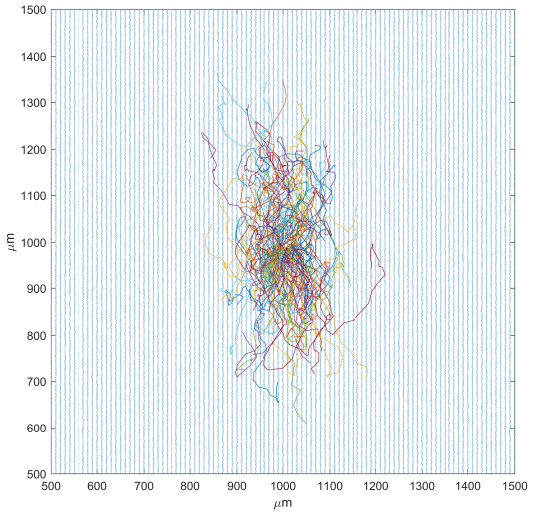

(d) 9μm groove width. $\rho = 0.5$.

Figure 2.14: Model migration trajectories (multi-colour) over gradient fields (blue) of four topographies with linear 9μm groove and 1μm ridge width topographic features, perturbed in the manner described using four different 'noise' levels determined by feature perturbation parameter ρ: (a) $\rho = 0$, (b) $\rho = 0.2$, (c) $\rho = 0.35$ and (d) $\rho = 0.5$. Trajectories clearly become more directionally random with the introduction of feature perturbation, the degree also dependent on ρ (similarly, increase to ρ). Grid dimensions: $2000 \times 2000\mu\text{m}^2$. Depth: 0.4$\mu$m. Migration parameters: (a)-(d) $\beta = 0.1$, $\alpha = 0.013$, $\kappa = 1$. Simulation parameters: (a)-(d) $n = 100$ cell paths, $T = 540$ minutes, $N = 36$ increments, $X_{init} = (1000\mu\text{m},1000\mu\text{m})$ is the fixed initial position.

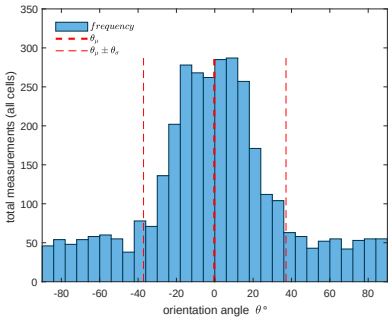

(a) 9μm groove width. $\rho = 0.$ θ°.

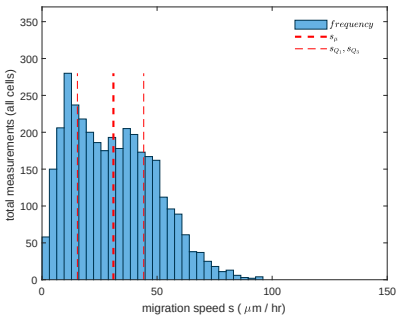

(b) 9μm groove width. $\rho = 0.$ s μm/h.

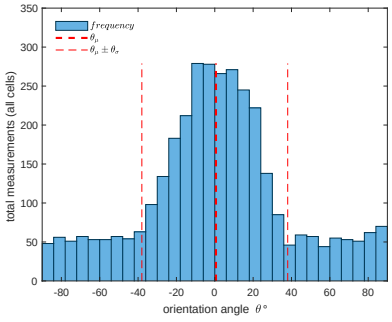

(c) 9μm groove width. $\rho = 0.2.$ θ°.

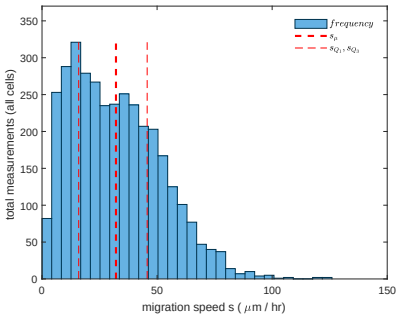

(d) 9μm groove width. $\rho = 0.2.$ s μm/h.

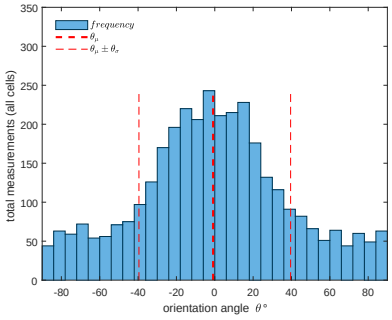

(e) 9μm groove width. $\rho = 0.35.$ θ°.

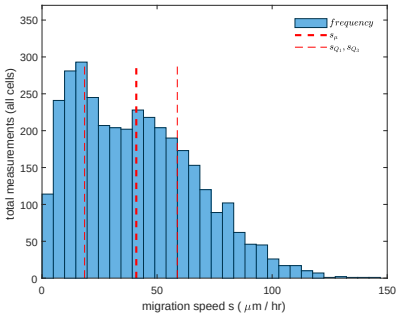

(f) 9μm groove width. $\rho = 0.35.$ s μm/h.

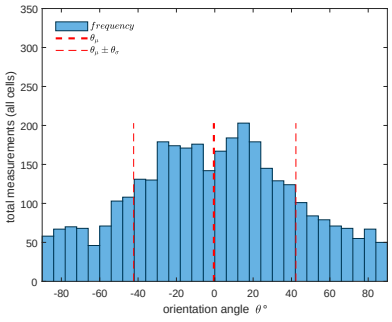

(g) 9μm groove width. $\rho = 0.5.$ θ°.

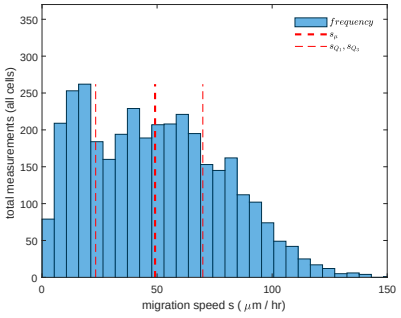

(h) 9μm groove width. $\rho = 0.5.$ s μm/h.

Figure 2.15: Orientation angle, θ°, and migration speed, s (μm/h), distributions (left and right column, respectively) for the four topographies in Figure 2.14 (rows): (a)-(h) 9μm groove width; (a)-(b) $\rho = 0$, (c)-(d) $\rho = 0.2$, (e)-(f) $\rho = 0.35$ and (g)-(h) $\rho = 0.5$. We see in θ distributions (left column) a stable Gaussian character which flattens and only a small increase to θ_σ (red, light) with increase to ρ. We see s distributions (right column) maintain a consistent positive-skew with broadening quartiles s_{Q_1} and s_{Q_3} (red, light) and a moderate increase in s_μ (red, heavy) with increase to ρ. Grid dimensions, migration and simulation parameters: (see Figure 2.14).

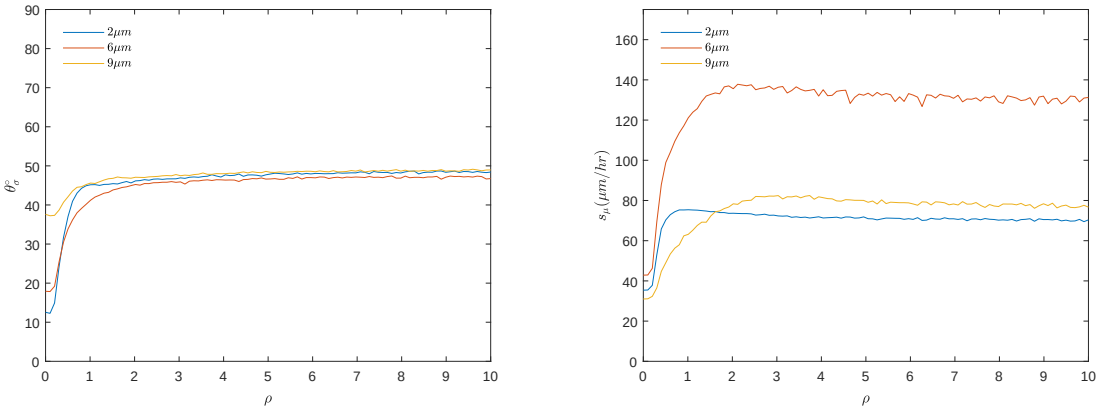

(a) θ°_{σ} vs ρ.

(b) s_{μ} (μm/h) vs ρ.

Figure 2.16: Orientation angle standard deviation, θ°_{σ}, (a) and mean migration speed, s_{μ} (μm/h), (b) against feature perturbation parameter, ρ, for 2μm (blue), 6μm (red) and 9μm (yellow) groove width topographies. (a) curves for θ°_{σ} over ρ increase rapidly in the interval $0 < \rho \leq 1$ for all topographies, the gradient dependent on groove width. (b) curves for s_{μ} ($\mu m/h$) also increase rapidly with ρ but, after the initial transient, decrease gradually with increasing ρ. Grid dimensions: $2000 \times 2000\mu m^2$. Migration parameters: (blue) $\beta = 0.11$, $\alpha = 0.005$, $\kappa = 0.5$; (red) $\beta = 0.06$, $\alpha = 0.004$, $\kappa = 0.75$; (yellow) $\beta = 0.1$, $\alpha = 0.013$, $\kappa = 1$. Simulation parameters: $\rho = 0, ..., 10$ in 100 increments, $n = 1000$ cell paths, $T = 540$ minutes, $N = 36$ increments, $X_{init} = (1000\mu$m,1000μm) is the fixed initial position.

teristics of this important interaction with a simple stochastic model and probe how migration might be affected if linear topographies sustained surface imperfections resulting from coarse surface processing methods.

The model was based on an Ornstein-Uhlenbeck (OU) process, biased to respond to physical surface gradients determined by the arrangement of surface topographic features. To do this we introduced to the OU cell velocity model a topographic bias term which guided cell velocity direction away from steep gradients and along contour directions. We parametrised the model using migration metric data ('polarisation angle', θ^*, and migration speed, s^*) for four different topographies (one flat and three linear with different groove widths) derived from a study by Kim et al. [105]. We used a grid search optimisation method to fit model simulations with MATLAB-generated topographies to this metric data, parametrising the model by estimation methods.

We presented parametrised model output comprising sample migration trajectories, and accompanying 'orientation angle', θ, and migration speed, s, metric distributions

for four different topographies. The MATLAB-generated topographies were designed to mimic topography dimensions in the study by Kim et al. [105] we use to parametrise the model: one flat topography (featuring no gradient) and three topographies with uniform linear $1 \times 0.4\mu$m ridge features spaced in the intervals 9μm, 6μm and 2μm. Migration trajectories showed markedly more directional linearity when introduced to the linear topographies, clearly increasing with decreasing groove width. This observation was reflected in distributions for θ, which changed in character from uniform when flat to Gaussian when linear; standard deviation, θ_σ, decreasing significantly with groove width. Migration speed s showed an optimal groove width for mean migration speed, s_μ, observed for the 6μm groove width topography.

We then tested the model for the same linear topographies but with incrementally introduced 'noise', the linear features randomly perturbed in the plane orthogonal to ridge/groove direction, the 'noise' level determined by feature perturbation parameter ρ. We found that trajectories lost directional linearity with increase to ρ for all groove width topographies, mirroring the 'disorderedness' in the arrangement of the surface topography. The observation was supported by distributions for θ, θ_σ clearly increasing with ρ for all topographies. The distributions also changed character for the 2μm and 6μm groove width topographies with increase to ρ, shifting distinctly from Gaussian to bimodal in the interval $0 \leq \rho \leq 0.5$. Trajectory displacement also appeared to significantly increase with ρ, evident in distributions for s which shifted markedly positive for all topographies, s_μ increasing monotonically with ρ up to a maximum s_μ for each set of topographies and steadily tapered down with ρ, as topographies became more and more disordered.

Results from the study demonstrate the proposed cell migration model is able to closely

reproduce migration characteristics of fibroblasts traversing linear topographies with comparable dimensions to those employed experimentally by Kim et al. [105]. We present in Figure 2.5, error surfaces for the flat, 9μm, and 6μm and 2μm groove width topographies at sample κ values chosen arbitrarily from a permissible range for κ, which illustrate how closely simulated metrics used in the calculation for ϵ, θ_σ and s_μ, could approximate experimental metrics, θ^*_σ and s^*_μ. We also see illustrated graphically in Figure 2.6 how close sample parametrised θ_σ and s_μ appear compared to their experimental counterparts, θ^*_σ and s^*_μ.

Results also reproduce general trends in migration behaviour for topographies with varied groove widths reported in Kim et al. [105]. We see a clear optimal groove width for s_μ, the highest observed for the 6μm groove width topography. This pattern was reported in the study by Kim et al., the highest average migration speed, s^*_μ, recorded on intermediate groove widths (an average width of 6.3μm). We also see a monotonic decrease in θ_σ with groove width which was also reported in the Kim et al. study.

We see that intermediate groove widths appear to optimise speed (highest: 6μm) and narrower groove widths appear to optimise for directionality (most directional: 2μm). In the study by Kim et al., this finding was probed further with more detailed analysis of how the arrangement of focal adhesions for cells differed between different groove widths, the difference in behaviour between groove widths proposed to be prompted by differences in physical confinement by the ridge density of the topography acting on focal adhesions. The findings in this study were later formalised into a general theoretical model for focal adhesion based cell alignment and orientation to topography proposed by Ray et al. [128], recognised as a leading candidate mode of action for these interactions [101].

Model predictions suggest that when random perturbations are introduced to uniform linear features, such as that resulting from coarse surface fabrication methods, linear directionality of migration trajectories degrades dependent on the degree of perturbation and groove width. Predictions also suggest that more randomly arranged topographic features could increase migration speed compared to uniform linear features, suggesting that when random perturbations are introduced we see trade-off between migration directionality and speed. This finding could potentially be exploited to enhance or diminish either cell characteristic, or to pursue a topographic configuration to optimise both characteristics; if the finding was to be supported experimentally. Prediction output also suggests there could be a level of tolerance in trajectory directionality to surface imperfections. If this is the case, it could help to tailor the processing methods applicable for prompting directional migration and open the door for the adoption of carefully selected coarse processing methods that are more time and cost efficient than lithography-based methods.

To take this work forward, we would in the first instance like to address the non-identifiability of our model parameters. It may be possible to improve the situation with model equation manipulations and stochastic dynamic analysis of the model. If a comparable data set was available, we could also fit to another data set and this could help to filter parameter regions further and enable greater confidence in model output. We could also increase the scope of the model by fitting to data sets with different topographic features e.g. lattice.

For model predictions we used random perturbations in only one plane (horizontal axis, orthogonal to ridge / groove direction), we could also explore the effect of perturbations in other planes (vertical axis, ridge / groove direction, and depth) and perhaps

begin to approach patterns of topographic arrangement produced by certain surface processing methods (e.g. abrasive polishing by variable mechanical motion).

In their *Biomaterials* study, Kim et al. [105] reported similar behavioural responses to topographies in cell monolayers as individual cells. Based upon this observation, the derived migration model could be a useful foundation from which to derive a population (PDE) model.

Chapter 3

A mathematical model for connexin 43 cycling and its dynamical modulation by connexin mimetic peptide Gap27

3.1 Introduction

3.1.1 Connexin 43 structure and life cycle

Connexins are polytopic transmembrane proteins which, upon intracellular oligomerisation, trafficking and insertion into the plasma membrane, function as part of intercellular communication channels [132]. There exist 21 connexin proteins, each conventionally labelled according to molecular weight but also categorised by structural similarity and order of discovery [132, 133, 134]. Connexin 43 (Cx43) is the most widely expressed connexin, found in 34 tissues and 46 different cell types and is the primary connexin in many cell lines [135].

Cx43 is crucial to the functioning of many vital physiological systems. For instance, Cx43 is known to influence the spatio-temporal coordination of cellular events during cutaneous wound repair [136], and forms the individual component units of gap

junctions at intercalated cell junctions in cardiac tissue, functioning as 'gatekeepers' that enable transferral and subsequent propogation of electrical signals between cardiac cells [137]. Cx43 dysregulation and dysfunction is associated with a number of related pathophysiologies such as chronic nonhealing wounds (e.g. cutaneous ulcers) [24, 25], cardiomyopathies [138], tumour progression and metastasis in various different cancer types (including breast [139], prostate [140] and colorectal [141]), and the autoimmune disorder psoriasis [142, 143, 144].

The structure of Cx43 is similar to that of other connexins, featuring 2 extracellular domains (loops), 4 transmembrane domains (spanning proteins) and 3 intracellular domains (N-terminal, loop and a C-terminal); measuring 7.5$\mathring{A}$ in the membrane plane and 21$\mathring{A}$ in the transmembrane plane [145]. The C-terminal is the main source of structural variation between connexin proteins and the region is subject to rapid post-translational modifications (PTMs) which regulate protein behaviour e.g. Cx43 PTMs coordinate switching between electrophoretic isoforms associated with different stages in the Cx43 life cycle [132, 133, 135]. The structure and life cycle of Cx43 is illustrated in Figure 3.1 **A** and **B**.

Connexin synthesis is associated with the endoplasmic reticulum (ER), the ER membrane is thought to be where the characteristic transmembrane topology of connexins is established [132]. Once trafficked through the Golgi apparatus, connexins undergo oligomerisation to form hemichannels, hexameric structures composed of six connexin subunits [133, 134]. Hemichannels (also known as connexons) may be homotypic or heterotypic in construction, whereby channels are formed either from combinations of the same or different connexin types respectively. It is thought subunit composition influences channel properties such as conductance and gating [134]. Once formed,

hemichannels are trafficked in a closed state by vesicular carriers along microtubules for insertion into the plasma membrane [132]. Trafficking is thought to be evenly distributed across the cell since hemichannels are observed either individually or in small groups across the entire non-junctional membrane [132]. Hemichannels at the plasma membrane are thought to be able to laterally accrete in the membrane plane to reach junctional membrane, where another cell is close enough to establish contact [76, 132]. Facilitated by Ca^{2+} dependent adhesion molecules, hemichannels at the junctional membrane are able to dock and interlock extracellular domains belonging to those of hemichannels attached to the proximal cell to form a tight seal around a $2 - 3n$m gap, establishing an intercellular communication channel, known as a gap junction channel [132, 133, 134]. Gap junction channels represent a direct cell-cell communication line, enabling the exchange of ions and small molecules between contacting cells [134]. Gap junction channels assume a dodecameric structure consisting of twelve connexin subunits and, like hemichannels, can be homotypic or heterotypic, influencing channel function [134, 145]. Microtubules can attach directly to the intracellular domain of Cx43-based gap junction channels, thus implicating gap junctions in possible structural and mechanotransductive roles, in addition to their well established role in cell-cell communication [132]. The structure and function of gap junction channels are illustrated in Figure 3.1 **C**. Gap junction channels are known to aggregate into larger junctional structures known as gap junction plaques [132]. Gap junction plaques may contain tens to hundreds of thousands of channels, forming a hub of metabolite exchange between cells at the junctional plasma membrane [132, 146]. Gap junction plaques are known to form through lateral accretion of gap junction channels along the membrane, with newly formed channels joining to the periphery of the plaque whilst

older channels are found nearer the centre of the structure [132]. Internalisation of the channels is signalled through PTMs, e.g. phosphorylation [132] and ubiquitylation [133], at the C-terminal of constituent connexin proteins. Typically removed from the centre of a plaque, whole gap junction channels are drawn into the cytoplasm of one of the contacting cells, producing internalised structures termed 'annular gap junctions' [132]. These structures, now intracellular, are sorted into the endocytic pathway or recognised by autophagy adaptors, both of which results in lysosomal degradation [132, 133]. Some of these internalised proteins may be rescued from lysosomal degradation through additional PTMs and redeployed as recycled hemichannels [133].

3.1.2 Connexin mimetic peptides

Connexin mimetic peptides (CMPs) have been widely used across cell and tissue types both to study hemichannel and gap junction function, and investigated as potential therapeutic agents [147]. CMPs are engineered to mimic amino acid sequences native to specifc intra or extracellular domains of connexin proteins. Gap20 for example targets the intracellular loop of Cx43, αCT1 the intracellular C-terminal. Gap26 and Gap27 mimic sequences on the extracellular domain of Cx43, Gap26 (a tridecapeptide) is targeted to the first loop, Gap27 (a undecapeptide) is targeted to the second loop [148]. The presence of highly conserved sequences in these particular CMPs enables efficacy across other types of connexin, such as Cx32, Cx40 and Cx37 [146, 149].
Cx43-Gap27 binding occurs extracellularly at the plasma membrane, the primary mode of interaction thought occur with unpaired hemichannel-based free Cx43, although it has been suggested interaction could also occur with gap junction bound hemichannels [146]. CMPs have been widely reported to affect gap junction based intercellular communication (GJIC), able to block intercellular dye transfer and cause disruption

to Ca^{2+} signalling [149]. The principal mechanism by which GJIC is interrupted is thought to be through disruption to gap junction channel formation and / or function. Hemichannels bound by Gap27 are thought either to couple atypically or couple regularly but exhibit disrupted channel function, both resulting in dysfunctional gap junction channels [146, 149]. It is unclear exactly how CMPs such as Gap27 are able to affect hemichannel function, it is proposed CMP binding could either physically block the hemichannel 'pore' or induce closure by modifying channel gating behaviour [148]. Connexin-peptide binding to hemichannels also introduces the possibility of indirect effects on hemichannel coupling and gap junction gating behaviours, through disruption to intracellular Ca^{2+} dynamics [146].

3.1.3 Modelling studies

The physiological importance of gap junctions (and constituent connexins) and their influence in various pathologies (e.g. chronic non-healing wounds [24] and cardiac arrythmias [150]) has prompted numerous mathematical and computational modelling studies of their properties and function. Many modelling studies have focused in particular on channel conductance characteristics and its influence on channel gating behaviour, study motivation often stimulated by the role gap junctions play in electrical impulse propagation in cardiac tissue and their implicated role in cardiac dysfunction. Vogel and Weingart looked into conductance behaviour of gap junction channels in response to transjunctional voltage. The model treated a gap junction as an electrical circuit, composed of two identical submodels of hemichannels in series, each with a switch between high and low conductance states describing channel gating dynamics. The authors focused on the four different conductance states of the gap junction channel conferred by each hemichannel conductance switch, presenting conductance-

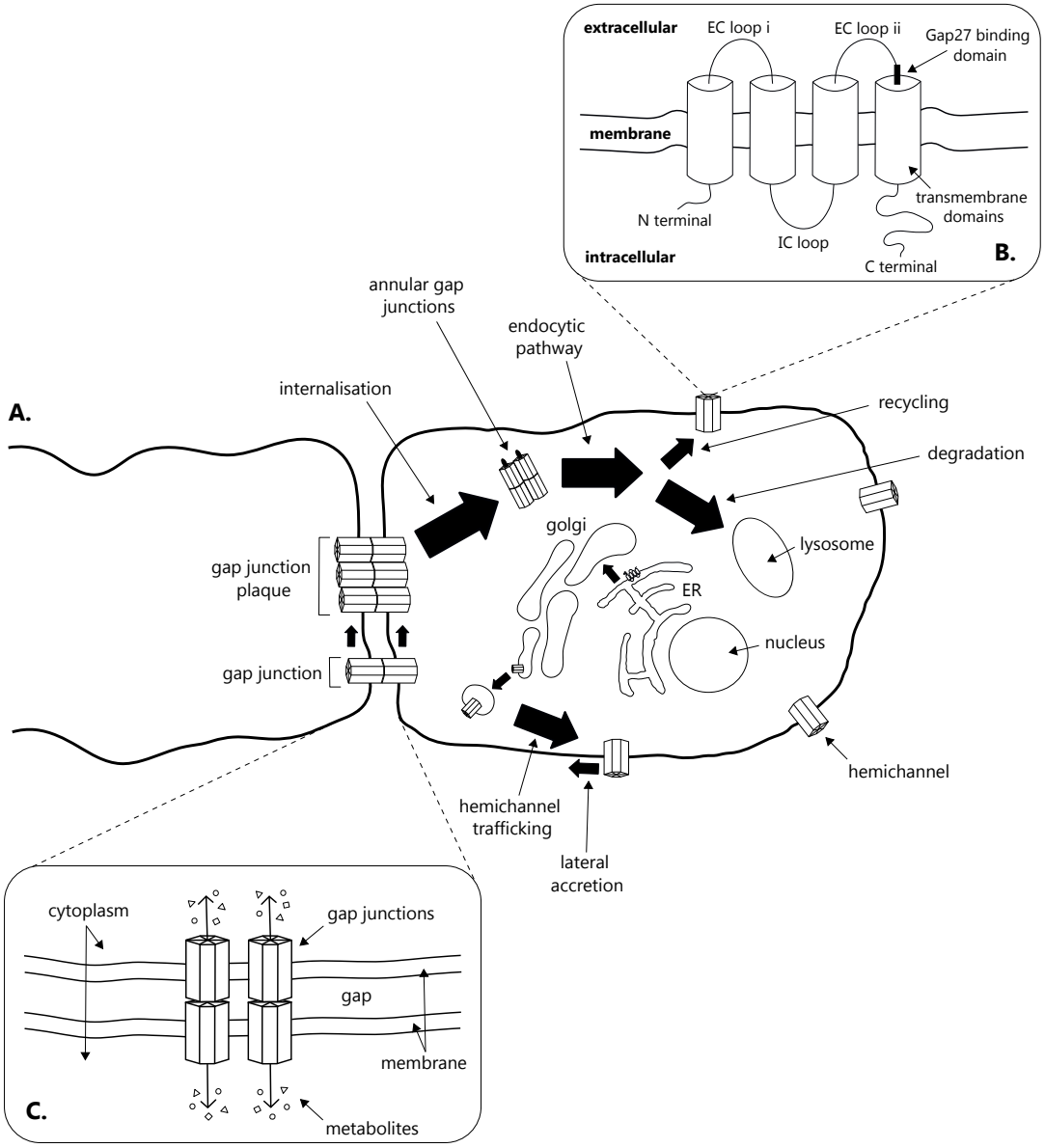

Figure 3.1: Three diagrams to illustrate **A.** the Cx43 cycling process, **B.** the structure of Cx43 and **C.** the structure and function of gap junction channels. **A.** Flow diagram to illustrate the life cycle of Cx43. Cx43 synthesis is associated with the endoplasmic reticulum (ER) from which the proteins are trafficked to the golgi apparatus for oligomerisation into hemichannels. Hemichannels are then trafficked from the golgi to the cell membrane where they become functional, able to operate as individual channels or dock with opposing hemichannels to form gap junction channels. Gap junctions can then accrete to form gap junction plaques. Once internalised, gap junctions are known as 'annular gap junctions' which follow an endocytic pathway and its component hemichannels either redeployed via a recycling mechanism or degraded via the lysosome. **B.** Schematic diagram to illustrate the general structure of Cx43. Cx43 has three intracellular (IC) domains (N terminal, loop and C terminal), four transmembrane domains and two extracellular (EC) domains (loops i and ii). Gap27 binds to the second extracellular loop. **C.** Schematic diagram to illustrate the general structure and function of gap junction channels. Gap junction channels form when two opposing hemichannels dock and interdigitate at the cell membrane. They enable direct cytoplasmic exchange of large metabolites between the two docked cells.

voltage relationships for both homotypic and hetertypic channels. Results were able to characterise the conductance-voltage relationship for the experimentally hard-to-detect low-low channel conductance state [70].

Loppini et al. investigated synchronisation of electrical activity via gap junctions in β-cell clusters with a model based on an interacting neighbourhood, each cell assigned membrane potential dynamics. Results found cluster synchrony of spiking behaviour to be particularly dependent on gap junction conductance, which could also induce transformation of bursts into spiking behaviour [72].

Casaleggio, Hines and Migliore propose a 2-d computational model of cardiac tissue comprised of a cell network coupled with gap junction channels to explore the influence of gap junction conductance on cardiac arrhythmias. The authors found dynamic changes to gap junction conductance around a model 'ischemic' region of tissue resulted in signal motifs that qualitatively reproduced those of six different types of arrhythmia [71].

In addition to channel conductance, many modelling studies have investigated flux properties of gap junctions. Mondal et al. proposed a 3-d computational model of a gap junction channel 'pore' to investigate whether changes in pore morphology, imparted by the presence of different connexin types, could induce asymmetric flux of molecules of a certain size. The authors found asymmetric pore shapes to induce asymmetric fluxes, but only in the presence of charged particles [74].

Bressloff probed gap junction permeability with a 1-d model of diffusing particles within a domain of connected cells, each cell interface representing a gap junction in randomly opening and closing states. Limiting the domain to two cells, the author could derive, via mean steady-state concentration and flux, effective permeability of the gap junction

joining the two cells, subsequently showing effective permeability of the gap junctions depended on the number of cells (in the simplified system) [75].

Dougoud et al. proposed a network-based model for Ca^{2+} wave propagation through a cell population via gap junction channels. The model described an interacting cell population using a graph coupled with Ca^{2+} dynamics, the nodes representing individual cells, the vertices interaction through gap junction channels with prescribed properties. Simulation results showed spatio-temporal signal patterns were heavily dependent on gap junction coupling strength (implying an effect on channel permeability), only strongly coupled gap junctions induced propagating Ca^{2+} waves, more weakly coupled channels showed only isolated Ca^{2+} bursts and non-synchronous oscillations [73].

3.1.4 Motivations and contributions

Connexins are physiologically important. They comprise the functional transmembranous components of hemichannels and subsequently gap junction channels, enabling both direct and long range metabolite exchange with other cells and the extracellular space. Connexin 43 (Cx43) is the most ubiquitous connexin in the human body, supporting critical functions fundamental to many important physiological systems, the derangement of which is implicated in a number of serious health conditions.

Connexins are typically cycled rapidly (with a half-life of just a few hours [133]). Synthesised intracellularly, they assemble into hemichannels which deploy at the cell membrane where some will establish gap junction channels if close enough to another cell, and subsequently recruited to gap junction conglomerates, 'plaques', from which they are internalised and either recycled or degraded.

Connexin mimetic peptides (CMPs) are targeted to specific connexin domains and shown in experimental studies capable of modifying different connexin-based channel

behaviours. A number of CMPs, including 'Gap27', are under investigation as potential promotive agents for wound healing. Gap27 has been shown to increase cell migration rates and accelerate healing in a number of experimental models [32, 151, 152].

Mathematical and computational modelling work relating to the structure and behaviour of connexins and connexin-based species exist in abundance. Much of the literature appears to focus on connexin-channel properties and functions e.g. conductance, permeability and flux. The fundamental connexin cycling process, gap junction formation and aggregation underpinning channel functions however appear to have been largely unexplored.

We aim to develop a mathematical model based on the Cx43 life cycle and include binding kinetics for extracellularly binding CMP Gap27. The intention is to explore the dynamical behaviour of this important physiological process and consider how the introduction of Gap27 modulates this behaviour.

In the presented work, we contribute the following:

(i) **Derive a mass action model for Cx43 cycling with Gap27 binding.** We use the biological literature to formulate a reaction scheme for the Cx43 life cycle and include binding kinetics for CMP Gap27. We use the reaction scheme to derive a full ODE model for the system based on mass action kinetics. See *Methods* 3.2.1.

(ii) **Derive an averaged model of the original ODE system.** We reduce the ODE system by deriving moment ODEs for the large sub-system of gap junction plaque ODEs, introducing them into the model to obtain an averaged model for the original system. See *Methods* 3.2.5.

(iii) **Explore model dynamics without and with Gap27.** We examine time-

course and steady-state behaviour of the model under variation to initial concentrations and model parameters both without and with Gap27 binding. We find, in-keeping with the biological literature, introduction of Gap27 affects only transient behaviour of Cx43-based cycling species. See *Results*.

3.2 Methods

3.2.1 Model formulation

To create the model, we formulate a set of reaction equations to define connexin cycling events upon the interaction of two neighbouring cells. We assume the system to be symmetric such that under equal initial conditions both interacting cells behave equally. In our model, we assume connexins have already been synthesised and undergone intracellular oligomerisation to form hemichannels $[H]$, produced at a rate k_p, and in receipt of additional input from a recycling mechanism. We assume individual hemichannels $[H]$ from either cell, $[H^1]$ and $[H^2]$, are able to bind with each other to form gap junction channels $[G]$ conjoining cells for direct intercellular communication. We then assume $[G]$ is able to accrue to form gap junction plaque structures $[P_i]$, which we define to be at least two unit $[G]$ up to a theoretical maximum unit $[G]$, n, such that intermediate plaque states m are defined $i = 2 \leq m \leq n$. We further assume unit $[G]$ is internalised from within plaque structures $[P_i]$ and into one of the two conjoined cells to form annular gap junction structures $[E]$, which are subsequently sorted into either a recycling or degradation pathway. Gap27 $[G27]$ binding is assumed for simplicity as an additional one-step reaction whereby $[G27]$ attaches to binding sites harboured by $[H]$ on either cell to form the hemichannel-peptide complex $[H \cdot G27]$. The reaction scheme is detailed in *Methods* 3.2.2.

Since the formulation does not account for connexin-specific structure or channel functions, the resulting model could be viewed as a general model for connexin cycling with homotypic and heterotypic hemichannel and gap junction composition, with additional binding of an extracellularly acting CMP. We focus, for our application, on the connexin 'Cx43' and connexin mimetic peptide 'Gap27', with hemichannels and gap junctions being Cx43-homotypic.

3.2.2 Reaction scheme

(i) **Hemichannel production.** Under the condition that two cells are already interacting and assuming connexin oligomerisation, $[H]$ production is assumed at a constant rate k_p. Reaction equations for each interacting cell (denoted by superscripts ^{1} and ^{2}) are given by Eq. (3.1) and Eq. (3.2).

$$production \rightarrow [H^1], \tag{3.1}$$

$$production \rightarrow [H^2]. \tag{3.2}$$

(ii) **Gap junction formation.** Since both cells are assumed to already be interacting, a junctional nexus is assumed present at the cell membranes, providing the conditions under which gap junction channels are able to form by the docking and interdigitation of hemichannels from both cells. We assume constant association and dissociation rates, k_1 and k_{-1} respectively. The reaction equation for gap junction channels $[G]$ is given by Eq. (3.3).

$$[H^1] + [H^2] \rightleftharpoons [G]. \tag{3.3}$$

(iii) **Gap junction plaque formation.** Once gap junction channels form we assume

accrual into larger gap junction plaque structures occurs, for simplicity, at constant rate k_2, interpreted as an average association rate across plaque states. It is also assumed that once gap junction channels form part of a plaque structure, they do not separate once more into individual or groups of channels and are removed from the structure through internalisation. Reaction equations for initial, intermediate and maximum gap junction plaque states $[P_i]$, where $i = 3, ..., n$, are given by Eq. (3.4) and Eq. (3.5).

$$[G] + [G] \rightarrow [P_2], \tag{3.4}$$

$$[G] + [P_{i-1}] \rightarrow [P_i]. \tag{3.5}$$

(iv) **Gap junction internalisation.** In our formulation of internalisation we do not account for any specific post-translational modifications (PTMs), only the general process of internalisation which translates gap junction channels $[G]$ into the intracellular structures annular gap junctions $[E]$ within either cell. We assume gap junction channels are internalised at a constant rate k_u. Reaction equations for internalisation of $[G]$ for initial, intermediate and maximum plaque states, where $i = 3, ..., n$, are given by Eq. (3.6) and Eq. (3.7).

$$[P_2] \rightarrow [G] + [E^1] \quad or \quad [P_2] \rightarrow [G] + [E^2], \tag{3.6}$$

$$[P_i] \rightarrow [P_{i-1}] + [E^1] \quad or \quad [P_i] \rightarrow [P_{i-1}] + [E^2]. \tag{3.7}$$

(v) **Internalised gap junction recycling and degradation.** Once gap junction channels are internalised, we assume the subsequent annular gap junction structures $[E]$ are sorted intracellularly into recycling and degradation pathways. We

assume individual hemichannels within these internalised structures may be rescued from degradation and redeployed once more as functional channels via a recycling mechanism (see Ribeiro et al. [133]). We assume a constant recycling rate k_r and specify that recycled hemichannels $[H]$ are only to originate from annular gap junctions $[E]$ within the same cell. Any remaining annular gap junctions not utilised for recycling are assumed to degrade at a constant rate k_d via a lysosomal degradation pathway. Reaction equations for recycling and degradation are given by Eq. (3.8)-(3.9) and Eq. (3.10).

$$[E^1] \rightarrow [H^1], \tag{3.8}$$

$$[E^2] \rightarrow [H^2], \tag{3.9}$$

$$[E] \rightarrow 0. \tag{3.10}$$

(vi) **Hemichannel degradation.** Hemichannels which are not recruited for gap junction formation and thus remain free and unbound we assume are internalised and degraded at a constant rate k_{dh}, the reaction equation given by Eq. (3.11).

$$[H] \rightarrow 0. \tag{3.11}$$

(vii) **Gap27 binding.** We assume that Gap27 $[G27]$ binds extracellularly to free hemichannels $[H]$ of both cells in a simple one-step reaction which forms hemichannel-Gap27 complex $[H \cdot G27]$. We do not consider any additional binding behaviour reported in the literature (e.g. Gap27 binding to hemichannels already situated within gap junction channels). We assume constant association and dissociation rates, k_{G27} and k_{-G27}, respectively. Reaction equations are given by Eq. (3.12)

and Eq. (3.13).

$$[H^1] + [G27] \rightleftharpoons [H \cdot G27^1], \tag{3.12}$$

$$[H^2] + [G27] \rightleftharpoons [H \cdot G27^2]. \tag{3.13}$$

3.2.3 ODE system

Assuming mass action kinetics for the reaction scheme we now define the system equations. Employing the defined notation for system variables, the full model describing Cx43 cycling with Gap27 binding is defined by the autonomous ODE system Eq. (3.14)-(3.24).

$$\frac{d[H^1]}{dt} = k_p - k_1[H^1][H^2] + k_{-1}[G] + k_r[E^1] - k_{dh}[H^1] - k_{G27}[H^1][G27] + k_{-G27}[H \cdot G27^1], \tag{3.14}$$

$$\frac{d[H^2]}{dt} = k_p - k_1[H^1][H^2] + k_{-1}[G] + k_r[E^2] - k_{dh}[H^2] - k_{G27}[H^2][G27] + k_{-G27}[H \cdot G27^2], \tag{3.15}$$

$$\frac{d[G]}{dt} = k_1[H^1][H^2] - k_{-1}[G] - 2k_2[G]^2 - [G]\sum_{i=2}^{n-1} k_2[P_i], \tag{3.16}$$

$$\frac{d[P_2]}{dt} = k_2[G]^2 - 2k_u[P_2] - k_2[G][P_2], \tag{3.17}$$

for $j = 3, ..., n-1$,

$$\frac{d[P_j]}{dt} = k_2[G][P_{j-1}] - jk_u[P_j] - k_2[G][P_j], \tag{3.18}$$

$$\frac{d[P_n]}{dt} = k_2[G][P_{n-1}] - nk_u[P_n], \tag{3.19}$$

$$\frac{d[E^1]}{dt} = -k_r[E^1] - k_d[E^1] + \frac{k_u}{2}\sum_{i=2}^{n} i[P_i], \tag{3.20}$$

$$\frac{d[E^2]}{dt} = -k_r[E^2] - k_d[E^2] + \frac{k_u}{2}\sum_{i=2}^{n} i[P_i], \tag{3.21}$$

$$\frac{d[G27]}{dt} = k_{-G27}\left([H \cdot G27^1] + [H \cdot G27^2]\right) - k_{G27}\left([H^1][G27] + [H^2][G27]\right), \quad (3.22)$$

$$\frac{d[H \cdot G27^1]}{dt} = k_{G27}[H^1][G27] - k_{-G27}[H \cdot G27^1], \quad (3.23)$$

$$\frac{d[H \cdot G27^2]}{dt} = k_{G27}[H^2][G27] - k_{-G27}[H \cdot G27^2]. \quad (3.24)$$

Note that,

$$\frac{d[G27]}{dt} + \frac{d[H \cdot G27^1]}{dt} + \frac{d[H \cdot G27^2]}{dt} = 0. \quad (3.25)$$

We find through integration, conservation of mass for Gap27 is preserved

$$[G27] + [H \cdot G27^1] + [H \cdot G27^2] = S(t), \quad (3.26)$$

where $S(t)$ is a constant concentration.

The sub-system defined by Eq. (3.14)-(3.21), when $[G27](0) = 0$, can be thought of as a model only for Cx43 cycling and utilisation during the interaction of two contacting cells. The sub-system defined by Eq. (3.22)-(3.24), when $[G27](0)$ is non-zero, introduces additional Gap27 binding into the model. In the coming sections, we use this to introduce Gap27 as a treatment and consider the model both without and with treatment of Gap27.

3.2.4 Nondimensionalisation

We nondimensionalise the full system described by Eq. (3.14)-(3.24) using the following notations. We rescale system variables using the hat notation $[\widehat{H}]$ to denote some constant $[\widehat{H}] \in \mathbb{R}_+$. We use superscripts within square brackets to represent the dimensionless variable $[H^*]$. The substitutions used are summarised in Table 3.1 and the rescalings used in Table 3.2.

Table 3.1: Substitutions used for the nondimensionalisation of system Eq. (3.14)-(3.24)

$[H] = [\widehat{H}][H^*]$	$[G] = [\widehat{G}][G^*]$	$[E] = [\widehat{E}][E^*]$
$[P_2] = [\widehat{P}_2][{P_2}^*]$	$[P_j] = [\widehat{P}_j][{P_j}^*]$	$[P_n] = [\widehat{P}_n][{P_n}^*]$
$[G27] = [\widehat{G}27][G27^*]$	$[HG27] = [\widehat{H}G27][HG27^*]$	$t = \widehat{t}t^*$

Table 3.2: Rescalings used for the nondimensionalisation of system Eq. (3.14)-(3.24)

$\widehat{t} = \dfrac{1}{k_{dh}}$	$[\widehat{H}] = [\widehat{G}] = [\widehat{E}] = [\widehat{P}_N] = [\widehat{G}27] = [\widehat{H}G27] = \dfrac{k_p}{k_{dh}}$		
$\widehat{k}_1 = \dfrac{k_1 k_p}{k_{dh}^2}$	$\widehat{k}_2 = \dfrac{k_2 k_p}{k_{dh}^2}$	$\widehat{k}_{-1} = \dfrac{k_{-1}}{k_{dh}}$	$\widehat{k}_u = \dfrac{k_u}{k_{dh}}$
$\widehat{k}_r = \dfrac{k_r}{k_{dh}}$	$\widehat{k}_d = \dfrac{k_d}{k_{dh}}$	$\widehat{k}_{G27} = \dfrac{k_{G27} k_p}{k_{dh}^2}$	$\widehat{k}_{-G27} = \dfrac{k_{-G27}}{k_{dh}}$

To distinguish between the original and nondimensionalised systems we adopt lower case notation for the nondimensionalised system, such that $[H^1] = [h^1]$ and equivalent for all other variables (superscripts within square brackets, $[h^1]$ and $[h^2]$, still denoting to which cell in the system the species belongs). The full nondimensionalised system for Cx43 cycling with Gap27 binding is given by Eq. (3.27)-(3.37).

$$\frac{d[h^1]}{dt} = 1 - \widehat{k}_1[h^1][h^2] + \widehat{k}_{-1}[g] + \widehat{k}_r[e^1] - [h^1] - \widehat{k}_{G27}[h^1][g27] + \widehat{k}_{-G27}[h \cdot g27^1], \quad (3.27)$$

$$\frac{d[h^2]}{dt} = 1 - \widehat{k}_1[h^1][h^2] + \widehat{k}_{-1}[g] + \widehat{k}_r[e^2] - [h^2] - \widehat{k}_{G27}[h^2][g27] + \widehat{k}_{-G27}[h \cdot g27^2], \quad (3.28)$$

$$\frac{d[g]}{dt} = \widehat{k}_1[h^1][h^2] - \widehat{k}_{-1}[g] - 2\widehat{k}_2[g]^2 - \widehat{k}_2[g]\sum_{i=2}^{n-1}[p_i], \quad (3.29)$$

$$\frac{d[p_2]}{dt} = \widehat{k}_2[g]^2 - 2\widehat{k}_u[p_2] - \widehat{k}_2[g][p_2], \quad (3.30)$$

where $3 \leq j \leq n-1$,

$$\frac{d[p_j]}{dt} = \widehat{k}_2[g][p_{j-1}] - j\widehat{k}_u[p_j] - \widehat{k}_2[g][p_j], \tag{3.31}$$

$$\frac{d[p_n]}{dt} = \widehat{k}_2[g][p_{n-1}] - n\widehat{k}_u[p_n], \tag{3.32}$$

$$\frac{d[e^1]}{dt} = -\widehat{k}_r[e^1] - \widehat{k}_d[e^1] + \frac{\widehat{k}_u}{2}\sum_{i=2}^{n} i[p_i], \tag{3.33}$$

$$\frac{d[e^2]}{dt} = -\widehat{k}_r[e^2] - \widehat{k}_d[e^2] + \frac{\widehat{k}_u}{2}\sum_{i=2}^{n} i[p_i], \tag{3.34}$$

$$\frac{d[g27]}{dt} = \widehat{k}_{-G27}\left([h \cdot g27^1] + [h \cdot g27^2]\right) - \widehat{k}_{G27}\left([h^1][g27] + [h^2][g27]\right), \tag{3.35}$$

$$\frac{d[h \cdot g27^1]}{dt} = \widehat{k}_{G27}[h^1][g27] - \widehat{k}_{-G27}[h \cdot g27^1], \tag{3.36}$$

$$\frac{d[h \cdot g27^2]}{dt} = \widehat{k}_{G27}[h^2][g27] - \widehat{k}_{-G27}[h \cdot g27^2], \tag{3.37}$$

where $\widehat{k}_1$, $\widehat{k}_{-1}$, $\widehat{k}_2$, $\widehat{k}_u$, $\widehat{k}_r$, $\widehat{k}_d$, $\widehat{k}_{G27}$, $\widehat{k}_{-G27} \geq 0$.

The system defined by Eq. (3.27)-(3.34), where $[g27](0) = 0$, is the nondimensionalised system describing Cx43 cycling without Gap27. We visualise the model system without Gap27 in Figure 3.2 for a reference parameter set, where system variables $[h]$, $[g]$, $[e]$ and log-transformed $[p_i]$, where $i = 2, ..., 20$, are plotted against nondimensional time unit t. Plaque states at numerically approximated steady-state, $[p_i^*]$ (corresponding to plaque state trajectories $[p_i]$ in Figure 3.2 (d) when stationary) are represented as a discrete distribution in Figure 3.3. Largest plaque state n is chosen to illustrate system behaviour, $n = 20$, and otherwise arbitrarily.

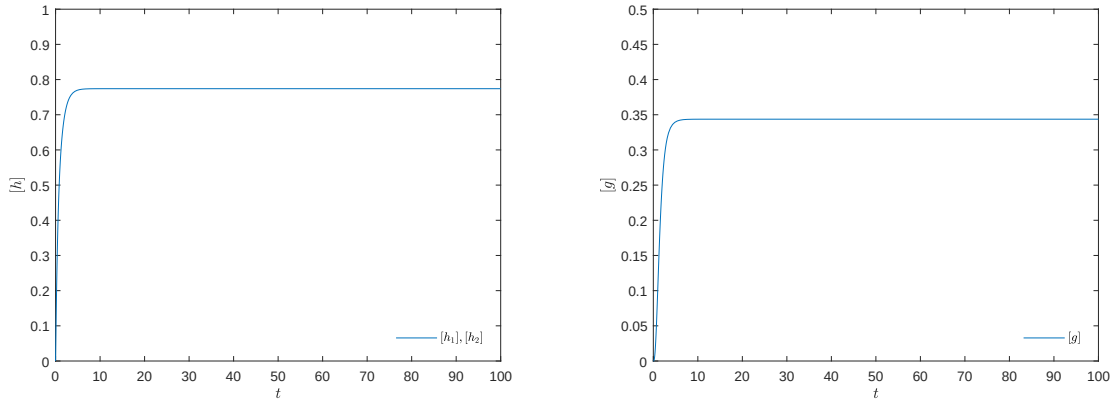

(a) $[h]$ over t.

(b) $[g]$ over t.

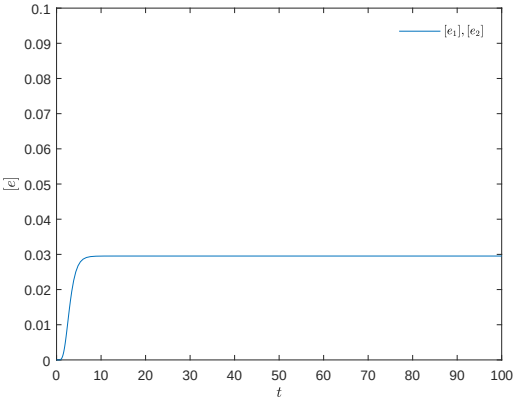

(c) $[e]$ over t.

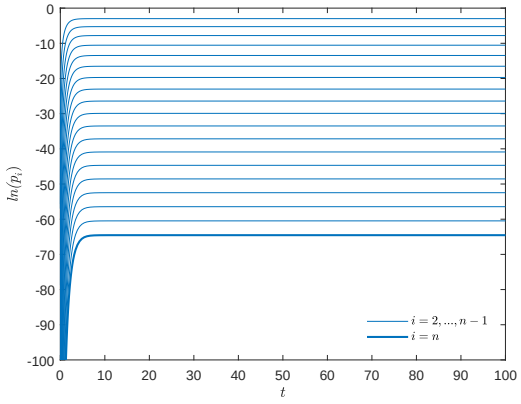

(d) $ln(p_i)$ over t.

Figure 3.2: Nondimensionalised system without Gap27 ($[g27](0) = 0$) variables $[h]$, $[g]$, $[e]$ and natural log-transformed $[p_i]$ solved for time t with all model parameters set equal. (a) $[h]$ over t. (b) $[g]$ over t. (c) $[e]$ over t. (d) natural log-transformed $[p_i]$ over t. Each trajectory represents a plaque state i, where $i = 2, ..., 20$. Plaque states at equilibrium decrease in concentration from state $i = 2$ (trajectory closest to zero over t) to $i = 20$ (thick). Initial conditions: $[h](0) = [g](0) = [e](0) = [p_i](0) = 0$, where $i = 2, ..., n$, $n = 20$. Parameters: $\widehat{k}_1 = \widehat{k}_{-1} = \widehat{k}_2 = \widehat{k}_u = \widehat{k}_r = \widehat{k}_d = 1$. Time: 100 nondimensional time steps.

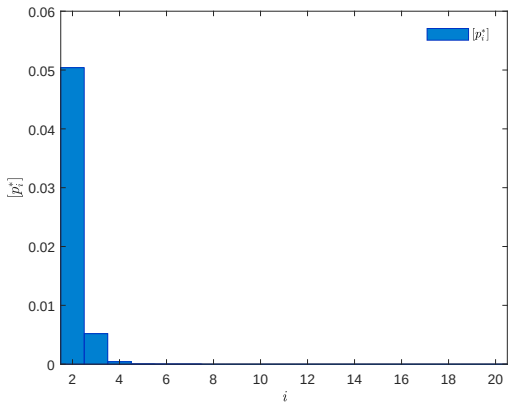

Figure 3.3: Plaque states at equilibrium $[p_i^*]$ represented as a discrete distribution of plaque states i. The distribution clearly shows an approximate exponential decay in $[p_i^*]$ as states i increase. Initial conditions: $[h](0) = [g](0) = [e](0) = [p_i](0) = 0$, where $i = 2, ..., n$, $n = 20$. Parameters: $\widehat{k}_1 = \widehat{k}_{-1} = \widehat{k}_2 = \widehat{k}_u = \widehat{k}_r = \widehat{k}_d = 1$. Time: 100 nondimensional time steps.

3.2.5 Plaque state distribution $p_i(t)$: derivation of moment ODEs

We recall from *Introduction* 3.1.1 that the unit quantity of gap junction channels composing large plaque structures can be enormous, perhaps hundreds of thousands of individual channels [146]. Under current model assumptions, we place a theoretical maximum unit $[g]$ that cells in the model system are able to recruit to construct plaque structures $[p_i]$, n, which we left undefined. We now update this assumption and let $n \to \infty$. Under the assumption that $n \to \infty$, the dimension of the model sub-system of plaque states $[p_i](t)$, Eq. (3.30)-(3.32), and therefore the model system itself, now tends to infinity. To evaluate the system numerically we could fix n arbitrarily large to give a reasonable approximation of the system, but this could become computationally expensive. The question is whether there is utility in calculating each individual plaque state $[p_i](t)$ in the entire plaque state distribution. We determine it is more useful to consider the distribution characteristics. To do this we derive moment ODEs for the sub-system defined by Eq. (3.30)-(3.32). We introduce four new time-dependent variables for the zeroeth, first, second and third order moments and derive three new differential equations at the zeroeth, first and second orders which we then use to replace Eq. (3.30)-(3.32) and associated variables, updating the model and adopting this 'averaged' model thereafter. We truncate the system at the third order by approximation, using the associated definition for skewness from the geometric distribution, adopted as a reasonable model for the plaque state distribution. This approach negates the need to solve the model for all plaque states $[p_i](t)$ and reduces the overall size of the system considerably, resulting in more interpretable solution output for gap junction plaques in the model.

The method we use to derive our averaged model for Cx43 cycling with Gap27 binding is described in the ecological modelling work "The effect of landscape heterogeneity and host movement on a tick-borne pathogen" by Jones et al., which described the accrual of parasitic ticks in grouse and deer populations and the subsequent effect of a spreading tick-borne pathogen on the suseptible grouse population [153]. The method also appears in an unpublished work "Modelling the Gyrodactylus salaris life cycle" by Webb, Norman and Porter, describing the life cycle of a parasitic fluke worm and the subsequent effect on a fish population.

For the derivation, we drop square brackets for convenience such that $[p_i](t) = p_i(t)$. To derive our averaged model, we start by summing over the interval $2 \leq j \leq n$, obtaining an expression for the total plaque concentration $p(t)$,

$$p(t) = \sum_{j=2}^{n} p_j(t). \tag{3.38}$$

The derivative with respect to time t of Eq. (3.38) can be obtained through summation of Eq. (3.30)-(3.32),

$$\frac{dp}{dt} = \widehat{k}_2 g^2 - \widehat{k}_u \sum_{j=2}^{n} j p_j. \tag{3.39}$$

If we define the average gap junction concentration per unit concentration of plaque as variable p_{avg},

$$p_{avg} = \frac{\sum_{j=2}^{n} j p_j}{\sum_{j=2}^{n} p_j} = \frac{1}{p} \sum_{j=2}^{n} j p_j. \tag{3.40}$$

Eq. (3.39) may be re-written as

$$\frac{dp}{dt} = \widehat{k}_2 g^2 - \widehat{k}_u p_{avg} p. \tag{3.41}$$

We aim now to obtain the derivative of p_{avg} with respect to time. The derivative of Eq. (3.40), with respect to time is given by

$$\frac{dp_{avg}}{dt}p + \frac{dp}{dt}p_{avg} = \sum_{j=2}^{n} j\frac{dp_j}{dt}. \tag{3.42}$$

By substitution of Eq. (3.41) and Eq. (3.30)-(3.32), Eq. (3.42) becomes

$$\frac{dp_{avg}}{dt}p + \left(\widehat{k}_2 g^2 - \widehat{k}_u p_{avg} p\right) p_{avg} = 2\widehat{k}_2 g^2 + \widehat{k}_2 g \sum_{j=2}^{n-1} p_j - \widehat{k}_u \sum_{j=2}^{n} j^2 p_j. \tag{3.43}$$

Since $n \to \infty$, the contribution of the highest order term p_n in the summation is insignificant, so we assume

$$p(t) = \sum_{j=2}^{n-1} p_j(t), \tag{3.44}$$

and

$$p_{avg} p = \sum_{j=2}^{n-1} j p_j. \tag{3.45}$$

By definition, the second order moment is

$$p_{var} = \frac{1}{p}\sum_{j=2}^{n} j^2 p_j - \left(\frac{1}{p}\sum_{j=2}^{n} j p_j\right)^2, \tag{3.46}$$

recalling Eq. (3.40), we get the expression

$$\frac{1}{p}\sum_{j=2}^{n} j^2 p_j = p_{var} + p_{avg}^2. \tag{3.47}$$

By substitution, Eq. (3.43) can be simplified further,

$$\frac{dp_{avg}}{dt}p + \left(\widehat{k}_2 g^2 - \widehat{k}_u p_{avg} p\right) p_{avg} = 2\widehat{k}_2 g^2 + \widehat{k}_2 g p - \widehat{k}_u \left(p_{var} + p_{avg}^2\right) p, \tag{3.48}$$

rearranging gives Eq. (3.49)

$$\frac{dp_{avg}}{dt} = \widehat{k}_2 \left[g + \frac{g^2}{p} (2 - p_{avg}) \right] - \widehat{k}_u p_{var}, \tag{3.49}$$

the ODE with respect to time t for the first order moment, p_{avg}.
Assuming $\sum_{i=2}^{n-1} p_i \approx \sum_{i=2}^{n} p_i$, we can now express Eq. (3.29) in terms of p

$$\frac{dg}{dt} = \widehat{k}_1 h_1 h_2 - \widehat{k}_{-1} g - 2\widehat{k}_2 g^2 - \widehat{k}_2 g p. \tag{3.50}$$

To obtain time derivative for p_{var} recall Eq. (3.47), differentiating with respect to time gives

$$\sum_{j=2}^{n} j^2 \frac{dp_j}{dt} = \frac{dp}{dt} \left(p_{var} + p_{avg}^2 \right) + p \left(\frac{dp_{var}}{dt} + 2p_{avg} \frac{dp_{avg}}{dt} \right). \tag{3.51}$$

Again by substitution of Eq. (3.30)-(3.32), the left side of Eq. (3.51) expands to

$$\sum_{j=2}^{n} j^2 \frac{dp_j}{dt} = 4\widehat{k}_2 g^2 + \widehat{k}_2 g \sum_{j=2}^{n-1} (2j+1) p_j - \widehat{k}_u \sum_{j=2}^{n} j^3 p_j. \tag{3.52}$$

By again recalling $n \to \infty$, and given the definition for the third order moment p_{skew} in terms of the first two moments,

$$p_{skew} = \frac{1}{p_{var}^{3/2}} \left(\frac{1}{p} \sum_{j=2}^{n} j^3 p_j - 3p_{avg} p_{var} - p_{avg}^3 \right), \tag{3.53}$$

by substitution, Eq. (3.52) becomes

$$\sum_{j=2}^{n} j^2 \frac{dp_j}{dt} = 4\widehat{k}_2 g^2 + \widehat{k}_2 g \left[p(2p_{avg} + 1) \right] - \widehat{k}_u p \left(p_{skew} p_{var}^{3/2} + 3p_{avg} p_{var} + p_{avg}^3 \right).$$

Recalling Eq. (3.39) and Eq. (3.49), then rearranging, Eq. (3.51) becomes

$$p\frac{dp_{var}}{dt} = 4\widehat{k}_2 g^2 + \widehat{k}_2 gp(2p_{avg}+1) - \widehat{k}_2 g^2 p_{var} - 2\widehat{k}_2 g p_{avg} p - 4\widehat{k}_2 g^2 p_{avg} + \widehat{k}_2 g^2 p_{avg}^2 \\ -\widehat{k}_u p\left(p_{skew} p_{var}^{3/2} + 3p_{avg}p_{var} + p_{avg}^3\right) + \widehat{k}_u p_{avg}^3 p + 3\widehat{k}_u p_{avg} p_{var} p,$$

reordering for factorisation and cancellation gives

$$p\frac{dp_{var}}{dt} = \widehat{k}_2 gp + 4\widehat{k}_2 g^2 - 4\widehat{k}_2 g^2 p_{avg} + \widehat{k}_2 g^2 p_{avg}^2 - \widehat{k}_2 g^2 p_{var} + 2\widehat{k}_2 g p_{avg} p - 2\widehat{k}_2 g p_{avg} p \\ -\widehat{k}_u p_{skew} p_{var}^{3/2} p - \widehat{k}_u p_{avg}^3 p + \widehat{k}_u p_{avg}^3 p + 3\widehat{k}_u p_{avg} p_{var} p - 3\widehat{k}_u p_{avg} p_{var} p,$$

dividing through by p gives Eq. (3.54)

$$\frac{dp_{var}}{dt} = \widehat{k}_2\left[g + \frac{g^2}{p}\left(4 - 4p_{avg} + p_{avg}^2 - p_{var}\right)\right] - \widehat{k}_u p_{skew} p_{var}^{3/2}, \tag{3.54}$$

which is the ODE with respect to time t for the second order moment, p_{var}.

The third order moment p_{skew}, appearing in the right-hand side of Eq. (3.54), is, under the current definition in Eq. (3.53), still defined in terms of the plaque state distribution p_j. Rather than continue to pursue further derivations to express this in terms of higher order moments, we choose to model the distribution with an appropriate discrete probability distribution and thereby approximate the third order central moment using the associated model definition.

We adopt a shifted geometric distribution to model the plaque state distribution, and thus adopt the associated definition for the third order central moment to approximate p_{skew}, truncating the system at the third order and removing the requirement to derive further equations for higher order moments.

We first present a definition for the geometric distribution [154]. If we let the random

variable X assume the values 0,1,2,... with probabilities

$$\rho_\nu = \mathrm{P}\{X = \nu\} = (1-\rho)\rho^\nu, \quad \nu = 0, 1, ..., \tag{3.55}$$

where $0 < \rho < 1$, X has a geometric distribution with the parameter ρ denoted by

$$X \sim G(\rho). \tag{3.56}$$

We shift the distribution $G(\rho)$ in ν such that the range for ν aligns with the plaque state distribution defined by p_j. Where $\nu_s = \nu - 2$, if we let the random variable Y take the values 2,3,4,... with probabilities

$$\rho_{\nu_s} = \mathrm{P}\{Y = \nu_s\} = (1-\rho)\rho^{\nu_s}, \quad \nu = 2, 3, ..., \tag{3.57}$$

where $0 < \rho < 1$, Y has a shifted geometric distribution which we denote by

$$Y \sim G_s(\rho). \tag{3.58}$$

We find parameter ρ by setting the expected value of $G_s(\rho)$ equal to p_{avg}, rearranging for ρ

$$\rho = \frac{1}{p_{avg} - 1}, \tag{3.59}$$

where $p_{avg} > 2$.

By substituting into the geometric distribution definition for the third order central moment, we obtain in Eq. (3.60) an expression for p_{skew}

$$p_{skew} = \frac{2 - \rho}{\sqrt{1 - \rho}}, \tag{3.60}$$

enabling us to approximate the third order moment of the averaged model system for Cx43 cycling with Gap27 binding, completing the definition by moment closure.

In Figure 3.4 we present concentration-adjusted plaque state distributions at equilibrium, p_i^*/p, across different distribution shapes (prompted by changes to $\widehat{k}_1/\widehat{k}_{-1}$, $\widehat{k}_2$ and $\widehat{k}_u$) plotted alongside corresponding shifted geometric distributions, $G_s(\rho)$, using values for ρ determined by p_{avg}. We see in Figure 3.4, the shifted geometric distribution model, $G_s(\rho)$, is a close approximation for the p_i^*/p distribution shapes presented.

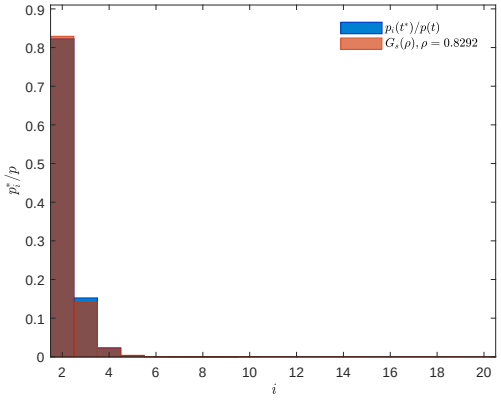

(a) $\widehat{k}_1/\widehat{k}_{-1} = 1 \times 10^3$. $\rho = 0.8292$.

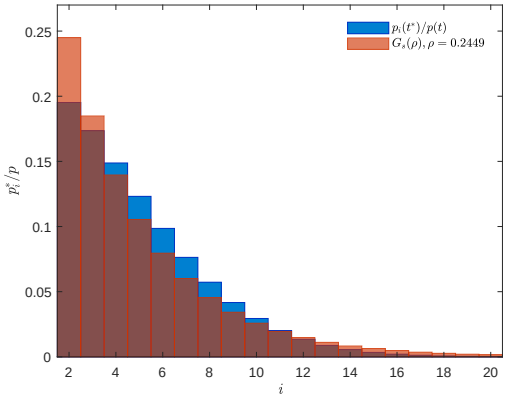

(b) $\widehat{k}_2 = 1 \times 10^4$. $\rho = 0.2449$.

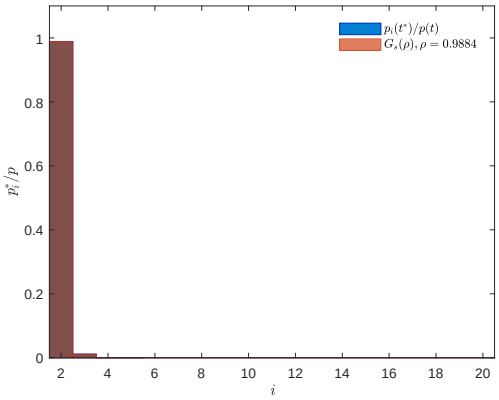

(c) $\widehat{k}_u = 1 \times 10^1$. $\rho = 0.9884$.

Figure 3.4: Concentration-adjusted plaque state distributions at equilibrium, p_i^*/p (blue), plotted alongside shifted geometric distributions, $G_s(\rho)$ (red), where ρ is determined by p_{avg} using Eq. (3.59), for parameters (a) $\widehat{k}_1/\widehat{k}_{-1} = 1 \times 10^3$, (b) $\widehat{k}_2 = 1 \times 10^4$ and (c) $\widehat{k}_u = 1 \times 10^1$. The model distribution $G_s(\rho)$ (red) is a reasonable approximation for p_i^*/p (blue) distribution shapes tested in (a), (b) and (c). Initial conditions: $[h](0) = [g](0) = [e](0) = [p_i](0) = 0$. Parameters: $\widehat{k}_1 = \widehat{k}_{-1} = \widehat{k}_2 = \widehat{k}_u = \widehat{k}_r = \widehat{k}_d = 1$ (unless varied), $n = 100$. Time: 500 nondimensional time steps.

3.2.6 Updated model system

We now present in full the derived averaged system. Since plaque states p_i no longer appear in the model equations, for notation clarity we adopt subscripts in place of superscripts describing to which cell hemichannel, annular gap junctions and hemichannel-peptide complex species belongs. We discard square brackets, such that $[h^1] = h_1$ and similar for all model variables. We also rename hemichannel-peptide complex variables so that $C_1 = [h \cdot g27^1]$ and $C_2 = [h \cdot g27^2]$, and refer to the hemichannel-peptide complex species generally as C. We can now express the system in terms of derived moment variables $p(t)$, $p_{avg}(t)$, $p_{var}(t)$ and $p_{skew}(t)$. The ODEs describing hemichannel, Gap27 and hemichannel-peptide complex concentrations remain unchanged in the updated system but for notation. The averaged system is defined by Eq. (3.61)-(3.71).

$$\frac{dh_1}{dt} = 1 - \widehat{k}_1 h_1 h_2 + \widehat{k}_{-1} g + \widehat{k}_r e_1 - h_1 - \widehat{k}_{G27} h_1 g_{27} + \widehat{k}_{-G27} C_1, \tag{3.61}$$

$$\frac{dh_2}{dt} = 1 - \widehat{k}_1 h_1 h_2 + \widehat{k}_{-1} g + \widehat{k}_r e_2 - h_2 - \widehat{k}_{G27} h_2 g_{27} + \widehat{k}_{-G27} C_2, \tag{3.62}$$

$$\frac{dg}{dt} = \widehat{k}_1 h_1 h_2 - \widehat{k}_{-1} g - 2\widehat{k}_2 g^2 - \widehat{k}_2 g p, \tag{3.63}$$

$$\frac{dp}{dt} = \widehat{k}_2 g^2 - \widehat{k}_u p_{avg} p, \tag{3.64}$$

$$\frac{dp_{avg}}{dt} = \widehat{k}_2 \left[g + \frac{g^2}{p}(2 - p_{avg}) \right] - \widehat{k}_u p_{var}, \tag{3.65}$$

$$\frac{dp_{var}}{dt} = \widehat{k}_2 \left[g + \frac{g^2}{p}(4 - 4p_{avg} + p_{avg}^2 - p_{var}) \right] - \widehat{k}_u p_{skew} p_{var}^{3/2}, \tag{3.66}$$

where p_{skew} is defined by Eq. (3.60).

$$\frac{de_1}{dt} = -\widehat{k}_r e_1 - \widehat{k}_d e_1 + \frac{\widehat{k}_u}{2} p_{avg} p, \tag{3.67}$$

$$\frac{de_2}{dt} = -\widehat{k}_r e_2 - \widehat{k}_d e_2 + \frac{\widehat{k}_u}{2} p_{avg} p, \tag{3.68}$$

$$\frac{dg_{27}}{dt} = \widehat{k}_{-G27}\left(C_1 + C_2\right) - \widehat{k}_{G27}\left(h_1 g_{27} + h_2 g_{27}\right), \tag{3.69}$$

$$\frac{dC_1}{dt} = \widehat{k}_{G27} h_1 g_{27} - \widehat{k}_{-G27} C_1, \tag{3.70}$$

$$\frac{dC_2}{dt} = \widehat{k}_{G27} h_2 g_{27} - \widehat{k}_{-G27} C_2, \tag{3.71}$$

where $\widehat{k}_1$, $\widehat{k}_{-1}$, $\widehat{k}_2$, $\widehat{k}_u$, $\widehat{k}_r$, $\widehat{k}_d$, $\widehat{k}_{G27}$, $\widehat{k}_{-G27} \geq 0$.

To compare the original nondimensionalised system defined by Eq. (3.27)-(3.37) and the averaged nondimensionalised system defined by Eq. (3.61)-(3.71), we run numerical simulations with equivalent initial conditions through a large parameter space, and graphically examine approximated system moments at equilibria from the averaged nondimensionalised system, p^*_{avg}, p^*_{var} and p^*_{skew}, with corresponding moments at equilibria calculated numerically from the original nondimensional system, $\hat{p}^*_{avg}$, $\hat{p}^*_{var}$ and $\hat{p}^*_{skew}$.

In Figure 3.5, we see that p^*_{avg}, p^*_{var} and p^*_{skew} are close approximations for $\hat{p}^*_{avg}$, $\hat{p}^*_{var}$ and $\hat{p}^*_{skew}$ under variation to key model parameters $\widehat{k}_1/\widehat{k}_{-1}$, $\widehat{k}_2$ and $\widehat{k}_u$ across a substantive parameter space. The approximation is particularly close for the first order moment p_{avg} (a)-(c). We see that second order moment p_{var} (d)-(f) maintains a reasonable approximation under variation of parameters $\widehat{k}_1/\widehat{k}_{-1}$ and $\widehat{k}_u$, divergence becoming apparent only when $\widehat{k}_2$ becomes large. We see the approximation used for third order moment p_{skew} is reasonable under variation to parameters $\widehat{k}_1/\widehat{k}_{-1}$ and $\widehat{k}_2$ (g)-(h), and we see divergence only when $\widehat{k}_u$ becomes large (i).

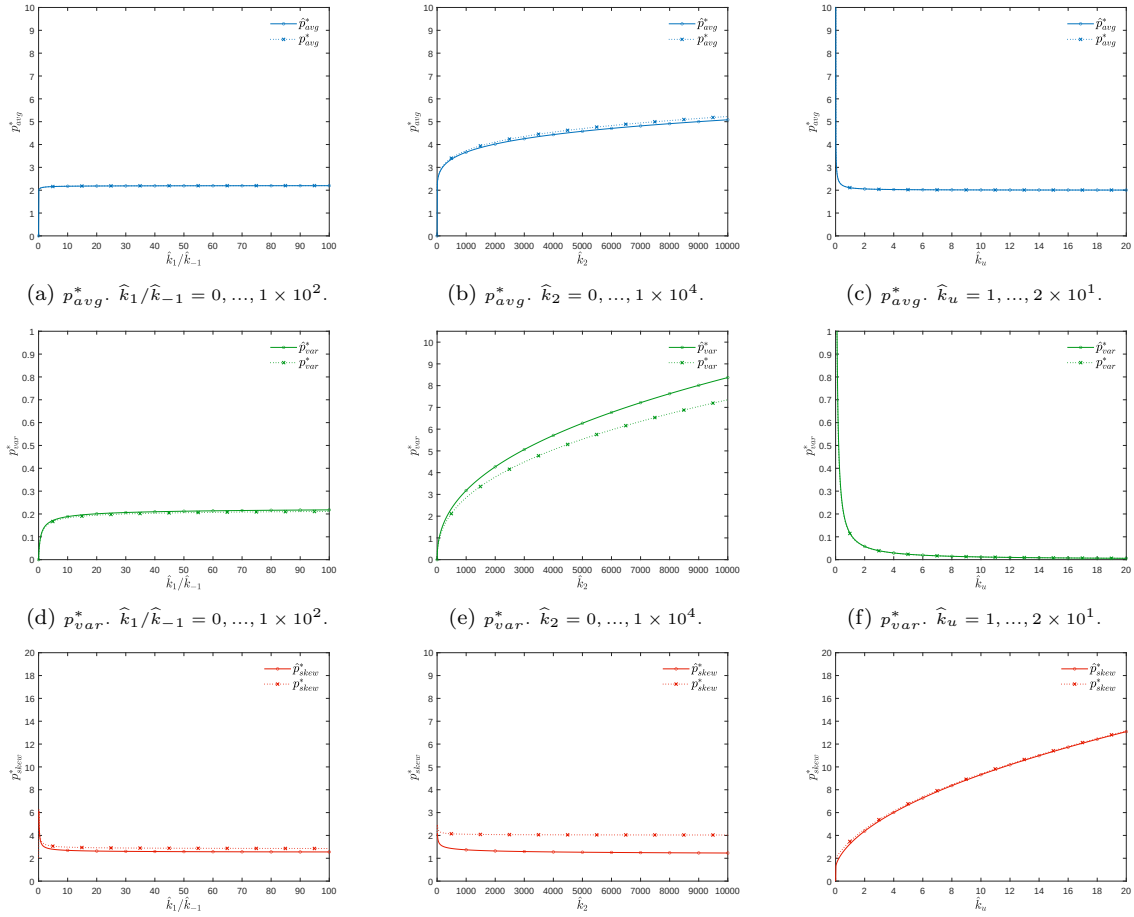

(a) p^*_{avg}. $\widehat{k}_1/\widehat{k}_{-1} = 0, ..., 1 \times 10^2$. (b) p^*_{avg}. $\widehat{k}_2 = 0, ..., 1 \times 10^4$. (c) p^*_{avg}. $\widehat{k}_u = 1, ..., 2 \times 10^1$.

(d) p^*_{var}. $\widehat{k}_1/\widehat{k}_{-1} = 0, ..., 1 \times 10^2$. (e) p^*_{var}. $\widehat{k}_2 = 0, ..., 1 \times 10^4$. (f) p^*_{var}. $\widehat{k}_u = 1, ..., 2 \times 10^1$.

(g) p^*_{skew}. $\widehat{k}_1/\widehat{k}_{-1} = 0, ..., 1 \times 10^2$. (h) p^*_{skew}. $\widehat{k}_2 = 0, ..., 1 \times 10^4$. (i) p^*_{skew}. $\widehat{k}_u = 1, ..., 2 \times 10^1$.

Figure 3.5: Derived moment equilibria, p^*_{avg}, p^*_{var} and p^*_{skew} (dotted-crossed), with $\hat{p}^*_{avg}$, $\hat{p}^*_{var}$ and $\hat{p}^*_{skew}$ (solid-circle), rows, under variation to parameters $\widehat{k}_1/\widehat{k}_{-1}$, $\widehat{k}_2$ and $\widehat{k}_u$ (columns). (a)-(c) p^*_{avg} and $\hat{p}^*_{avg}$ (blue) over (a) $\widehat{k}_1/\widehat{k}_{-1}$, (b) $\widehat{k}_2$ and (c) $\widehat{k}_u$. (d)-(f) p^*_{var} and $\hat{p}^*_{var}$ (green) over (d) $\widehat{k}_1/\widehat{k}_{-1}$, (e) $\widehat{k}_2$ and (f) $\widehat{k}_u$. (g)-(i) p^*_{skew} and $\hat{p}^*_{skew}$ (red) over (g) $\widehat{k}_1/\widehat{k}_{-1}$, (h) $\widehat{k}_2$ and (i) $\widehat{k}_u$. Note: line markers (circle, cross) are included only to aid in distinguishing between trajectories. Initial conditions: $h(0) = g(0) = e(0) = p_i(0) = p_{var}(0) = 0$, $p_{avg}(0) = 2 + 1 \times 10^{-10}$, $p(0) = 1 \times 10^{-10}$, $p_{skew}(0) = 1 \times 10^5$. Parameters: $\widehat{k}_1 = \widehat{k}_{-1} = \widehat{k}_2 = \widehat{k}_u = \widehat{k}_r = \widehat{k}_d = 1$ (unless varied), $n = 100$. Time: 500 nondimensional time steps.

3.2.7 Numerical implementation

We input both the non-averaged and averaged nondimensional model systems into Mathworks MATLAB 2020a and solve numerically using in-built stiff ODE solver *ode23s* (a modified Rosenbrock scheme, detailed in [155]).

We locate model equilibria using mathematical continuation software MATCONT [156], which, given an initial point, solves the initial value problem for the system by numerical integration. We use the integrator *ode23s*, set relative and absolute toler-

ances small (1×10^{-7}) and time to 500 numerical steps. To establish an early indication of equilibrium stability, we construct phase portraits for a subset of model variables by varying initial points around an equilibrium point and reviewing the resulting orbit behaviour. We corroborate MATCONT results with solution output in MATLAB, approximating equilibria by identifying where variables remain approximately constant over a large interval for time t.

To determine equilibria stability we use MATCONT to compute corresponding eigenvalues for an equilibrium point and search for candidate bifurcation parameters. For a given equilibrium point, we let MATCONT compute the 'equilibrium curve' over a given parameter (equilibria as a function of some model parameter) and monitor the corresponding eigenvalue output and any accompanying bifurcations. We systematically iterate in this manner through model parameters $\widehat{k}_1$, $\widehat{k}_{-1}$, $\widehat{k}_2$, $\widehat{k}_u$, $\widehat{k}_r$ and $\widehat{k}_d$ for the model without Gap27. For the model with Gap27, we approximate equilibria and estimate their stability directly from MATLAB output in the manner described, under variation to initial concentrations and model parameters.

3.3 Results

3.3.1 Initial conditions

To explore model behaviour through numerical simulations, we choose to maintain consistency between initial conditions whilst we investigate the effect of varying some parameter of the model. For this 'base' model we first assume all initial concentrations (at $t = 0$) of connexin-based variables (for which it is permissable) equal to zero, $h(0) = g(0) = e(0) = p_{var}(0) = 0$. By definition $p(0) \neq 0$, so we consider only the case in which plaques already exist between the two interacting cells, choosing $p(0)$ arbitrar-

ily small, $p(0) = 1 \times 10^{-10}$. Also by definition $p_{avg}(0) > 2$, resulting from the minimum defined plaque state, so we choose $p_{avg}(0)$ arbitrarily close to 2, $p_{avg}(0) = 2 + 1 \times 10^{-10}$. By Eq. (3.60) $p_{avg}(0)$ determines the initial value for p_{skew}, thus $p_{skew}(0) = 1 \times 10^{5}$.

To further define this 'base' model, we set all rates such that their associated parameter ratios are equal to one, so any particular rate is not favoured. Rate values we choose arbitrarily equal to one, $\widehat{k}_1 = \widehat{k}_{-1} = \widehat{k}_2 = \widehat{k}_u = \widehat{k}_r = \widehat{k}_d = \widehat{k}_{G27} = \widehat{k}_{-G27} = 1$.

We set a limit on time parameter t by choosing a value which allows for the system to come to steady-state, identified approximately using the methods defined in *Methods* 3.2.7, $t = 500$ nondimensional time steps.

We interpret our 'base' model, at $t = 0$, as a scenario in which cells are already interacting and have established small plaque structures at extremely low concentration. We may think of these conditions as being those we might expect for cells that have recently begun to interact.

For the subsequent sections we consider the model presented first without and later with Gap27 treatment. In the case without Gap27, we set initial concentrations for Gap27 and hemichannel-Gap27 complex to zero, $g_{27}(0) = C_1(0) = C_2(0) = 0$, which take variables g_{27}, C_1 and C_2 out of model output. In the case where we introduce Gap27 treatment, we let $g_{27}(0)$ take non-zero values and, since we assume there are no other Gap27 treatments prior to $t = 0$, $C_1(0) = C_2(0) = 0$.

3.3.2 Cx43 cycling without Gap27

To explore Cx43 cycling dynamics, and particularly how this influences gap junction and plaque formation and degradation, we temporarily ignore the effect of Gap27 and focus solely on Cx43 cycling. For this section, initial values for Gap27 and hemichannel-Gap27 complex variables are all set equal to zero ($g_{27}(0) = C_1(0) = C_2(0) = 0$), such

that the last two terms of Eq. (3.61) and (3.62) and Eq. (3.69), (3.70) and (3.71) all reduce to zero. The remaining model system, defined by Eq. (3.61)-(3.68), contains only variables for the connexin-based species hemichannels, gap junctions, plaques and annular gap junctions.

Effect of varied initial concentrations, e.g. $h(0)$

First, we test the model for a range of initial concentrations (at $t = 0$) across model variables for a constant parameter set defined in *Results* 3.3.1. We present the illustrative case for $h(0)$ in Figure 3.6, for three sample nondimensional concentrations $h(0) = 0$ (blue), $h(0) = 1$ (red) and $h(0) = 10$ (yellow) across all model variables.

We notice the transient behaviour of the system over t is affected by $h(0)$, for all variables. In particular, if $h(0)$ is large ($h(0) = 10$, yellow) we see an exponential decay in h to steady-state (a), and we observe clear transient spiking in concentrations of g (b), p (c), p_{avg} (d), p_{var} (e) and e (g), before also decaying exponentially to steady-state. As $h(0)$ increases (blue to yellow), it is clear the transient spike in variable concentrations grows and there is a unique equilibrium that is not affected by $h(0)$. For the 'base' parameter set presented, we find only one equilibrium which appears robust to changes in $h(0)$, even for large orders of magnitude, suggesting the point might be globally stable. We will further explore the stability of the system equilibrium in the next section.

We also explore how the system behaves under (non-negative) variations to other initial concentrations $g(0)$, $p(0)$, $p_{avg}(0)$, $p_{var}(0)$, $p_{skew}(0)$ and $e(0)$ (results not presented). To summarise, variation to all initial concentrations appear to only affect transient behaviour of the system over t, the system returning the same equilibrium point over t under this variation, further indicating the point may be globally stable. Transient behaviour is qualitatively similar under variation to $g(0)$, $p(0)$ and $e(0)$ to that of $h(0)$,

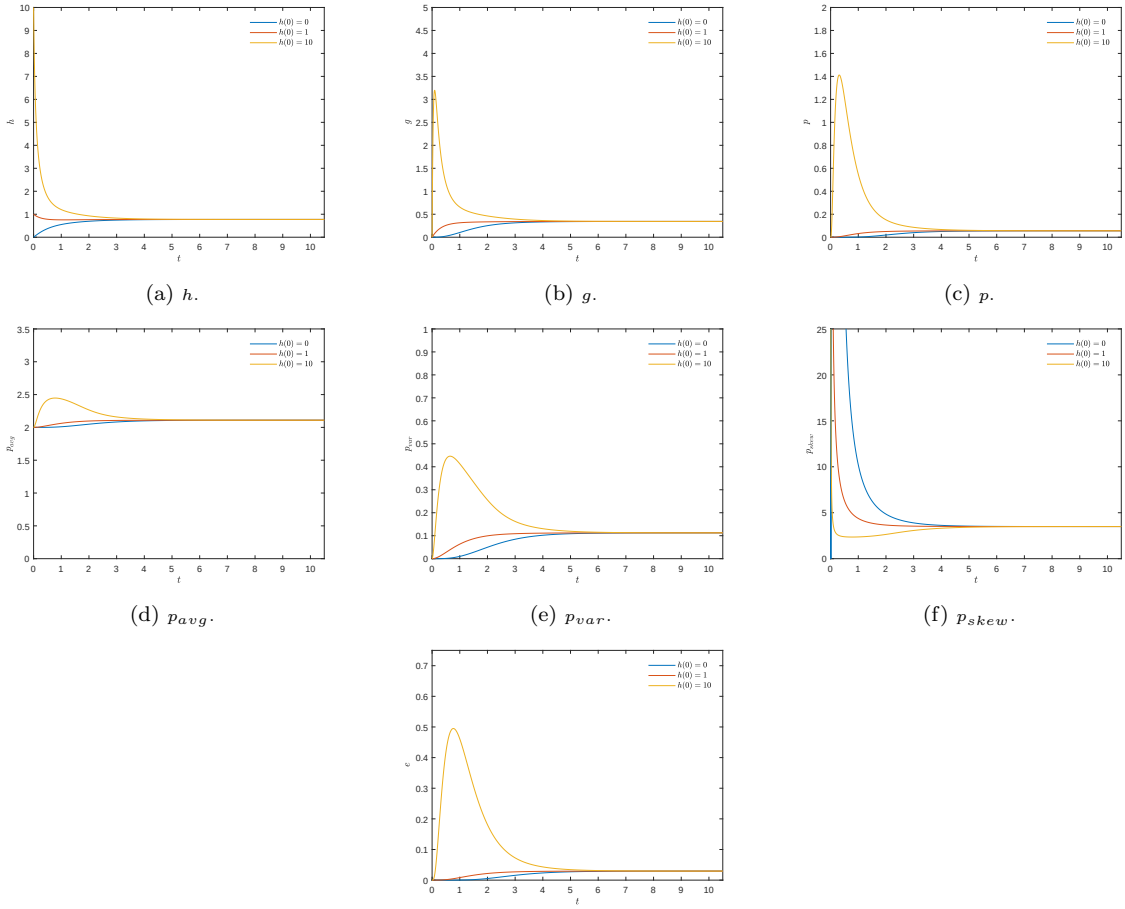

(a) h.

(b) g.

(c) p.

(d) p_{avg}.

(e) p_{var}.

(f) p_{skew}.

(g) e.

Figure 3.6: Averaged system without Gap27 variables over t for three different initial (nondimensional) concentrations of hemichannels h, $h(0) = 0$ (blue), $h(0) = 1$ (red), $h(0) = 10$ (yellow). Transient behaviour over t is affected by variation to $h(0)$ for all variables but the system equilibrium over t appears robust to these changes, even for large $h(0)$. Initial conditions: $g(0) = e(0) = p_{var}(0) = 0$, $p_{avg}(0) = 2 + 1 \times 10^{-10}$, $p(0) = 1 \times 10^{-10}$, $p_{skew}(0) = 1 \times 10^{5}$, $g_{27}(0) = 0$. Parameters: $\widehat{k}_1 = \widehat{k}_{-1} = \widehat{k}_2 = \widehat{k}_u = \widehat{k}_r = \widehat{k}_d = 1$. Time: 500 nondimensional time steps.

as is that of $p_{avg}(0)$ and $p_{var}(0)$ but with minor variance to transient characteristics.

Equilibrium curves

Upon solving the system in MATLAB for the 'base' parameter set detailed in *Results* 3.3.1, the system appeared to have only one equilibrium solution which, under varied initial concentrations, also appeared to be globally stable. We corroborate these observations using MATCONT to approximate this equilibrium point, repeat the analysis undertaken with MATLAB by varying initial concentrations and then compute the corresponding eigenvalues for the equilibrium to determine local stability. For the parameter set $\widehat{k}_1 = \widehat{k}_{-1} = \widehat{k}_2 = \widehat{k}_u = \widehat{k}_r = \widehat{k}_d = 1$, where $g_{27}(0) = 0$, MATCONT identifies, over $t = 500$ (nondimensional) time steps, only one equilibrium point ϵ_p, approximated to 4 d.p. in Table 3.3. All corresponding eigenvalues for ϵ_p evaluate to negative real parts, indicating the point is locally stable.

We now explore how key model parameters affect the system equilibrium, without Gap27. With MATCONT, we select ϵ_p as the initial point and compute the equilibrium curve for a given parameter or parameter ratio, both towards zero and up to three orders of magnitude, whilst holding other initial conditions and all other parameters constant. We focus analysis to $\widehat{k}_1/\widehat{k}_{-1}$, $\widehat{k}_2$ and $\widehat{k}_u$ and omit results for $\widehat{k}_r$ and $\widehat{k}_d$, which have negligible effect on the system equilibrium. We denote the approximated steady-state of a particular variable using * notation, e.g. hemichannel concentration for cell 1 at the system steady-state $x' = f(x, \alpha) = 0$, $x \in \mathbb{R}^{11}$, $\alpha \in \mathbb{R}^8$ is denoted by h_1^*. Since concentration trajectories over time t with equal initial conditions are identical for the same species from different cells and come to the same concentration at steady-state, e.g. $h_1^* = h_2^*$, we present the repeated steady-state concentration for h_1^* and h_2^* and use notation h^* to represent species from both cells.

The analysis indicates that the system exhibits only simple equilibrium behaviour un-

der parameter variation. We find only one equilibrium point which is locally stable for non-negative parameter values (this holding for up to the three orders of magnitude investigated), which evolves with a given parameter but remains locally stable under this parameter variation. Thus we observe no bifurcations for the system for any of the parameters $\widehat{k}_1, \widehat{k}_{-1}, \widehat{k}_2, \widehat{k}_u, \widehat{k}_r, \widehat{k}_d$.

Table 3.3: Equilibrium point ϵ_p for the 'base' model (without Gap27), approximated using MATCONT.

Variable	Value (4 d.p.)
h_1	0.7740
h_2	0.7740
g	0.3436
e_1	0.0295
e_2	0.0295
p	0.0562
p_{avg}	2.1019
p_{var}	0.1295

Gap junction association/dissociation ratio $\widehat{k}_1/\widehat{k}_{-1}$

We first review the effect of gap junction association/dissociation parameter ratio $\widehat{k}_1/\widehat{k}_{-1}$, where $\widehat{k}_{-1} > 0$, on the system equilibrium. We illustrate this in Figure 3.7 where we present the equilibrium curve in which the system equilibrium is a function of $\widehat{k}_1/\widehat{k}_{-1}$. We see clearly that $\widehat{k}_1/\widehat{k}_{-1}$ most significantly affects the equilibrium over a relatively small range (approximately $0 \leq \widehat{k}_1/\widehat{k}_{-1} \leq 100$), having a relatively insignificant effect at higher orders of magnitude. Variables most affected are hemichannels and gap junctions h and g. We see that h^* decays exponentially as $\widehat{k}_1/\widehat{k}_{-1}$ increases (a), whilst all other variable steady-state functions (other than p^*_{skew}) grow logarithmically and begin to stabilise as h^* tends to zero.

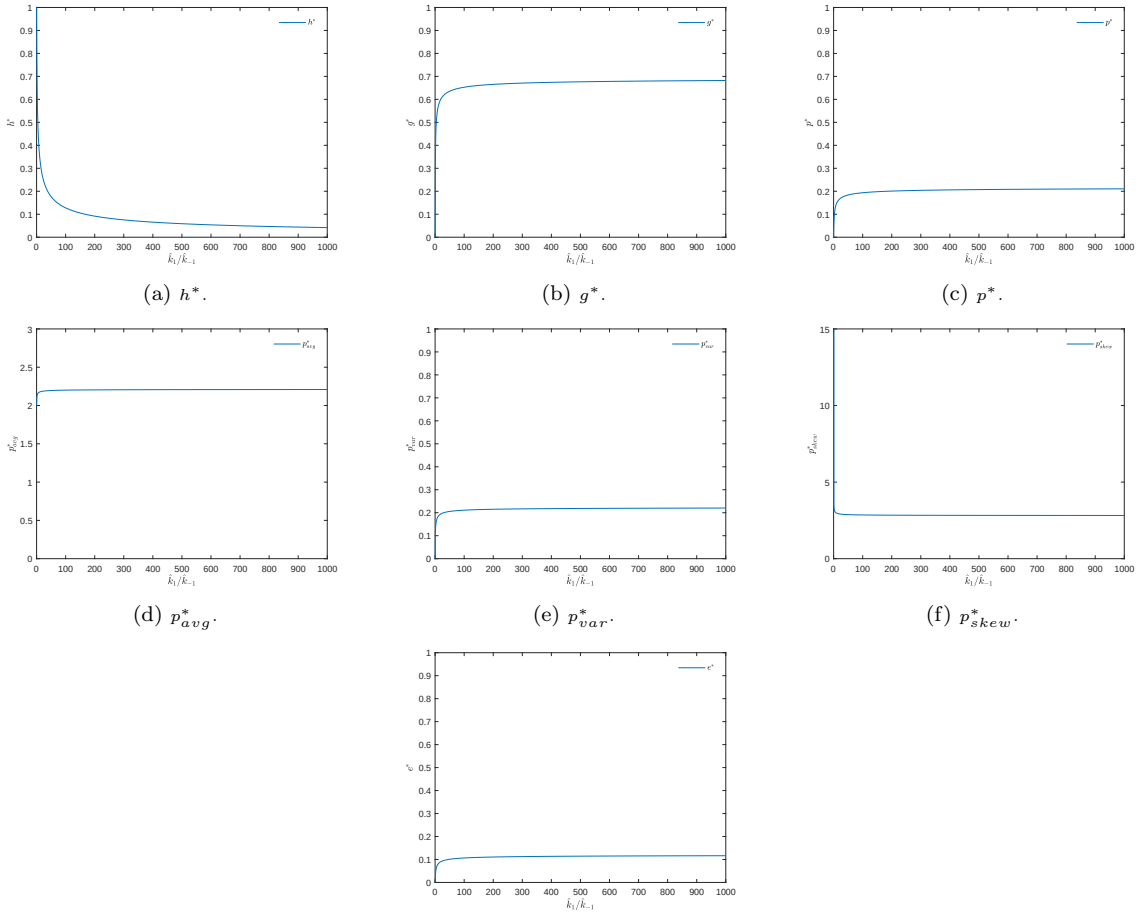

(a) h^*. (b) g^*. (c) p^*.

(d) p^*_{avg}. (e) p^*_{var}. (f) p^*_{skew}.

(g) e^*.

Figure 3.7: Averaged system without Gap27 equilibria as a function of gap junction formation/dissociation parameter ratio $\widehat{k}_1/\widehat{k}_{-1}$ for all model variables h^*, g^*, p^*, p^*_{avg}, p^*_{var}, p^*_{skew} and e^*. As $\widehat{k}_1/\widehat{k}_{-1}$ increases h^* decays exponentially (a), whilst all other variable functions (other than p^*_{skew}) increase logarithmically, stabilising as $\widehat{k}_1/\widehat{k}_{-1}$ becomes large and h^* approaches zero (b)-(e), (g). p^*_{skew} decays rapidly with $\widehat{k}_1/\widehat{k}_{-1}$, stabilising as $\widehat{k}_1/\widehat{k}_{-1}$ becomes large (f). Initial conditions: $h(0) = g(0) = e(0) = p_{var}(0) = 0$, $p_{avg}(0) = 2+1\times10^{-10}$, $p(0) = 1\times10^{-10}$, $p_{skew}(0) = 1\times10^5$, $g_{27}(0) = 0$. Parameters: $\widehat{k}_1/\widehat{k}_{-1} = 0, ..., 1\times10^3$, $\widehat{k}_2 = \widehat{k}_u = \widehat{k}_r = \widehat{k}_d = 1$. Time: 500 nondimensional time steps.

Gap junction plaque formation rate $\widehat{k}_2$

In a similar manner we explore the effect that plaque formation rate $\widehat{k}_2$ has on the system equilibrium by examining the associated equilibrium curve, presented in Figure 3.8. We see the variables most affected by $\widehat{k}_2$ are gap junction and plaque variables g, p, p_{avg} and p_{var} which, in contrast to $\widehat{k}_1/\widehat{k}_{-1}$, continues to significantly influence steady-state functions g^*, p^*, p^*_{avg} and p^*_{var} over a large range for $\widehat{k}_2$, up to and beyond $\widehat{k}_2 = 1\times10^4$. g^* decays rapidly as $\widehat{k}_2$ increases, tending to zero, gap junctions increasingly

recruited to form plaque structures (b), p^*_{avg} and p^*_{var} subsequently growing (d)-(e). p^* also decays, smaller plaque structures accruing to form larger plaque structures (c). p^*_{skew} decays rapidly, tending to two, reflecting increasing variability in plaque size (f).

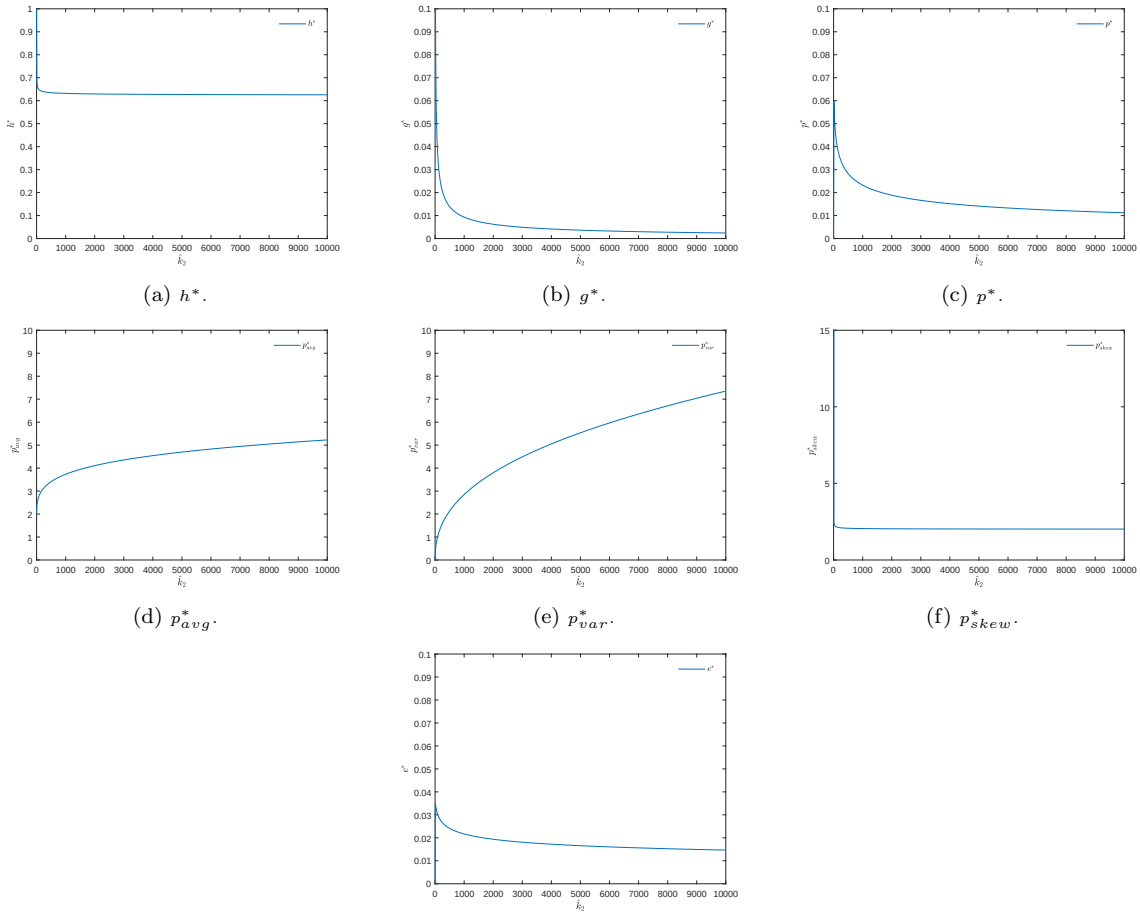

(a) h^*. (b) g^*. (c) p^*.

(d) p^*_{avg}. (e) p^*_{var}. (f) p^*_{skew}.

(g) e^*.

Figure 3.8: Averaged system without Gap27 equilibria as a function of gap junction/plaque binding parameter $\widehat{k}_2$ for all model variables h^*, g^*, p^*, p^*_{avg}, p^*_{var}, p^*_{skew} and e^*. As $\widehat{k}_2$ increases h^*, g^*, p^* and e^* decay exponentially (a)-(c), (g), g^* approaching zero as $\widehat{k}_2$ gets large (b), whilst p^*_{avg} and p^*_{var} grow logarithmically, continuing to grow beyond four orders of magnitude (d)-(e). p^*_{skew} decays rapidly with $\widehat{k}_2$ but stabilises as $\widehat{k}_2$ gets large (f), qualitatively similar to variation in $\widehat{k}_1/\widehat{k}_{-1}$. Initial conditions: $h(0) = g(0) = e(0) = p_{var}(0) = 0$, $p_{avg}(0) = 2 + 1 \times 10^{-10}$, $p(0) = 1 \times 10^{-10}$, $p_{skew}(0) = 1 \times 10^5$, $g_{27}(0) = 0$. Parameters: $\widehat{k}_2 = 0, ..., 1 \times 10^4$, $\widehat{k}_1 = \widehat{k}_{-1} = \widehat{k}_u = \widehat{k}_r = \widehat{k}_d = 1$. Time: 500 nondimensional time steps.

Gap junction plaque internalisation rate $\widehat{k}_u$

We now consider the effect gap junction internalisation parameter $\widehat{k}_u$ has on the system equilibrium, presented in Figure 3.9. We first notice how steady-state functions of plaque variables p^* (c), p^*_{avg} (d) and p^*_{var} (e) decay rapidly to approach their respective minimum defined limits, $p^*_{avg} \to 2$, $p^* \to 0$ and $p^*_{var} \to 0$. p^*_{skew} grows reflecting the rapid reduction in p^*_{avg} (f). For most variables (other than p_{skew}) $\widehat{k}_u$ has the most significant effect on concentration over a much smaller range than for either $\widehat{k}_1/\widehat{k}_{-1}$ and $\widehat{k}_2$, approximately $0 \leq \widehat{k}_u \leq 1$. If we consider what happens as $\widehat{k}_u$ decreases towards zero, we see significant growth in the steady-state functions of plaque variables p^*, p^*_{avg} and p^*_{var}, when internalisation rate $\widehat{k}_u$ reduces below plaque formation rate $\widehat{k}_2$.

Recycling and degradation rates $\widehat{k}_r$ and $\widehat{k}_d$

Recycling and degradation parameters, $\widehat{k}_r$ and $\widehat{k}_d$ respectively, have a negligible effect on the system equilibrium under variation. Only the steady-state functions for internalised gap junction variables e^* exhibit discernible alteration from the initial equilibrium point ϵ_p. To summarise, as we increase $\widehat{k}_d$, e^* decays exponentially, approaching zero as $\widehat{k}_d$ becomes large. If we increase $\widehat{k}_r$, we see qualitatively similar behaviour for e^*, but we also observe a small growth in h^* due to the recycling mechanism, which also propagates through the system to cause insubstantial growth in gap junction and plaque variable steady-state functions.

Biological example: large gap junction plaque structures

As earlier discussed, plaque structures at the junctional nexus can become extremely large through recruitment and aggregation of gap junction channels. Due to physical constraints imposed by the cell membrane, such enormous plaque structures are typ-

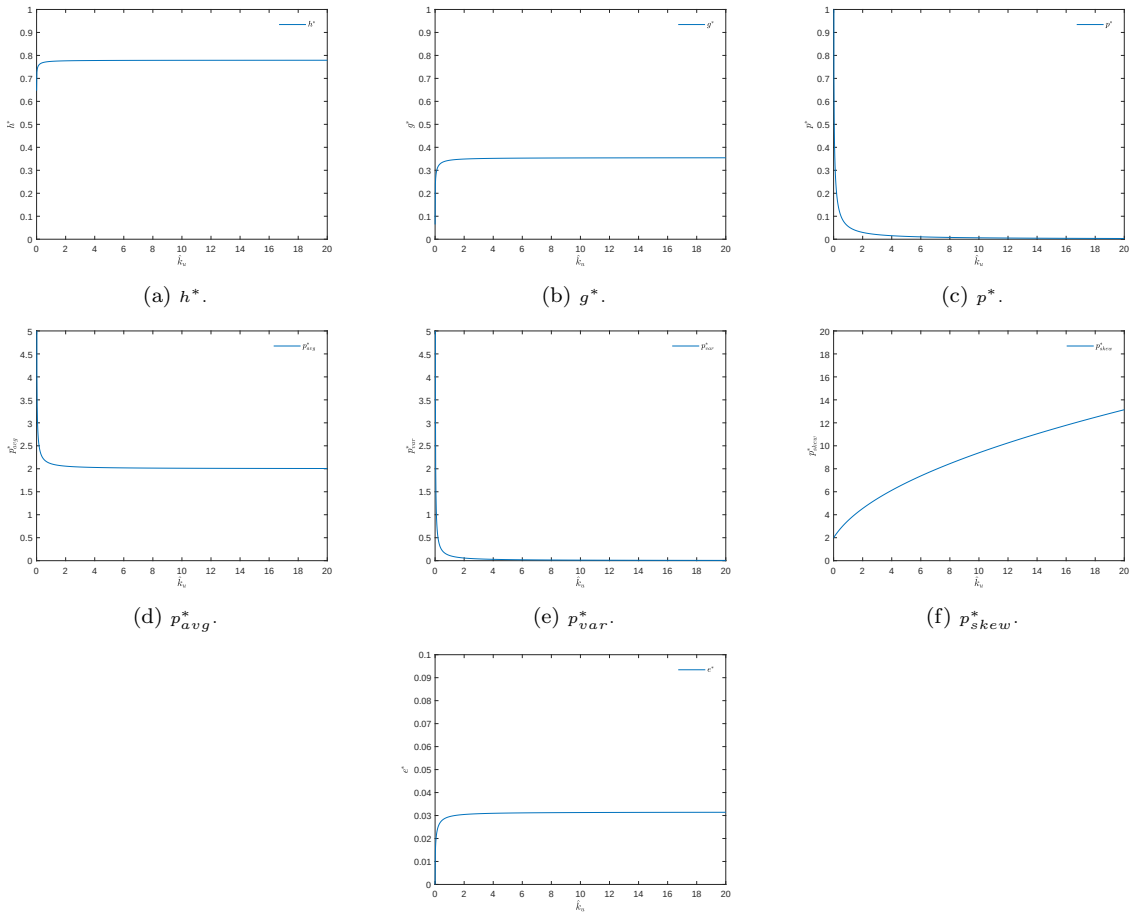

(a) h^*. (b) g^*. (c) p^*.

(d) p^*_{avg}. (e) p^*_{var}. (f) p^*_{skew}.

(g) e^*.

Figure 3.9: Averaged system without Gap27 equilibria as a function of (within plaque) gap junction internalisation parameter $\widehat{k}_u$ for all model variables h^*, g^*, p^*, p^*_{avg}, p^*_{var}, p^*_{skew} and e^*. As $\widehat{k}_u$ increases h^*, g^*, p^*_{skew} and e^* (a)-(b), (f)-(g) increase logarithmically, typically stabilising for relatively small $\widehat{k}_u$ (the exception being p^*_{skew}), whilst p^*, p^*_{avg} and p^*_{var} (c)-(e) decay exponentially, p^* and p^*_{var} approaching zero and p^*_{avg} approaching two. Initial conditions: $h(0) = g(0) = e(0) = p_{var}(0) = 0$, $p_{avg}(0) = 2 + 1 \times 10^{-10}$, $p(0) = 1 \times 10^{-10}$, $p_{skew}(0) = 1 \times 10^5$, $g_{27}(0) = 0$. Parameters: $\widehat{k}_u = 0, ..., 20$, $\widehat{k}_1 = \widehat{k}_{-1} = \widehat{k}_2 = \widehat{k}_r = \widehat{k}_d = 1$. Time: 500 nondimensional time steps.

ically thought to occur only in small concentrations [134]. To demonstrate how the model might reproduce this biologically observed plaque dynamic, we present output for the model in which parameters are selected to induce the formation of a small steady-state concentration of large plaques (small p^* and large p^*_{avg}).

In our model, it is important that hemichannels are not preserved as undocked channels if large plaques are to form, thus gap junction formation must be rapid, so we set the association/dissociation ratio $\widehat{k}_1/\widehat{k}_{-1}$ large. We see in Figure 3.10 (a) the effect on h,

where h comes to a low concentration at steady-state. In addition, plaque formation must be rapid enough for accrual to occur such that smaller plaques are preserved only in low concentrations, so $\widehat{k}_2$ must also be large. Finally, to enable growth and maintenance of large plaques, internalisation has to be slower than plaque formation, so we set $\widehat{k}_u$ small compared to $\widehat{k}_2$. This dynamic keeps low and high concentrations for p, p_{avg} and p_{var} respectively at steady-state. We see this in Figure 3.10, where relatively high p^*_{avg} and p^*_{var} and low p^*_{skew} indicate the presence of large plaque structures in a highly spread plaque state distribution at steady-state (d)-(f).

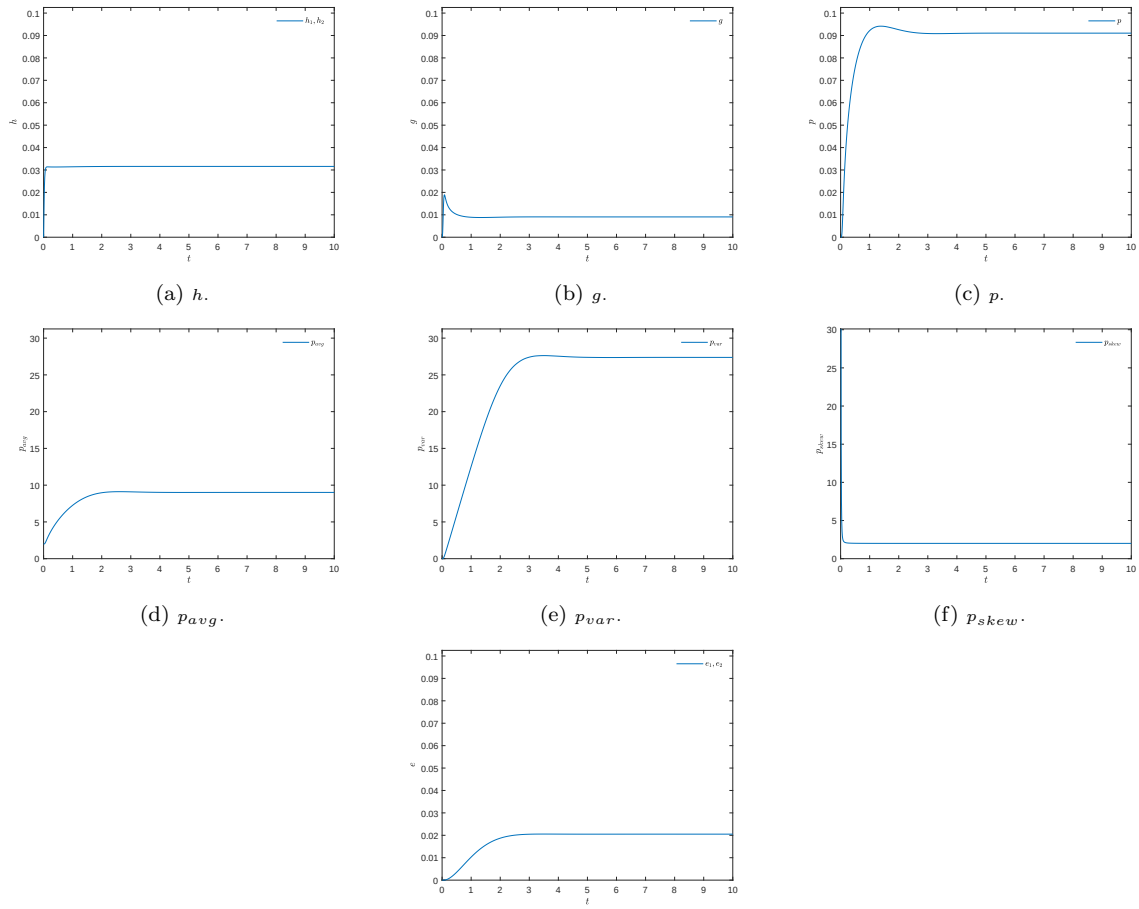

(a) h. (b) g. (c) p.

(d) p_{avg}. (e) p_{var}. (f) p_{skew}.

(g) e.

Figure 3.10: An example scenario in which a small concentration of large plaques form over t for averaged system (with no Gap27) variables. Note the low magnitude of hemichannels h (a), gap junctions g (b) and total plaque concentration p (c) at steady-state compared with average plaque size p_{avg} (d) and plaque variance p_{var} (e). Initial conditions: $h(0) = g(0) = e(0) = p_{var}(0) = 0$, $p_{avg}(0) = 2 + 1 \times 10^{-10}$, $p(0) = 1 \times 10^{-10}$, $p_{skew}(0) = 1 \times 10^{5}$, $g_{27}(0) = 0$. Parameters: $\widehat{k}_1/\widehat{k}_{-1} = 1 \times 10^{3}$, $\widehat{k}_2 = 1 \times 10^{3}$, $\widehat{k}_u = 1 \times 10^{-1}$, $\widehat{k}_r = \widehat{k}_d = 1$. Time: 500 nondimensional time steps.

3.3.3 Cx43 cycling with Gap27

We now consider Cx43 cycling with the addition of Gap27. For this section $g_{27}(0)$ will take non-zero values, invoking non-zero solutions to Gap27 and hemichannel-Gap27 equations and introducing variables for g_{27}, C_1 and C_2 into solution output.

Effect of varied initial concentration of Gap27, $g_{27}(0)$

We first test the model for different initial concentrations (at $t = 0$) for Gap27, $g_{27}(0)$, for model variables over t. We test three different initial (non-dimensional) concen-

trations $g_{27}(0) = 0$, $g_{27}(0) = 10$ and $g_{27}(0) = 100$, this describing the 'base' model without Gap27 and then the model with Gap27 at two different initial concentrations, each $g_{27}(0)$ chosen arbitrarily an order of magnitude apart. We set Gap27 binding and dissociation rates equal and choose the value arbitrarily $\widehat{k}_{G27} = \widehat{k}_{-G27} = 1$ for illustration.

We can see in Figure 3.11 (a)-(g), there is a significant $g_{27}(0)$ dependent effect on transient behaviour over t for Cx43-based variables h, g, p, p_{avg}, p_{var}, p_{skew} and e. For all these variables, it takes longer for concentrations to approach an equilibrium as $g_{27}(0)$ increases. For h, g, p, p_{avg}, p_{var} and e we observe this as slower growth in variable concentrations and for p_{skew} as a slower decay, over t. The equilibrium for variables shown in (a)-(g) remain unaffected by the introduction of $g_{27}(0)$, for all concentrations tested.

For Gap27-based variables g_{27} and C, (h) and (i), we see the equilibrium change according to the magnitude of $g_{27}(0)$. The equilibrium for both g_{27} and C increase with $g_{27}(0)$, concentrations for g_{27} and C decaying and growing over t to the equilibrium, respectively. For the chosen ratio, $\widehat{k}_{G27}/\widehat{k}_{-G27}$, the equilibrium g_{27}^{*} is typically at two-fifths the initial concentration $g_{27}(0)$.

Hemichannel-Gap27 binding/dissociation ratio $\widehat{k}_{G27}/\widehat{k}_{-G27}$

We now consider system behaviour under variation to hemichannel-Gap27 binding/dissociation parameter ratio, $\widehat{k}_{G27}/\widehat{k}_{-G27}$. To generate the simulation output presented in Figure 3.12, we set $g_{27}(0)$ large enough to be able to clearly observe changes to transient behaviour ($g_{27}(0) = 100$) and choose three different ratios to present, each separated by an order of magnitude to illustrate the range of behaviours prompted under this variation, $\widehat{k}_{G27}/\widehat{k}_{-G27} = 0.1$, $\widehat{k}_{G27}/\widehat{k}_{-G27} = 1$ and $\widehat{k}_{G27}/\widehat{k}_{-G27} = 10$. We interpret the

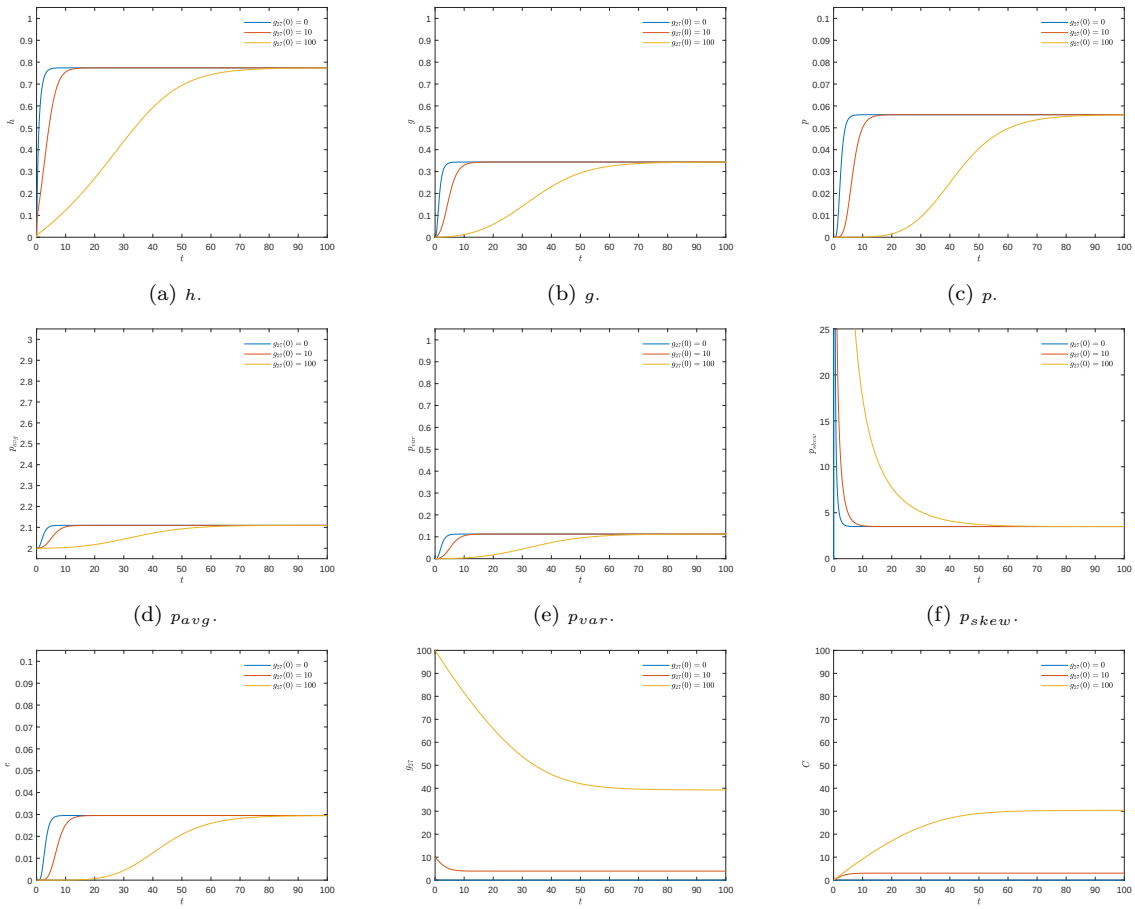

(a) h. (b) g. (c) p.

(d) p_{avg}. (e) p_{var}. (f) p_{skew}.

(g) e. (h) g_{27}. (i) C.

Figure 3.11: Averaged system with Gap27 variables h, g, p, p_{avg}, p_{var}, p_{skew}, e, g_{27} and C over t for three different initial concentrations of g_{27}, $g_{27}(0) = 0$ (blue), $g_{27}(0) = 10$ (red) and $g_{27}(0) = 100$ (yellow). $g_{27}(0)$ affects transient behaviour for Cx43-based variables (a)-(g) and changes the location of the equilibrium for Gap27-based variables (h) and (i), in a concentration dependent manner. Initial conditions: $h(0) = g(0) = e(0) = p_{var}(0) = C(0) = 0$, $p_{avg}(0) = 2+1\times10^{-10}$, $p(0) = 1 \times 10^{-10}$, $p_{skew}(0) = 1 \times 10^{5}$. Parameters: $\widehat{k}_1 = \widehat{k}_{-1} = \widehat{k}_2 = \widehat{k}_u = \widehat{k}_r = \widehat{k}_d = \widehat{k}_{G27} = \widehat{k}_{-G27} = 1$. Time: 500 nondimensional time steps.

ratio as follows: when $\widehat{k}_{G27}/\widehat{k}_{-G27} = 1$ the rate of association and dissociation of the hemichannel-peptide complex is balanced, increasing $\widehat{k}_{G27}/\widehat{k}_{-G27}$ from this equilibrium speeds up association relative to dissociation, whereas decreasing $\widehat{k}_{G27}/\widehat{k}_{-G27}$ has the opposite effect.

We see in Figure 3.12 (a)-(g), $\widehat{k}_{G27}/\widehat{k}_{-G27}$ has significant effects on transient behaviour over t for Cx43-based model species, h, g, p, p_{avg}, p_{var}, p_{skew} and e. As $\widehat{k}_{G27}/\widehat{k}_{-G27}$ increases we see a delay in these variables approaching equilibrium, though the equilibrium is clearly not affected. As $\widehat{k}_{G27}/\widehat{k}_{-G27}$ is increased to larger values, transients begin

to assume a sigmoidal shape, approaching step function-like behaviour as $\widehat{k}_{G27}/\widehat{k}_{-G27}$ becomes very large. p_{skew} continues to decay exponentially to equilibrium as $\widehat{k}_{G27}/\widehat{k}_{-G27}$ increases but, as with the other Cx43-based variables, causes a delay in approaching the equilibrium.

We see in Figure 3.12 (h)-(i), $\widehat{k}_{G27}/\widehat{k}_{-G27}$ changes the equilibrium of both g_{27} and C. We see that when $\widehat{k}_{G27}/\widehat{k}_{-G27}$ is small, g_{27} maintains a high and C a low steady-state concentration, respectively; g_{27} not significantly depleting since association is comparatively non-rapid to dissociation. If $\widehat{k}_{G27}/\widehat{k}_{-G27}$ is increased however, we see that g_{27} maintains a low and C a high steady-state concentration, respectively; g_{27} now depleting to form the complex C since association is now rapid compared to dissociation.

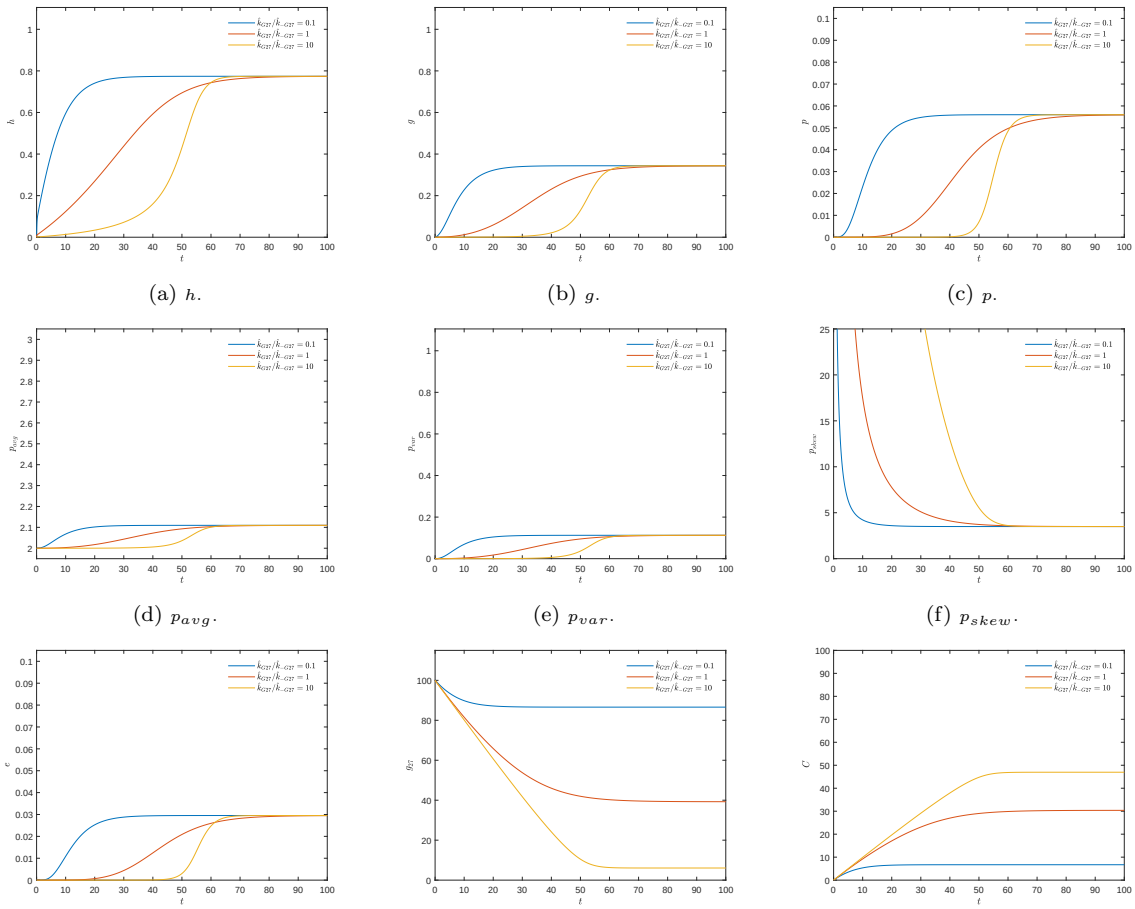

(a) h. (b) g. (c) p.

(d) p_{avg}. (e) p_{var}. (f) p_{skew}.

(g) e. (h) g_{27}. (i) C.

Figure 3.12: Averaged system with Gap27 variables h, g, p, p_{avg}, p_{var}, p_{skew}, e, g_{27} and C over t for variations to hemichannel-Gap27 association/dissociation parameter ratio $\widehat{k}_{G27}/\widehat{k}_{-G27}$, $\widehat{k}_{G27}/\widehat{k}_{-G27} = 0.1$ (blue), $\widehat{k}_{G27}/\widehat{k}_{-G27} = 1$ (red) and $\widehat{k}_{G27}/\widehat{k}_{-G27} = 10$ (yellow). $g_{27}(0)$ is fixed. Transient behaviour over t is affected for Cx43-based species (a)-(g), equilibria for Gap27-based species (h) and (i) are affected. Initial conditions: $h(0) = g(0) = e(0) = p_{var}(0) = C(0) = 0$, $p_{avg}(0) = 2 + 1 \times 10^{-10}$, $p(0) = 1 \times 10^{-10}$, $p_{skew}(0) = 1 \times 10^{5}$, $g_{27}(0) = 100$. Parameters: $\widehat{k}_1 = \widehat{k}_{-1} = \widehat{k}_2 = \widehat{k}_u = \widehat{k}_r = \widehat{k}_d = 1$. Time: 500 nondimensional time steps.

3.4 Discussion

Connexins, though diminutive, are of crucial importance to normal physiological function. Their cycling generates and delivers the intercellular communication channels they compose, hemichannels and gap junctions, both of which are critical in enabling both direct and indirect cell-cell communication and coordination within a cell population. Connexin 43 (Cx43) is the most ubiquitous connexin in the human body, and dysfunction of its cycling or channel functions is implicated in many different

pathologies, including the impaired healing characteristic of chronic wounds. Connexin mimetic peptides (CMPs), such as the extracellularly binding Gap27, have been used extensively in the experimental literature to study channel functions, shown to block gap junction based intercellular communication and disrupt hemichannel function. The efficacy with which CMPs have shown to influence channel functions has led to experimental exploration for potential therapeutic applicability. One particular CMP , αCT-1, has even been approved for Phase III clinical trials for the treatment of diabetic foot ulcers [152].

Gap junction channel functions, conductance and flux properties in particular, have been considered extensively in the modelling literature and is still frequently explored. Connexin cycling dynamics underpinning channel functions appears however, to have been comparatively overlooked by modellers. The physiological significance and ubiquity of Cx43 alone makes greater understanding of cycling dynamics, and particularly its influence on gap junction and plaque formation and degradation, deeply valuable and carries potential implications to a range of pathophysiologies in which Cx43 dysfunction is thought to play a key role, beyond cutaneous wound healing. Exploration of the dynamical modulation of Cx43 cycling with Gap27 has immediate applicability to experimental wound healing research, where Gap27 is proposed as a potential therapeutic agent. Greater understanding of the dynamics of this interaction can help biologists to further characterise the efficacy of Gap27, and could, downstream, help experimentalists design experiments for potential dosing regimes.

Thus, we proposed a new mathematical model for Cx43 cycling dynamics with additional Gap27 binding kinetics. The aim being to explore the dynamical behaviour of the cycling system and its modulation by an extracellularly binding CMP, in this case

Gap27.

To derive the model, we first formulated a reaction scheme, guided by the theoretical and experimental biological literature, for hemichannel, gap junction, plaque, annular gap junction, Gap27 peptide and hemichannel-Gap27 complex species. We used the reaction scheme to derive a full ODE system for Cx43 cycling with Gap27 binding assuming mass action kinetics. We then derived moment ODEs for the large sub-system of plaque states, reducing the full plaque state distribution $p_i(t)$ to three ODEs defining its zeroeth, first and second order moments, closing the system by approximation of the third order moment. We then explored the dynamics of the cycling model both without and with Gap27.

Through our numerical analysis with MATLAB and MATCONT, we found the system to exhibit overall simple steady-state behaviour, whereby for a given parameter set there was only one equilibrium point which we determined was locally stable and remained so under parameter variation.

When tested without Gap27, we found initial concentrations of hemichannel, gap junction, plaque and annular gap junction variables to only transiently affect the system steady-state. We found variables most sensitive to gap junction association/dissociation ratio $\widehat{k}_1/\widehat{k}_{-1}$ at steady-state were hemichannels and gap junctions h^* and g^*, h^* decaying exponentially and g^* growing logarithmically with $\widehat{k}_1/\widehat{k}_{-1}$. Gap junction and plaque moment variables at steady-state, g^*, p^*, p^*_{avg}, p^*_{var} and p^*_{skew}, were most sensitive to plaque formation rate $\widehat{k}_2$, g^*, p^* and p^*_{skew} decaying exponentially, p^*_{avg} and p^*_{var} growing logarithmically with $\widehat{k}_2$. Plaque moment variables at steady-state were also sensitive to plaque internalisation rate $\widehat{k}_u$, p^*, p^*_{avg} and p^*_{var} decaying exponentially, p^*_{skew} growing logarithmically with $\widehat{k}_u$.

We found the model was able to qualitatively reproduce gap junction plaque dynamics reported experimentally, the steady-state preservation of a small concentration of large plaques. This was achieved by sweeping through model parameters to search for regions that could produce small p^* with large p^*_{avg} and p^*_{var}. We present output from a sample parameter set in which $\widehat{k}_1/\widehat{k}_{-1}$ and $\widehat{k}_2$ were both large and $\widehat{k}_u$ small.

When tested with Gap27, we found the initial concentration of Gap27, $g_{27}(0)$, affected only the transient behaviour of hemichannels, gap junctions, plaques and annular gap junctions and steady-state of Gap27 and the hemichannel-peptide complex (depleting and growing with increased $g_{27}(0)$, respectively) over t. Both effects were found to be concentration dependent. We also found hemichannel-peptide association/dissociation ratio $\widehat{k}_{G27}/\widehat{k}_{-G27}$ reproduced this pattern, affecting transient behaviour of hemichannels, gap junctions, plaques and annular gap junctions and steady-state of Gap27 and the hemichannel-peptide complex, the effect amplified with increasing ratio $\widehat{k}_{G27}/\widehat{k}_{-G27}$, the transient behaviour sigmoidal, approaching a step-function limit and Gap27 zero.

Though model results are theoretical, the dynamically modulating effect of Gap27 on model cycling behaviour is qualitatively comparable to what is typically reported experimentally. The model suggests Gap27 has only a transient effect on hemichannel, gap junction, plaque and annular gap junction species. A study by Martin, Wall and Griffith reported that dye transfer (indicating the presence of gap junction intercellular communication, GJIC) between co-cultured rat aortic endothelial and rat aortic smooth muscle cells could be drastically reduced when incubated with Gap27 (at $600n$M concentration) for 5 hours, but that washout of the peptide could recover control levels of dye transfer within an hour [157]. A study by Wright et al. also suggests Gap27 acts transiently on GJIC within a migrating population, the peptide

reapplied every 12 hours (at $100n$M concentration) to maintain a therapeutic effect on migrating populations of dermal fibroblasts and epidermal keratinocytes during scrape wound closure [32]. Such studies indicate Gap27 likely invokes a transient disruption to gap junction channel and plaque function.

The model also indicates the transient effect that Gap27 has on hemichannel, gap junction, plaque and annular gap junction species is concentration-dependent. The aforementioned study by Wright et al. showed dye transfer in clusters of both dermal fibroblasts and Cx43-transfected HeLa cells could be significantly reduced by treatment with Gap27 over 90 minutes in a dose-dependent manner (most significantly reduced for fibroblasts at concentrations of $100n$M and $50n$M for the HeLa cells) [32]. Given the primary mode of interaction for Gap27 is thought to occur via unpaired hemichannels, the implication is that Gap27 prevents some proportion of gap junction channels from either forming or functioning in the typical manner, this effect amplified when Gap27 is increased in concentration.

Martin, Wall and Griffith also studied the influence of connexin mimetic peptides, including Gap27, on plaque integrity and formation dynamics using staining techniques, finding no difference in treated compared to control cells [157]. This finding may require us to reinterpret the model plaque variables as describing the 'functional' plaque concentration rather than 'total' plaque concentration in the two-cell system.

Chapter 4

A mathematical model for connexin 43 based cell-cell interaction influenced cell migration and its dynamical modulation by connexin mimetic peptide Gap27 during 2-d scrape wound closure

4.1 Introduction

4.1.1 Connexins and cutaneous wound repair

Human skin has approximately ten different connexins expressed differentially through its strata, typically varying across different regions of the body [21, 158]. Connexin 43 (Cx43) is the most ubiquitous connexin in human skin and typically the predominanting connexin in the epidermis, with high expression amongst suprabasal keratinocytes but with lower expression in basal layers. Cx43 is also expressed in dermal fibroblasts [21, 158].

Connexin expression across the strata is regulated dynamically during wound repair.

Healthy wound repair typically requires specific and highly coordinated changes to connexin expression through cell layers within, proximal to and surrounding the wounded region. Upon wounding to the epidermis and dermis, Cx43 in epidermal keratinocytes and dermal fibroblasts at the wound edge is normally downregulated within the first twenty-four hours of injury (the first changes typically observed within a couple of hours), whilst in the same region Cx26 and Cx30 are upregulated [19, 23, 24, 25, 136]. Twenty-four to forty-eight hours post-injury Cx43 expression is typically reported at very low levels around the wound edge, recovering to normal levels a few days post-injury [19]. These events coincide with wound edge keratinocytes and fibroblasts migrating into the wounded region, subsequent degradation of fibrin and deposition of new granulation tissue [19, 21]. Keratinocytes in basal regions which are adjacent to the wound edge region upregulate Cx43 post-injury and experience localised post-translational modifications (PTMs) associated with modulation of Cx43 channel conductance levels and therefore likely, communicative properties [20]. Connexins Cx26 and Cx30 are functionally compatible, being able to form functional heterotypic hemichannels and gap junctions with each other, but not with Cx43, having different coupling properties (Cx26 and Cx30 also have different dye transfer properties to Cx43 [19]). These events, taken in addition with other associated connexin PTMs [20], is thought to induce a dynamic compartmentalisation across the strata in response to injury, which aid in coordinating appropriate cell responses to the appropriate regions around and within the wounded region itself [19, 20].

Abnormal connexin expression during wound repair has been associated with poor healing and disruption to cell processes necessary for effective healing. Brandner et al. reported the presence of Cx43 at epidermal wound edges in chronic non-healing wounds

of different types [22]. Sutcliffe et al. found elevated wound edge epidermal Cx43 (in addition to normally upregulated wound edge connexins Cx30 and Cx26) and dermal Cx43 to be a characteristic shared among three different types of chronic wound (venous leg, diabetic foot and pressure ulcers) [25]. In a separate study, Cx43 was found to be upregulated approximately 10-fold above normal levels in fibroblasts from wound edge regions of human diabetic foot ulcers [27]. Elevated wound edge Cx43 appears to be a common feature among chronic non-healing wounds of different pathologies and is proposed to interrupt the finely balanced dynamic coordination of cellular behaviours post-injury, ultimately contributing to preservation of the pathological state [159].

Studies involving Cx43 deficiency and application of agents suppressing Cx43 expression or channel function typically report improvements in wound healing, including increased closure rates and reduced inflammatory response. Kretz et al. reported Cx43-deficient mice heal much more rapidly (epidermal wound closure occuring approximately twenty-four hours earlier) than mice without the deficiency and exhibit significantly reduced dye transfer (an indication of reduced gap junctional activity) between keratinocytes [29]. Similar results were reported by Qiu et al. using Cx43 antisense oligonucleotides to induce transient knockdown of Cx43 gene expression. Cx43 knockdown significantly increased closure rates of wounds in neonatal and adult mice, with reduced inflammation [28]. Connexin mimetic peptides (CMPs) such as Gap27 have been shown to accelerate healing in a variety of different experimental settings (2-d and 3-d *in vitro* models, and *ex vivo* human tissue) [160]. Gap27 has also been shown to increase keratinocyte and fibroblast migration rates *in vitro* and reduce dye transfer in *ex vivo* tissues [160]. Such studies highlight the importance of connexin response post-injury and particularly the influence of Cx43 levels in either enabling or

disrupting critical early stages in wound healing.

A central process to wound repair is the migration of keratinocytes and fibroblasts into the wounded region post-injury, and these events appear to be particularly sensitive to changes in connexin expression and connexin functionality. Goliger and Paul showed migrating wound edge rat keratinocytes to exhibit significantly reduced Cx43 levels early on in the healing process, proposing this to be influential in the keratinocytes switch to a migratory phenotype, critical in the early stages of healing [23].

Inversely, a study by Wang et al. showed upregulation of Cx43 within twenty-four hours of injury correlated with aggregation of keratinocytes at the edges of epidermal wounds in diabetic rats [26]. Mendoza-Naranjo et al. reported similar cellular behaviour in cultured fibroblasts, showing an upregulation of Cx43 can inhibit migration *in vitro* [27].

Wright et al. demonstrated that *in vitro* migration rates in both human keratinocytes and fibroblasts could be increased using CMPs to block gap junction channel function, inducing a reduction in connexin mediated cell-cell communication [32]; these results further supported by additional *in vitro* and *ex vivo* studies published by Pollok et al. [160].

Clearly, connexins play an influential role in determining the outcome of migration events within and around both the epidermis and dermis post-injury. Migration of keratinocytes and fibroblasts appear particularly susceptible to disruption when Cx43 is expressed at elevated levels. Exactly how Cx43 acts to affect migration is not yet well established, though it is typically proposed there may be different mechanisms of action responsible, involving: alteration to direct intercellular communication via gap junctions (subsequently affecting cell-cell signalling and coordination events between

cells), gap junction-independent hemichannel activity and adhesive/structural properties of individual connexin proteins and those associated with gap junction plaques [161].

In addition to channel functions, connexins possess mechanical properties which may influence many functions important for cell motility. Some of these functions include supporting adhesive cell-cell and cell-matrix contacts, and both direct and indirect influence of cytoskeletal organisation [162]. The intracellular carboxyl tail of Cx43 has been shown to interact with numerous cytoskeletal and scaffolding proteins, including F-actin and tubulin, via various binding domains [161]. Cx43-tubulin binding is thought able to secure microtubules to the junctional nexus (region of cell-cell contact at the plasma membrane) and appears to be critical in maintaining directionality during migration [21]. This intracellular region is also central for interactions with many signalling molecules and subject to PTMs, and is hypothesised may be involved in the induction of intracellular signalling cascades indirectly affecting cell motility mechanisms [161, 163]. Connexin also appears to both affect and become affected by cell-matrix interactions, epithelial Cx43 expression becoming significantly variable when cultured upon different ECM component proteins and gap junction activity influencing organisation of ECM fibrils. It is thought Cx43 may be able to interact indirectly with cytoskeletal-ECM connecting integrin proteins [21].

Gap junction plaques are typically associated with adherens junctions, formed mostly of adhesive cadherin proteins, both located proximately or even embedded together (as in cardiomyocytes) in the junctional nexus [162, 164]. Gap junctions and cadherin proteins have been shown to support each other's functions, with suppression of Cx43 shown to disrupt the formation of adherens junctions and, similarly alteration to E-

cadherin and N-cadherin expression shown to perturb gap junction function [162, 164]. The interplay between these proteins at the junctional nexus is considered critical to support functional cell coupling.

Clearly, connexins play an integral role in cutaneous wound repair, their spatio-temporal expression highly synchronised and intricately linked to many cellular events crucial for repair. Connexins, and specifically Cx43, are particularly influential in the regulation of cell motility and migration events, likely through multiple modes of action. Collective and individual migration events are most likely to be regulated through a combination of channel dependent mechanisms i.e. gap junction and hemichannel activity, and extracellular guidance via adhesive properties of plaques and integrin-mediated interactions with ECM, with smaller-scale motility events likely affected by connexin interactions with the cytoskeleton. Many of the functions of connexins discussed have however only recently emerged and the corresponding systems responsible for their modes of action are not yet well understood.

4.1.2 Modelling studies

Mathematical and computational modelling studies relating to the influence of connexins in cutaneous wound repair in general appear to be quite uncommon and typically restricted only to a distinct couple of groups of authors.

A recent interdisciplinary study by Montgomery et al. investigated how connexin mimetic peptide αCT1 affected scar tissue formation by both histological analysis of Phase I clinical trials and animal wound models and, subsequently, *in vitro* and computational scrape wound models to further probe how αCT1 influenced fibroblast migration during healing. The model (an agent-based approach developed by Richardson and Holmes [165]) could reasonably reproduce *in vitro* migration trajectory and

directionality behaviour if the cell model's sensitivity to fibril direction was blunted, producing more directionally random migration and less organised scar tissue, implying the peptide by some mechanism impairs a cell's ability to respond to physical guidance cues provided by ECM fibrils [79].

Other significant attempts to mathematically model connexin influence in wound healing events can be found within a single study group report published by Roberts et al. [76]. The report proposes four different models of wound repair which focus on Cx43 influence on migration, proliferation and cell invasion of some 'wounded region' modelled on either an *in vitro* scrape wound assay or an idealised *in vivo* epidermal/dermal wound environment.

Al-Husari et al. used a 2-d cellular Potts approach to model the migration and proliferation of a cell population into a wound *in vivo*. The model had three main components: a cell volume constraint, cell-cell adhesion which accounted for adhesive pull between cells, and chemotaxis. A chemoattractant was assumed to be produced from within the wounded region, modelled by coupling a reaction-diffusion equation to the Potts model, to bias cell migration towards the centre of the wound. Cells were also assigned with free and bound connexin concentrations, and the cell behaviour favoured depended on chemoattractant concentration and free-to-bound connexin ratio. Cells had higher probability of proliferating when local chemoattractant concentration was low (thus further from wound) and connexin ratio high, whilst likelier to migrate when local chemoattractant concentration was high (i.e. closer to the wound) and connexin ratio high. This cellular Potts model is capable of describing interactions between cells within a small population, incorporating connexin and chemoattractant dependent switches in cell behaviour (between migration and proliferation), which is a key

characteristic of cells proximal to a wound in both *in vitro* models and *in vivo*. The model enabled simulation of associated dynamic changes to cell morphologies under these conditions and show the evolution of the cell population across the wounded region [76].

Caffrey focused on fibroblast migration within wound edges using a cellular automata approach. The model domain was restricted to the region within the wound, the lattice defined thirty columns wide within a wound 600μm wide accommodating $20 \times 20\mu\text{m}^2$ grid cells, with no defined upper bound on rows. Migration across the lattice was determined by a directionally biased stochastic process, to ensure the general direction of movement was into the wound. A cell source was defined at domain boundaries (wound edges) and, since the domain is restricted to the wound, no proliferation was permitted in the model. Grid cells were assigned an associated Cx43 concentration modelled dynamically with additional ODEs. Moderate Cx43 concentration prompted grouping between lattice neighbours and high concentration induced extensive cell aggregation at wound edges. The introduction of a connexin-mimetic peptide (CMP), modelled with additional an reaction-diffusion equation, reduced the binding effects of connexin, and aided in cell dispersal and wound closure. This approach was able to recapitulate some defining features of chronic wound pathology and CMP application, including cell aggregation at wound edges, reduced migration with high Cx43 concentration, and increased migration and wound closure rates with introduction of a CMP [76].

Ward et al. used a continuum (PDE) approach to model the effect of Cx43 concentration on cell population behaviour within a 1-d model of an *in vitro* scrape wound assay. The model had four main components: surface density of cells, surface Cx43 concentration, signalling molecule concentration and CMP concentration. The (unspecified)

signalling molecule reduced Cx43 concentration within the cell population, included to model the transient downregulation of Cx43 at wound edges. The production of this molecule was dependent on local cell density, low density inducing production and growth in concentration of the molecule. Cell behaviour stratified dependent primarily on local cell density and Cx43 concentration. If cell density and Cx43 concentration were low, migration was favoured and signalling molecule production was increased, further enhancing the stimulatory effect. If cell density and Cx43 concentration were high, cell aggregation was favoured and signalling molecule concentration decayed. At intermediate levels of cell density and Cx43, proliferation was favoured with some signalling molecule production maintained, prompting some migration behind the leading edge. The introduction of a CMP was modelled to induce a global reduction in Cx43 concentration across the cell population, dependent on a diffusion rate. This approach was able to qualitatively reproduce some of the cellular behaviours reported in experimental scrape wound assays cited in the study [32]. This included a CMP-prompted reduction in global Cx43 concentration followed by a significant population advance into the wounded region [76].

McDougall and Watson propose a discrete-point migration model based on previous work published by Dallon, Sherratt and Maini [64, 78]. Their work discards any chemotaxis term and, for preliminary simulations, collagen terms, modelling migrating cells which interact via a 'connexin pull' within a 2-d domain describing a scrape wound. Cells migrate in the model only according to a time lag velocity and an adhesive pull from neighbouring cells such that cells move along a linear trajectory until interrupted by interaction with another cell. The 'connexin pull' models Cx43-based cell-cell adhesion and is proximity dependent as a net effect of an interacting neighbourhood, the

closest neighbour having greatest influence on velocity. The full model incorporates the effect of ECM fibrils described by Dallon, Sherratt and Maini, to investigate migration on ECM-coated substrata. Preliminary simulations of the model without ECM components produced clustering patterns in migrating cells due to the adhesive 'connexin pull'.

4.1.3 Motivations and contributions

Connexins are known to possess an influential role in cutaneous wound repair. The spatio-temporal regulation of Cx43 in particular appears critical to early cell response post-injury, shown in many experimental studies to heavily influence keratinocyte and fibroblast migration. Elevated wound edge Cx43 post-injury is strongly associated with perturbed healing. Restoration of the typical post-injury reduction in Cx43 with Cx43-targeted agents such as connexin mimetic peptide (CMP) Gap27, has shown to be effective in rescuing healing in experimental models. It remains unclear exactly how this pattern promotes migration and effective healing. It is possible the reduction in functional cell hemichannel and gap junction concentration may limit cell-cell coupling and coordination locally within a cell population, encouraging cells to adopt more migratory phenotypes.

Mathematical and computational models for the role of connexins and connexin-based species (such as gap junctions) in healing appear to be quite scarce. The most detailed modelling attempts appears in an unpublished study group report, suggesting this area of research is inordinately under-explored considering the prominent role of connexin regulation in healing outcomes. Much of the mathematical modelling literature relating to wound healing tend focus on other well-known mediators of healing such as growth factors. The relatively recent emergence of the multitude of functions connexins maintain in wound repair, and associated mechanisms of action not yet being well defined, may contribute to the current deficiency of modelling work related to this area.

We aim to develop a mathematical model to describe Cx43-based gap junction influenced cell-cell interactions within a migrating cell population, with the intention to explore how these interactions affect population invasion of a wound and how the in-

troduction of a Cx43-binding CMP, e.g. Gap27, modulates this behaviour.

We adopt an approach similar to that used by McDougall and Watson [76], based on a discrete-point cell migration model which we extend with additional spatial components to enable cells to interact in 2-d. We assume a similar cell-cell adhesive pull occurs when cells interact, however we scale this pull using solution output for the Cx43 cycling model presented in *Chapter* 3, which we also use to introduce Gap27. We also introduce an OU process to model 'intrinsic' migration for a cell and assume cell velocity is determined by a biased OU process, rather than assume migration velocity follows a simple linear trajectory until disrupted by cell-cell interaction.

To summarise, the presented work contributes the following:

(i) **Derive a mathematical model for Cx43-based cell-cell interaction influenced cell migration.** Using a mass action model describing Cx43 cycling dynamics and an individual point-cell migration model, we derive a coupled model for individual cell migration influenced by within population cell-cell interactions dependent on Cx43 cycling dynamics. Discrete-point cells are assigned spatial components and interact according to proximity to neighbouring cells and total gap junction plaque concentration p. See *Methods* 4.2.1.

(ii) **Develop a computational framework for a 2-d scrape wound (within which to test the migration model).** To approximate the general experimental set-up of an *in vitro* scrape wound assay, we initiate cell positions on a continuous 2-d spatial domain to either side of a region unpopulated by cells. We use an experimental data sheet for human dermal fibroblasts [166] to approximate experimental cell density and then use a circle packing algorithm to distribute cells within the population without overlap. See *Methods* 4.2.2.

(iii) **Explore how plaque concentration and Gap27 variables, p and g_{27}, affect migration and closure of the 2-d scrape wound model.** We find that when plaque concentration at steady-state, p^*, is large, cell-cell interactions are persistent and cells begin to cluster, stunting migration and preserving the scrape wound over time. By contrast, the introduction of Gap27 induces discernible changes to interaction and migration behaviour, reducing cell clustering and allowing the scrape wound to close over time, in a Gap27-concentration dependent manner. See *Results* 4.3.2-4.3.3.

4.2 Methods

4.2.1 Model

The primary focus for our model is the physical influence of gap junction plaques (both structural and functional) on cell-cell interactions between migrating cells within a population, both in the absence and presence of Gap27. We aim to explore how the addition of Gap27 affects cell-cell interactions and subsequent scrape wound closure within a model population. To create the model, we couple two models developed in earlier chapters: a connexin cycling model (see *Chapter* 3) and an OU model adopted for individual migration trajectories (see *Chapter* 2). We use this approach to introduce connexin dynamics into a migration framework for individual cells. We then generate a model population distributed to each side of an unpopulated 'scrape wound' and assign the developed migration model to each cell in the population. We then use simulations to determine how the introduction of Gap27 influences the subsequent population invasion and 'closure' of this computational scrape wound model.

We base the model on the general assumption that individual cells can be represented as

discrete points and are able to migrate within a 2-dimensional (2-d) space. We also assume migrations occur simultaneously across some homogeneous cell population, and that any migrating cell is able to interact with any other migrating cell within this population. Connexin dynamics are assumed to have an important influence on the outcome of cell-cell interactions within this population. In our model, we determine that total plaque concentration has a pertinent influence on the strength of cell-cell interactions during migration. To couple the models we use a variable from the connexin cycling model which defines total plaque concentration for two interacting cells, $p(\tau)$. We introduce $p(\tau)$ into the migration model through the construction of a new directional bias term, which determines the cumulative effect interacting cells k have on the migration velocity of cell i.

Cell-cell interactions

To enable cells to interact spatially, we extend our discrete point representation of individual cells by introducing additional spatial components into the model. We now define each discrete point as the centroid of a cell's 2-d area and attach two kernels to each centroid, each radial from the centroid and with distinct spatial representations. The smaller kernel, defined by radius R_M, is chosen to represent a centroid-centroid distance whereby cell membranes contact, below which we assume cells do not interact via hemichannels (see Figure 4.1). The larger kernel, defined by radius R_I, is chosen to define a boundary which establishes an 'interaction space' for hemichannels, defined by $R_I - R_M$, within which they are able to interdigitate and establish gap junctions. We consider only direct interactions between hemichannels at the cell membrane and currently discard any indirect interactions through extracellular signalling. We stipulate that $R_I/R_M > 1$ and, since we consider only the effect of direct interactions between

hemichannels, assume R_I/R_M is never large and typically close to 1.

To model cell-cell interactions, we use R_M and R_I as thresholds to define different interaction behaviours based on centroid-centroid distance between cells within the population. We determine that if a centroid-centroid distance is greater than R_I, as in Figure 4.1 (a), cells are separated by a distance too significant to be able to directly interact via hemichannels, so have no effect on each other and continue to migrate as unaffected by cell-cell interaction. If however, a centroid-centroid distance is less than or equal to R_I but greater than R_M, as in Figure 4.1 (b), cells are considered close enough to be able to establish hemichannel-hemichannel interactions and exert a mutual interaction pull on each other, thus introducing a cell-cell instigated directional bias to respective migrations. The cell-cell interaction is influenced by total plaque concentration $p(\tau)$, where τ is the time unit chosen for connexin cycling. If however, centroid-centroid distance is less than or equal to R_M, as in Figure 4.1 (c), we determine for simplicity there is no effect and cells migrate as unaffected by cell-cell interaction. To enable this we permit cell-cell overlap at $R_M/2$ in 2-d during model simulations (assuming actual cell membranes are physically deformable).

In the model equation for cell-cell interactions, Eq. (4.1), $\boldsymbol{c}^k$ is defined such that the influence of an interacting cell k on the migration velocity of cell i is dependent on centroid-centroid distance between cells i and k, $\parallel \boldsymbol{f}^i(t) - \boldsymbol{f}^k(t) \parallel$, where $\boldsymbol{f}^i(t)$ is defined as the 2-d centroid position for cell i at time t. We see in Eq. (4.1), this contribution is either zero, if $\parallel \boldsymbol{f}^i(t) - \boldsymbol{f}^k(t) \parallel > R_I$ or $\parallel \boldsymbol{f}^i(t) - \boldsymbol{f}^k(t) \parallel \leq R_M$, otherwise cell k exerts $p(\tau)$ influenced unit pull on cell i along the chord connecting centroids i

and k, determined by a coupling function $\boldsymbol{F}(p)$.

$$\boldsymbol{c}^k = \begin{cases} \mathbf{0}, & \| \boldsymbol{f}^i(t) - \boldsymbol{f}^k(t) \| > R_I. \\ \boldsymbol{F}(p), & R_M < \| \boldsymbol{f}^i(t) - \boldsymbol{f}^k(t) \| \leq R_I. \\ \mathbf{0}, & \| \boldsymbol{f}^i(t) - \boldsymbol{f}^k(t) \| \leq R_M. \end{cases} \tag{4.1}$$

where $\boldsymbol{F}(p) = \gamma_k p(\tau) \dfrac{\boldsymbol{f}^i(t) - \boldsymbol{f}^k(t)}{\| \boldsymbol{f}^i(t) - \boldsymbol{f}^k(t) \|}$, with $\gamma_k \in \mathbb{R}_+$ a scaling factor for each cell k. The coupling function $\boldsymbol{F}(p)$ is based on $p(\tau)$ under the assumption that a dependency exists between total plaque concentration and the connectedness of interacting cells. Under this assumption, if plaque concentration is large, cells are assumed strongly connected and engaged in extensive direct cell-cell communication (e.g. ion transfer). Conversely, if plaque concentration is small, cells are assumed weakly connected with direct cell-cell communication limited. To keep the model simple, we do not distinguish between plaques composed of large or small concentrations of gap junctions in the coupling and choose $\boldsymbol{F}(p)$ only to depend linearly on $p(\tau)$.

Cell-cell interactions are time-dependent, thus we see cells that interact over longer time intervals approach a steady-state total plaque concentration p^*, whereas brief interactions maintain only some transient total plaque concentration. Consequently, cells that interact uninterrupted over longer time intervals form larger plaque concentrations. We implement this into the model by tracking numerical time increments a neighbouring centroid k is within the interaction 'halo' of i (satisfying $R_M < \| \boldsymbol{f}^i(t) - \boldsymbol{f}^k(t) \| \leq R_I$), and use this to determine τ and subsequently $p(\tau)$. We determine τ through a conversion, $\Delta t / \Delta \tau \geq 1$, since we assume connexin cycling can be more rapid than migrating cells. We depict the influence of both cell-cell interactions and numerical time increments on $p(\tau)$ conceptually in Figure 4.2.

We calculate $p(\tau)$ from the Cx43 cycling model presented in *Chapter* 3, thus the magnitude of p^* is determined by key Cx43 cycling model parameters $\widehat{k}_1/\widehat{k}_{-1}$ (gap junction formation and dissociation ratio), $\widehat{k}_2$ (gap junction / plaque formation rate) and $\widehat{k}_u$ (internalisation rate). For example, if $\widehat{k}_1/\widehat{k}_{-1}$ is large and $\widehat{k}_u$ is small, producing abundant gap junctions for accrual and enabling growth and preservation of a large plaque concentration at the membrane, p^* is large.

To further simplify coupling, we generate only a single $p(\tau)$ for a given simulation, assumed an average $p(\tau)$ for the cell population, so that interactions are homogeneous across the population. Thus, for a given simulation (if γ_k is held constant), $\boldsymbol{F}(p)$ varies only by τ which gives a distinct $p(\tau)$ for every cell-cell interaction in the population over time.

Cells in the surrounding population, $k = 1, ..., N$, $k \neq i$, that are within the interacting neighbourhood of i (satisfying $R_M <\| \boldsymbol{f}^i(t) - \boldsymbol{f}^k(t) \|\leq R_I$) contribute towards a cumulative effect on cell i. This consists of a net pull from each cell towards their respective centroid positions, the contribution of each cell k determined by $\gamma_k p(\tau)$. The contribution for all other cells (not within the interacting neighbourhood) in the population sums by Eq. (4.1) to zero. The cumulative effect of the cell population on cell i is defined by $\boldsymbol{C}^i(p)$, Eq. (4.2).

$$\boldsymbol{C}^i(p) = \sum_{k=1,k\neq i}^{N} \boldsymbol{c}^k. \tag{4.2}$$

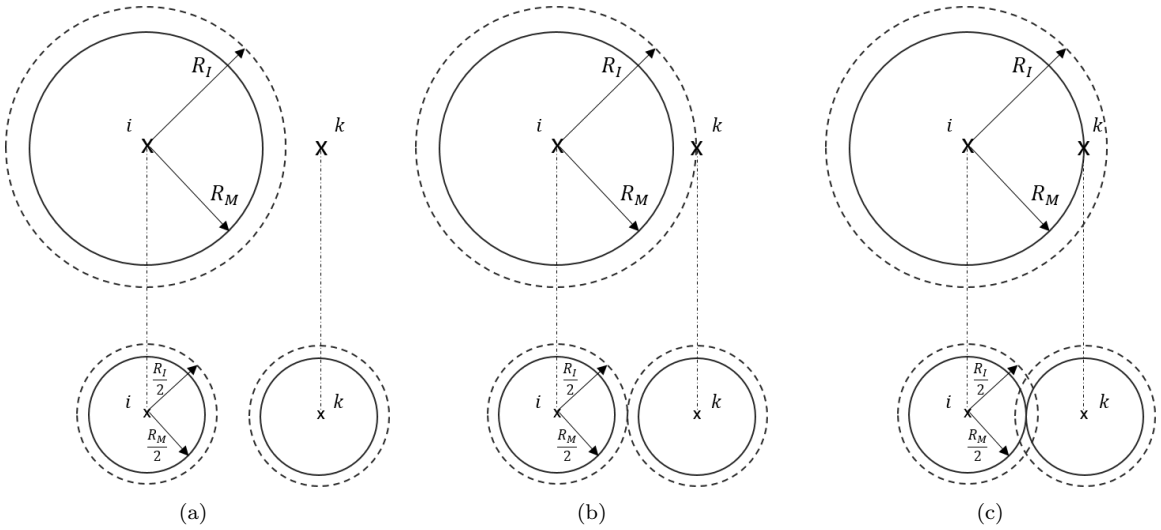

Figure 4.1: The three different cell-cell interaction scenarios considered in the model, (a), (b) and (c), between neighbouring cells i and k. The top row shows radii R_M (solid) and R_I (dashed) around cell centroid i and in relation to centroid k. The bottom row shows their respective cell-cell interpretations for i and k, where membrane radius is $R_M/2$. (a) centroid-centroid distance between i and k is greater than R_I so cells do not interact. We see cell-cell interaction boundaries for i and k do not overlap. (b) centroid-centroid distance between i and k is less than or equal to R_I but greater than R_M and so interact. We see cell-cell contact/overlap between interaction boundaries. (c) centroid-centroid distance between i and k is less than or equal to R_M and so do not interact. We see cell-cell contact/overlap at membrane boundaries, $R_M/2$, for each cell.

Cell-cell influenced migration model

To model cell migration we assume, based on preceding chapters, that the Ornstein-Uhlenbeck (OU) process is a reasonable model for 2-d *in vitro* migration trajectories. In the migration equation, Eq. (4.3), $\boldsymbol{v}^i(t)$ is defined as the 2-d velocity $\boldsymbol{v}(t)$ for cell i

$$d\boldsymbol{v}^i(t) = \Big(\boldsymbol{C}^i(p) - \beta \boldsymbol{v}^i(t)\Big)dt + \sqrt{\alpha} d\boldsymbol{W}(t), \tag{4.3}$$

with $\boldsymbol{f}^i(t)$ being the associated position at time t. $\boldsymbol{C}^i(p)$ is defined as the directional bias on $\boldsymbol{v}^i(t)$ caused by interaction with cells from a surrounding population $k = 1, ..., N$, such that $k \neq i$. The 2-d Wiener process is represented by the time-dependent variable $\boldsymbol{W}(t)$. Model parameters α and β control unbiased migration.

The resulting migration model, Eq. (4.1)-(4.3), is a 2-d cell-cell biased OU process, enabling us to describe how migration trajectories are influenced by Cx43 mediated cell-cell interactions within a population. We now implement this model numerically and

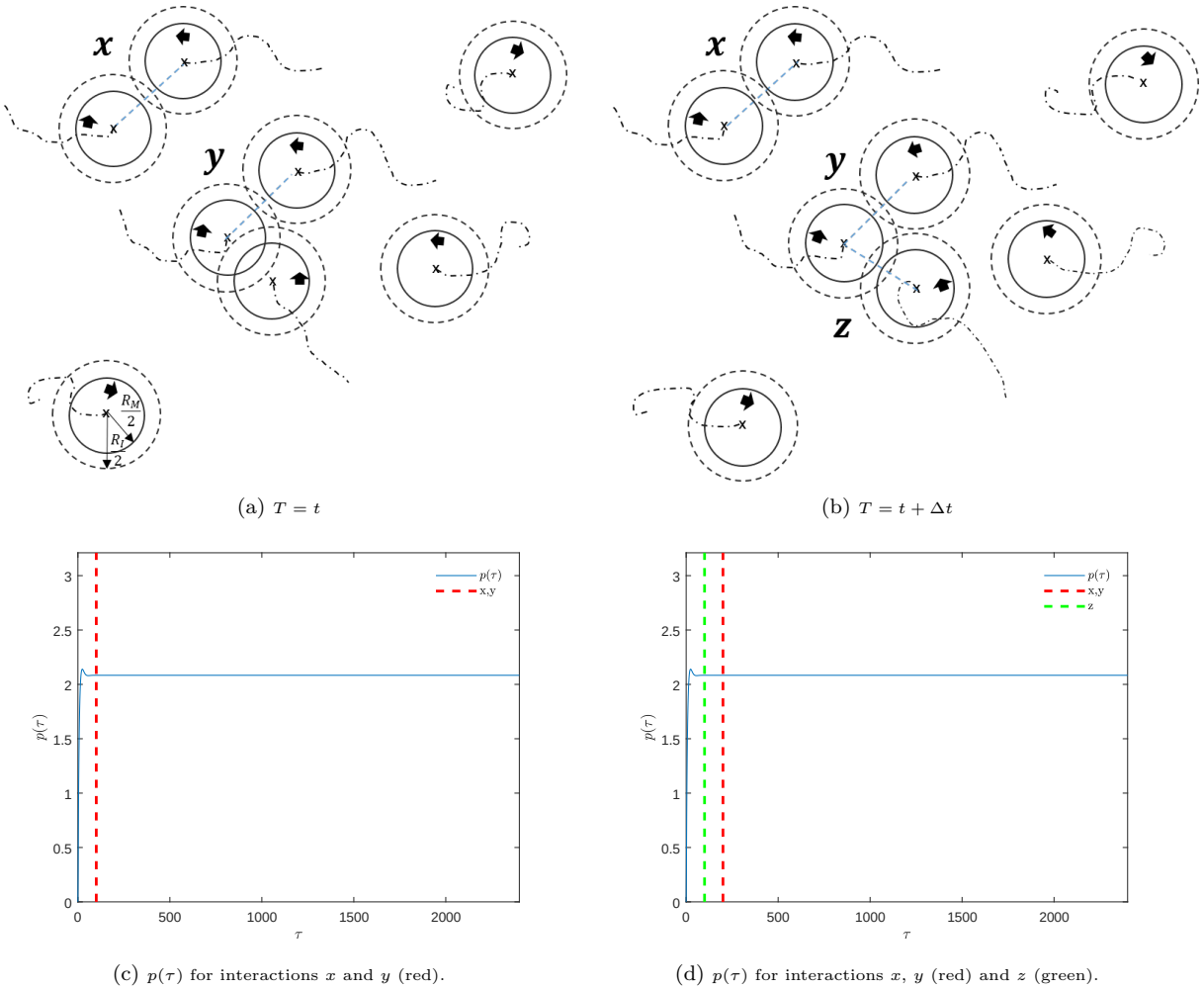

(a) $T = t$

(b) $T = t + \Delta t$

(c) $p(\tau)$ for interactions x and y (red).

(d) $p(\tau)$ for interactions x, y (red) and z (green).

Figure 4.2: Diagram to illustrate the time-dependency of $p(\tau)$ in the cell-cell influenced migration model. (a) two cell-cell interactions, x and y, occur within the migrating cell population at numerical time point $T = t$. (c) shows a corresponding $p(\tau)$ for both interactions x and y, represented by the red dashed line. (b) at time point $T = t + \Delta t$, cell-cell interactions x and y are maintained after a time interval Δt, after which another cell-cell interaction, z, occurs. (d) shows corresponding $p(\tau)$ for the interactions x and y (red dashed) and z (green dashed).

set up an *in silico* spatio-temporal framework to approximate a typical experimental set-up of an *in vitro* scrape wound assay. We then intend to use the model to investigate how Cx43 mediated cell-cell interactions affect migration and wound closure, and how the introduction of Gap27 via the coupled Cx43 cycling model modulates this spatial behaviour.

4.2.2 Numerical implementation

We implement the model using MathWorks MATLAB R2020a, and obtain solutions by numerical methods. We first solve the model for Cx43 cycling with Gap27 binding, a system of eleven coupled ODEs, using ODE solver *ode23s*, a modified Rosenbrock scheme [155]. The solution output for this system of equations across time τ includes total plaque concentration variable $p(\tau)$, which is coupled to migration model, Eq. (4.3), via the cell-cell term $\boldsymbol{C}^i(p)$. Eq. (4.3) is solved iteratively for each individual cell in the population across time t. For each cell, the influence of any interacting neighbourhood is first established using Eq. (4.1)-(4.2), we then solve Eq. (4.3) using an Euler-Maruyama scheme to attain the resultant cell velocity and position. As in earlier chapters we use a sub-increment for Euler-Maruyama increments smaller than experimental increments. The result of the simulation is an array of cell positions at every numerical increment which, across time, defines the individual migration trajectories for all cells in the population. The approach used to implement this model numerically is outlined in Figure 4.3.

Initial cell configuration

The initial configuration for a typical *in vitro* scrape wound assay consists of two cell monolayers separated by a region that is unpopulated by cells. This region may have been either physically scraped to remove cells from an original single monolayer or intentionally designated unpopulated with cell monolayers seeded either side [32]. To approximate this experimental set-up *in silico*, we define a 2-d space on which cells can interact and initiate cell positions separately either side of a centrally located unpopulated region. To approximate monolayers with an individual cell model, we use

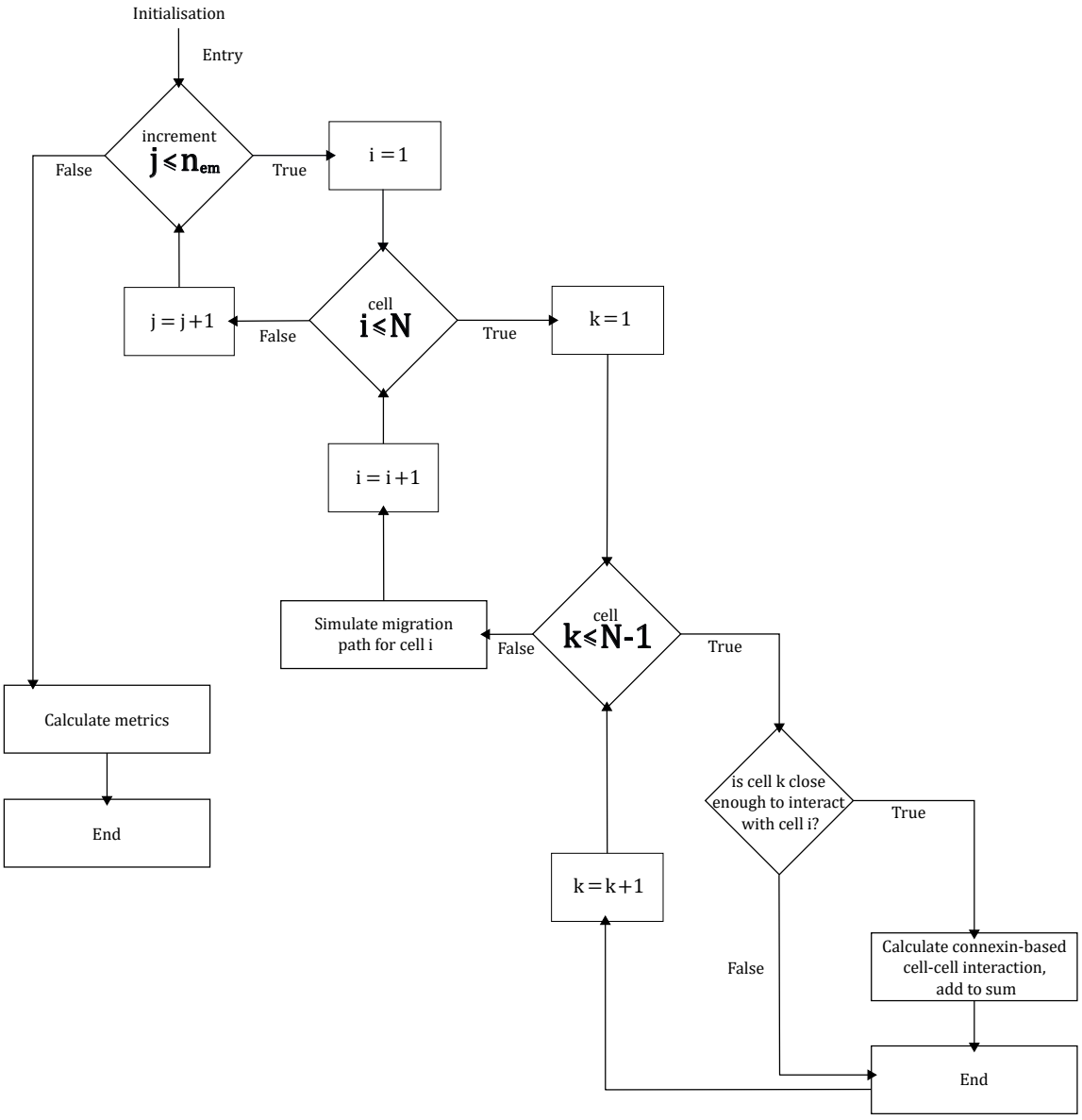

Figure 4.3: Flow chart to illustrate the algorithmic approach to numerical implementation of the model outlined in Section 4.2.2. The general approach taken is to, at each numerical time increment j in total increments n_{em}, for each cell i of N, iterate through the surrounding population of cells k and calculate the distance between each individual pair of cells. If close enough to interact, satisfying the condition $R_M <\| \boldsymbol{f}^i(t) - \boldsymbol{f}^k(t) \| \leq R_I$, we calculate a connexin-based cell-cell interaction between the cells and add to a cumulative sum of interactions contributing to the calculation of velocity for cell i. If cells are not close enough to interact, we skip to the next cell in the population and repeat the calculation. This allows us to establish an interacting neighbourhood of cells around cell i. Once we have iterated through all cells $N-1$ that could interact with cell i, we select the next cell and repeat the calculations, repeating through all cells N in the population at increment j. We then repeat through all increments n_{em} through the simulation. Once complete, we calculate simulation metrics (e.g. wound width, mean-squared displacement) for the cell population. With the initial conditions outlined in Section 4.3.1, this algorithm would typically take 2-3 hours to run and then terminate.

a basic circle packing algorithm to pack cells both densely but randomly within these two populations without 2-d overlapping between membranes.

The general approach we use for the circle packing algorithm is to populate each side of the unpopulated region first through pseudo-random position generation and then iterative trial and regeneration through all positions, conditional on proximity of current to prior positions. We first generate pseudo-random positions to produce temporarily unpacked populations to each side of the unpopulated region, see Figure 4.5 (a), using MATLAB's pseudo-random number generator. We then iterate through each population of positions separately and for each calculate all distances between current and prior positions. If all distances are greater than R_M, we move to the next position, if not we generate a new pseudo-random position to 'trial'. We then once again test whether all distances between the new trial position and prior positions are greater than R_M, if not we iteratively test, regenerate and test new trial positions until all distances are greater than R_M. We then store the trial position as an updated position and move to the next cell position and repeat until no cells overlap at $R_M/2$ as in Figure 4.5 (b). To avoid unnecessarily considering overlap between cells separated by the large unpopulated region, the algorithm is executed for each unpacked population separately. Both populations once packed are used as the initial cell configuration for simulations.

This algorithm is relatively inefficient for packing populations that are particularly dense, due to the iterative pseudo-random regeneration of positions. This is, for our purposes, permissible since we do not use the algorithm frequently and keep the initial cell configuration constant across simulations. The algorithm has the additional advantages of being simple both conceptually and to program. The algorithm used to

pack cells into their initial configuration is outlined by the flow chart in Figure 4.4.

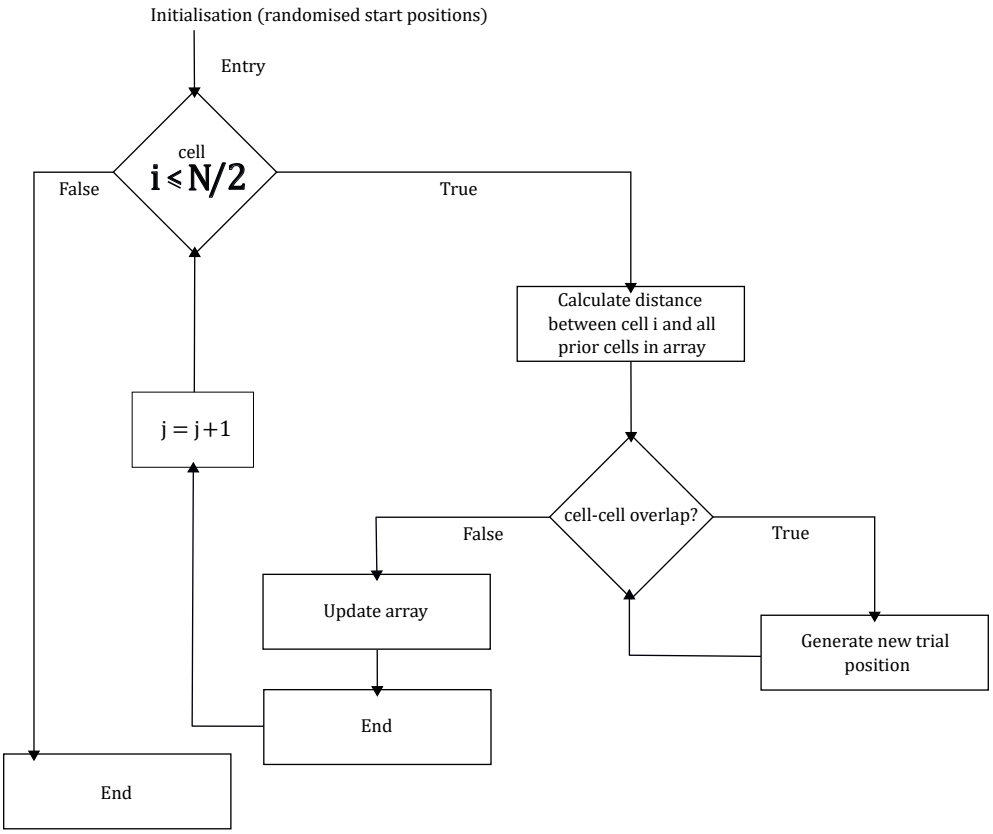

Figure 4.4: Flow chart to illustrate the cell packing algorithm outlined in Section 4.2.2. For efficiency, we split the spatial domain to either side of the 'wound' region and pack each population of $N/2$ cells separately (repeating this algorithm for two separate populations). The general approach taken is to start with randomised initial cell positions and iterate over the population, correcting cell-cell overlap using trial and randomised regeneration of cell positions.

Numerical estimation of wound width

To more clearly quantify and visualise population invasion in our *in silico* scrape wound model, we divide our 2-d domain into a coarse grained space from which we infer the average movement of the cell population and subsequently derive metrics to estimate wound location and width over time.

To create this coarse grained space we divide the 2-d domain at each increment into

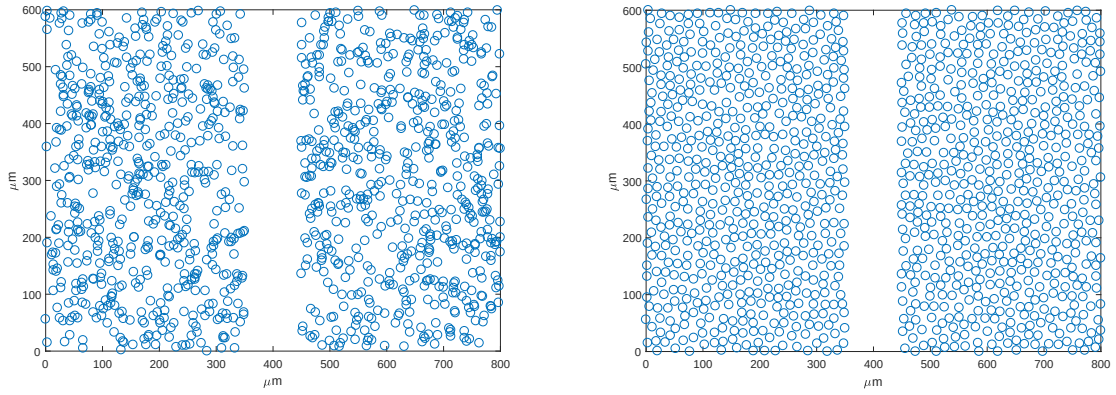

(a) Unpacked (b) Packed

Figure 4.5: Unpacked (a) and packed (b) initial cell configuration for 1200 cells, across a 2-d domain $600 \times 800\mu$m. $R_M = 15\mu$m, marker diameter $= 15\mu$m. Units assigned using data on the average diameter of human dermal fibroblasts.

a grid of 'windows' which, for simplicity, are square. The general approach we take to approximate a population density is to count cells in each window across the grid, enabling us to quantitatively capture the spatial distribution of the individual cell positions. We repeat for each increment across time, generating an array which captures how local cell densities change over the time course of the simulation.

The size of windows used within the grid i.e. coarseness, has a critical influence on the population estimation. If we choose larger window sizes, the cell population becomes an unchanging homogeneous mass, offering no insight into the invasive behaviour of the population into the wound. Conversely, smaller window sizes capture only the behaviour of individual cells which we can extract directly from the model output. We instead approximate an optimal window size for the problem which is small enough to capture the wound region within the coarse grained grid (i.e. a distinct set of windows containing no cells) but large enough to accommodate more than a couple of non-overlapping cells to estimate local cell densities. We then use this to infer the average movement of the cell population.

To estimate population fronts (i.e. wound boundaries) from the coarse grained space,

we average over the coarse grained grid in the wound plane to obtain an average cell population per square for each grid column in the wound plane. This enables us to represent the grid space in 1-d. To illustrate, the initial configuration in this 1-d array comprises two non-zero regions (populations) separated by a central region of zeroes (wound). If the wound is to close over time, this central region of zeroes gradually becomes non-zero and approaches average local densities approximately equivalent to the surrounding population.

Our method for the approximation of population fronts is to apply a threshold to classify average local densities as either 'population' or 'wound'. We do this simply by iterating through all average local densities at a given increment and storing which array indices are below a predefined threshold to classify as population. The array resulting from this iteration contains every index location classified as wound by testing against the threshold value, providing a coarse estimate of the location of the wound and therefore wound boundaries. We repeat for all increments across time.

The value chosen for this population threshold, like grain space coarseness, has a critical effect on the resulting wound estimation. Thus, we choose our population threshold value based on average local densities across the population at both the start and end of the simulation.

To further explore average trajectory behaviour of the model population we calculate mean-squared displacement (MSD) of cells over time, as in earlier chapters. For each cell over time, we calculate the squared displacement from their initial position at each increment, then average over all cells to find MSD over time for all cells in the population. With this metric we are most interested in whether strongly interacting cells have stunted trajectories on average compared to a non-interacting population

and if so, whether Gap27 could restore this behaviour and if so, to what degree.

4.3 Results

4.3.1 Initial conditions

As stated in earlier sections, primarily we are interested in how Cx43-based cell-cell interactions affect cell migration and population invasion of a 2-d wound, without and with Gap27. To explore this with our model, we approximate an *in vitro* scrape wound assay *in silico* and, within this computational framework, simulate our migration model, Eq. (4.1)-(4.3), without and with Gap27 treatment. We then track the subsequent migration behaviour over time.

To create our computational scrape wound model, we define a 2-d domain $800 \times 600\mu$m on which cells can migrate and interact, and distribute initial cell positions either side of an unpopulated central region $100 \times 600\mu$m we define as the 'wound' (as outlined in *Methods* 4.2.2). Dimensions are chosen to balance model population size with computation time and resolution. Spatial units are assigned using R_M, which we set using experimental approximations for the average diameter of human neonatal fibroblasts [167].

Within this domain we aim to approximate monolayer-like density with our model cell population. As a guide we use MatTek's data sheet for normal human dermal fibroblasts (NHDFs) recommended seeding density and use approximately 3000 cells/cm^2, scaled down to $N = 1200$ cells for our domain [166]. At this relatively high density, cells are able to interact extensively across the domain during their respective migrations, encounters between cells typically frequent.

The initial cell population is configured using the circle packing algorithm described

in *Methods* 4.2.2, the resulting configuration containing cells whose membranes do not overlap in each population either side of the wound. We recall that since the local effects of hemichannels and gap junctions are small in extension, and we discard the effects of extracellular signalling that would enable long-range interactions, $R_I/R_M \approx 1$, for simulations we set $R_I = 16\mu$m and $R_M = 15\mu$m. For figures we use a cell marker diameter which represents the membrane defined by R_M and to relative scale. To enable comparisons between simulations, we keep the initial cell configuration constant. The initial cell configuration (at $t = 0$) for all simulations is presented in Figure 4.6.

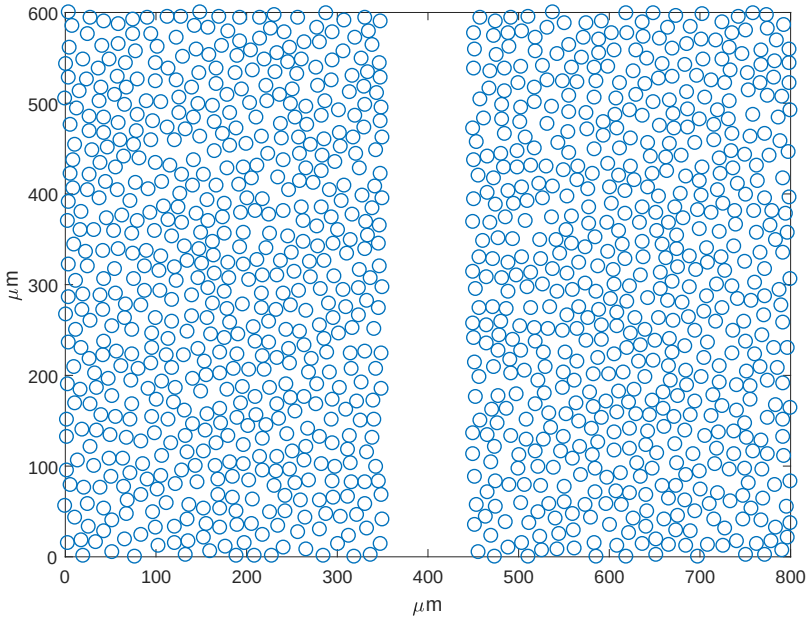

Figure 4.6: Initial cell configuration for the 2-d computational scrape wound model. Spatial domain is $800 \times 600\mu$m, the 'wound' measures $100 \times 600\mu$m. Total number of cells on the domain is $N = 1200$, the resulting cell density approximates NHDF seeding density used for *in vitro* assays. Cell positions are generated using a pseudo-random circle packing algorithm to ensure no initial overlapping in the population. Cell markers represent membrane boundaries defined by R_M, cell marker diameter = 15μm.

We choose initial concentrations for the Cx43 cycling model (at $t = 0$) by adopting a similar approach as used in *Chapter* 3. We fix all connexin-based variables (for which we can) equal to zero, $h(0) = g(0) = e(0) = p_{var}(0) = 0$. We choose $p(0)$ arbitrarily

small, $p(0) = 1 \times 10^{-10}$, since $p \neq 0$. We choose $p_{avg}(0) = 2 + 1 \times 10^{-10}$, since $p_{avg} > 2$. In simulations without Gap27, we set $g_{27}(0) = 0$ and $hg_{27}(0) = 0$. We introduce Gap27 by letting $g_{27}(0)$ take non-zero values and, since we again assume no treatment with Gap27 prior to $t = 0$ for simulations, $C(0) = 0$. We test a range of non-zero concentrations for $g_{27}(0)$, approximately $100 \leq g_{27}(0) \leq 1500$ unit concentration, across a range for p^* but present results only for $g_{27}(0) = 1500$ unit concentration when p^* is large. We find larger $g_{27}(0)$ concentrations exhibit more significant effects on spatial behaviour when p^* is large.

To initiate the migration model computationally, we assign initial cell velocities with MATLAB's standard pseudo-random number generator ('*Mersenne Twister*') and pre-allocate a time-step adjusted array of pseudo-random numbers across time, accessed in the velocity simulation for numerical approximations of the Wiener process.

We set initial connexin model parameters by (again) adopting a similar approach used in *Chapter* 3, setting all rates so that all parameter ratios equal to one. For this 'base' model, rate values we choose arbitrarily equal to one, $\widehat{k}_1 = \widehat{k}_{-1} = \widehat{k}_2 = \widehat{k}_u = \widehat{k}_r = \widehat{k}_d = \widehat{k}_{G27} = \widehat{k}_{-G27} = 1$. To generate different values for p^*, which we explore for both with and without Gap27, we adjust gap junction formation/dissociation, accrual and internalisation rates $\widehat{k}_1/\widehat{k}_{-1}$, $\widehat{k}_2$ and $\widehat{k}_u$.

To set parameters for the migration model, we choose to fix α and β using values obtained from fitting the original unbiased migration (OU) model to experimental data in *Chapter* 2. The experimental data comprised angle and speed metrics extracted from migration trajectories tracked over time-lapse of *in vitro* fibroblasts (NIH-3T3) across a flat surface (undirected) published by Kim et al. [105]. As discussed in *Chapter* 2, we find through the parameter estimation method multiple parametrisations are fea-

sible, and so we fit a polynomial function through approximated minima to generate individual parameter combinations. We use this function to determine the parameter combination we use for *Chapter* 4. Arbitrarily choosing $\beta = 1.10$ gives the approximation $\alpha = 2.27$, which we fix for simulations. We also fix the scaling factor for cell-cell interaction, γ_k, constant for all cells, $k = 1, ..., N$, and across simulations. To help illustrate the impact of $p(\tau)$ on spatial behaviour we set $\gamma_k = 1$.

We set time parameters for the migration model to allow for the unpopulated 'wound' region to become populated to a cell density approaching homogeneity with the surrounding population, under simulation conditions where cell-cell interactions are infrequent and so migration behaviour is over time more roaming. We start migration simulations at $t = 0$ and set the time limit $t_{end} = 2400$ nondimensional units of time. To maintain a reasonable degree of approximation for the Euler-Maruyama method we use time increments of size $ds = 0.06$, generating a total $n_{em} = 4 \times 10^4$ increments for a simulation.

As earlier discussed, we take into account the processes that govern connexin cycling and physical translocation during migration could occur on different time scales. We assign the connexin model with its own time variable τ and move between t and τ with the conversion $t = n_\tau \tau$. For simplicity, we set $n_\tau = 1$ and assume connexin and migration models operate on equal time scales. We initiate simulations of the connexin model at $\tau = 0$ and run for $n_{cx} = 4 \times 10^4$ increments over $\tau_{end} = 2400$ nondimensional units of time. Even at the largest g_{27} concentration presented, $g_{27}(0) = 1500$, the system reaches equilibrium prior to τ_{end}.

As a rudimentary model for membrane deformation, cells are permitted to overlap in 2-d at R_M during simulations ($t > 0$). To aid in comparison between simulation out-

put, we seed MATLAB's pseudo-random number generator ('*Mersenne Twister*') to make stochastic contributions to the model consistent between simulations.

4.3.2 Scrape wound model with Gap27

We now explore how connexin-mimetic peptide Gap27 affects migration behaviour and wound closure when introduced to the computational scrape wound model. For comparison, we run two model simulations each with different initial Gap27 concentrations, $g_{27}(0) = 0$ and $g_{27}(0) = 1500$ unit concentration, and otherwise equal initial conditions. Gap27 appears to have greatest influence when both $g_{27}(0)$ and p^* are large, and so we focus on model simulations with these initial conditions in presenting Gap27 results. For brevity we omit most simulation results for ranges of both $g_{27}(0)$ and p^* tested and instead select the most pertinent results to describe.

p^* large with Gap27

For model simulations both with and without Gap27, we adjust connexin parameters so p^* is large, $p^* = 2.0835$, attained using large gap junction association/dissociation ratio $\widehat{k}_1/\widehat{k}_{-1} = 1 \times 10^3$ and small gap junction internalisation rate $\widehat{k}_u = 1 \times 10^{-2}$. For our 'control' simulation, i.e. with no Gap27, we set $g_{27}(0) = 0$ unit concentration. For our simulation with Gap27 treatment, we set $g_{27}(0) = 1500$ unit concentration. We assume rapid hemichannel-Gap27 binding and slow dissociation, thus set association/dissociation ratio large, $\widehat{k}_{G27}/\widehat{k}_{-G27} = 1 \times 10^2$. The introduction of Gap27 into the system has a transient effect on $p(\tau)$ and is concentration dependent on $g_{27}(0)$, we can see this in Figure 4.7 for varied $g_{27}(0)$ and $p(\tau)$ adopted for the simulations to follow. For simulations without Gap27 ($g_{27}(0) = 0$), when p^* is large ($p^* = 2.0835$), we see in Figure 4.8 (left column) migration trajectories across the whole domain tend rarely to

roam and instead coalesce around distinct regions early in time T, evident in Figure 4.8 (a). This behaviour persists over T, most migration trajectories restricted to local and largely disconnected neighbourhoods of the domain throughout the simulation, see Figure 4.8 (e).

In Figure 4.9 (left column) we see cells in fact coalesce into well-defined clusters which grow over T, becoming increasingly tightly packed. This behaviour was clearly observable during the simulations, in which cell-cell interactions were typically lengthy, cells tended to gather rather than break apart and continue to roam, over time these growing cell conglomerates might typically comprise some ten to twenty cells. The final cell configuration is so extensively clustered that almost every cell, with few exceptions, forms part of some cell cluster. These clusters are evenly distributed across each cell population, approximately equidistant from each other, and have rarely, if at all, advanced into the wounded region (see Figure 4.9 (e)).

The lack of a significant population invasion into the wound is clear in Figure 4.10 (a), in which we see the wound region (black) remain virtually unpopulated (by blue) over T; the 'scrape wound' preserved. Cell clustering observed in the final cell configuration is also evident as regions of high average cell density which develop rapidly over initial increments (observed as regions of light aqua, grey and white which streak across T).

We also see in Figure 4.11 (a) that wound width is stable over T, staying approximately constant (fluctuations being due to the classification method described in *Methods* 4.2.2).

Finally, we see in Figure 4.12 (blue), mean-squared displacement (MSD) over T is clearly sub-linear when p^* is large.

For simulations with $g_{27}(0) = 1500$ unit concentration, we see in Figure 4.8 (right col-

umn) trajectories typically roam much more randomly across the domain over T and tend not to coalesce, exploring much of the domain including the initially unpopulated 'wound' region. We see in Figure 4.9 (right column) some cell clustering is present from early in the simulation, though many cells roam freely and clusters typically remain small and sparse over T. We also see that the wound region becomes gradually populated by cells over T, the cell population approaching spatial homogeneity at $T = 2400$, Figure 4.9 (f). In Figure 4.10 (b) we see the population advance into the wound region in greater temporal resolution, the wound region (black) clearly being gradually populated (by blue) over T. Cell population fronts appear to have begun to merge at $T = 2400$ and the 'scrape wound' closed, though there is some spatial heterogeneity present within the population. The wound width metric in Figure 4.11 (b) corroborates, showing a distinct and consistent reduction in wound width over T (apparent even with fluctuations owing to the classification method). We see a marked difference in displacement behaviour in Figure 4.12 (red), where MSD appears approximately linear over T when Gap27 is introduced at $g_{27}(0) = 1500$ unit concentration, meaning on average migrations are much more roaming and consequently cells are moving much greater distances away from their starting positions over the simulation.

For the simulation scenarios presented in Figures 4.8 - 4.11 we observe that introduction of Gap27 at a high initial concentration can effectively 'rescue' healing of the scrape wound when p^* is large. In the simulation, introduction of Gap27 appeared to reduce both overall levels and density of cell clustering, enabling cells to migrate more freely on the domain. This effect is dependent on $g_{27}(0)$. Increasing $g_{27}(0)$ leads to more substantial effects on transient behaviour of $p(\tau)$. When p^* is large, the effect of increasing $g_{27}(0)$ on $p(\tau)$ is evident in the spatial behaviour, where we see a reduction in cluster-

ing, more unbound cells and greater, more rapid population of the wound region. As p^* is reduced the effect of $g_{27}(0)$ becomes less apparent in the spatial behaviour. When p^* approaches zero, there is no significant effect on cell behaviour with the addition of Gap27 and does not change dependent on $g_{27}(0)$. This was clear in migration trajectories, cell configurations and population fronts for simulations without compared to with $g_{27}(0)$, where trajectories, cell groupings and population front advances all appear indistinguishable, for all $g_{27}(0)$ concentrations tested. This suggesting that migration behaviour when p^* is small is not significantly altered by the introduction of g_{27}.

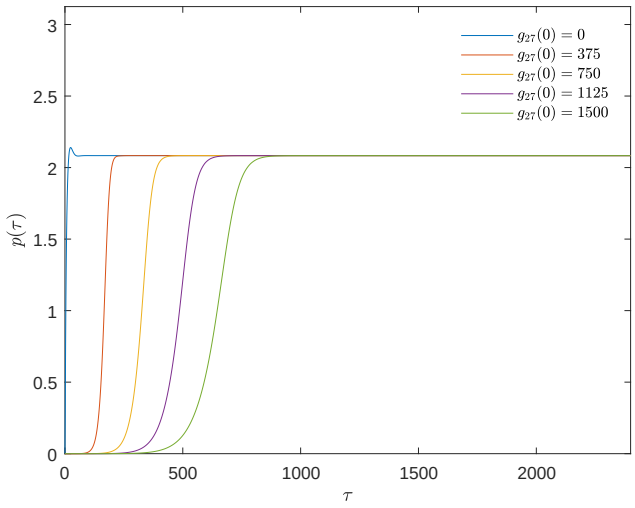

Figure 4.7: $p(\tau)$, where $p^* = 2.0835$, with varied initial concentrations for Gap27, $g_{27}(0)$: $g_{27}(0) = 0$ (blue), $g_{27}(0) = 375$ (orange), $g_{27}(0) = 750$ (yellow), $g_{27}(0) = 1125$ (purple) and $g_{27}(0) = 1500$ (green) unit concentration. $g_{27}(0)$ has a clear transient effect on $p(\tau)$ that is concentration dependent, the effect magnifying as $g_{27}(0)$ increases. Connexin parameters: $\widehat{k}_1 = 1 \times 10^3$, $\widehat{k}_u = 1 \times 10^{-2}$, $\widehat{k}_{-1} = \widehat{k}_2 = \widehat{k}_r = \widehat{k}_d = 1$, $\widehat{k}_{G27}/\widehat{k}_{-G27} = 1 \times 10^2$.

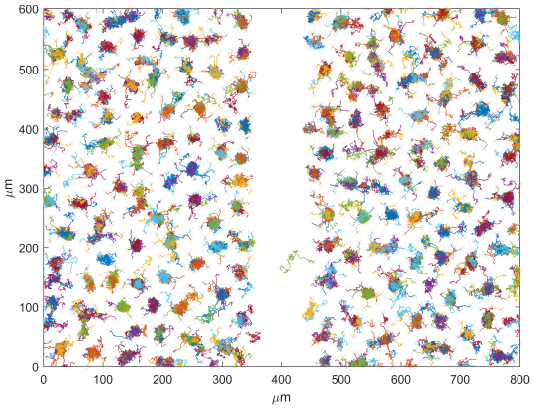

(a) $T = 300.\ g_{27}(0) = 0.$

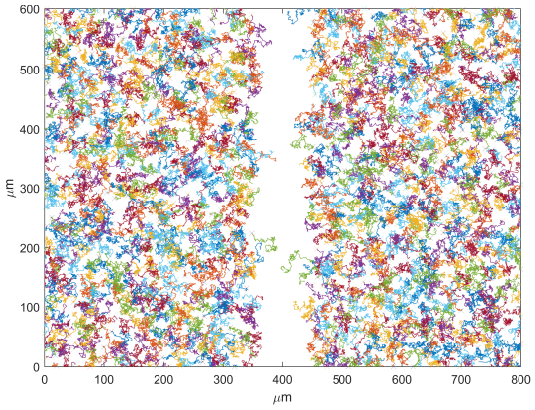

(b) $T = 300.\ g_{27}(0) = 1500.$

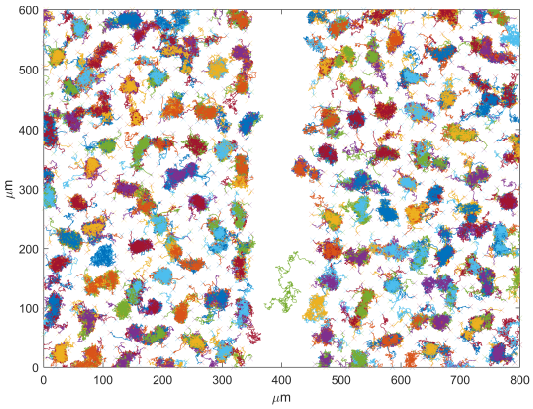

(c) $T = 1350.\ g_{27}(0) = 0.$

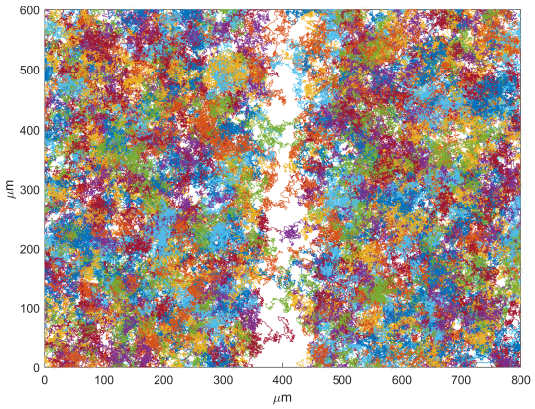

(d) $T = 1350.\ g_{27}(0) = 1500.$

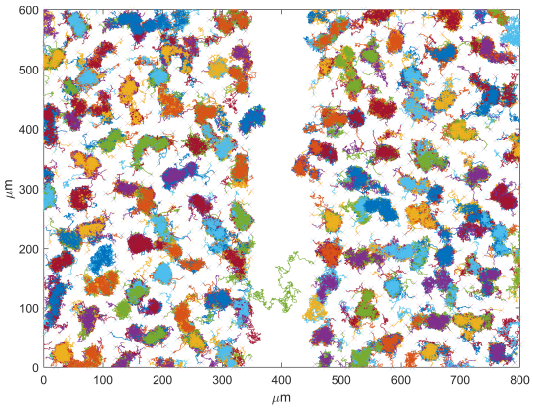

(e) $T = 2400.\ g_{27}(0) = 0.$

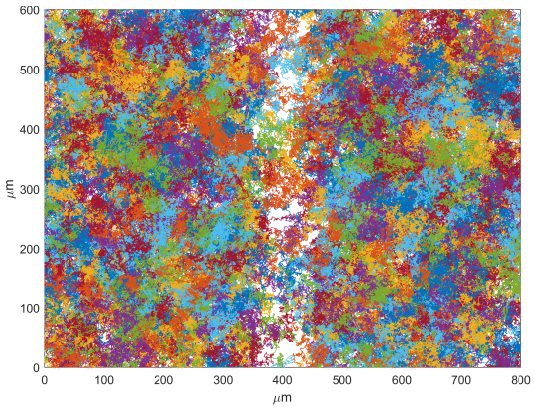

(f) $T = 2400.\ g_{27}(0) = 1500.$

Figure 4.8: Migration trajectories across the domain at time points $T = 300$, $T = 1350$ and $T = 2400$ (rows) with no Gap27, $g_{27}(0) = 0$ (left), and with Gap27, $g_{27}(0) = 1500$ (right), when p^* is large ($p^* = 2.0835$). Without Gap27 (left column), trajectories tend to coalesce across time T, the wound region of the domain being largely unexplored at $T = 2400$ (e). With the introduction of Gap27 (right column), trajectories tend not to coalesce and explore greater territory over time T, enabling extensive exploration of the wound region at $T = 2400$ (f). Connexin parameters: $\widehat{k}_1/\widehat{k}_{-1} = 1 \times 10^3$, $\widehat{k}_u = 1 \times 10^{-2}$, $\widehat{k}_2 = \widehat{k}_r = \widehat{k}_d = 1$, $\widehat{k}_{G27}/\widehat{k}_{-G27} = 1 \times 10^2$. Migration parameters: $\alpha = 2.27, \beta = 1.1, \gamma_k = 1, R_I = 16, R_M = 15, dt = 0.3, ds = 0.06$.

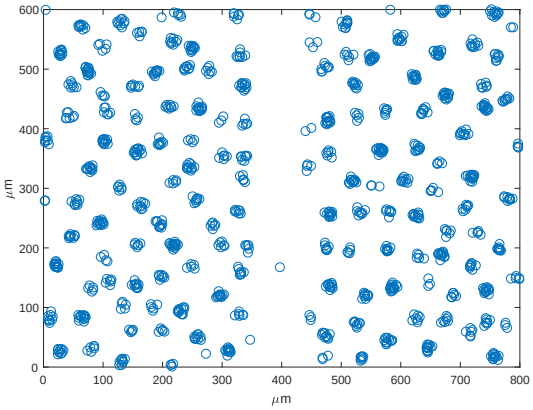

(a) $T = 300.\ g_{27}(0) = 0.$

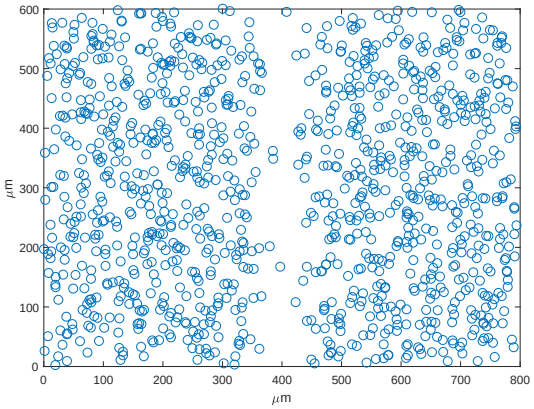

(b) $T = 300.\ g_{27}(0) = 1500.$

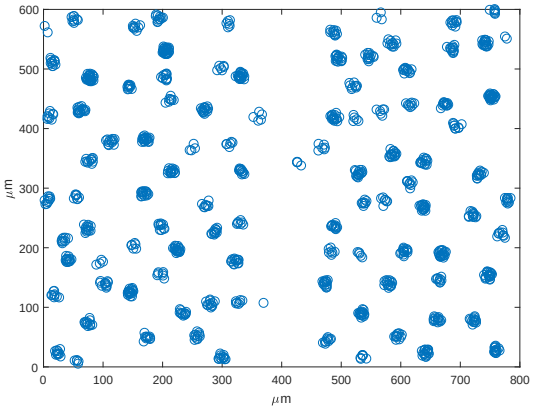

(c) $T = 1350.\ g_{27}(0) = 0.$

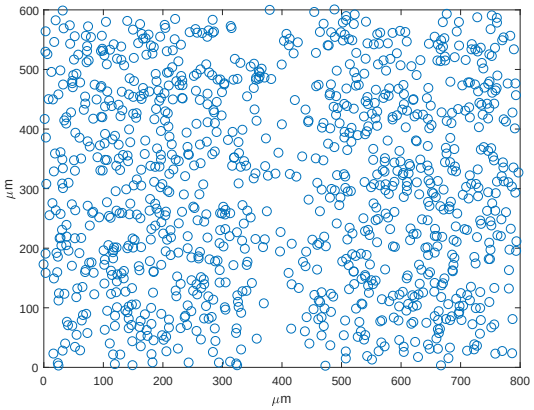

(d) $T = 1350.\ g_{27}(0) = 1500.$

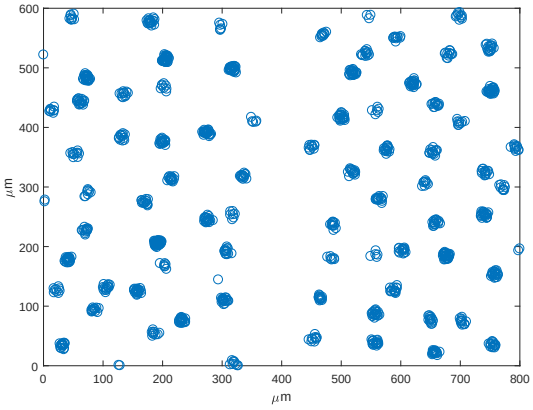

(e) $T = 2400.\ g_{27}(0) = 0.$

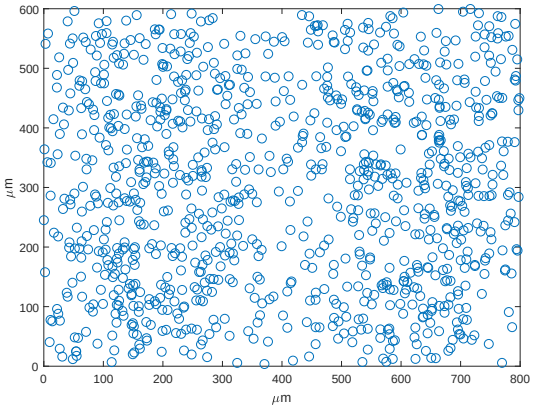

(f) $T = 2400.\ g_{27}(0) = 1500.$

Figure 4.9: Cell configurations across the domain at time points $T = 300$, $T = 1350$ and $T = 2400$ (rows) with no Gap27, $g_{27}(0) = 0$ (left), and with Gap27, $g_{27}(0) = 1500$ (right), when p^* is large ($p^* = 2.0835$). Without Gap27 (left column), cells barely populate the wound region over T, instead grouping into tight clusters that aggregate over T. With the introduction of Gap27 (right column), notice how cells populate the wound over T, forming only small sparse clusters with many cells free and unbound. Connexin parameters: $\widehat{k}_1/\widehat{k}_{-1} = 1 \times 10^3$, $\widehat{k}_u = 1 \times 10^{-2}$, $\widehat{k}_2 = \widehat{k}_r = \widehat{k}_d = 1$, $\widehat{k}_{G27}/\widehat{k}_{-G27} = 1 \times 10^2$. Migration parameters: $\alpha = 2.27, \beta = 1.1, \gamma_k = 1, R_I = 16, R_M = 15, dt = 0.3, ds = 0.06$. Cell marker diameter = 15μm

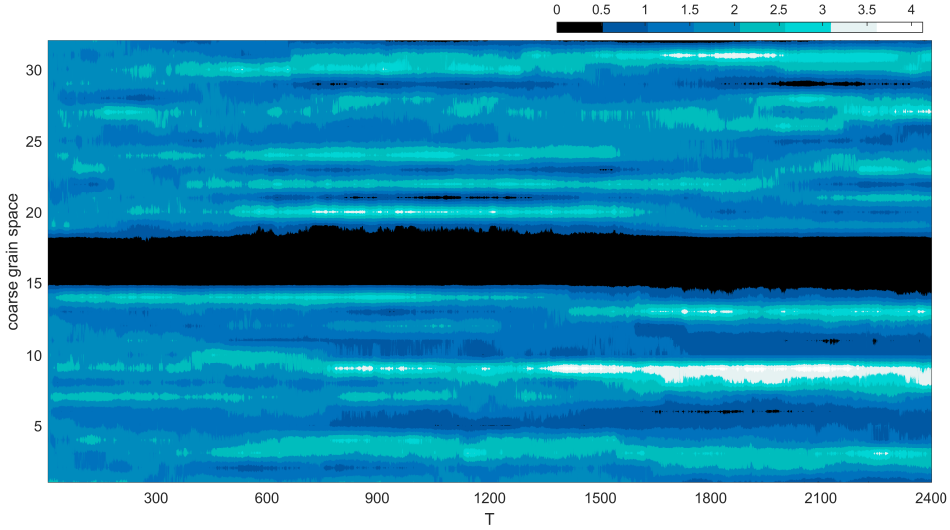

(a) Coarse grained domain over T. $g_{27}(0) = 0$.

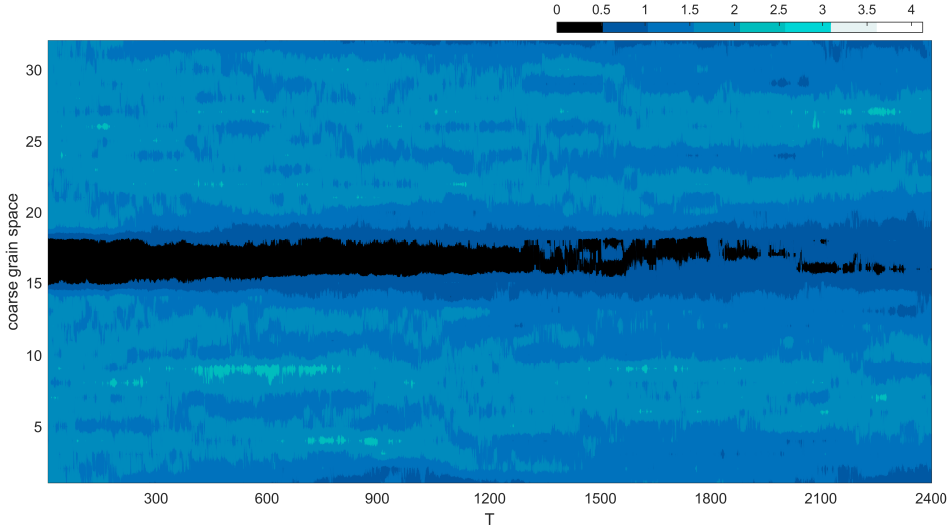

(b) Coarse grained domain over T. $g_{27}(0) = 1500$.

Figure 4.10: Coarse grained space of the spatial domain over T with no Gap27, $g_{27}(0) = 0$ (top), and with Gap27, $g_{27}(0) = 1500$ (bottom) when p^* is large ($p^* = 2.0835$), where colour bar represents an average cell quantity per $25 \times 25\mu$m on the domain. The coarse grained space is generated by the methods described in *Methods* 4.2.2. Briefly, at each time increment the spatial domain is segmented into 32×15 windows each $25 \times 25\mu$m and cell quantity in each determined, each of the 32 columns are then averaged over reducing to 1-d, which is plotted over T. (a) without Gap27, we see the wound remains unpopulated over T, preserved by stationary population fronts. (b) introduction of Gap27 sees the wound become gradually populated over T with clearly invasive population fronts. Connexin parameters: $\widehat{k}_1/\widehat{k}_{-1} = 1 \times 10^3$, $\widehat{k}_u = 1 \times 10^{-2}$, $\widehat{k}_2 = \widehat{k}_r = \widehat{k}_d = 1$, $\widehat{k}_{G27}/\widehat{k}_{-G27} = 1 \times 10^2$. Migration parameters: $\alpha = 2.27, \beta = 1.1, \gamma_k = 1, R_I = 16, R_M = 15, dt = 0.3, ds = 0.06$.

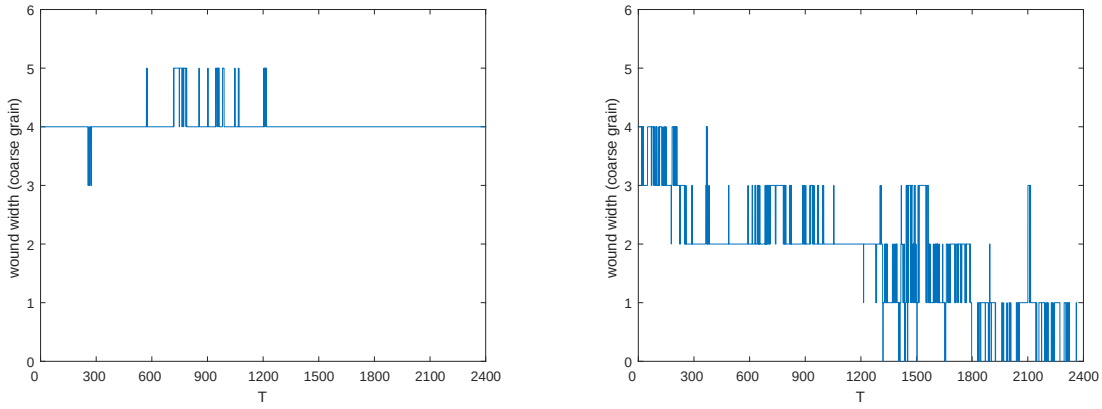

(a) Wound width over T. $g_{27}(0) = 0$.

(b) Wound width over T. $g_{27}(0) = 1500$.

Figure 4.11: Wound width (computed from coarse grained space) over T with (a) no Gap27, $g_{27}(0) = 0$, and (b) with Gap27, $g_{27}(0) = 1500$, and p^* large ($p^* = 2.0835$). (a) when $g_{27}(0) = 0$, wound width is typically stable over T. (b) when $g_{27}(0) = 1500$, a decreasing trend in wound width over T is clearly observable. Connexin parameters: $\widehat{k}_1/\widehat{k}_{-1} = 1 \times 10^3$, $\widehat{k}_u = 1 \times 10^{-2}$, $\widehat{k}_2 = \widehat{k}_r = \widehat{k}_d = 1$, $\widehat{k}_{G27}/\widehat{k}_{-G27} = 1 \times 10^2$. Migration parameters: $\alpha = 2.27, \beta = 1.1, \gamma_k = 1, R_I = 16, R_M = 15, dt = 0.3, ds = 0.06$.

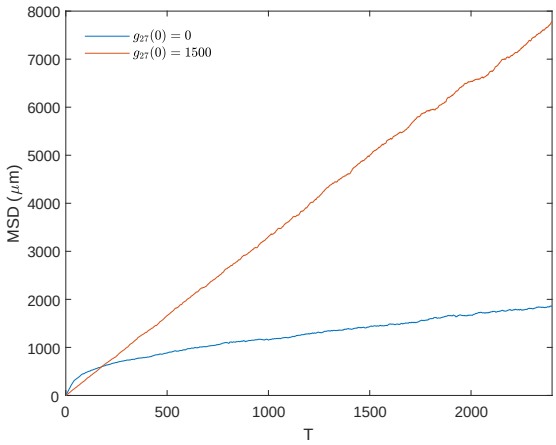

Figure 4.12: Mean squared displacement (MSD, μm) over T with no Gap27, $g_{27}(0) = 0$ (blue), and Gap27, $g_{27}(0) = 1500$ (red), and p^* large ($p^* = 2.0835$). When $g_{27}(0) = 0$, MSD over T is sub-linear. When $g_{27}(0) = 1500$, MSD over T is approximately linear. Connexin parameters: $\widehat{k}_1/\widehat{k}_{-1} = 1\times10^3$, $\widehat{k}_u = 1\times10^{-2}$, $\widehat{k}_2 = \widehat{k}_r = \widehat{k}_d = 1$, $\widehat{k}_{G27}/\widehat{k}_{-G27} = 1\times10^2$. Migration parameters: $\alpha = 2.27, \beta = 1.1, \gamma_k = 1, R_I = 16, R_M = 15, dt = 0.3, ds = 0.06$.

4.3.3 Scrape wound model without Gap27

We further explore the computational scrape wound model without Gap27. We begin by exploring how coupling variable $p(\tau)$ affects the behaviour of model migration trajectories and wound closure. To do this we vary connexin model parameters as described to obtain a small and large p^*, $p^* = 4.9974 \times 10^{-8}$ and $p^* = 2.0838$ respectively,

which we use in separate simulations with the initial conditions outlined.

In *Results* 4.3.2, we considered migration behaviour of the model when p^* is large ($p^* = 2.0838$). Cells tend to cluster into aggregates over T, restricting migration to domain regions local to each aggregate and stunting any significant population invasion into the wound. To enable comparison with when p^* is small, we present migration trajectories and cell configurations over T once more in Figures 4.13 and 4.14 (right column).

When p^* is small, $p^* = 4.9974 \times 10^{-8}$, we see in Figure 4.13 (left column) that migration trajectories are, on average, long and tortuous, extensively exploring the whole domain over T, including the wound region, absent of the kind of coalescing behaviour we observed with simulations for large p^*.

We see in Figure 4.14 (left column) cell clustering is significantly reduced compared to when p^* large, we instead typically see many cells migrating freely without contact from other cells and form only small cell aggregates. Again, this behaviour was observable during simulations, where cells tended to interact weakly, interactions usually being brief, often breaking loose within short time spans and not typically contacting for long enough to aggregate more than a few cells at any given time point. We see the cells observably advance into the wound over T, extensively populating the scrape wound at $T = 2400$ units of time, see Figure 4.14 (e).

The qualitative similarity in migration behaviour between the scenarios when p^* is small and when p^* is large but with Gap27 is notable. Both scenarios appear to diminish the effects of cell-cell interactions on individual migration, encouraging migration as the dominant cell behaviour. In the simulations this appears critical in enabling the cell population to advance into the wound.

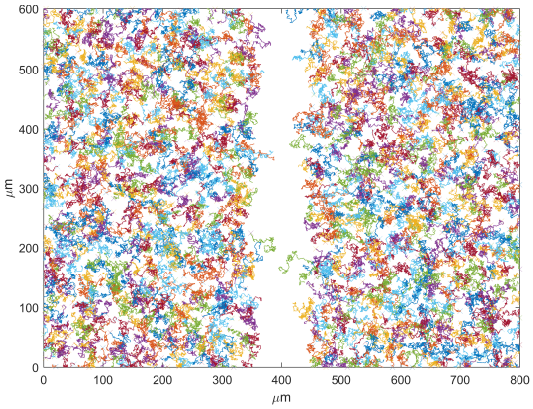

(a) $T = 300$. $p^* = 4.9974 \times 10^{-8}$.

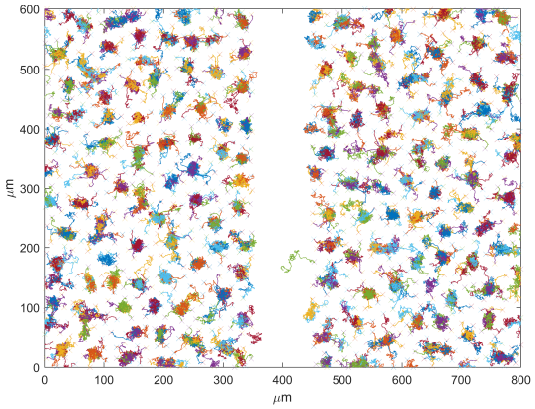

(b) $T = 300$. $p^* = 2.0838$.

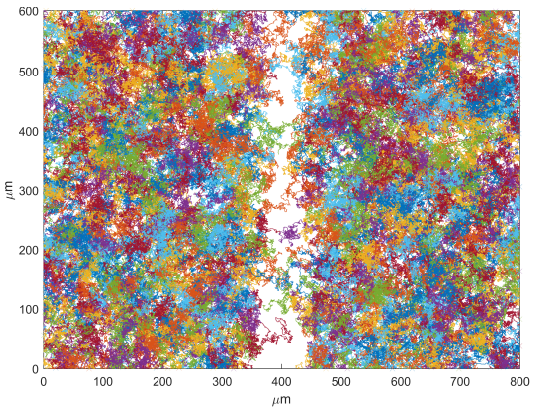

(c) $T = 1350$. $p^* = 4.9974 \times 10^{-8}$.

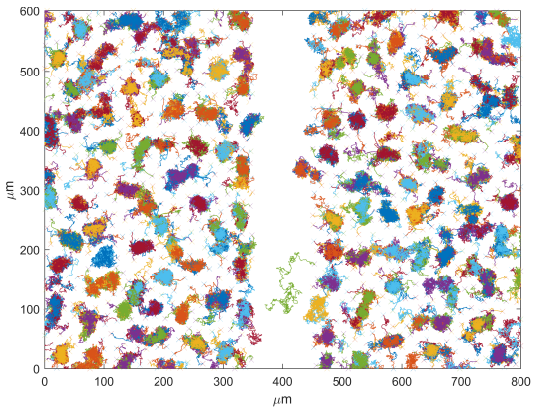

(d) $T = 1350$. $p^* = 2.0838$.

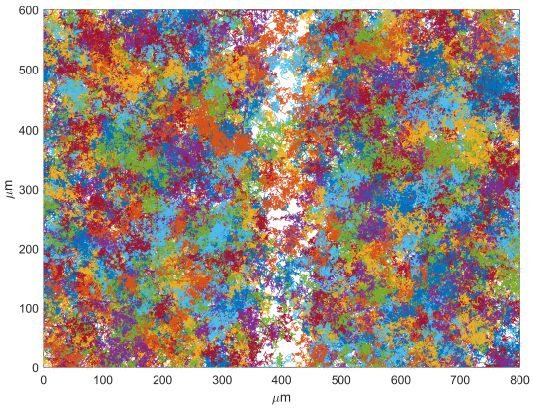

(e) $T = 2400$. $p^* = 4.9974 \times 10^{-8}$.

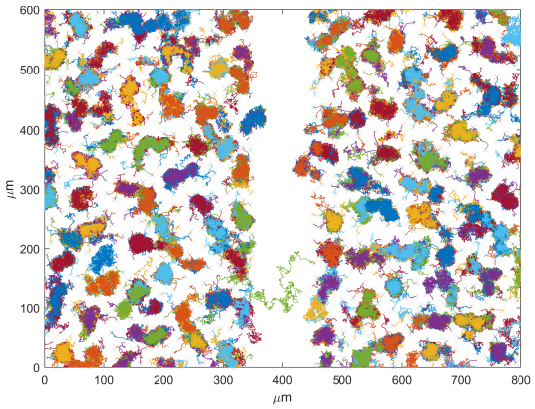

(f) $T = 2400$. $p^* = 2.0838$.

Figure 4.13: Migration trajectories across the domain at time points $T = 300$, $T = 1350$ and $T = 2400$ (rows) for small and large p^* (columns). Notice how the wounded region is gradually explored over time when p^* is small ($p^* = 4.9974 \times 10^{-8}$, left column) such that the wound begins to close at $T = 2400$ (e). However, when p^* is large ($p^* = 2.0838$, right column) the wound region is largely unexplored by migration trajectories across time which instead appear to coalesce, signifying extensive cell grouping. Connexin parameters: $\widehat{k}_1 = 1 \times 10^{-4}$, $\widehat{k}_u = 1 \times 10^{-1}$ (left column), $\widehat{k}_1 = 1 \times 10^3$, $\widehat{k}_u = 1 \times 10^{-2}$ (right column), $\widehat{k}_{-1} = \widehat{k}_2 = \widehat{k}_r = \widehat{k}_d = 1, \widehat{k}_{G27} = \widehat{k}_{-G27} = 0$. Migration parameters: $\alpha = 2.27, \beta = 1.1, \gamma_k = 1, R_I = 16, R_m = 15, dt = 0.3, ds = 0.06$.

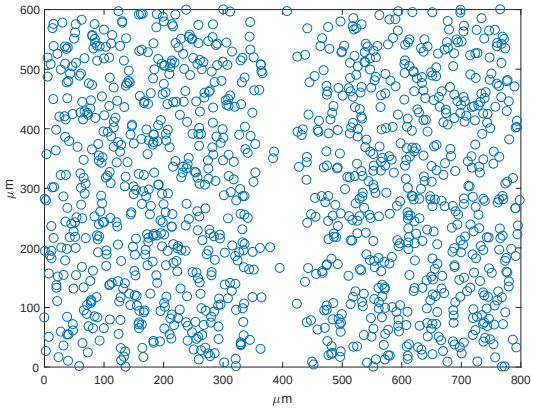

(a) $T = 300.\ p^* = 4.9974 \times 10^{-8}$.

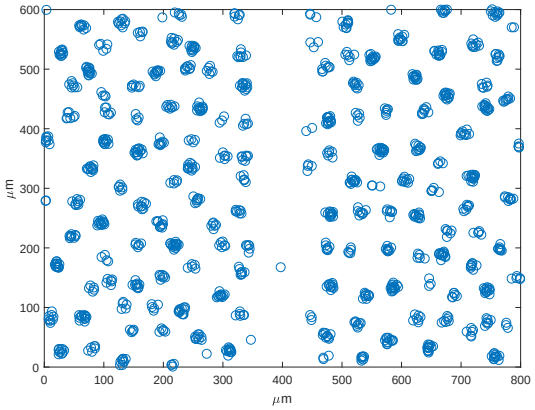

(b) $T = 300.\ p^* = 2.0838$.

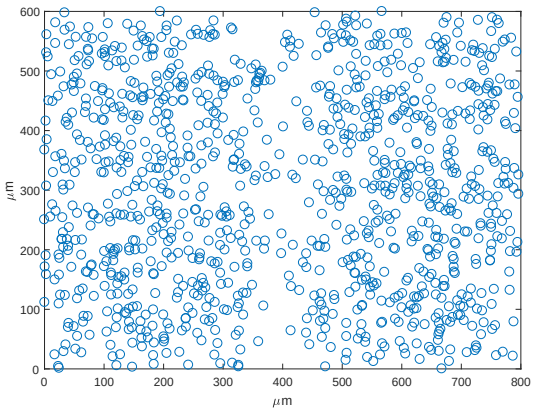

(c) $T = 1350.\ p^* = 4.9974 \times 10^{-8}$.

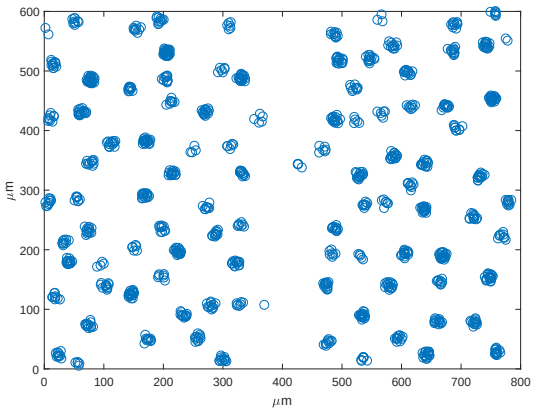

(d) $T = 1350.\ p^* = 2.0838$.

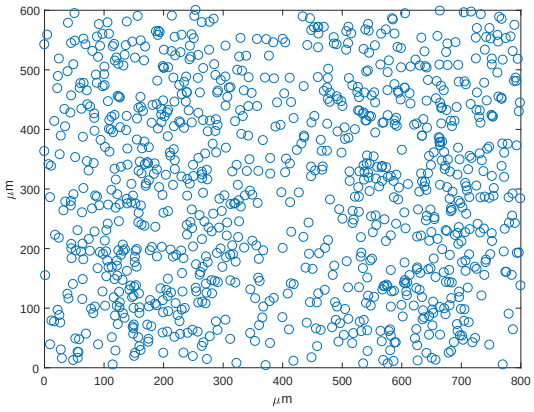

(e) $T = 2400.\ p^* = 4.9974 \times 10^{-8}$.

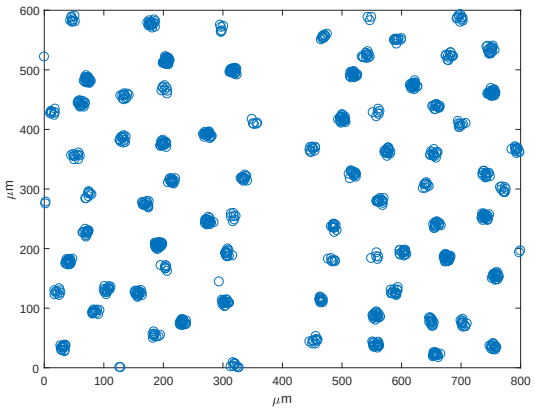

(f) $T = 2400.\ p^* = 2.0838$.

Figure 4.14: Cell configurations across the domain at time points $T = 300$, $T = 1350$ and $T = 2400$ (rows) for small and large p^* (columns). Notice how when p^* is small ($p^* = 4.9974 \times 10^{-8}$, left column) cells populate the wound region over time and tend only to weakly interact with each other, typically forming only small groups. When p^* is large ($p^* = 2.0838$, right column) cells barely populate the wounded region at all over time and group into tight clusters, appearing to grow larger over time. Connexin parameters: $\widehat{k}_1 = 1 \times 10^{-4}$, $\widehat{k}_u = 1 \times 10^{-1}$ (left column), $\widehat{k}_1 = 1 \times 10^3$, $\widehat{k}_u = 1 \times 10^{-2}$ (right column), $\widehat{k}_{-1} = \widehat{k}_2 = \widehat{k}_r = \widehat{k}_d = 1, \widehat{k}_{G27} = \widehat{k}_{-G27} = 0$. Migration parameters: $\alpha = 2.27, \beta = 1.1, \gamma_k = 1, R_I = 16, R_m = 15, dt = 0.3, ds = 0.06$. Cell marker diameter = 15μm.

4.4 Discussion

In our study, we presented a model for Cx43-based gap junction influenced cell-cell interactions between individual migrating cells to investigate how connexin mimetic peptide Gap27 and Cx43 cycling can affect population advance into a computational model of a 2-d scrape wound. The principle aim was to understand more about how Cx43 cycling and Gap27 can affect wound healing, there currently existing open mechanistic questions regarding connexin influence in cutaneous wound repair. For example, how disruption to connexin regulation can lead to chronic non-healing wounds and why CMPs like Gap27 can accelerate healing under certain conditions (e.g. healthy tissue) but be ineffective under other conditions (e.g. diabetic tissue) [160].

The model we created is based on an Ornstein-Uhlenbeck (OU) process for individual cell migration velocity over time, this modified to incorporate a directional bias for when cells encounter and interact with each other. The cell-cell interaction term utilises solution output from *Chapter* 3's Cx43 cycling model, specifically the total gap junction plaque concentration, $p(\tau)$, to determine the magnitude of interaction. The Cx43 cycling model also incorporated Gap27 binding via a simple one-step association/dissociation reaction, enabling us to introduce Gap27 indirectly into the spatial model through its transient effect on $p(\tau)$.

To test this model, we defined a computational scrape wound where all individual cells within two wound-separated populations migrate over time according to the developed migration-interaction model. We then ran simulations focusing on varied initial concentrations for Gap27, $g_{27}(0)$, across varied p^* and without Gap27 ($g_{27}(0) = 0$) and varied p^*, keeping all other conditions constant.

We found that introduction of Gap27, g_{27}, into the model ($g_{27}(0)$ is non-zero) prompts

closure of the computational scrape wound over time when p^* is large, compared to control simulations where there is no Gap27 ($g_{27}(0) = 0$), and all other conditions are equal. We found the rate of wound closure is dependent on $g_{27}(0)$, increasing with $g_{27}(0)$ up to concentrations where the transient effect on $p(\tau)$ is so substantial the closure rate approximates model simulations where p^* approaches zero and cell-cell interactions have an insignificant effect on migration behaviour. We found the effect g_{27} has on spatial behaviour decreases with p^*, g_{27} having little observable effect as p^* approaches zero. We also found that spatial behaviour is similar when p^* is small without Gap27 as when p^* and $g_{27}(0)$ is large, g_{27}, in effect, appearing to transiently mimic what happens when p^* is small, weakening interactions and creating the conditions for cells to become more migratory.

In model terms, the introduction of Gap27 (where $g_{27}(0) \neq 0$) means that cells can come into close contact without exerting an immediate interaction pull on each other. There is a 'window of opportunity' for cells to co-exist closely with neighbours without interacting. The size of this temporal window is determined by $g_{27}(0)$, extending with increasing $g_{27}(0)$, via Gap27's transient effect on $p(\tau)$. When p^* is large we found g_{27} would reduce both intensity and instance of interactions and free cells to migrate across the domain, less encumbered by other cells, to gradually populate the wound over time. Though effective in disrupting spatial behaviour when p^* is large, g_{27} had little effect spatially as p^* became small. As p^* decreases, the g_{27} transient effect on $p(\tau)$ becomes less and less discernible in the spatial behaviour because cell-cell interactions become weaker (and scarcer), so we see the effect of g_{27} gradually dampen with reduction to p^*. As p^* approaches zero, there is no observable effect on spatial behaviour, where effectively there are no interactions in the population to disrupt. This also helps to

explain why we see similar spatial behaviour when p^* is small without g_{27} and with p^* and g_{27} large. In effect, g_{27} transiently approximates what happens spatially when p^* approaches zero, both reducing intensity and instance of interactions, only with g_{27} the effect 'wears off' with time and $p(\tau)$ returns to p^* pre-determined by Cx43 model parameters. If $g_{27}(0)$ is large enough, the transient effect on $p(\tau)$ can be significant enough to see little difference between simulations when p^* is small without g_{27} and when both p^* and g_{27} are large.

Results from the modelling study suggest Gap27 ought to prompt an effective migratory response for closely interacting cells if applied in a large enough concentration, and aid scrape wound closure under these conditions. This concentration-dependence of Gap27 has been reported in a number of experimental studies. For instance, Faniku et al. observed a dose-dependent effect of Gap27 on scrape wound closure in adult keratinocytes *in vitro*. The authors found Gap27 at 1nM and 10nM moderately reduced the wound area compared the control over 24 hours, but concentrations of 100nM and 100μM were enough to completely close the wound [168].

In dysfunctional scrape wound repair, if cells are closely interacting and Gap27 doesn't prompt a migratory response, it is possible there may be other factors preventing this e.g. poor gap junction turnover, which could potentially block the primary route to disrupting this type of interaction.

When p^* is small, cells migrate more freely and interact less. Qualitatively, this spatial behaviour is akin to cells within the wound front (within a 2-d *in vitro* scrape wound assay) in the hours immediately post-injury where Cx43 is down-regulated and cells adopt something like a more migratory phenotype. It might be expected that cells which have little propensity for gap junction based interaction not to exhibit signifi-

cant changes with the introduction of a CMP like Gap27, unless hemichannel activity plays a more significant role in cell-cell interactions than anticipated, which has been a focus in more recent experimental literature [133].

As p^* becomes larger cells cluster ever more densely, migrations being constrained by constant interactions with other cells. Again, qualitatively this may be akin to the cell population adjacent to the wound front immediately post-injury, where cells jointly coordinate to generate a forthcoming proliferative response. We might expect cells engaged in extensive gap junction based interaction to be significantly affected by Gap27, preventing new gap junctions from forming and adjoining established plaques.

Results could suggest that Gap27 may operate (on a population level) to enlist the more stationary cells adjacent to the migrating front to the migratory effort into the wound, rather than necessarily speeding up the already existing wound front of migrating cells, thus speeding up the population invasion instead by expanding the migrating front and increasing the number of migratory cells present around the wound. It would seem reasonable already migratory cells may not be too affected by the introduction of Gap27 unless affecting an indirect (e.g. hemichannel-based) mode of cell-cell interaction.

This effect may be expected since, if p^* is small i.e. close to zero, the transient effect of $g_{27}(0)$ (whilst still present on $p(\tau)$) is not likely to be registered in the spatial behaviour since the effect of p^* being small is itself relatively insignificant.

In putting forth potential biological interpretations of the model, it is necessary to reconsider and perhaps fully recognise the limitations of the model brought about by the formulation and modelling assumptions. The assumption that cell-cell interactions between migrating cells are dependent on plaque concentration would not appear to

be unreasonable given the structural role gap junction plaques hold in maintaining direct cell-cell communication. Cx43 at the plasma membrane can anchor directly to the cytoskeleton and adhesion proteins are known to gather around plaque structures for stabilisation, forming the junctional nexus (see *Introduction*). Defranco et al. found that migrating cells could interact directly via gap junction plaques and retained plaques even upon physical separation to other cells [169].

The coupling function, $\boldsymbol{F}(p)$, used to couple the Cx43 cycling and migration models accounts only for plaque concentration through $p(\tau)$, and is indiscriminate of plaque size. It is possible in the Cx43 cycling model for similar total plaque concentrations to exist for both all large and all small plaque structures which, biologically, one might expect to exhibit different adhesive properties. We might expect, for example, a small concentration of large plaques to impose a greater adhesive influence on cell-cell interactions than a small concentration of small plaques. We chose for simplicity to limit terms in the coupling function, though we could consider introducing more solution output from the Cx43 model to account for plaque size e.g. average gap junction concentration per plaque concentration, p_{avg}, the coupling function then becoming multivariate, $\boldsymbol{F}(p, p_{avg})$.

We recall that in healthy wound repair, the regulation of Cx43 is temporarily modulated in a localised manner to enable the healing cascade to progress. In future work, it might be possible to incorporate this dynamic into the model by introducing a spatio-temporal variation in the coupling function $\boldsymbol{F}(p)$ across the cell population.

Chapter 5

Discussion

Cutaneous wounds incur a huge economic and human cost for many developed nations. Chronic cutaneous wounds in particular consume a substantial share of annual healthcare expenditures, as high as 4-5% in the U.K. [4], and often come with serious health complications and stark mortality rates. Already prevalent, about 1-2% of people in developed nations likely to develop a chronic wound in their lifetime [7], chronic wounds are predicted to rise further in prevalence with increasing rates of obesity, diabetes and ageing populations [7].

Cutaneous wound repair is a complex and finely balanced process. It relies on a specific sequence of carefully regulated spatio-temporally dependent healing phases, within which a highly organised network of cell and tissue interactions operates to prevent further tissue degradation and infection, then subsequently reconstitute lost tissue; returning mechanical structure and anatomical function to the injured region. The normal healing process can sometimes become deranged, particularly under local or systemic conditions which cause disruption to the healing cascade, leading to impaired healing.

Connexin proteins, the sub-components of cellular communication channels 'hemichan-

nels' and 'gap junctions', are proposed to hold a crucial role in cutaneous wound repair. It is thought that the dynamic regulation of the different connexins expressed in human skin aids in dynamic compartmentalisation of tissue around an injured region post-injury, enabling effective local cellular responses [19, 20]. Connexin-based dysfunction has been strongly associated with impaired healing. The abnormal wound edge up-regulation of connexin 43 (Cx43) in particular has been shown to be a common feature among different types of chronic wound in humans (diabetic, venous and pressure ulcers) [25]. Experimental studies probing the use of connexin-targeted agents (e.g. antisense oligonucleotides and connexin mimetic peptides) as potential treatments show considerable promise in restoring repair. Unmodified oligonucleotide is the main active ingredient in the candidate corneal wound treatment, '*Nexagon*' [21, 31], and the connexin mimetic peptide (CMP), αCT-1, has successfully completed Phase II clinical trials for the treatment of diabetic foot ulcers [152]. The CMP, Gap27, is another promising wound healing therapeutic. Gap27 has been shown to accelerate healing in a number of 2-d and 3-d *in vitro* models and *ex vivo* human tissue, increase migration rates of keratinocytes and fibroblasts *in vitro* and disrupt intercellular communication with reduction to cell-cell dye transfer reported in *ex vivo* tissue models [160].

Many cell types must migrate to carry out their various restorative functions during wound repair. To migrate within the extracellular environment cells must traverse a diverse range of topographic configurations presented by different physiological structures. Such topographies have been shown to influence a number of cellular behaviours, including adhesion, migration, proliferation and even differentiation. The capacity for topography to influence different cellular behaviours has motivated extensive study in the biotechnology and bioengineering literature, with significant applications to bio-

material and bioimplant design, including further development of skin substitutes as advanced wound healing treatments.

Mathematical and computational modelling for both connexin-based influence in wound repair and topographically regulated cellular behaviours would be advantageous to experimentalists in helping to reduce experimental hypotheses and focus wet-lab experiments, streamlining research and accelerating the design process for such connexin-based and topographically influenced treatments already described. There does however, appear to exist a relative paucity in the modelling literature for both applications. Connexin-based mathematical and computational models tend to focus heavily on the properties and functions of gap junction channels, rarely paying attention to the cycling of connexin proteins underpinning such channel functions, nor the influential role connexins have on cell migration and wound repair. Mathematical migration models to incorporate directional cues from some underlying topography have traditionally focused on a cell-matrix based mesenchymal mode of migration in which cells and fibrils interact in a reciprocative manner. Only recently have models begun to explore migration influenced by the specific classes of highly organised topographic configuration studied in the experimental literature, e.g. linear ridge/groove, lattice, pillar, pit and curvature, in an effort to understand exactly how these topographic features affect migration and how they could be used to control and regulate cell behaviour.

In this thesis, we proposed three new mathematical models to further explore topographically influenced cell migration, Cx43 cycling dynamics and its modulation by CMP Gap27, the influence of Cx43 cycling dynamics on cell migration via gap junction based cell-cell interactions and how the introduction of Gap27 may function to prompt scrape wound closure. To do this, we use two well-established modelling ap-

proaches familiar in the mathematical biology literature to develop an individual-based model for topographically influenced cell migration and a mass action model for Cx43 cycling with Gap27 binding kinetics. We then couple the two models to construct a cell-cell influenced migration model based on Cx43 dynamics. We then test the migration model within a computational model of a 2-d scrape wound assay, using the Cx43 cycling model to introduce Gap27 dynamics.

In the first part of the thesis, *Chapter* 2, we develop the individual-based model for topographically influenced cell migration using an Ornstein-Uhlenbeck (OU) process, directionally biased based on the gradient field of an underlying topography, to describe the time evolution of cell velocity for a discrete-point cell. We use this model to probe the influence of linearly and randomly organised topographies on migration trajectory behaviour and how the gradual introduction of random perturbations to linear features changes this behaviour, with the intention to further understand how surface imperfections introduced by coarse methods of surface fabrication might impact migration. We parametrise the model using experimental data for *in vitro* fibroblast migration on a precisely fabricated linearly ridged/grooved topography with constant ridge (1μm) and varied groove widths (1-9.1μm) and with numerically generated topographies featuring comparable dimensions (constant ridge width, 1μm, and 9μm, 6μm and 2μm groove widths). We use the parametrised model to predict how random perturbations in the plane orthogonal to ridge/groove direction modulate spatial behaviour over time. We found that the parametrised model was able to closely reproduce migration metric statistic data derived from the experimental study by Kim et al. [105], as well as general trends in migration behaviour reported. Results showed that standard deviation for orientation angle distributions, θ_σ, decreased monotonically with decrease to groove

width, smallest θ_σ observed for the 2μm groove width which prompted the most directionally aligned migration trajectories. We also saw evident an optimal groove width for mean migration speed, s_μ, observed for the 6μm groove width which prompted trajectories to exhibit the highest displacements of the groove widths tested.

We also found that introducing graded random perturbations to the linear features dispersed migration, and increasing the perturbation level reduced trajectory alignment and increased speed for all groove widths, 9μm, 6μm and 2μm. This finding could potentially be explored by experimentalists as an approach to either enhance or diminish cell directionality, displacement or dispersal.

In the first section of the second part of the thesis, *Chapter* 3, we derive a model for Cx43 cycling dynamics with Gap27 binding. Based on the established biology, we formulated a reaction scheme for hemichannel, gap junction, plaque and annular gap junction species in the Cx43 life cycle and, by mass action kinetics, derive the associated ODE system. We circumvent consideration of all individual plaque states, p_i, where $i = 2, ..., n$, in the model by deriving ODEs for the zeroeth, first and second order moments of the plaque state distribution, closing by approximation of the third order moment, reducing the infinite-dimensional sub-system of plaque states by considering only its time-dependent moment variables and adopting the 'averaged' model thereafter.

We considered cycling model dynamics both without and with Gap27, to investigate how the introduction of Gap27 affected Cx43-based species dynamics. We found the model exhibited simple steady-state behaviour, identifying only stable one equilibrium point which shifted monotonically under parameter variation. Without Gap27, we found the model could qualitatively reproduce gap junction plaque dynamics reported

in the experimental literature, in which large plaques were able to form in small concentration [133].

Results showed the introduction of Gap27 modulated only transient behaviour of Cx43-based species, hemichannels, gap junctions, plaques and annular gap junctions, over time. This effect was found to be dependent on both Gap27 concentration and hemichannel-Gap27 association/dissociation ratio. The modulating effect of Gap27 increased with concentration and with the association/dissociation ratio, but approached a step-function-like limit for the latter.

The transiently modulating, concentration-dependent efficacy of Gap27 observed in the model is typical of what is reported in experimental studies. Gap27 has been shown to reduce dye transfer in fibroblast and HeLa cell clusters in a concentration-dependent manner in a study by Wright et al. [32] and is typically reapplied intervallically in experiments to maintain its therapeutic effect (see [20, 32]). Further work on this model, including parametrisation, could provide further insight into how Gap27 could be used experimentally to optimally disrupt functional plaque formation and subsequent cell-cell metabolite exchange.

In the last section of the second part of the thesis, *Chapter* 4, we develop a Cx43-based cell-cell interaction influenced migration model based on earlier introduced models for Cx43 cycling with Gap27 binding and individual cell migration. We assign each discrete-point cell in the model 2-d spatial dimensions within which they can interact with neighbouring cells within a cell population, the interaction determined to depend on Cx43 dynamics. We develop a computational framework to approximate the 2-d spatial configuration of a 'scrape wound' assay, in which two cell populations are initially separated by an unpopulated 'wound', attaching spatial units and assigning a

population density using experimental data. We use this model to investigate how Cx43 dynamics could affect cell migration and subsequent population invasion into a scrape wound and how the introduction of a CMP like Gap27 might function to modulate these cellular behaviours.

We consider how model dynamics affect migration behaviour and scrape wound closure both without and with Gap27. We found that if steady-state concentration for gap junction plaque species, p^*, was large, migrating cells clustered into isolated neighbourhoods in each separated population over the domain and rarely entered the wound region, which remained virtually unpopulated over time. The introduction of Gap27 however, reduced clustering in migrating cells and restored typical migration behaviour, which, over time, collectively invaded the wound region; closing the 'scrape wound'. The rate of wound closure was dependent on initial concentration of Gap27, $g_{27}(0)$, the spatial effect of which reduced discernibly with p^*. Results also showed that when p^* is small, migration behaviour is qualitatively similar to when p^* and $g_{27}(0)$ are both large, significantly reducing clustering and promoting population of the wound region over time.

These results suggest a potential mechanism for delayed cellular response and stunted migration in non-healing wounds. It is possible that Cx43-influenced local cell clustering could disrupt typical migration patterns into the wounded region post-injury, encouraging cells to adopt interactive and communicative rather than necessary migratory behaviours. Results also suggest that Gap27 may function to rescue cells from clustering and restore typical post-injury migratory behaviour to induce wound closure, potentially offering insight into why Gap27 might be less effective in treating some types of chronic wound, e.g. diabetic [160].

An interesting question raised by the work presented in this thesis is whether topographies and CMPs like Gap27 could work synergistically to improve scrape wound closure. Both the experimental study by Kim et al. [105] and topographically influenced cell migration model in *Chapter* 2 suggested topographic configurations able to prompt optimal linear directionality and migration speed in fibroblasts (e.g. linearly ridged/grooved with approximately 2μm and 6μm groove widths, respectively), and predicted migration speed and dispersal might be enhanced by the introduction of random feature perturbations. Kim et al. probed experimentally how linearly ridged/grooved topographies affected fibroblast invasion of a scrape wound *in vitro*. The authors found that linear topographic features arranged parallel to the wound region restricted migration into the wound, whereas if arranged perpendicularly migration into the wound could be enhanced, even speeding up wound closure dependent on groove width [80].

It could be interesting, using the models developed in this thesis, to compare how rate of scrape wound closure differed when modulated topographically rather than with a connexin mimetic peptide. Further still, it could be possible to integrate both topographically and Cx43 influenced migration models to investigate how these powerful regulators of cellular behaviour could interact to affect healing. Could the introduction of an underlying topography provide enough of a directional stimulus to guide cells into the wound, or would clustering prevail? Combining treatments would raise many more interesting propositions. Could the introduction of a topography, as experimental studies might suggest [80], accelerate or perturb wound closure? Could this be dependent on spatial pattern, orientation and dimension of the topography? Future studies to investigate such questions could help to generate potential new treatment regimen for

experimental testing.

Bibliography

[1] T. Velnar, T. Bailey, and V. Smrkolj, "The wound healing process: an overview of the cellular and molecular mechanisms," *Journal of International Medical Research*, vol. 37, no. 5, pp. 1528–1542, 2009.

[2] A. J. Singer and R. A. Clark, "Cutaneous wound healing," *New England journal of medicine*, vol. 341, no. 10, pp. 738–746, 1999.

[3] C. Lindholm and R. Searle, "Wound management for the 21st century: combining effectiveness and efficiency," *International wound journal*, vol. 13, pp. 5–15, 2016.

[4] J. Guest, K. Vowden, and P. Vowden, "The health economic burden that acute and chronic wounds impose on an average clinical commissioning group/health board in the uk," *Journal of wound care*, vol. 26, no. 6, pp. 292–303, 2017.

[5] J. F. Guest, N. Ayoub, T. McIlwraith, I. Uchegbu, A. Gerrish, D. Weidlich, K. Vowden, and P. Vowden, "Health economic burden that different wound types impose on the uk's national health service," *International wound journal*, vol. 14, no. 2, pp. 322–330, 2017.

[6] P. Scarborough, P. Bhatnagar, K. K. Wickramasinghe, S. Allender, C. Foster, and M. Rayner, "The economic burden of ill health due to diet, physical inactivity,

smoking, alcohol and obesity in the uk: an update to 2006–07 nhs costs," *Journal of public health*, vol. 33, no. 4, pp. 527–535, 2011.

[7] C. K. Sen, G. M. Gordillo, S. Roy, R. Kirsner, L. Lambert, T. K. Hunt, F. Gottrup, G. C. Gurtner, and M. T. Longaker, "Human skin wounds: a major and snowballing threat to public health and the economy," *Wound repair and regeneration*, vol. 17, no. 6, pp. 763–771, 2009.

[8] M. Olsson, K. Järbrink, U. Divakar, R. Bajpai, Z. Upton, A. Schmidtchen, and J. Car, "The humanistic and economic burden of chronic wounds: a systematic review," *Wound Repair and Regeneration*, vol. 27, no. 1, pp. 114–125, 2019.

[9] C. K. Sen, "Human wound and its burden: updated 2020 compendium of estimates," *Advances in wound care*, vol. 10, no. 5, pp. 281–292, 2021.

[10] D. L. Hunt, "Diabetes: foot ulcers and amputations," *BMJ clinical evidence*, vol. 2009; 0602, pp. 1–16, 2009.

[11] H. M. Khor, J. Tan, N. I. Saedon, S. B. Kamaruzzaman, A. V. Chin, P. J. Poi, and M. P. Tan, "Determinants of mortality among older adults with pressure ulcers," *Archives of gerontology and geriatrics*, vol. 59, no. 3, pp. 536–541, 2014.

[12] P. Martin, "Wound healing–aiming for perfect skin regeneration," *Science*, vol. 276, no. 5309, pp. 75–81, 1997.

[13] J. McGrath, R. Eady, and F. Pope, "Anatomy and organization of human skin," *Rook's textbook of dermatology*, vol. 1, pp. 3–2, 2004.

[14] M. Rodrigues, N. Kosaric, C. A. Bonham, and G. C. Gurtner, "Wound healing: a cellular perspective," *Physiological reviews*, vol. 99, no. 1, pp. 665–706, 2019.

[15] R. O. Hynes, "The extracellular matrix: not just pretty fibrils," *Science*, vol. 326, no. 5957, pp. 1216–1219, 2009.

[16] C. Frantz, K. M. Stewart, and V. M. Weaver, "The extracellular matrix at a glance," *Journal of cell science*, vol. 123, no. 24, pp. 4195–4200, 2010.

[17] A. D. Theocharis, S. S. Skandalis, C. Gialeli, and N. K. Karamanos, "Extracellular matrix structure," *Advanced drug delivery reviews*, vol. 97, pp. 4–27, 2016.

[18] N. S. Greaves, K. J. Ashcroft, M. Baguneid, and A. Bayat, "Current understanding of molecular and cellular mechanisms in fibroplasia and angiogenesis during acute wound healing," *Journal of dermatological science*, vol. 72, no. 3, pp. 206–217, 2013.

[19] D. L. Becker, C. Thrasivoulou, and A. R. Phillips, "Connexins in wound healing; perspectives in diabetic patients," *Biochimica et Biophysica Acta (BBA)-Biomembranes*, vol. 1818, no. 8, pp. 2068–2075, 2012.

[20] P. E. Martin, J. A. Easton, M. B. Hodgins, and C. S. Wright, "Connexins: sensors of epidermal integrity that are therapeutic targets," *FEBS letters*, vol. 588, no. 8, pp. 1304–1314, 2014.

[21] C. Lorraine, C. S. Wright, and P. E. Martin, "Connexin43 plays diverse roles in co-ordinating cell migration and wound closure events," *Biochemical Society Transactions*, vol. 43, no. 3, pp. 482–488, 2015.

[22] J. M. Brandner, P. Houdek, B. Hüsing, C. Kaiser, and I. Moll, "Connexins 26, 30, and 43: differences among spontaneous, chronic, and accelerated human wound

healing," *Journal of investigative dermatology*, vol. 122, no. 5, pp. 1310–1320, 2004.

[23] J. A. Goliger and D. L. Paul, "Wounding alters epidermal connexin expression and gap junction-mediated intercellular communication," *Molecular biology of the cell*, vol. 6, no. 11, pp. 1491–1501, 1995.

[24] P. Coutinho, C. Qiu, S. Frank, K. Tamber, and D. Becker, "Dynamic changes in connexin expression correlate with key events in the wound healing process," *Cell biology international*, vol. 27, no. 7, pp. 525–541, 2003.

[25] J. Sutcliffe, K. Chin, C. Thrasivoulou, T. Serena, S. O'neil, R. Hu, A. White, L. Madden, T. Richards, A. Phillips, *et al.*, "Abnormal connexin expression in human chronic wounds," *British Journal of Dermatology*, vol. 173, no. 5, pp. 1205–1215, 2015.

[26] C. M. Wang, J. Lincoln, J. E. Cook, and D. L. Becker, "Abnormal connexin expression underlies delayed wound healing in diabetic skin," *Diabetes*, vol. 56, no. 11, pp. 2809–2817, 2007.

[27] A. Mendoza-Naranjo, P. Cormie, A. E. Serrano, C. M. Wang, C. Thrasivoulou, J. E. Sutcliffe, D. J. Gilmartin, J. Tsui, T. E. Serena, A. R. Phillips, *et al.*, "Overexpression of the gap junction protein cx43 as found in diabetic foot ulcers can retard fibroblast migration," *Cell biology international*, vol. 36, no. 7, pp. 661–667, 2012.

[28] C. Qiu, P. Coutinho, S. Frank, S. Franke, L.-y. Law, P. Martin, C. R. Green, and D. L. Becker, "Targeting connexin43 expression accelerates the rate of wound repair," *Current Biology*, vol. 13, no. 19, pp. 1697–1703, 2003.

[29] M. Kretz, C. Euwens, S. Hombach, D. Eckardt, B. Teubner, O. Traub, K. Willecke, and T. Ott, "Altered connexin expression and wound healing in the epidermis of connexin-deficient mice," *Journal of cell science*, vol. 116, no. 16, pp. 3443–3452, 2003.

[30] B. Cogliati, M. Vinken, T. C. Silva, C. M. Araújo, T. P. Aloia, L. M. Chaible, C. M. Mori, and M. L. Dagli, "Connexin 43 deficiency accelerates skin wound healing and extracellular matrix remodeling in mice," *Journal of dermatological science*, vol. 79, no. 1, pp. 50–56, 2015.

[31] M. Ziaei, C. Greene, and C. R. Green, "Wound healing in the eye: therapeutic prospects," *Advanced drug delivery reviews*, vol. 126, pp. 162–176, 2018.

[32] C. S. Wright, M. A. Van Steensel, M. B. Hodgins, and P. E. Martin, "Connexin mimetic peptides improve cell migration rates of human epidermal keratinocytes and dermal fibroblasts in vitro," *Wound repair and regeneration*, vol. 17, no. 2, pp. 240–249, 2009.

[33] R. Ananthakrishnan and A. Ehrlicher, "The forces behind cell movement," *International journal of biological sciences*, vol. 3, no. 5, p. 303, 2007.

[34] A. Aman and T. Piotrowski, "Cell migration during morphogenesis," *Developmental biology*, vol. 341, no. 1, pp. 20–33, 2010.

[35] D. A. Lauffenburger and A. F. Horwitz, "Cell migration: a physically integrated molecular process," *cell*, vol. 84, no. 3, pp. 359–369, 1996.

[36] H. L. Sweeney and A. Houdusse, "Structural and functional insights into the myosin motor mechanism," *Annual review of biophysics*, vol. 39, pp. 539–557, 2010.

[37] R. J. Petrie, A. D. Doyle, and K. M. Yamada, "Random versus directionally persistent cell migration," *Nature reviews Molecular cell biology*, vol. 10, no. 8, pp. 538–549, 2009.

[38] J. A. Sherratt, "Chemotaxis and chemokinesis in eukaryotic cells: the Keller-Segel equations as an approximation to a detailed model," *Bulletin of mathematical biology*, vol. 56, no. 1, pp. 129–146, 1994.

[39] C.-M. Lo, H.-B. Wang, M. Dembo, and Y.-l. Wang, "Cell movement is guided by the rigidity of the substrate," *Biophysical journal*, vol. 79, no. 1, pp. 144–152, 2000.

[40] R. B. Dickinson and R. T. Tranquillo, "A stochastic model for adhesion-mediated cell random motility and haptotaxis," *Journal of mathematical biology*, vol. 31, no. 6, pp. 563–600, 1993.

[41] J.-P. Kaiser, A. Reinmann, and A. Bruinink, "The effect of topographic characteristics on cell migration velocity," *Biomaterials*, vol. 27, no. 30, pp. 5230–5241, 2006.

[42] G. Charras and E. Sahai, "Physical influences of the extracellular environment on cell migration," *Nature reviews Molecular cell biology*, vol. 15, no. 12, pp. 813–824, 2014.

[43] S. A. Biela, Y. Su, J. P. Spatz, and R. Kemkemer, "Different sensitivity of human endothelial cells, smooth muscle cells and fibroblasts to topography in the nano–micro range," *Acta biomaterialia*, vol. 5, no. 7, pp. 2460–2466, 2009.

[44] M. Irving, M. F. Murphy, F. Lilley, P. W. French, D. R. Burton, S. Dixon, and M. C. Sharp, "The use of abrasive polishing and laser processing for developing polyurethane surfaces for controlling fibroblast cell behaviour," *Materials Science and Engineering: C*, vol. 71, pp. 690–697, 2017.

[45] N. Gomez, S. Chen, and C. E. Schmidt, "Polarization of hippocampal neurons with competitive surface stimuli: contact guidance cues are preferred over chemical ligands," *Journal of The Royal Society Interface*, vol. 4, no. 13, pp. 223–233, 2007.

[46] B. A. Dalton, X. F. Walboomers, M. Dziegielewski, M. D. Evans, S. Taylor, J. A. Jansen, and J. G. Steele, "Modulation of epithelial tissue and cell migration by microgrooves," *Journal of Biomedical Materials Research: An Official Journal of The Society for Biomaterials, The Japanese Society for Biomaterials, and The Australian Society for Biomaterials and the Korean Society for Biomaterials*, vol. 56, no. 2, pp. 195–207, 2001.

[47] J. Mai, C. Sun, S. Li, and X. Zhang, "A microfabricated platform probing cytoskeleton dynamics using multidirectional topographical cues," *Biomedical microdevices*, vol. 9, no. 4, pp. 523–531, 2007.

[48] M. Nikkhah, F. Edalat, S. Manoucheri, and A. Khademhosseini, "Engineering microscale topographies to control the cell–substrate interface," *Biomaterials*, vol. 33, no. 21, pp. 5230–5246, 2012.

[49] A. Curtis and M. Riehle, "Tissue engineering: the biophysical background," *Physics in Medicine & Biology*, vol. 46, no. 4, p. R47, 2001.

[50] E. M. Tottoli, R. Dorati, I. Genta, E. Chiesa, S. Pisani, and B. Conti, "Skin wound healing process and new emerging technologies for skin wound care and regeneration," *Pharmaceutics*, vol. 12, no. 8, p. 735, 2020.

[51] D. W. Hamilton, S. Ghrebi, H. Kim, B. Chehroudi, and D. M. Brunette, "Surface topography and cell behaviour," in *Encyclopedia of biomaterials and biomedical engineering*, pp. 1–15, Taylor and Francis New York, 2006.

[52] V. Kearns, R. McMurray, and M. Dalby, "Biomaterial surface topography to control cellular response: technologies, cell behaviour and biomedical applications," in *Surface modification of biomaterials*, pp. 169–201, Elsevier, 2011.

[53] P. Thomsen and C. Gretzer, "Macrophage interactions with modified material surfaces," *Current Opinion in Solid State and Materials Science*, vol. 5, no. 2-3, pp. 163–176, 2001.

[54] J. D. Murray, *Mathematical biology II: spatial models and biomedical applications*, vol. 3. Springer New York, 2001.

[55] P. K. Maini, L. Olsen, and J. A. Sherratt, "Mathematical models for cell-matrix interactions during dermal wound healing," *International Journal of Bifurcation and Chaos*, vol. 12, no. 09, pp. 2021–2029, 2002.

[56] A. Guerra, J. Belinha, and R. N. Jorge, "Modelling skin wound healing angiogenesis: A review," *Journal of theoretical biology*, vol. 459, pp. 1–17, 2018.

[57] J. A. Sherratt and J. C. Dallon, "Theoretical models of wound healing: past successes and future challenges," *Comptes Rendus Biologies*, vol. 325, no. 5, pp. 557–564, 2002.

[58] A. B. Tepole and E. Kuhl, "Systems-based approaches toward wound healing," *Pediatric research*, vol. 73, no. 2, pp. 553–563, 2013.

[59] S. N. Jorgensen and J. R. Sanders, "Mathematical models of wound healing and closure: a comprehensive review," *Medical & biological engineering & computing*, vol. 54, no. 9, pp. 1297–1316, 2016.

[60] J. A. Sherratt and J. D. Murray, "Models of epidermal wound healing," *Proceedings of the Royal Society of London. Series B: Biological Sciences*, vol. 241, no. 1300, pp. 29–36, 1990.

[61] R. T. Tranquillo and J. Murray, "Continuum model of fibroblast-driven wound contraction: inflammation-mediation," *Journal of theoretical biology*, vol. 158, no. 2, pp. 135–172, 1992.

[62] C. L. Stokes, D. A. Lauffenburger, and S. K. Williams, "Migration of individual microvessel endothelial cells: stochastic model and parameter measurement," *Journal of cell science*, vol. 99, no. 2, pp. 419–430, 1991.

[63] M. P. Neilson, D. M. Veltman, P. J. van Haastert, S. D. Webb, J. A. Mackenzie, and R. H. Insall, "Chemotaxis: a feedback-based computational model robustly predicts multiple aspects of real cell behaviour," *PLoS biology*, vol. 9, no. 5, p. e1000618, 2011.

[64] J. C. Dallon, J. A. Sherratt, and P. K. Maini, "Mathematical modelling of extracellular matrix dynamics using discrete cells: fiber orientation and tissue regeneration," *Journal of theoretical biology*, vol. 199, no. 4, pp. 449–471, 1999.

[65] F. Stefanoni, M. Ventre, F. Mollica, and P. A. Netti, "A numerical model for durotaxis," *Journal of theoretical biology*, vol. 280, no. 1, pp. 150–158, 2011.

[66] T. Heydari, M. Heidari, O. Mashinchian, M. Wojcik, K. Xu, M. J. Dalby, M. Mahmoudi, and M. R. Ejtehadi, "Development of a virtual cell model to predict cell response to substrate topography," *ACS nano*, vol. 11, no. 9, pp. 9084–9092, 2017.

[67] N. Loy and M. Conte, "Multi-cue kinetic model with non-local sensing for cell migration on a fibers network with chemotaxis," *arXiv preprint arXiv:2006.09707*, 2020.

[68] V. H. Barocas and R. T. Tranquillo, "An anisotropic biphasic theory of tissue-equivalent mechanics: the interplay among cell traction, fibrillar network deformation, fibril alignment, and cell contact guidance," *Journal of Biomechanical engineering*, vol. 119, no. 2, pp. 137–145, 1997.

[69] B. Winkler, I. S. Aranson, and F. Ziebert, "Confinement and substrate topography control cell migration in a 3d computational model," *Communications Physics*, vol. 2, no. 1, pp. 1–11, 2019.

[70] R. Vogel and R. Weingart, "Mathematical model of vertebrate gap junctions derived from electrical measurements on homotypic and heterotypic channels," *The Journal of physiology*, vol. 510, no. Pt 1, p. 177, 1998.

[71] A. Casaleggio, M. L. Hines, and M. Migliore, "Computational model of erratic arrhythmias in a cardiac cell network: the role of gap junctions," *PLoS One*, vol. 9, no. 6, p. e100288, 2014.

[72] A. Loppini, M. Braun, S. Filippi, and M. G. Pedersen, "Mathematical modeling of gap junction coupling and electrical activity in human β-cells," *Physical biology*, vol. 12, no. 6, p. 066002, 2015.

[73] M. Dougoud, L. Vinckenbosch, C. Mazza, B. Schwaller, and L. Pecze, "The effect of gap junctional coupling on the spatiotemporal patterns of ca2+ signals and the harmonization of ca2+-related cellular responses," *PLoS computational biology*, vol. 12, no. 12, p. e1005295, 2016.

[74] A. Mondal, D. A. Appadurai, N. W. Akoum, F. B. Sachse, and A. P. Moreno, "Computational simulations of asymmetric fluxes of large molecules through gap junction channel pores," *Journal of theoretical biology*, vol. 412, pp. 61–73, 2017.

[75] P. C. Bressloff, "Diffusion in cells with stochastically gated gap junctions," *SIAM Journal on Applied Mathematics*, vol. 76, no. 4, pp. 1658–1682, 2016.

[76] F. Roberts, M. Al-Husari, U. George, K. Giorgakoudi, J. Caffrey, A. Shabala, C. Bell, E. Chang, S. Webb, J. Ward, *et al.*, "Connexins: A novel target for wound healing." `https://mmsg.mathmos.net/uk/2010/diabetic-wounds`, 2010.

[77] F. Graner and J. A. Glazier, "Simulation of biological cell sorting using a two-dimensional extended Potts model," *Physical review letters*, vol. 69, no. 13, p. 2013, 1992.

[78] J. C. Dallon, J. A. Sherratt, and P. K. Maini, "Modeling the effects of transforming growth factor-β on extracellular matrix alignment in dermal wound repair," *Wound Repair and Regeneration*, vol. 9, no. 4, pp. 278–286, 2001.

[79] J. Montgomery, W. J. Richardson, S. Marsh, J. M. Rhett, F. Bustos, K. Degen, G. S. Ghatnekar, C. L. Grek, L. J. Jourdan, J. W. Holmes, *et al.*, "The connexin 43 carboxyl terminal mimetic peptide αct1 prompts differentiation of a collagen scar matrix in humans resembling unwounded skin," *The FASEB Journal*, vol. 35, no. 8, p. e21762, 2021.

[80] H. N. Kim, Y. Hong, M. S. Kim, S. M. Kim, and K.-Y. Suh, "Effect of orientation and density of nanotopography in dermal wound healing," *Biomaterials*, vol. 33, no. 34, pp. 8782–8792, 2012.

[81] G. Dunn and A. Brown, "A unified approach to analysing cell motility," *Journal of Cell Science*, vol. 1987, no. Supplement_8, pp. 81–102, 1987.

[82] T. Gowers, J. Barrow-Green, and I. Leader, *The Princeton companion to mathematics*. Princeton University Press, 2008.

[83] S. Särkkä and A. Solin, *Applied stochastic differential equations*, vol. 10. Cambridge University Press, 2019.

[84] Y. Pomeau and J. Piasecki, "The Langevin equation," *Comptes Rendus Physique*, vol. 18, no. 9-10, pp. 570–582, 2017.

[85] O. Contreras-Vergara, N. Lucero-Azuara, N. Sánchez-Salas, and J. Jiménez-Aquino, "Langevin original approach and Ornstein–Uhlenbeck-type processes," *Physica A: Statistical Mechanics and its Applications*, p. 126349, 2021.

[86] J. L. Doob, "The Brownian movement and stochastic equations," *Annals of Mathematics*, pp. 351–369, 1942.

[87] D. J. Higham, "An algorithmic introduction to numerical simulation of stochastic differential equations," *SIAM review*, vol. 43, no. 3, pp. 525–546, 2001.

[88] J. D. Logan and W. Wolesensky, *Mathematical methods in biology*, vol. 96. John Wiley & Sons, 2009.

[89] J. Duan, *An introduction to stochastic dynamics*, vol. 51. Cambridge University Press, 2015.

[90] G. E. Uhlenbeck and L. S. Ornstein, "On the theory of the Brownian motion," *Physical review*, vol. 36, no. 5, p. 823, 1930.

[91] D. T. Gillespie, "Exact numerical simulation of the Ornstein-Uhlenbeck process and its integral," *Physical review E*, vol. 54, no. 2, p. 2084, 1996.

[92] P. Kloeden and E. Platen, *Numerical Solution of Stochastic Differential Equations*, vol. 3. Springer-Verlag Berlin, 1999.

[93] R. G. Harrison, "The reaction of embryonic cells to solid structures," *Journal of Experimental Zoology*, vol. 17, no. 4, pp. 521–544, 1914.

[94] P. Weiss, "Nerve patterns: the mechanisms of nerve growth," *Growth*, vol. 5, pp. 163–203, 1941.

[95] A. Curtis and M. Varde, "Control of cell behavior: topological factors," *Journal of the National Cancer Institute*, vol. 33, no. 1, pp. 15–26, 1964.

[96] H. Rostam, S. Singh, N. Vrana, M. Alexander, and A. Ghaemmaghami, "Impact of surface chemistry and topography on the function of antigen presenting cells," *Biomaterials science*, vol. 3, no. 3, pp. 424–441, 2015.

[97] J. Kim, Y. Cao, C. Eddy, Y. Deng, H. Levine, W.-J. Rappel, and B. Sun, "The mechanics and dynamics of cancer cells sensing noisy 3d contact guidance," *Proceedings of the National Academy of Sciences*, vol. 118, no. 10, 2021.

[98] I. A. Janson and A. J. Putnam, "Extracellular matrix elasticity and topography: Material-based cues that affect cell function via conserved mechanisms," *Journal of biomedical materials research Part A*, vol. 103, no. 3, pp. 1246–1258, 2015.

[99] A. D. Doyle, R. J. Petrie, M. L. Kutys, and K. M. Yamada, "Dimensions in cell migration," *Current opinion in cell biology*, vol. 25, no. 5, pp. 642–649, 2013.

[100] L. Ge, L. Yang, R. Bron, J. K. Burgess, and P. van Rijn, "Topography-mediated fibroblast cell migration is influenced by direction, wavelength, and amplitude," *ACS Applied Bio Materials*, vol. 3, no. 4, pp. 2104–2116, 2020.

[101] C. Leclech and A. I. Barakat, "Is there a universal mechanism of cell alignment in response to substrate topography?," *Cytoskeleton*, vol. 78, no. 6, pp. 284–292, 2021.

[102] C. Dai, S. Shih, and A. Khachemoune, "Skin substitutes for acute and chronic wound healing: an updated review," *Journal of Dermatological Treatment*, vol. 31, no. 6, pp. 639–648, 2020.

[103] A. Vishwakarma, N. S. Bhise, M. B. Evangelista, J. Rouwkema, M. R. Dokmeci, A. M. Ghaemmaghami, N. E. Vrana, and A. Khademhosseini, "Engineering im-

munomodulatory biomaterials to tune the inflammatory response," *Trends in biotechnology*, vol. 34, no. 6, pp. 470–482, 2016.

[104] N. Gomez, S. Chen, and C. E. Schmidt, "Polarization of hippocampal neurons with competitive surface stimuli: contact guidance cues are preferred over chemical ligands," *Journal of The Royal Society Interface*, vol. 4, no. 13, pp. 223–233, 2006.

[105] D.-H. Kim, K. Han, K. Gupta, K. W. Kwon, K.-Y. Suh, and A. Levchenko, "Mechanosensitivity of fibroblast cell shape and movement to anisotropic substratum topography gradients," *Biomaterials*, vol. 30, no. 29, pp. 5433–5444, 2009.

[106] J.-P. Kaiser and A. Bruinink, "Investigating cell–material interactions by monitoring and analysing cell migration," *Journal of Materials Science: Materials in Medicine*, vol. 15, no. 4, pp. 429–435, 2004.

[107] A. D. Doyle, F. W. Wang, K. Matsumoto, and K. M. Yamada, "One-dimensional topography underlies three-dimensional fibrillar cell migration," *The Journal of cell biology*, vol. 184, no. 4, pp. 481–490, 2009.

[108] M. T. Frey, I. Y. Tsai, T. P. Russell, S. K. Hanks, and Y.-l. Wang, "Cellular responses to substrate topography: role of myosin ii and focal adhesion kinase," *Biophysical journal*, vol. 90, no. 10, pp. 3774–3782, 2006.

[109] R. D. Sochol, A. T. Higa, R. R. Janairo, S. Li, and L. Lin, "Unidirectional mechanical cellular stimuli via micropost array gradients," *Soft Matter*, vol. 7, no. 10, pp. 4606–4609, 2011.

[110] A. Saez, M. Ghibaudo, A. Buguin, P. Silberzan, and B. Ladoux, "Rigidity-driven growth and migration of epithelial cells on microstructured anisotropic substrates," *Proceedings of the National Academy of Sciences*, vol. 104, no. 20, pp. 8281–8286, 2007.

[111] C. C. Berry, G. Campbell, A. Spadiccino, M. Robertson, and A. S. Curtis, "The influence of microscale topography on fibroblast attachment and motility," *Biomaterials*, vol. 25, no. 26, pp. 5781–5788, 2004.

[112] H. N. Kim, A. Jiao, N. S. Hwang, M. S. Kim, D.-H. Kim, K.-Y. Suh, *et al.*, "Nanotopography-guided tissue engineering and regenerative medicine," *Advanced drug delivery reviews*, vol. 65, no. 4, pp. 536–558, 2013.

[113] D.-H. Kim, P. P. Provenzano, C. L. Smith, and A. Levchenko, "Matrix nanotopography as a regulator of cell function," *Journal of Cell Biology*, vol. 197, no. 3, pp. 351–360, 2012.

[114] K. Anselme and M. Bigerelle, "Role of materials surface topography on mammalian cell response," *International Materials Reviews*, vol. 56, no. 4, pp. 243–266, 2011.

[115] H. Jeon, C. G. Simon Jr, and G. Kim, "A mini-review: cell response to microscale, nanoscale, and hierarchical patterning of surface structure," *Journal of biomedical materials research Part B: applied biomaterials*, vol. 102, no. 7, pp. 1580–1594, 2014.

[116] H. Jeon, H. Hidai, D. J. Hwang, K. E. Healy, and C. P. Grigoropoulos, "The effect of micronscale anisotropic cross patterns on fibroblast migration," *Biomaterials*, vol. 31, no. 15, pp. 4286–4295, 2010.

[117] D.-H. Kim, C.-H. Seo, K. Han, K. W. Kwon, A. Levchenko, and K.-Y. Suh, "Guided cell migration on microtextured substrates with variable local density and anisotropy," *Advanced functional materials*, vol. 19, no. 10, pp. 1579–1586, 2009.

[118] M. J. Dalby, M. O. Riehle, D. S. Sutherland, H. Agheli, and A. S. Curtis, "Changes in fibroblast morphology in response to nano-columns produced by colloidal lithography," *Biomaterials*, vol. 25, no. 23, pp. 5415–5422, 2004.

[119] C.-H. Choi, S. H. Hagvall, B. M. Wu, J. C. Dunn, R. E. Beygui, *et al.*, "Cell interaction with three-dimensional sharp-tip nanotopography," *Biomaterials*, vol. 28, no. 9, pp. 1672–1679, 2007.

[120] T. Steinberg, S. Schulz, J. P. Spatz, N. Grabe, E. Mussig, A. Kohl, G. Komposch, and P. Tomakidi, "Early keratinocyte differentiation on micropillar interfaces," *Nano letters*, vol. 7, no. 2, pp. 287–294, 2007.

[121] S. McDougall, J. Dallon, J. Sherratt, and P. Maini, "Fibroblast migration and collagen deposition during dermal wound healing: mathematical modelling and clinical implications," *Philosophical Transactions of the Royal Society A: Mathematical, Physical and Engineering Sciences*, vol. 364, no. 1843, pp. 1385–1405, 2006.

[122] K. Painter, "Modelling cell migration strategies in the extracellular matrix," *Journal of mathematical biology*, vol. 58, no. 4, pp. 511–543, 2009.

[123] D. K. Schlüter, I. Ramis-Conde, and M. A. Chaplain, "Computational modeling of single-cell migration: the leading role of extracellular matrix fibers," *Biophysical journal*, vol. 103, no. 6, pp. 1141–1151, 2012.

[124] M. H. Zaman, R. D. Kamm, P. Matsudaira, and D. A. Lauffenburger, "Computational model for cell migration in three-dimensional matrices," *Biophysical journal*, vol. 89, no. 2, pp. 1389–1397, 2005.

[125] P. Moreo, J. M. García-Aznar, and M. Doblaré, "Modeling mechanosensing and its effect on the migration and proliferation of adherent cells," *Acta Biomaterialia*, vol. 4, no. 3, pp. 613–621, 2008.

[126] C. Borau, R. Kamm, and J. García-Aznar, "Mechano-sensing and cell migration: a 3d model approach," *Physical biology*, vol. 8, no. 6, p. 066008, 2011.

[127] I. V. Dokukina and M. E. Gracheva, "A model of fibroblast motility on substrates with different rigidities," *Biophysical journal*, vol. 98, no. 12, pp. 2794–2803, 2010.

[128] A. Ray, O. Lee, Z. Win, R. M. Edwards, P. W. Alford, D.-H. Kim, and P. P. Provenzano, "Anisotropic forces from spatially constrained focal adhesions mediate contact guidance directed cell migration," *Nature communications*, vol. 8, no. 1, pp. 1–17, 2017.

[129] D. Conway, *Integrating In-Silico Models with In-Vitro Data to Generate Novel Insights into Biological Systems*. PhD thesis, Liverpool John Moores University, 2019.

[130] M. J. Dalby, "Topographically induced direct cell mechanotransduction," *Medical engineering & physics*, vol. 27, no. 9, pp. 730–742, 2005.

[131] K. B. Ensor and P. W. Glynn, "Stochastic optimization via grid search," *Lectures in Applied Mathematics-American Mathematical Society*, vol. 33, pp. 89–100, 1997.

[132] D. Segretain and M. M. Falk, "Regulation of connexin biosynthesis, assembly, gap junction formation, and removal," *Biochimica et Biophysica Acta (BBA)-Biomembranes*, vol. 1662, no. 1-2, pp. 3–21, 2004.

[133] T. M. Ribeiro-Rodrigues, T. Martins-Marques, S. Morel, B. R. Kwak, and H. Girão, "Role of connexin 43 in different forms of intercellular communication–gap junctions, extracellular vesicles and tunnelling nanotubes," *J cell Sci*, vol. 130, no. 21, pp. 3619–3630, 2017.

[134] D. A. Goodenough and D. L. Paul, "Beyond the gap: functions of unpaired connexon channels," *Nature reviews Molecular cell biology*, vol. 4, no. 4, pp. 285–295, 2003.

[135] J. L. Solan and P. D. Lampe, "Connexin43 phosphorylation: structural changes and biological effects," *Biochemical Journal*, vol. 419, no. 2, pp. 261–272, 2009.

[136] X.-F. Zhang and X. Cui, "Connexin 43: key roles in the skin," *Biomedical reports*, vol. 6, no. 6, pp. 605–611, 2017.

[137] T. A. van Veen, H. V. Van Rijen, and T. Opthof, "Cardiac gap junction channels: modulation of expression and channel properties," *Cardiovascular research*, vol. 51, no. 2, pp. 217–229, 2001.

[138] M. S. Fontes, T. A. van Veen, J. M. de Bakker, and H. V. van Rijen, "Functional consequences of abnormal cx43 expression in the heart," *Biochimica et Biophysica Acta (BBA)-Biomembranes*, vol. 1818, no. 8, pp. 2020–2029, 2012.

[139] Q. Shao, H. Wang, E. McLachlan, G. I. Veitch, and D. W. Laird, "Down-regulation of cx43 by retroviral delivery of small interfering rna promotes an ag-

gressive breast cancer cell phenotype," *Cancer research*, vol. 65, no. 7, pp. 2705–2711, 2005.

[140] C. Lamiche, J. Clarhaut, P.-O. Strale, S. Crespin, N. Pedretti, F.-X. Bernard, C. C. Naus, V. C. Chen, L. J. Foster, N. Defamie, *et al.*, "The gap junction protein cx43 is involved in the bone-targeted metastatic behaviour of human prostate cancer cells," *Clinical & experimental metastasis*, vol. 29, no. 2, pp. 111–122, 2012.

[141] L. Kanczuga-Koda, M. Koda, S. Sulkowski, A. Wincewicz, B. Zalewski, and M. Sulkowska, "Gradual loss of functional gap junction within progression of colorectal cancer—a shift from membranous cx32 and cx43 expression to cytoplasmic pattern during colorectal carcinogenesis," *In vivo*, vol. 24, no. 1, pp. 101–107, 2010.

[142] M.-P. Labarthe, J.-H. Saurat, D. Salomon, D. Bosco, and P. Meda, "Upregulation of connexin 26 between keratinocytes of psoriatic lesions," *Journal of investigative dermatology*, vol. 111, no. 1, pp. 72–76, 1998.

[143] M. L. Tan, H. L. Kwong, C. C. Ang, H. L. Tey, J. S. Lee, and D. L. Becker, "Changes in connexin 43 in inflammatory skin disorders: Eczema, psoriasis, and steven-johnson syndrome/toxic epidermal necrolysis," *Health science reports*, vol. 4, no. 1, p. e247, 2021.

[144] E. M. O'Shaughnessy, W. Duffy, L. Garcia-Vega, K. Hussey, A. D. Burden, M. Zamiri, and P. E. Martin, "Dysregulation of connexin expression plays a pivotal role in psoriasis," *International journal of molecular sciences*, vol. 22, no. 11, p. 6060, 2021.

[145] W. H. Evans and P. E. Martin, "Gap junctions: structure and function," *Molecular membrane biology*, vol. 19, no. 2, pp. 121–136, 2002.

[146] W. H. Evans and L. Leybaert, "Mimetic peptides as blockers of connexin channel-facilitated intercellular communication," *Cell communication & adhesion*, vol. 14, no. 6, pp. 265–273, 2007.

[147] D. R. King, M. W. Sedovy, X. Leng, J. Xue, S. Lamouille, M. Koval, B. E. Isakson, and S. R. Johnstone, "Mechanisms of connexin regulating peptides," *International Journal of Molecular Sciences*, vol. 22, no. 19, p. 10186, 2021.

[148] L. Leybaert, K. Braet, W. Vandamme, L. Cabooter, P. E. Martin, and W. H. Evans, "Connexin channels, connexin mimetic peptides and atp release," *Cell communication & adhesion*, vol. 10, no. 4-6, pp. 251–257, 2003.

[149] W. H. Evans and S. Boitano, "Connexin mimetic peptides: specific inhibitors of gap-junctional intercellular communication," *Biochemical Society Transactions*, vol. 29, no. 4, pp. 606–612, 2001.

[150] N. J. Severs, S. Rothery, E. Dupont, S. R. Coppen, H.-I. Yeh, Y.-S. Ko, T. Matsushita, R. Kaba, and D. Halliday, "Immunocytochemical analysis of connexin expression in the healthy and diseased cardiovascular system," *Microscopy research and technique*, vol. 52, no. 3, pp. 301–322, 2001.

[151] H. M. Elbadawy, P. Mirabelli, M. Xeroudaki, M. Parekh, M. Bertolin, C. Breda, C. Cagini, D. Ponzin, N. Lagali, and S. Ferrari, "Effect of connexin 43 inhibition by the mimetic peptide gap27 on corneal wound healing, inflammation and neovascularization," *British journal of pharmacology*, vol. 173, no. 19, pp. 2880–2893, 2016.

[152] J. Montgomery, G. S. Ghatnekar, C. L. Grek, K. E. Moyer, and R. G. Gourdie, "Connexin 43-based therapeutics for dermal wound healing," *International journal of molecular sciences*, vol. 19, no. 6, p. 1778, 2018.

[153] E. O. Jones, S. D. Webb, F. J. Ruiz-Fons, S. Albon, and L. Gilbert, "The effect of landscape heterogeneity and host movement on a tick-borne pathogen," *Theoretical Ecology*, vol. 4, no. 4, pp. 435–448, 2011.

[154] N. Balakrishnan and V. B. Nevzorov, *A primer on statistical distributions*. John Wiley & Sons, 2004.

[155] L. F. Shampine and M. W. Reichelt, "The matlab ode suite," *SIAM journal on scientific computing*, vol. 18, no. 1, pp. 1–22, 1997.

[156] A. Dhooge, W. Govaerts, and Y. A. Kuznetsov, "Matcont: a matlab package for numerical bifurcation analysis of odes," *ACM Transactions on Mathematical Software (TOMS)*, vol. 29, no. 2, pp. 141–164, 2003.

[157] P. E. Martin, C. Wall, and T. M. Griffith, "Effects of connexin-mimetic peptides on gap junction functionality and connexin expression in cultured vascular cells," *British journal of pharmacology*, vol. 144, no. 5, pp. 617–627, 2005.

[158] G. Richard, "Connexins: a connection with the skin," *Experimental Dermatology: Review Article*, vol. 9, no. 2, pp. 77–96, 2000.

[159] M. Chanson, M. Watanabe, E. M. O'Shaughnessy, A. Zoso, and P. E. Martin, "Connexin communication compartments and wound repair in epithelial tissue," *International journal of molecular sciences*, vol. 19, no. 5, p. 1354, 2018.

[160] S. Pollok, A.-C. Pfeiffer, R. Lobmann, C. S. Wright, I. Moll, P. E. Martin, and J. M. Brandner, "Connexin 43 mimetic peptide gap27 reveals potential differences in the role of cx43 in wound repair between diabetic and non-diabetic cells," *Journal of cellular and molecular medicine*, vol. 15, no. 4, pp. 861–873, 2011.

[161] P. Kameritsch, K. Pogoda, and U. Pohl, "Channel-independent influence of connexin 43 on cell migration," *Biochimica et Biophysica Acta (BBA)-Biomembranes*, vol. 1818, no. 8, pp. 1993–2001, 2012.

[162] N. Prochnow and R. Dermietzel, "Connexons and cell adhesion: a romantic phase," *Histochemistry and cell biology*, vol. 130, no. 1, p. 71, 2008.

[163] L. Leybaert, P. D. Lampe, S. Dhein, B. R. Kwak, P. Ferdinandy, E. C. Beyer, D. W. Laird, C. C. Naus, C. R. Green, and R. Schulz, "Connexins in cardiovascular and neurovascular health and disease: pharmacological implications," *Pharmacological reviews*, vol. 69, no. 4, pp. 396–478, 2017.

[164] M. Cotrina, J.-C. Lin, and M. Nedergaard, "Adhesive properties of connexin hemichannels," *Glia*, vol. 56, no. 16, pp. 1791–1798, 2008.

[165] W. J. Richardson and J. W. Holmes, "Emergence of collagen orientation heterogeneity in healing infarcts and an agent-based model," *Biophysical journal*, vol. 110, no. 10, pp. 2266–2277, 2016.

[166] M. Corporation, "Human dermal fibroblasts data sheet." `https://www.mattek.com/wp-content/uploads/Human-Dermal-Fibroblasts-Data-Sheet.pdf`, 2021.

[167] C. Borel, P. G. Ferreira, F. Santoni, O. Delaneau, A. Fort, K. Y. Popadin, M. Garieri, E. Falconnet, P. Ribaux, M. Guipponi, *et al.*, "Biased allelic expression in human primary fibroblast single cells," *The American Journal of Human Genetics*, vol. 96, no. 1, pp. 70–80, 2015.

[168] C. Faniku, E. O'Shaughnessy, C. Lorraine, S. R. Johnstone, A. Graham, S. Greenhough, and P. Martin, "The connexin mimetic peptide gap27 and cx43-knockdown reveal differential roles for connexin43 in wound closure events in skin model systems," *International journal of molecular sciences*, vol. 19, no. 2, p. 604, 2018.

[169] B. H. Defranco, B. M. Nickel, C. J. Baty, J. S. Martinez, V. L. Gay, V. C. Sandulache, D. J. Hackam, and S. A. Murray, "Migrating cells retain gap junction plaque structure and function," *Cell communication & adhesion*, vol. 15, no. 3, pp. 273–288, 2008.